Numerical Investigation of Liquid Film Dynamics and Atomisation in Jet Engine Fuel Injectors

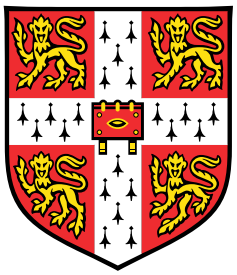

Camille Bilger

Supervisor: **Prof. R. Stewart Cant**

Department of Engineering
University of Cambridge

This dissertation is submitted for the degree of
Doctor of Philosophy

Newnham College September 2017

"Writing this book is not just me encouraging others to lean in. This is me leaning in. Writing this book is what I would do if I weren't afraid."

– Sheryl Sandberg *in*
Lean In: Women, Work, and the Will to Lead

"There is no reason to think that the same phenomenology and ideas would not apply to the opposite situation of bubbles forming in a continuous liquid phase: the fundamental instability, that of a hollow ligament in a liquid, is of the same nature as that of a liquid ligament in a vacuum."

Villermaux 2007 citing Chandrasekhar 1961

Declaration

I hereby declare that except where specific reference is made to the work of others, the contents of this dissertation are original and have not been submitted in whole or in part for consideration for any other degree or qualification in this, or any other university. This dissertation is my own work and contains nothing which is the outcome of work done in collaboration with others, except as specified in the text and Acknowledgements. This dissertation contains fewer than 65,000 words including appendices, bibliography, footnotes, tables and equations and has fewer than 150 figures.

Camille Bilger
September 2017

Acknowledgements

I arrived at Cambridge with a crippling inferiority complex, convinced that they must have made some dreadful administrative error and that sooner or later I would be found out and hounded out of town by gowned academics. I am embarrassed to say that I still do feel this way at times. I was not sure if Cambridge, with its bicycles and its brains, was where I belonged, but I could not wait to be part of this intriguing community. After an abysmal first week, that culminated with one or two narcissistic comments on my lack of ability to face an Engineering degree when coming from a Physics background, I unleashed my inner engineer and in the inspiring environs of the Engineering Department started to aspire to prove them wrong.

It is difficult to express how much I value the guidance of my thesis supervisor, Prof. Stewart Cant, for his invaluable help and discussions on my work, his constant optimistic encouragement, kindness and consideration, his faith in my work – more faith than I usually gratify my own self with – enlivened by his great sense of humour. But beyond the purely professional aspect, what I will remember most and will remain close to my heart is our supervisor/student personal relationship, in which I found a mentor and a lifelong friend.
In addition, I wish to express my full gratitude to Dr. Andrea Giusti who assisted with never-ending computing issues, saving me significant amounts of time through his expertise. I am also grateful to the Engineering and Physical Sciences Research Council (EPSRC) and Rolls-Royce plc. for funding this research project, and for the fruitful discussions on my work with the senior staff. Finally, Mr. Peter Benie was an invaluable ally in conducting my computational research all these years. I am thankful for his support and friendship.
I would like to thank my scientific collaborators – Mr. Mahmoud Aboukhedr and Dr. Konstantina Vogiatzaki from City University of London and the University of Brighton – for the project described in Chapter 5. I would also like to thank Audrey Valreau for her valuable input to Chapter 7.

Of course, I could speak about the sweat-inducing coding problems and the interminable writing sessions, the caffeine-riddled nights and the worse-for-wear days. Which is why

I am extremely thankful to all who have provided friendship and kept me emotionally stable, without whom life would be very dull and those years would not have been as enjoyable.

To the people who unfortunately left Cambridge during the course of my Ph.D. but remain close to my heart and on the other end of the line: Andrea for all the laughters as well as escorting me to Royal Ascot and many other Cantabrigian events; my housemate Stefania who stepped into the role of my big sister when away from home; Pascale and Fabian, whose wisdom I miss dearly.

Cindy (and Ashley!) and Shobana for providing great company when writing up, I could't have asked for better friends and listeners to my emotional dramas. Sébastien and Romain for contributing to some insanity in our encounters, much needed to unwind from work. Thank you to Jo and Callum for feeding me many dinners and coaching me in the last few weeks leading up to this, I am happy to have reconnected with my St Andrews friends here in Cambridge. Thank you to Kelly for providing me with sisterhood across the pond; Petros for our writing sessions during Michaelmas and Lent terms – I will always cherish Jesus College library; André for always reminding me of the bigger picture; Rachel who believed in my capacity to do as well in Engineering as during our collaborative times in Astrophysics; Girish for the cherished memories of our time together, Janine, you enlightened my time in Cambridge, thank you for taking such good care of me and listening to me. Finally, my long-term friends Annick and Pauline, Christa and Calvyn, always in my mind and a plane-ride away.

My final thanks go to my lab-mates who provided constant support along the years and a pleasant working atmosphere in the laboratory, and Minki without which my need for pet's company would not have been complete.

• ∼ •

I also have very special thoughts for my boyfriend Pierre, who supported me and my academic endeavours – in distance – to the margins of what is bearable and this despite my moods, especially during the writing of the present work. I could not have asked for a better expert graphic eye on compiling this thesis, and for better times when reunited on week-ends.

Enfin, je tiens à embrasser mes parents, mon frère, ma marraine ainsi que mes grands parents qui, par leur amour et dévouement, m'ont permis d'être qui je suis aujourd'hui. Leur soutien, leur écoute et leur conseils tout au long de ma vie m'ont permis de croire en moi et de me dépasser, malgré mes fréquents moments de doute.

It is now with a face aglow with the flushed symptoms of “slight” caffeination and stress that I need to put an end to this work. A wave of sentimentality threatens to overcome me as I write these words. This academic journey was rather therapeutic for me. It made me realise how far I’d come in the years I’d been here – how my self-confidence has grown, how I (try to) no longer seek the forever unattainable prize of perfection, how I have learnt to be content with who I am. I realised that Cambridge will always be a place where I belong.

Abstract

Today's aerospace industry continues to exploit liquid hydrocarbon fossil fuels. Motivated by operational considerations, continued availability and cost, this is likely to be the case for many years, despite the obvious environmental concerns. The interplay of liquid atomisation, spray vaporisation and the combustion process are intricately linked. However, the physical process of fuel injection and its atomisation into tiny droplets prior to combustion remains poorly understood. Because atomisation governs the size of the fuel droplets, and therefore their subsequent evaporation rate, adjusting the injection sequence is of paramount importance and will have far-reaching repercussions on many aspects of the combustion process, for example pollutant formation.

In the context of jet engines, kerosene is usually injected in its liquid form via an airblast-type fuel injector. A coflowing high-speed airstream destabilises the liquid fuel, which is thus sprayed into fine droplets into the combustion chamber. The prediction of this phenomenon for various operating conditions relevant to the aeronautical industry requires a deeper understanding of the mechanisms involved in the interaction of the two fluids.

A key element in predicting the complex behaviour of spray formation and evolution in jet engines is accurate modelling of fuel atomisation. Atomisation represents one of the key challenges that remains to be undertaken to make predictive computational simulations possible. However, the inherent multi-physics and multi-scale nature of this process limits numerical investigations. Thanks to the steady progress in computer power and Computational Fluid Dynamics (CFD) methods, computational modelling of injection systems emerges as a promising tool that can drive the design of future devices.

This research project sets out to investigate the atomisation process in detail, in particular in providing physical insight into the fundamental physics of the phenomenon, in conjunction with an analysis on wetting behaviours and liquid droplet tracking. High-fidelity numerical simulations are performed using a novel in-house state-of-the-art multiphase flow modelling capability, *RCLSFoam*. The performance of the numerical scheme is demonstrated on typical two-dimensional and three-dimensional benchmark test cases relevant to both multiphase flow modelling and atomisation, and validated against other computational methods.

An informed and systematic qualitative assessment of the topological variations of the phase interface during primary atomisation of a liquid film is made through dynamical analysis, while investigating an extensive domain of operating conditions at ambient and aero-engine injection conditions relevant to industry. This analysis demonstrated the influence of shear-driven instabilities on the atomisation process. The shear stress and difference in inertia between liquid and gas are observed to play a significant role in the atomisation process. In addition, the key physical mechanisms and their competing effects have been mapped out in order to predict the evolution of the process according to the operating conditions of the injection system. The proposed cartography gathers four different atomisation mechanisms. In particular, for sufficiently high liquid injection speeds, three-dimensional wave modes were observed to co-exist (the "3-D wave mode" regime). For very low liquid flow rates, accumulated liquid at the atomising edge undergoes deformation by which droplets are generated (the "accumulation" regime). For an increasing gas injection speed and a fixed liquid velocity, the effects of surface tension were observed to result in the generation of streamwise ligaments only, which tend to pair up (the "ligament-merging" regime). Finally, "vortex action" is another observed mechanism by which the liquid film is fragmented. Overall, this research project culminated in (i) the study of dynamic wetting behaviours, with the implementation and validation against experimental data of the Kistler dynamic contact model; and (ii) the demonstration of an algorithm for droplet capture and subsequent post-processing analysis of the droplet characteristics.

Table of contents

List of figures

List of tables

Nomenclature

Roman Symbols

$\hat{n}$	Unit normal vector
$\boldsymbol{\mathcal{D}}$	Rate-of-strain tensor
$\boldsymbol{\mathcal{I}}$	Unit tensor
$\boldsymbol{\mathcal{S}}$	Stress tensor
$\mathbf{f_g}$	Body forces
$\mathbf{f}_c$	Capillary force
$\mathbf{u}$	Velocity vector
$\overline{u}$	Mean velocity
D_i	0-halo sub-domain
D_{h_i}	n-halo sub-domain
f_{Hoff}	Hoffman function
h	Lengthscale
L	Lengthscale for dimensional analysis
N_S	Periodicity of the re-initialisation
p	Static pressure

t	Time
u_x	Velocity component along the x–direction
u_{CL}	Dynamic contact angle velocity scale
A	Atwood number

Greek Symbols

δ_Γ	Distribution concentrated on the interface
ϕ	Level set function
δ	Boundary layer thickness
δ_w	Vorticity thickness $\delta_w = \dfrac{\bar{u}_{\mathrm{gas}} - \bar{u}_{\mathrm{liq}}}{\left(\dfrac{\partial u_{\mathrm{gas}}}{\partial y}\right)_\Gamma}$
ε	CLS coefficient
κ	Interface curvature
μ	Dynamic viscosity
ν	Kinematic viscosity
$\overline{\Delta_x}$	Characteristic average mesh-element size
ψ	Conservative level set function
ρ	Density
σ	Surface tension coefficient
τ	Artificial time step (re-initialisation procedure)
θ_{adv}	Limiting advancing contact angle
θ_{dyn}	Dynamic contact angle
θ_{eq}	Equilibrium contact angle

θ_{rec}	Limiting receding contact angle

Subscripts

Γ	Interface
gas	Gaseous phase
liq	Liquid phase
rel	Relative (between continuous and dispersed phases)
i, j	Spatial index
x	x–direction (streamwise)
y	y–direction (vertical)
z	z–direction (spanwise)
LG	Liquid-gas phase interfacce
SG	Solid-gas phase interface
SL	Solid-liquid phase interface

Other Symbols

Ca	Capillary number	$\text{Ca} = \dfrac{\text{We}}{\text{Re}}$
Fr	Froude number	$\text{Fr} = \dfrac{u^2}{gh}$
MFR	Momentum flux ratio	$\text{MFR} = \dfrac{\rho_{\text{gas}} \bar{u}^2_{\text{gas}}}{\rho_{\text{liq}} \bar{u}^2_{\text{liq}}}$
MR	Momentum ratio	$\text{MR} = \dfrac{\rho_{\text{gas}} \bar{u}^2_{\text{gas}} h_{\text{gas}}}{\rho_{\text{liq}} \bar{u}^2_{\text{liq}} h_{\text{liq}}}$
Oh	Ohnesorge number	$\text{Oh} = \dfrac{\mu_{\text{liq}}}{\rho_{\text{liq}} h_{\text{liq}} \sigma^{1/2}}$

Re	Reynolds number	$\mathrm{Re}_{\mathrm{gas,h_{liq}}} = \dfrac{\rho_{\mathrm{gas}} \bar{u}_{\mathrm{gas}} h_{\mathrm{liq}}}{\mu_{\mathrm{liq}}}$
We	Weber number	$\mathrm{We}_{\mathrm{rel,h_{liq}}} = \dfrac{\rho_{\mathrm{gas}} (\bar{u}_{\mathrm{gas}} - \bar{u}_{\mathrm{liq}})^2 h_{\mathrm{liq}}}{\sigma}$
We	Weber number	$\mathrm{We}_{\mathrm{gas,h_{liq}}} = \dfrac{\rho_{\mathrm{gas}} \bar{u}_{\mathrm{gas}}^2 h_{\mathrm{liq}}}{\sigma}$

Acronyms / Abbreviations

AMR	Adaptive Mesh Refinement
CFD	Computational Fluid Dynamics
CLS	Conservative Level Set method
CPU	Central Processing Unit
CSF	Continuum Surface Force method
CSF	Continuum Surface Force method
DIC	Simplified diagonal-based incomplete Cholesky preconditioner for symmetric matrices
DILU	Simplified diagonal-based incomplete LU preconditioner for asymmetric matrices
DNS	Direct Numerical Simulation
GAMG	Geometric agglomerated algebraic multigrid preconditioner
GFM	Ghost Fluid method
KH	Kelvin–Helmholtz instability
LES	Large Eddy Simulation
LPP	Lean Premixed Pre-vapourised combustion strategy
LS	Level Set method
MULES	Multidimensional Universal Limiter with Explicit Solution

PbiCG	Preconditioned bi-conjugate gradient solver for asymmetric matrices
PCG	Preconditioned conjugate gradient solver for symmetric matrices
PDA	Particle Doppler Anemometry
PISO	Pressure-Implicit with Splitting Operators method
PTV	Particle Tracking Velocimetry
RCLS	Robust Conservative Level Set method
RK	Runge–Kutta scheme
RTI	Rayleigh–Taylor instability
SMD	Sauter Mean Diameter
SPH	Smoothed Particle Hydrodynamics
TVD	Total Variation Diminishing
VoF	Volume of Fluid method
WENO	Weighted Essentially Non-Oscillatory scheme

Chapter 1

Introduction

1.1 The aeronautical application

1.1.1 Examples of multiphase flows and atomisation

Atomisation is the process whereby an intact volume of liquid is converted into a multiplicity of small drops [122] – etymologically "*subdivide down to the atom size*". As Villermaux [223] stated, "*the long history of the subject is certainly not a sign of lack of progress but rather reflects its ever-renewed fields of application*". The question of the principles of matter division arose from mineral grinding up to modern developments in nuclear fission [223]. It is a phenomenon that is involved in many natural and industrial operations. Understanding the dynamics of multiphase flows is therefore of critical engineering and scientific importance. Our everyday encounters with liquids is nearly always at a free surface, such as when drinking, washing or walking under the rain. Our daily lives involve a multiphase flow of one sort or another. Sometimes, one of the phases is a solid, such as in particle pollution and fluidized beds, but in a large number of applications one phase is a liquid and the other is a gas. The liquid droplets torn off by the wind at the wave crests in the ocean are an obvious example.

Spray formation is used in many industrial processes such as sprayed paint and medicines, ink-jet printers, agricultural sewage, diesel engines, and liquid propellant combustion in the aerospace industry. It seems appropriate to start our discussion on multiphase flows by showing a few "real" systems to give some insight into the kind of systems that can be examined in the workings of Nature and the enterprises of mankind. Fig. 1.1 shows a

few examples of how a liquid bulk is ejected from a nozzle to generate a spray of liquid droplets.

(a)

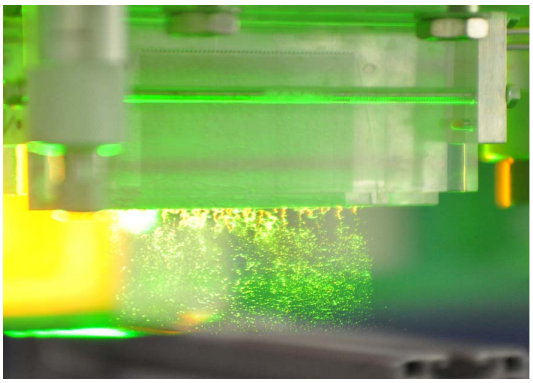

(b)

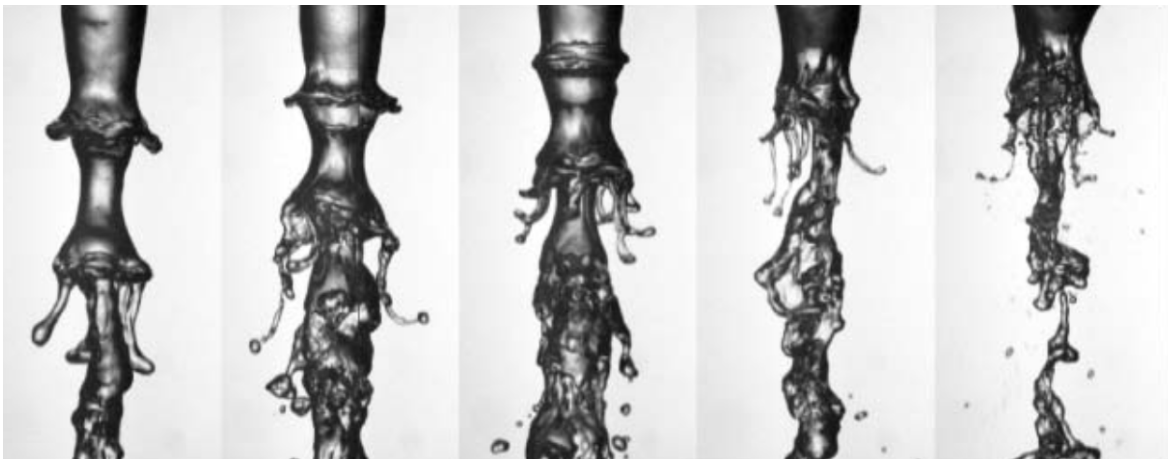

(c)

Fig. 1.1: (a) Flapping liquid sheet undergoing atomisation through an annular atomiser by Duke et al. [56]; **(b)** Close-up of a planar airblast atomiser, backlight illumination during the atomisation process [72]; **(c)** Snapshots of an 8mm-diameter water jet at 0.6m/s destabilised by a fast coaxial air stream by Marmottant & Villermaux [141].

Liquid droplets impacting solid or liquid surfaces generally splash, often disrupting the surface significantly, create a liquid crater and a rim that often breaks into droplets. Edgerton's famous 1936 photograph captures the moment when a drop of milk splashes into the shape of a crown (Fig. 1.2). As the crater collapses, air bubbles are sometimes trapped in the liquid. These air bubbles then typically rapidly collapse – implode – under the action of the surrounding liquid. The formation and collapse of bubbles within fluids can be a big engineering problem. Called cavitation, the process may erode vital pieces of mechanical

equipment such as turbines or propellers. Kobel et al. [113] notes that similar processes could be at work in the collapse of cavitation bubbles in larger spherical fluids, such as Type II supernovae which in the later stage of their lives collapse under their own weight, almost as if they were empty inside (Fig. 1.3).

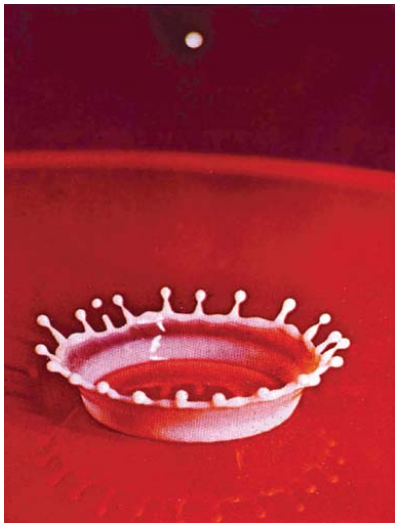

Fig. 1.2: Photograph by Harold Edgerton of a drop of milk splashing into a crown of droplets (1936). Taken from Yarin [234].

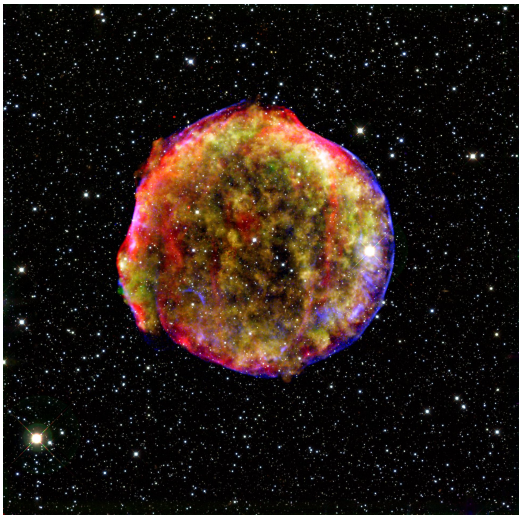

Fig. 1.3: The famous supernova remnant Tycho's Nova [94], imaged by NASA Chandra X-ray Observatory. The telescope is named after astrophysicist Subrahmanyan Chandrasekhar whose work on stability theories [29] will be discussed further in Chapter 5.

1.1.2 The thermodynamic cycle of gas turbines

Combustion is a chemical exothermic reaction between a fuel and an oxidant in its gaseous form. In aeronautical propulsion systems, combustion uses the oxygen contained in the ambient air as an oxidant and a hydrocarbon fuel is stored initially in liquid form in order to maximise its stored energy density. In gas turbine aero-engines (Fig. 1.4), the thermodynamic cycle begins with a compressor that raises the pressure of incoming air. In the combustor, the high-pressure and high-temperature air mixes with and vapourises the liquid fuel. The resulting mixture is combusted, releasing the chemical energy stored in the fuel as thermal energy [42, 232]. Upon exit of the combustor, the combustion gas passes through the turbine from which work is extracted to drive the compressor and finally is expanded to atmospheric pressure through the nozzle, resulting in an acceleration of the flow exiting the engine and generating a forward thrust.

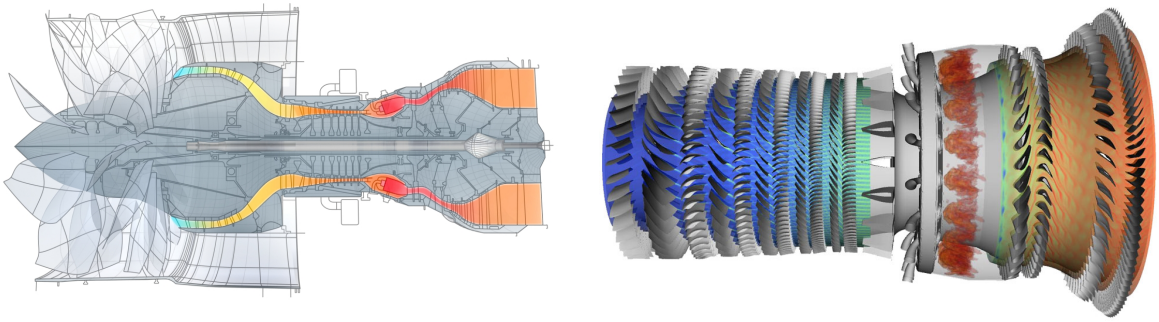

(a) **(b)**

Fig. 1.4: **(a)** Complete engine design with fan, compressor, shaft, turbine and nozzle. Taken from www.newac.eu; **(b)** Comprehensive simulation of a Pratt & Whitney compressor/combustor/turbine assembly by the Center for Integrated Turbulence Simulations at Stanford University. Contours of entropy in the high-pressure compressor and in the first two stages of the turbine, as well as contours of temperature in the combustor. The 18 fuel injectors and resulting burning flames (shown in red) are visible.

1.1.3 Liquid fuel atomisation

Today's air transport systems continue to exploit liquid hydrocarbon fossil fuels, which is likely to continue over time prioritised by operational considerations, continued availability and cost impact on the sector. Hence, aspects related to liquid fuel preparation and fuel-air

mixing are critical for the development of lean burn combustors, as well as addressing safety-related constraints including freezing point (given the low temperatures at high altitude). Liquid jet fuels are typically kerosene-type jet fuels such as Jet A, Jet A-1 or JP-8, which have a high energy density both by volume and mass. It is therefore necessary to vaporise first the liquid fuel in order to obtain a homogeneous gaseous fuel/air mixture. In the aeronautical industry, the aim is to produce a high ratio of surface area to volume in the liquid phase, resulting in very high evaporation rates for the subsequent combustion.

1.1.4 Fuel injectors: atomisation devices

In the commercial and military aircraft industry, aero-engines generally rely on fuel preparation systems known as atomisers to inject the liquid fuel in combustion chambers (Fig. 1.5). Atomisers eject a liquid bulk that then disintegrates into isolated liquid structures – primary breakup – which will further break up into the desired fuel spray – secondary breakup.

A review of the main injection systems has been done by Lefebvre [123]. For each of these, the quality and the properties of the atomisation will have a significant effect on the efficiency of the system [223]. Indeed, the performance of any given type of atomiser firstly depends on the geometry of the injection system that determines what disruptive forces will be at play upon interaction between the liquid and gas phases. It thus constitutes a first step towards determining the resulting spray characteristics and distribution pattern inside the combustion chamber, on which the combustion performance depends.

The liquid fuel is introduced into the combustion chamber by virtue of an ensemble of injectors (Fig. 1.5a); the function of which is to disintegrate the liquid bulk into a cloud of small liquid droplets. Currently, in order to achieve an effective injection under any flight condition, several types of atomisers are implemented [37, 123]. This way, “pressure atomisers” allow the formation of a spray of fine droplets in the presence of small velocities and small air densities, at take-off or high-altitude re-light conditions. “Airblast” injectors provide a higher flow injection rate. Both those atomiser devices employ a strong shearing intensity between the liquid and the ambient gas to provoke atomisation. In the case of pressure atomisers, the significant shearing intensity is due to a high liquid injection speed into quiescent air. The function of airblast type injectors on the other hand is to employ the momentum of a fast coflowing gas stream to shatter a parallel liquid flow of slow speed. Unfortunately, it has been shown that pressure atomisers give rise to high rates of soot formation when operating at high combustion pressures, resulting in high flame radiation and excessive exhaust smoke [175]. These complications have led in recent years to a renewal of

interest in airblast atomiser designs which is ideally suited for gas turbine applications since high-velocity air is always readily available due to the pressure drop across the combustion chamber [175].

Most of the systems now in service are of airblast prefilming type, in which a liquid fuel film flows over a solid cylindrical wall before forming an annular liquid sheet. These devices provide a fine atomisation and comparatively small changes in performance over a wide range of fuel rates and low pressures losses [124]. The geometry of the device in this instance is axisymmetric. It is exposed on both sides to separate annular air flow passages, to allow high-velocity air to impact both sides of the liquid sheet for atomisation. Those two coflowing air streams have a co- or counter-rotating swirl. One example is shown in Fig. 1.5b, designed to operate in the gas turbines of Rolls-Royce plc. [26, 178]. In this design, the fuel injector has, in order from radially inner to outer, a coaxial arrangement of an inner swirled air passage, an annular fuel passage, an annular outer swirled air passage. The fuel passage extends to a prefilming lip where the fuel is spread out in a thin continuous sheet of uniform thickness before being subjected to the atomising action of high-velocity air and being discharged at the atomising lip [122]. At the exit of the atomiser, at the atomising lip, the two air flows merge with the fuel liquid sheet and convey the fuel spray stream into the combustion zone. The atomisation of the bulk liquid fuel produces a spray of small drops whose surface area is large so that the rates of heat and mass transfer during combustion are greatly enhanced [232].

The quality of the atomisation process has a direct influence on the combustion efficiency and the formation of pollutants (NO_X, unburnt hydrocarbons), particulate matter and soot [123], of which the reasons will be further discussed in Section 1.2.3. Thus, a great deal of work is being done by engine manufacturers to optimise the geometry of injectors. Atomisation is one of the most decisive steps in fuel preparation. Atomisation is the mechanism from which all subsequent spray processes originate (evaporation and combustion). Fuel injectors are thus central to the nature of the primary zone flow field in combustion chambers and the chemical reactions happening within it. Historically, the development of reliable tools for the description of spray evaporation and spray combustion has taken priority over research in atomisation modelling, due to the lack of high-order numerical techniques and computational resources needed. However, the prediction of liquid fuel preparation should be improved since it inevitably influences all the combustion process and the flame dynamics. It is desirable to have an *a priori* knowledge of the principal spray characteristics such as the liquid dispersion structure, in particular its distribution of droplet sizes and spatial distribution as a function of the operating conditions and geometrical parameters.

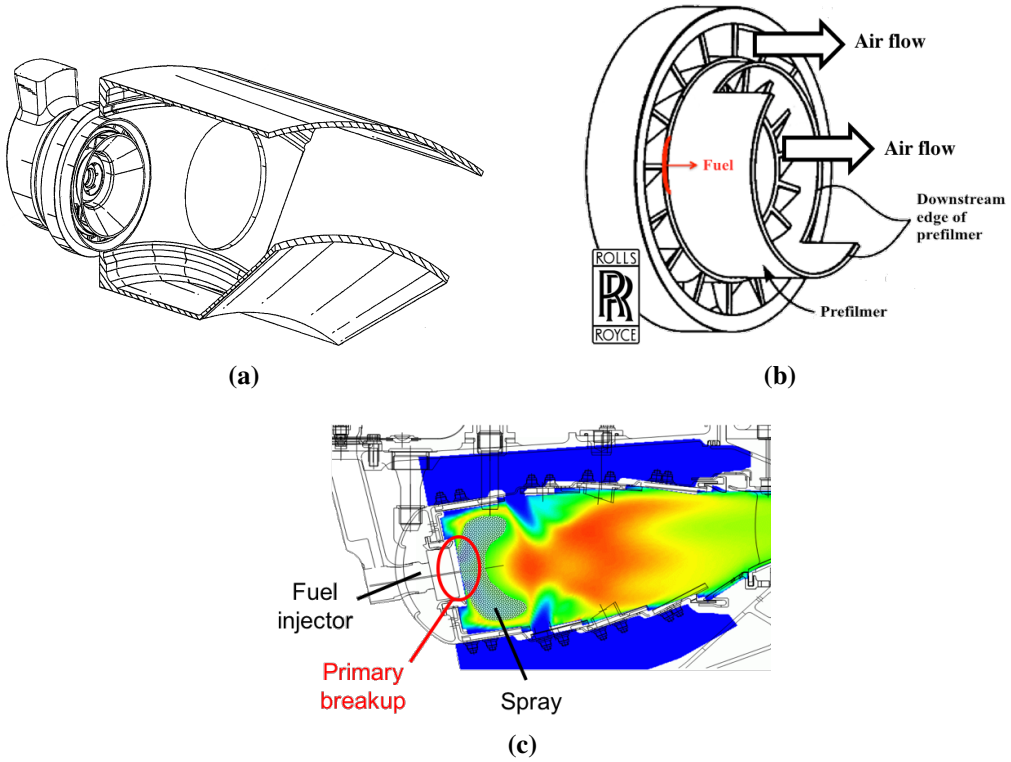

Fig. 1.5: **(a)** Perspective view of a lean direct injection fuel nozzle, shown within the combustion chamber of a gas turbine engine [26]; **(b)** Schematic view of an annular fuel injector apparatus with prefilmer. The fuel impinges on the surface and flows, by means of a passing airflow, to the downstream edge, from where the fuel is shed. Adapted from Sanders [180]; **(c)** Schematic representation of the kerosene spray overlaying the temperature contours in a combustion chamber (courtesy of Rolls-Royce plc).

1.1.5 Atomisation: an active research field

During the past decades, there has been a tremendous expansion of interest in the science and technology of atomisation and spray combustion. This major field of research is now accompanied by a proliferation of laser diagnostics for spray analysis and mathematical models for spray combustion processes. In general, techniques aimed at resolving the interface between liquid film and gas-phase require very high mesh resolutions and advanced numerical methods so that they are characterised by a very high computational cost to be used in conjunction with complex realistic configurations in the industrial design process. The solution to the flow dynamics will be as precise as the cell size used in the discretised computational domain. The computing time being approximatively linearly dependent on the

number of cells in the mesh can easily become extremely costly. It is necessary to recall that doubling the number of cells in each direction incurs a multiplication of the total number of cells by 8. With High Performance Computing (HPC) having gained considerable importance, capable of modelling complex geometries with an increasing number of technological details, three-dimensional numerical simulations of transient flows are becoming feasible and more sophisticated [31, 38, 46, 50, 158].

1.2 Motivations

1.2.1 Environmental concerns

Today's aerospace industry faces many challenges, such as globalisation, new markets and the need for innovation due to climate change and an increasing scarcity of resources. It is of central importance to align our efforts towards a long-term vision for this vital sector of our society and economy. Aviation's economic and societal contribution is substantial, worth around €220 billion and providing 4.5 million jobs worldwide. The disruption to the European air transport system of 2010's volcanic eruption in Iceland amounted to approximately €2.5 billion in the first week, which illustrates the value of the aviation's contribution and its economic impact. Aeronautics continues to be a catalyst for growth of an integrated high technology research development and manufacturing sector. Worldwide, air traffic is predicted to grow at a rate of $4-5\%$ per year, and even faster in the Middle East and Asia.

However, aviation continues to exploit liquid hydrocarbon fossil fuels. Therefore, environmental concerns are central to the policy debate and remain a prime driver in the development of air vehicles. A coordinated approach to fossil fuel-engine systems development must be taken to address their impact on the environment. The Advisory Council for Aviation Research and Innovation in Europe (ACARE) have set severe targets to improve fuel efficiency, achieve neutral carbon growth, and reduce net greenhouse gas emissions. These targets for 2020 include a reduction of fuel consumption and CO_2 emissions by 50% per passenger kilometre and a reduction of the NO_X emissions by 80%. Such targets require a focus on the development of low-emission aerospace combustion systems for the reduction of NO_X, CO_X and carbonaceous deposits, the by-products of poorly-controlled combustion.

1.2.2 Lean-burn combustor technology

To increase the engine performance and efficiency, combustion chambers operate at ever higher local pressures and temperatures, at the expense of more thermal NO_X production. Indeed, operating at higher peak flame temperatures in the combustion chamber leads to an increase in the production of highly-polluting thermal NO_X [232]. To prevent this, engines normally operate below the stoichiometric fuel-to-air ratio: lean combustion strategy. Lean burn operation of the combustor has been recognised as one of the most effective solutions for the new generation of aero-engines to meet low emission requirements [58]. However, the low NO_X potential of lean combustion is offset by the operational disadvantages of its narrow stability limits and its susceptibility to autoignition and flashback.

Indeed, the resulting drawback from a lower flame temperature environment is poorer flame stability as temperatures in the flame region can be drastically reduced compared to the values encountered in diffusion flames (stoichiometric mixture). The success of future engines is entrusted to the ability of engineers to gain a better control over the fuel droplet sizes and their spatial distribution in the combustion chamber, to achieve a good degree of mixing between the liquid fuel droplets with the oxidant, which would improve flame stability [232]. This is because discrete liquid drops have a range of sizes and move in different directions with different velocities to that of the main gas stream, if the droplet Stokes numbers are rather large. It leads to irregularities in the propagation of the flame front due to the lack of uniformity in the unburnt mixture [228].

1.2.3 Atomisation and fuel/oxidant mixing

The question is how to manage rapid, thorough mixing with complete combustion resulting in minimum polluted exhaust gases. A good homogeneous mixing of the fuel and oxidant is a direct consequence of a fine atomisation and fast vaporisation and thus a consequence of an optimised fuel injection. A controlled atomisation is of paramount importance – in terms of droplet size and droplet spatial distribution – so that the fuel vaporises and mixes more quickly with the oxidant. The quality of the homogeneity of the mixture is enhanced when one can control the spatial arrangement of the droplets in the combustion chamber as well as how small those droplets are. The latter is only possible if the necessary atomisation mechanism and atomisation conditions for the generation of small droplets are not implicitly imparting a specific (and therefore un-controlled) spatial distribution of droplets.

As a result, the heat transfer surface area between oxidant and fuel increases, the fuel will burn more quickly, leading to an increase in the combustion rate and ultimately allowing combustion chambers to be more compact. The overall effect is better efficiency – i.e. an increased heat release per unit volume maximises the performance of the gas turbine – and less pollutants.

1.2.4 Current state of knowledge

Various observations are brought together to give a unified picture of the overall transition between a compact macroscopic liquid volume and its subsequent dispersion into stable drops [223]. However, the ubiquity of fragmentation phenomena has prompted a number of interpretations and paradigms. In light of these facts, the physical process of fuel injection and its atomisation into tiny droplets before being burned remains poorly understood. No complete theory has yet been developed to describe the hydrodynamic and aerodynamic processes involved when liquid sheet disintegration occurs.

Experimental investigation is greatly handicapped as it involves multiple and repeated experimental trials – with the difficulty in observing and measuring flow properties in the dense spray region near the injection point – at the expense of time and cost. On the other hand, linear stability analyses are systemically limited to simplified cases because of the increasing complexity of the mathematical equations governing the fluid motion. When considering viscosity, no analytical solution exist. In addition, linear stability analyses are valid only for small departures from the basic state, and solely highlight the origin of the instability and not their transient evolution over a long period of time [38]. They mask, to some extent, the full picture of the fluid dynamics.

Computational modelling can provide an economical alternative to help improve and control atomisation and spray combustion, thereby increasing fuel-engine systems performance and efficiency, if the boundary conditions are well defined and the meshing used is sufficiently small compared to the smallest entities computed [194]. The future of research and industrial development therefore lies in the combination of three focal areas: experimental work, computational modelling and linear stability analyses.

In past years this problem has attracted the interest of many scientists who have developed a broad variety of multiphase flow numerical approaches to come closer to simulating the atomisation process and understanding real injection systems [31, 38, 41, 46, 50, 75, 160, 183]. However, as much as the accuracy of measurements in experiments depends on the quality and the technical sophistication of the tools, the precision of numerical solutions

depends greatly on the quality of the discretisation scheme employed. Also, it is necessary beforehand to validate those numerical methods on simplified configurations and in some cases, there is still a need for modelling. Indeed, a detailed and accurate description of all the physical phenomena is usually not practicable in typical industrial approaches without the introduction of assumptions and simplified models.

Due to the large density ratio and the intense multi-scale character of a realistic atomisation process, numerical simulations are extremely expensive and challenging. Rather than compute the breakup phenomena in detail, models are often used instead in industry to reproduce the main features of the required cloud of droplets. Industrial calculations have so far relied on over-simplistic definitions for fuel sprays. Among the assumptions used, the droplets being perfectly spherical, when in fact such sprays can contain a large proportion of irregularly-shaped droplets. The boundary condition for the liquid fuel is commonly imposed through the numerical injection of droplet parcels with given droplet characteristics. A droplet population assumed to have been generated by primary breakup, with a high level of uncertainty, is assigned as a boundary condition [35, 98]. Where the droplet characteristics – such as size and velocity distribution – have been defined using empirical relations obtained from experimental data [191].

Thus, the strong intrinsic coupling between the gas and liquid phases and the resulting flow unsteadiness during the first instants of liquid injection, which directly affects the flame behavior, are thus not taken into account. As primary atomisation influences the fuel distribution inside the reaction zone significantly, the simplification of ignoring the primary atomisation inside the nozzle – widely used in current modelling approaches – may lead to incorrect fuel distribution predictions during the design phases of combustion systems.

1.3 Aims and objectives – Thesis outline

The few research activities devoted to the atomisation of a liquid in the presence of a pre-film zone do not allow for an exhaustive analysis of the influence of the injection parameters on the atomisation process. Within this framework, a comprehensive overall description of the phenomenon of liquid spraying is still incomplete. This lack of understanding limits the optimisation of the injection systems and justifies the continuation of this research on this subject. We are here interested in the first stage of the atomisation process: primary breakup. The dissertation is organised as follows.

Chapter 2 The main aim of this chapter is to introduce the basic concepts of liquid fuel preparation and primary and secondary atomisation, identifying the most important parameters for the description of these phenomena – as reported in the literature – in particular for systems equipped with pre-filming airblast injection systems. The current state-of-the-art numerical and experimental works in the field are discussed, including a brief discussion of the different numerical methods to resolve the phase interface. In addition, an insight into atomisation regime classification is given, highlighting the handful attempts to systematically correlate the observed phenomenology to physical quantities and non-dimensional groups.

Chapter 3 The numerical implementation of the mathematical description of two-phase flows as developed by Pringuey [158] with interface-tracking, *RCLSFoam*, is described. We introduce an add-on numerical algorithm for the modelling of dynamic contact angles at wall boundaries that has been incorporated into this two-phase flow solver and assessed by means of specific test-cases.

Chapter 4 gives particular attention to the presentation of the droplet tracking algorithm implemented by Pringuey [158] in the *RCLSFoam* solver and to the demonstration of its efficiency on various benchmark test-cases.

Chapter 5 is dedicated to presenting collaborative work with City University of London and the University of Brighton. A new validation exercise on *RCLSFoam* has been performed using literature test-cases and compared against the new state-of-the-art multiphase flow solver by Aboukhedr et al. [1]. This work has been published in Bilger et al. [17].

Chapter 6 discusses the results from the high-fidelity transient three-dimensional calculations of the atomisation of a prefilming airblasted liquid sheet. From this fundamental investigation of atomisation, we provide detailed information on the physical processes and liquid structures emerging in the near nozzle region. Based on the findings of this parametric study, we can suggest some defining features of disintegration. Atomisation mechanisms are identified and a preliminary regime map has been constructed based on our numerical simulations. Three distinct types of "regime" are reported: accumulation, ligament-merging and 3-D wave modes.

Chapter 7 The subject of our research activity in Chapter 7 is to describe and study the mechanisms by which a liquid film fragments at higher pressure conditions. In addition, based on our observations, we propose three innovative prefilmer plate geometries that hint

at the need for further examination.

Chapter 8 A summary of the main achievements of this research is given together with conclusions and recommendations for future research.

Chapter 2

State of the Art in Primary Breakup

As discussed in Chapter 1, typical injection systems used in aeronautical gas turbine applications consist of airblast atomisers. In such systems, the fuel is usually injected in the form of a thin liquid sheet, which disintegrates at the exit of the injection system into droplets.

This chapter will address the background literature relevant to the effects of geometry and flow configuration on the primary breakup phenomenon, with particular focus on the many intertwined complex mechanisms characterising liquid fuel preparation and the physical structure and dynamics of a spray. As such, this chapter is organised into three sections: the experimental investigations and linear stability analyses that lead to the understanding of liquid atomisation with a particular emphasis on the body of work dedicated to airblast atomisation; the state-of-the-art numerical techniques available to simulate multiphase flows and liquid disintegration; the attempts that have been made at classifying liquid atomisation into regimes. For a more comprehensive analysis on atomisation in all possible geometrical and flow configurations – which is beyond the scope of this chapter – the reader is invited to consult specific literature and additional references cited therein.

2.1 Physics of primary breakup through experimental observations and linear stability analysis

Atomisation is visualised as a sequential process, as shown in Fig. 2.1. The four-steps process exhibits characteristics that echo each other in different geometrical configurations used as liquid atomisation nozzles: liquid round jets or pressure-atomised sprays [61, 141], liquid sheets [64, 137] or liquid films [15, 72, 142]. We shall not dwell here on a comprehensive

description of the atomisation of round liquid jets as the physical problem is rather different to airblasted liquid sheet atomisation, which is the subject of the present work. The reader is referred to Desjardins [50], Reitz [168] and Farago & Chigier [62] for a full account of jet atomisation.

The physical processes associated with primary breakup have been studied by only a fairly small number of research teams. Historically, the experimental approach was prevalent. In parallel, linear and non-linear stability analyses have highlighted quantitative characteristics in relation with the amplification of perturbations at the liquid interface. It is only recently that numerical simulations have successfully reproduced the experimentally observed physical phenomena.

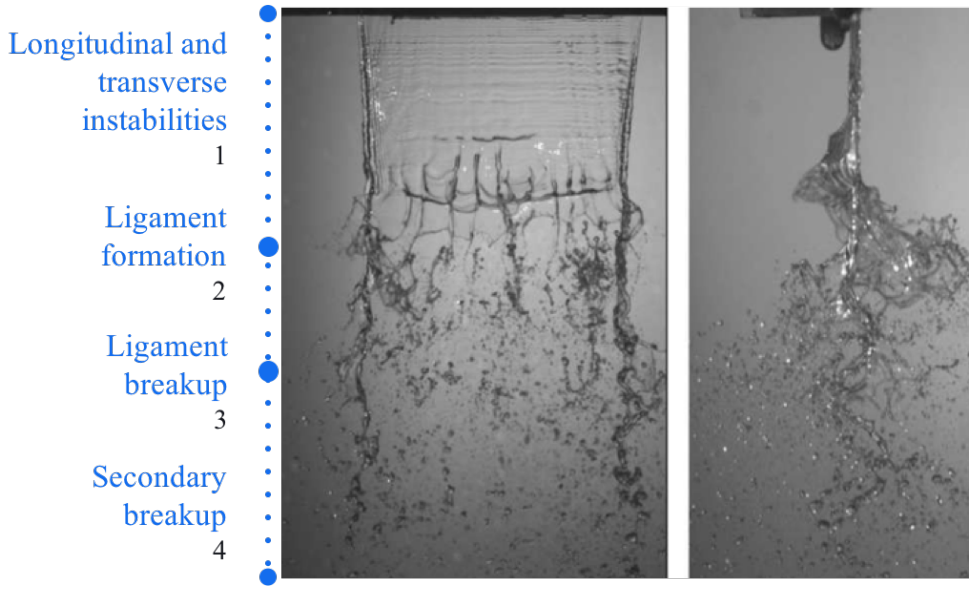

Fig. 2.1: Experimental investigation of an airblasted liquid sheet by a high speed coflowing air stream conducted at ONERA by Carentz [27].

Félix Savart is regarded as a pioneer in the field of liquid disintegration. In 1833, several of his memoirs [184–187] first reported work on the disintegration of a liquid sheet, in which he observed the unstable growth of disturbances on their surface. In this case, the sheet was formed by impinging a water jet onto a disk, forming a water bell. His work was closely followed by the experimental work of Taylor & Howarth [212] on a similar geometry. Disturbances are intrinsic to the liquid dynamics as they naturally arise as the liquid phase flows through the injection system and/or because of the subsequent interaction of the liquid with the ambient gas.

Later, Plateau [154] first realised the influence of surface tension on the small disturbances on the liquid surface and demonstrated the fastest growing wavelength to dominate the onset of the breakup. Rayleigh [165, 166] thereafter brought into mathematical consideration the effect of surface tension forces on the mechanisms of liquid jet breakup. On the analytical side, Hagerty & Shea [82], York et al. [239], Taylor [211] and Squire [201] were amongst the first to conduct theoretical linear stability analysis studies of a moving liquid sheet in quiescent air.

Experiments were resumed years later on the atomisation of a liquid sheet sandwiched between two high-speed coflowing gas streams to produce for the first time an airblast atomisation. Several works, among whom Rizk & Lefebvre [174], Arai & Hashimoto [6], Mansour & Chigier [138, 139] and Stapper & Samuelsen [202], were paramount to this new field of research. The presence of the high-speed coflowing gas streams brings about a profound change to the nature of the mechanisms of disintegration. Linear and non-linear stability analyses were thus repeated taking into account the effect of shearing from the gas stream [39].

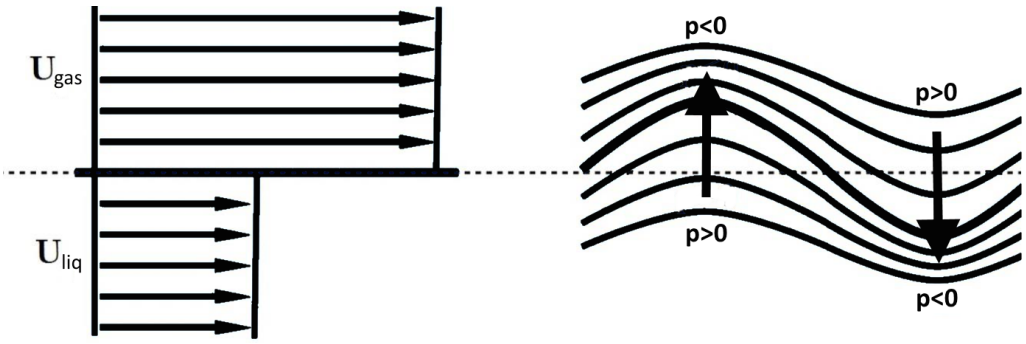

Fig. 2.2: Evolution of the phase interface between two coflowing fluid streams of different velocity. Adapted from Charru [30].

2.1.1 Interfacial wave formation

2.1.1.1 Longitudinal instabilities

The longitudinal instabilities are driven by the velocity difference between the two fluid phases, a result of the aerodynamic forces from the high-speed coflowing gas, believed to arise from a Kelvin–Helmholtz (KH) instability of the mixing layer. Indeed, the velocity shear at the boundary of the two mediums will become unstable to the KH instability, which

can result in large amplitude surface waves at the interface, much like wind shear on the ocean surface leads to surface waves.

The intrinsic liquid surface tension forces oppose any movement of the interface from its initial plane and attempt to restore equilibrium, while the velocity difference between the two fluids induces a pressure gradient, increasing any deviation from the interface [224]. This competition between cohesive and disruptive forces finally promotes an inviscid instability. When normal aerodynamic forces on the liquid core are expected to be significant, they expand the liquid film against the contracting effect of surface tension. The sheet deforms at constant thickness in a sinuous manner and wave crests form. This instability is described with success using linear stability analysis and weakly non-linear theories [29].

von Helmholtz [227] first observed the KH instability, foreshadowing the work of Kelvin [108] who conducted a linear stability analysis based on the experiments of von Helmholtz while including the effects of surface tension forces and gravitational forces. As depicted in Fig. 2.2, the Bernoulli effect for steadily flowing fluids indicates that as the base gas flow is forced to flow over a perturbation of the base flow (liquid film undulations), on the interface separating the two fluids, its velocity increases and its pressure falls. That is, an under-pressure is created at the crest of the sheet relative to its underside; thus encouraging the liquid to flow further into the space occupied by the gas. The pressure gradient amplifies the disturbance. As the fluid cannot support this pressure difference, the unsteady flow must involve a motion that counteracts the action of Bernoulli's equation. This means there will be an acceleration away from the convex side of the undulation and an acceleration towards the concave side. Such a system of accelerations amplifies the disturbance, the roll-up of the waves. The local decrease in static pressure (local increase in velocity) tends to expand the protuberance farther outward, thereby increasing the amplitude of the wave [217, 224].

On the other hand, Bachelor [9] describes the formation of KH rollers with the idea of a generated vortex sheet at the interface. The vorticity that is created at the phase interface is advected at the crest of the wave, towards the light fluid, before displacing itself in the trough of the wave. Much of the literature on 2-D numerical investigation of the disintegration of a liquid film via the KH instability come to the same conclusions [208, 235, 243].

Non-viscous liquid sheet linear stability analysis studies in two-dimensional designs were initiated by Hagerty & Shea [82] for a liquid sheet sandwiched between two infinite quiescent air phases. They concluded that only two modes of the KH instability could develop and be sustained: sinusoidal (symmetric oscillation in phase) and varicose (anti-symmetric). Their experimental observations allowed the observation of their theoretical predictions. The rapid growth of the sinuous mode downstream triggers large deformations of the liquid sheet into a

flapping motion, much like a flag in the wind. The inclusion of viscosity in the more recent 2-D linear stability problems of airblasted liquid sheets by Lozano & Barreras [135] revealed the importance of the two-phase boundary layer thickness and its great influence on the flapping of the liquid sheet. A comprehensive review on the linear stability analysis of liquid streams can be found in Sirignano & Mehring [199].

2.1.1.2 Transverse instabilities

The fragmentation of the liquid sheet proceeds via a two-stage mechanism, the first of which has been analysed in the previous section. A secondary instability of a different nature then comes into play which is responsible for the sheet indentations, the formation of ligaments, and subsequent droplets. While 2-D simulations of the KH instability are able to shed some light on the dynamics of the gaseous and liquid flows in interaction, and the rapid development of a strong curvature of the interface [69], the consecutive transverse instabilities as well as the global picture of the fragmentation process of an undulating sheet require a 3-D perspective. Indeed, only three-dimensional simulations can offer a full perspective of this phenomenon, as pointed out for example by Fuster et al. [69].

The formation of transverse interfacial waves can be explained as a response to different instabilities, which do not involve the same physical properties. In an attempt to determine what type of transverse instability would develop on the surface of round sheared jets, triggering as a result the topological transformation of the jet, Marmottant [140] concluded that the secondary transverse instability had to be the result of the acceleration of the KH instability-induced surface waves (introduced in Section 2.1.1.1). Indeed, liquid particles undergo an oscillation normal to the liquid/gas interface as they propagate through the KH instabilities. This acceleration results in a Faraday instability, which is commonly observed at the interface between stably stratified fluids. Bremond et al. [24] described the same atomisation scenario involving the so-called Faraday waves for the overall sheet–drop transition for a liquid sheet flowing in quiescent air. The periodic passage of the KH wave crests that propagate in the streamwise direction with a group velocity which is faster than the liquid bulk itself, accelerates the interface perpendicularly to the flow, in an oscillatory fashion, alternatively aimed in the direction of the gas and of the liquid. In the liquid sheet reference frame, a liquid particle propagates in a “wavy corridor” due to the previously mentioned longitudinal instabilities. In this scenario, a liquid particle is periodically accelerated upwards and downwards. It experiences transient accelerations perpendicular to the plane of the sheet whose intensity and direction depends on the curvature

of the sheet. Its maximal acceleration value is reached when the particle reaches an extremum of the primary wavy pattern, where the curvature is maximum.

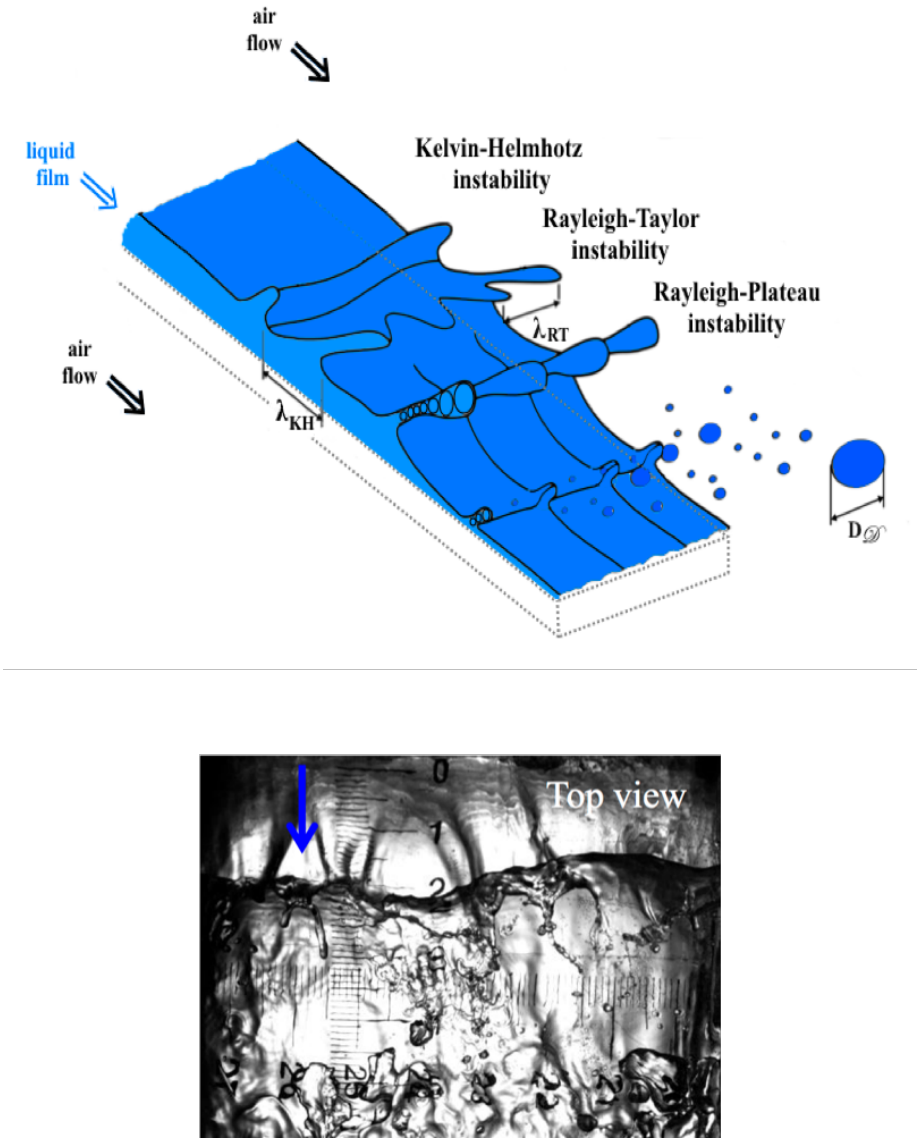

Fig. 2.3: *Top*: Schematic of the mechanisms involved in primary breakup – longitudinal and transverse instabilities – according to Hong [92]; *Bottom*: Top view of a shear-layer airblast atomisation with visible instabilities [143].

Hong [92] proposed a scenario in which the key effect responsible for the initiation of the secondary instability mechanism involved in primary atomisation is also due to the KH wave crest acceleration but this time owing to a variant instability due to the liquid sheet being periodically accelerated by the incoming longitudinal waves in the axial direction via a

Rayleigh–Taylor-like instability [164, 210], as depicted in Fig. 2.3. This axial acceleration would be caused by the aerodynamic drag of the gas onto the wave crests. Hong [92] has clearly shown that the mean drop size is proportional to the most amplified wavelength of the Rayleigh–Taylor instability [29]. The prediction of the expected drop sizes requires thus a good understanding of the transverse destabilising mechanism. The findings of Villermaux & Clanet [224] and Inamura et al. [95] point toward the same conclusions and also favours this theory on the formation of transverse waves. Therefore, the Rayleigh–Taylor instability of a liquid interface is a relevant mechanism to become acquainted with, as it foreshadows the process of drop formation in atomisation. The Rayleigh–Taylor instability will be the subject of a thorough investigation as part of Chapter 5.

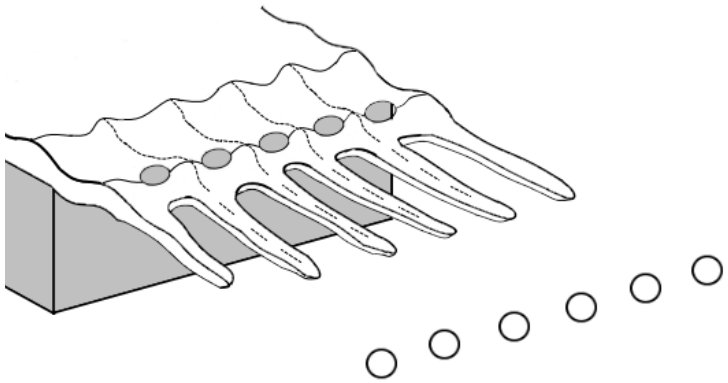

Fig. 2.4: Thickness modulations of the sheet and emergence of cell-like structures, followed by the formation of ligaments spaced in the transverse direction and elongated in the streamwise direction. They breakup under aerodynamic tearing, shedding droplets.

Similarly, Bhayaraju & Hassa [15] attempted to explain the appearance of this secondary instability by noting that as the spacing between the longitudinal KH capillary waves increases – the waves ahead travel at a higher velocity than the waves that are following – stresses are induced on the liquid surface. The surface tension forces try to balance the induced stresses by accumulating liquid mass and this causes the formation of both ligament-like structures, whereby the sheet thickness is greater than its mean height, and cell-like structures enclosed in-between two ligaments, whereby the sheet thickness is reduced. Such a combination of longitudinal and transverse undulations of similar wavelength leads to a periodic variation of the sheet thickness, as depicted in Fig. 2.4.

An additional interesting physical phenomenon in the context of liquid sheet indentation lies in the Taylor–Culick instability, which is linked to wetting behaviour and recession dynamics.

Chapter 3 gives a more thorough overview of these topics. For a growing mass of liquid collected at the rim of a liquid sheet, through the action of surface tension forces [220], the rim becomes much thicker than the sheet to which it is attached. As the rim recedes, the acceleration initiates the growth of corrugations. Lhuissier & Villermaux [127] reported on their own interpretation of the physical phenomena behind rim-driven retraction of flat fluid sheets. Rim corrugations are a consequence of the recession dynamics. An interface separating two fluid media and accelerated towards the denser phase is unstable in the sense of a Rayleigh–Taylor instability (inertia driven), as described above. However, one could equally invoke a mechanism where surface tension is the driving force of the instability: the Plateau–Rayleigh instability. That duality is not new, and has been discussed in the context for instance of the description of the indentations of Worthington crowns in splashing impacts [127] (see Chapter 4). In fact both mechanisms are driven by surface tension: the acceleration of the rim is only the result of the unbalanced tension force at the film edge [127]. According to Lhuissier & Villermaux [127], these two mechanisms are intrinsically undistinguishable. Brenner & Gueyffier [25] studied numerically rim-driven retraction of flat fluid sheets and subsequent destabilisation of its free edge for various Ohnesorge numbers Oh (see definition in Section 2.3.1). When Oh is small, the rim rapidly takes a circular shape [220], as depicted in Fig. 2.5. As Oh progressively increases, the capillary waves and then the rim disappear through the action of viscosity [188].

Fig. 2.5: Schematic illustration of the rim shape regime obtained for a retracting sheet (side view) at Oh$<$ 0.1. Adapted from Brenner & Gueyffier [25].

2.1.1.3 Disintegration of ligaments into droplets

The sheet is now destabilised further to induce another transition towards the formation of threads, or ligaments, whose breakup partially characterise the drop size distribution in the resulting spray [59, 154, 166, 167, 184, 223]. The last stage of the cascade of mechanisms is indeed the rupture of the ligaments into drops. Therefore, the sheet–drop transition is mediated by the birth of more or less corrugated ligaments. Their subsequent disintegration and subdivision into smaller units occur due to either aerodynamic elongation or according

to theories of varicose instability. The fragmentation mechanism and fragmentation direction of the threads appear to depend on the direction in which those ligaments were generated and elongated in the first place.

Following the liquid sheet thickness modulations outlined in Section 2.1.1.2, the liquid sheet is now a corrugated structure. Narrower regions or "cell-like" structures form at the troughs of the undulations between thicker thread regions. The details of the formation of cell-like structures between transverse and longitudinal waves are explained in the schematic of Fig. 2.4. We shall see that many authors have put great emphasis on them in Section 2.3 as precursors to ligaments in certain atomisation regimes. Eventually the liquid sheet is stretched to the point that the distance between the successive transverse waves and adjacent longitudinal waves reach a minimum, as well as the thickness of the connecting membranes, until they puncture and disintegrate into holes, thus shedding by aerodynamic tearing streamwise ligaments, spaced in the transverse direction and elongated in the streamwise direction. Membrane disintegration also leads to the entire transverse wave to detach.

In the context of an aerodynamic elongation, for any liquid structure to detach from the liquid core, the body force acting on it needs to overcome surface tension effects. Indeed, when inertial stresses developed by the surrounding gas exceed the surface tension stresses opposing the deformation sufficiently, the liquid ligaments, triggered by the fingering at the interface, will detach by pinching off their base. Smaller droplets in the resulting spray are attributed to the tearing of membranes, while bigger droplets originate from the fragmentation of ligaments under the shearing action of the air [202].

On the other hand, and following the model of Fraser et al. [67], for a liquid sheet injected in stationary gas, the most rapidly sinuous growing mode is detached at the leading edge in the form of a ribbon moving transversally through the ambient medium (Fig. 2.7). The ribbon's diameter mainly depends on the sheet thickness. The fact that a thicker liquid sheet produces thicker ligaments, which disintegrate into larger drops, highlights the importance of spreading the liquid into a very thin sheet to achieve the finest atomisation [176]. Under these quiescent ambient gas conditions, the gas-phase has no effect on the ribbon breakup. This ribbon rapidly contracts into an unstable ligament under the action of surface tension. With a nearly cylindrical shape, the ligament is *per se* sensitive to a varicose instability, the Plateau-Rayleigh instability, similar to the pinch-off of thin water jets emerging from kitchen taps (Fig. 2.6). Indeed, the transient development of this instability during a ligament elongation sets its corrugations of wavelength λ. The latter are visible in Fig. 2.7 around the transverse cylindrical ligament of diameter D_{ligament}. These corrugations are the premise of droplets of equal diameter $D_{\mathscr{D}}$.

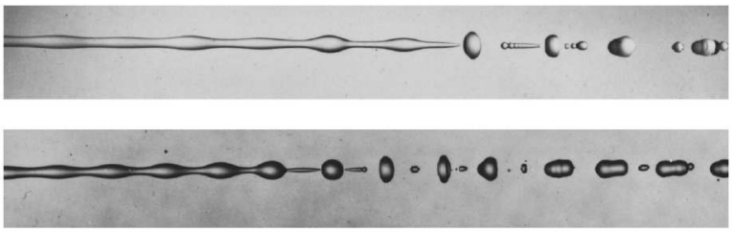

Fig. 2.6: Photographs of a decaying jet into drops for two different frequencies of excitation [179].

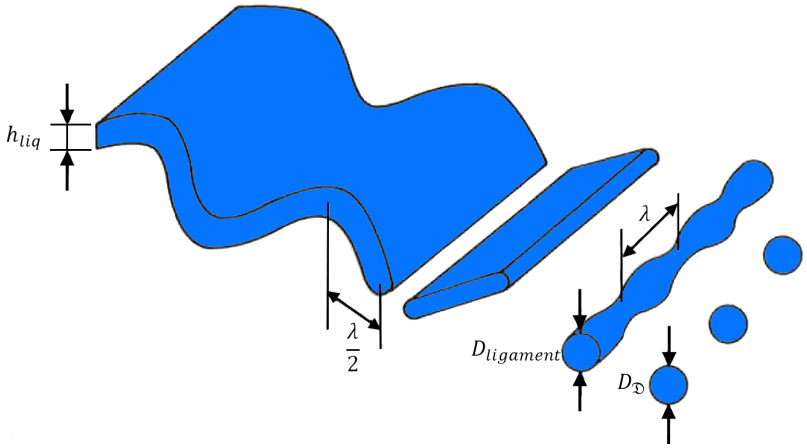

Fig. 2.7: Schematic of the successive stages of breakup of a planar liquid sheet in the spanwise direction. According to the model of Fraser et al. [67].

It is worth mentioning that in this model the "fingering of the interface" (ligament formation) is assumed to be connected to the development of film instabilities along the prefilmer surface. However, according to Gepperth et al. [70], the atomisation process and formation of ligaments were observed to be completely uncorrelated with the development of film surface instabilities, which is very much subject to debate, as shall be discussed in Section 2.1.5.

Finally, Fraser et al. [67] pointed out that the "orderliness" of the disintegration process matters on the final uniformity of the drop size distribution. For instance, in the case of cell-like structures forming on the liquid surface, perforations occurring at the same distance from the nozzle orifice have a similar hydrodynamic history, and thus thread diameters tend to be uniform and finally the drop sizes fairly constant.

It is important to note that for a fluid in equilibrium, surface tension acts against the disruption of the interface (this is the case for example of secondary atomisation, see Section 2.1.2), whereas if the liquid is not in an equilibrium configuration, as is the case here of a free

surface experiencing hydrodynamic instabilities and a strong curvature, surface tension could become an important factor in the liquid deformation and possible disintegration.

2.1.2 Secondary breakup

Characterising the final spray is essential for atomisation studies in order to understand the influence of injection parameters and primary breakup on the final sizes of droplets and their impact on the subsequent combustion process. The spray is commonly divided into two consecutive regions: the dense spray region near the injector exit – with the presence of the liquid core and pinched-off ligaments, big droplets and irregularly shaped liquid structures – and the dilute spray region far from the injector corresponding to a lower liquid volume fraction with roughly spherical drops [61]. The polydispersity of liquid structures in the dense spray region results from the dynamics of the liquid sheet primary breakup described above and the initial thickness of the liquid sheet, its velocity relative to the surrounding gas and liquid viscosity and surface tension [80, 123].

These structures may undergo further fragmentation (secondary breakup) in the dilute spray region. In fact, most outcomes of primary breakup are unstable to secondary breakup, depending on the relative importance of the forces acting on them [61, 223]. Indeed, any liquid droplet first ejected from the liquid core during primary breakup is a prelude to secondary breakup and thus small drop formation. The overall breakup is visualised as a sequential process or cascade process, where mother drops give rise to daughter drops, which break into smaller drops. The mechanisms for secondary atomisation that most commonly take place are outlined in Fig. 2.8. A more comprehensive analysis on secondary atomisation is available in the review article by Guildenbecher et al. [80] and the book by Lefebvre [123].

Thus the final range of droplet sizes depends on both the droplet sizes produced during primary atomisation and the importance of the secondary atomisation mechanisms. The absence of any general theoretical treatment of the atomisation process, as of yet, has led to the evolution of empirical correlations to express the relationship between the mean drop size in a spray, the physical and flow properties of gas and liquid employed and nozzle design features [72, 122]. The topic of droplet size distributions will be discussed in Chapter 4.

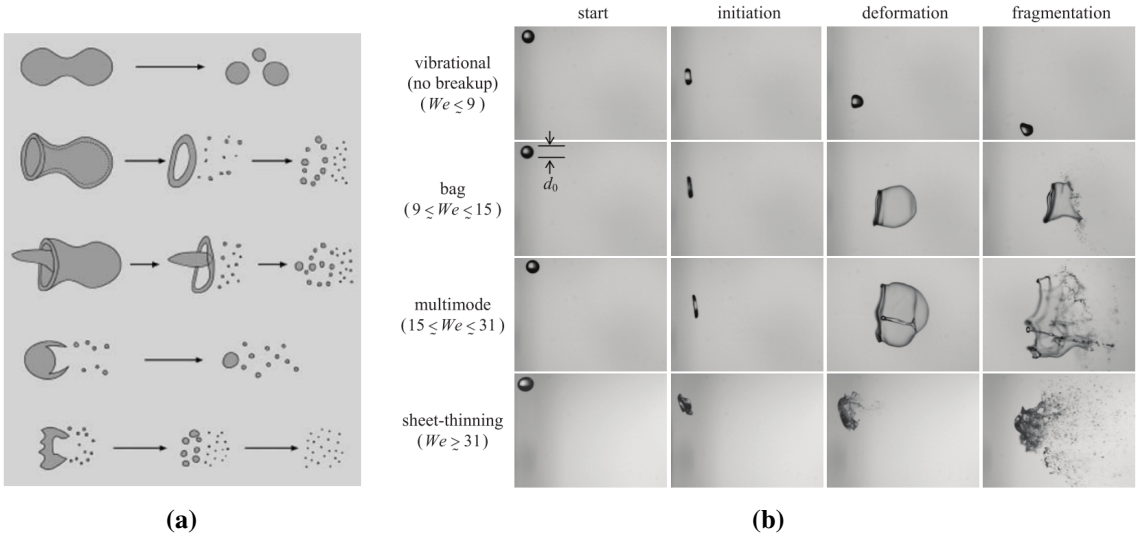

Fig. 2.8: **(a)** Illustration [80] and **(b)** shadowgraphs [79] of the different Newtonian secondary breakup modes depending on the flow conditions. From top to bottom the morphologies are termed vibrational, bag, multi-mode, sheet-thinning, and catastrophic.

2.1.3 Prefilming airblast atomisation

Pre-filming atomisation is the main technique currently used in the aircraft industry (see Chapter 1), whereby, as opposed to the liquid sheet being directly injected into the primary flame zone sandwiched between two coflowing gas streams (no prefilming zone), a liquid film is first driven along a solid surface by the coflowing upper gas stream, as depicted in Fig. 2.9. A thin film forms that wets homogeneously the prefilmer plate. The high gas velocity entrains the liquid towards the atomising edge of the prefilmer and induces high shear at the film surface, which is the major and dominant origin of the perturbation. Eventually, the liquid film detaches from the atomiser trailing edge after which both gas streams interact with it. Supported by the additional incoming gas stream from below, the liquid film starts flapping in the longitudinal direction – flag-like motion – behaving as a thin flexible membrane. This flapping zone, so-called “primary breakup” region corresponds to the initiation of the disintegration process. We can note from the side view of the sketch that the growth of the sinuous mode provoking the film flapping propagates downstream, before the final intermittent release of droplets. Most experimental works to date have been on non-prefilming liquid sheet atomising nozzle geometries. The literature available on the breakup of liquid films on prefilming surfaces is very limited. The first experiments were conducted by Sattelmayer & Witting [181] on the simplified cylindrical geometry to a

2-D abstraction of a prefilming airblast atomiser, followed by Gepperth et al. [71, 72] and Déjean et al. [47, 48] at ambient conditions and Bhayaraju & Hassa [15] at high-pressure operating conditions. It should be noted that the development of the liquid film over the solid prefilmer plate is an additional piece of physics in comparison to a non-prefilming configuration. Pre-filming nozzles present the merit of faster breakup, as was observed by Bhayaraju [14], and finer particle sizes [46], justifying the interest behind this geometrical configuration.

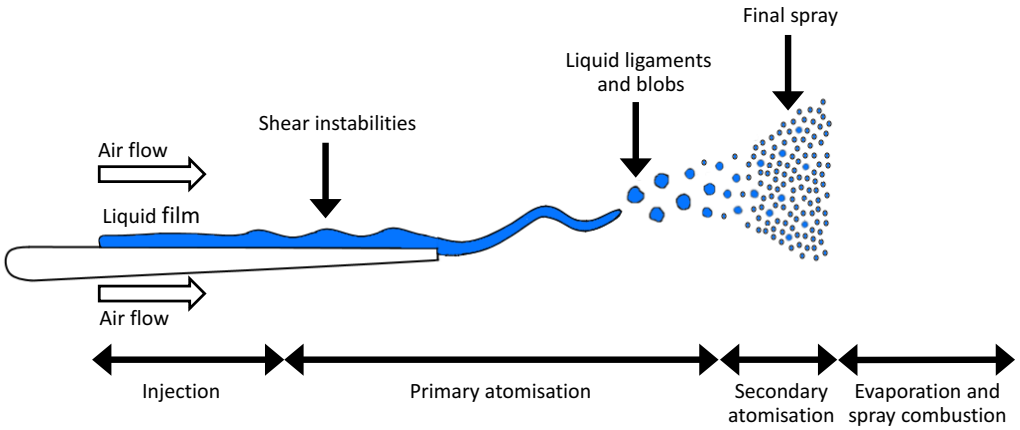

Fig. 2.9: Schematic representation of the different physical processes between liquid fuel injection and evaporation/combustion, as part of a prefilming airblast fuel nozzle.

2.1.4 Atomisation and spray characteristics

The atomisation characteristics reviewed so far were those resulting from simple visual (qualitative) observations. Lately, various experimental techniques were developed in order to refine measurements and extract quantitative spray characteristics downstream of the atomiser. Sophisticated video techniques with *a posteriori* image processing include: three-dimensional high-speed back light illumination (shadowgraphy), laser sheet illumination diagnostics in conjunction with Particle (and ligament) Tracking Velocimetry (PTV) and Particle Doppler Anemometry (PDA) measurements [e.g. 71, 72, 190]. These statistically reliable data enable a unique opportunity for accurate temporal and spatial comparisons to qualitative and quantitative data obtained by numerical simulations of primary breakup, leading to a profound understanding of this process. Some of the characteristics described therein are summarised in Fig. 2.10.

Wavelength and amplitude of longitudinal surface waves define the surface area in contact between both fluids. For greater surface area are observed shorter breakup times and lengthscales. A spectral analysis of the instantaneous position of the interface allows experimentalists to determine these wavelengths and associated amplitudes.

Wavelength and amplitude of transverse surface waves represent the spanwise distance between the ligaments, which helps to predict the number of ligaments responsible for droplet generation (see Section 2.1.1).

Global sinusoidal oscillation frequency is responsible for the flag-like motion of the liquid film observed in some instances, as described in Section 2.1.1.1. The magnitude of that frequency is a direct measure of the liquid structures generation rate, so a very large number of research projects focus on measuring that frequency [e.g. 137].

Spray angle helps to predict the final spray spatial distribution. The potential oscillation of the liquid film creates a droplet dispersion characterised by an aperture angle linked to the oscillation amplitude.

Breakup length represents the length span between the injection of the liquid and the occurrence of the first breakup event. The final spray penetration depends on the breakup length. This is an important primary breakup characteristic as it allows the determination of the position in the combustion chamber at which atomisation starts.

Droplet diameter A severe obstacle to the advancement of spray science is the lack of knowledge of the influence of primary breakup on the final droplet diameter (post- secondary breakup). The spatial and size droplet distributions are the two required final spray characteristics. In many cases, Rosin-Rammler or log-normal size distributions are obtained (see more in Chapter 4).

Liquid sheet thickness is commonly measured at the prefilmer lip.

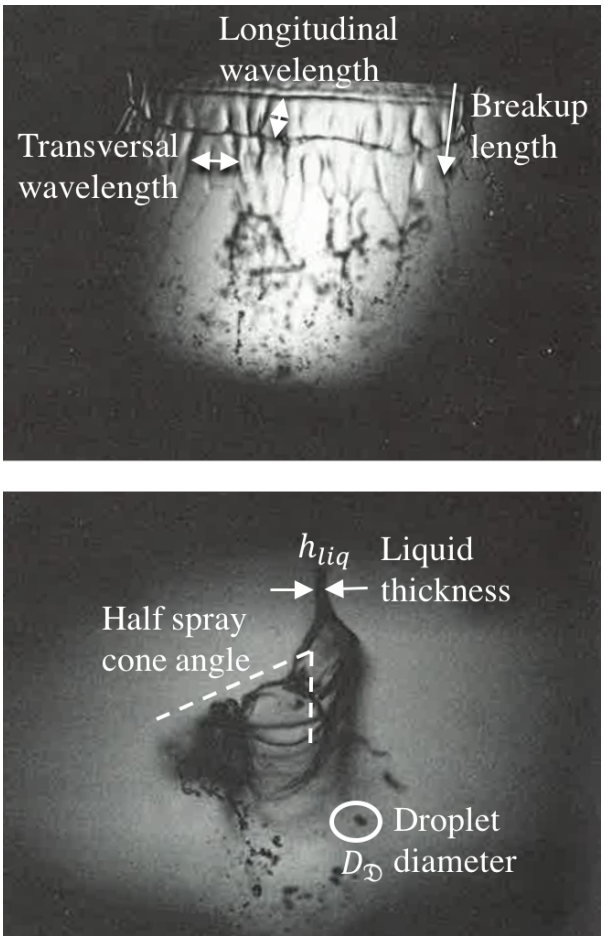

Fig. 2.10: Face view *(top)* and side view *(bottom)* of the "stretched streamwise ligament breakup" regime identified in the experiments of Stapper & Samuelsen [202]. A water sheet is injected at 1m/s with 20m/s co-flow air. Superimposed are drawn various characteristics representative of atomisation.

2.1.5 Effect of physical properties

From the physical evidence reviewed above, it becomes clear that numerous parameters will influence the behaviour of the liquid film dynamics and subsequent disintegration mechanisms, through the effects of physical factors such as surface tension, viscosities, velocities of gas and liquid phases, thickness of liquid sheet and geometrical lengthscales. Due to limited optical access and difficulties in performing measurements in the dense spray regime, little research is currently available on prefilming airblast atomisers that includes qualitative and quantitative information on the ligaments and droplets generated close to the atomising edge in the dense spray region during primary breakup. The experimental works of Gepperth et al. [71, 72, 73], Bhayaraju & Hassa [15], Inamura et al. [95] and Déjean et al. [47,

48] are, to the best of our knowledge, the most-recently published experimental investigations of prefilming airblast primary atomisation that provide high-quality experimental results for a wide range of operating conditions at ambient temperature and pressure conditions (see Table 2.1). To enhance optical accessibility, all authors use a planar two-dimensional abstraction of an axi-symmetric airblast atomiser, similar to the one in Fig. 2.11a.

Table 2.1: Operating conditions investigated in experiments on prefilming liquid sheet atomisation.

Quantity	Bhayaraju & Hassa [15]	Gepperth et al. [71, 72]	Inamura et al. [95]	Déjean et al. [48]
u_{gas} [m/s]	$30-90$	$20-70$	$17.0-76.5$	$20-100$[a]
u_{liq} [m/s]	$0.2-1.8$	$0.62-3.75$ [cm^3/s][b]	$4-16$ [cm^3/s][b]	$0.5-4.4$
Operating conditions	ambient and up to 6 bars	ambient	ambient	ambient
σ [N/m]	0.026 (jet A1)	$0.025-0.038$ (Shellsol fuels)	0.072 (water)	0.072 (water)
μ_{liq} [kg/(m.s)]	2×10^{-3}	$0.89\times10^{-3}-2.55\times10^{-3}$	1×10^{-3}	1×10^{-3}
h_{edge} [mm]	~0.1	1 and 2.5	~0.16	0.85
L_{pref} [mm]	2 and 4	20.6 and 47.6	40	$2-40$

[a] corresponds to the maximum of the air flow profile.

[b] the volume flow rate only is provided by the authors.

The properties of the medium into which the liquid is discharged influences the atomisation process [175]. The ambient gas varies widely in pressure and temperature over the range of operating conditions in aero-engines. Under real gas turbine conditions, fuel sprays are injected into highly turbulent, swirling, recirculating streams of reacting gases [100]. The effect of backward flame radiation, convection of heated reacting gases through recirculation, diffusive heat transfer from the high temperature compressed air to the cooler fuel film, remain unknown and an active field of research. The influence of local temperature on liquid and gas properties is presently not well known, especially at high temperatures. Pressure and density are commonly reported to be the most important quantities to be considered in atomisation. At higher ambient temperature, the decrease in gas density causes weaker aerodynamic interactions at the interface, hence longer breakup lengths and bigger droplet diameters, which is in accordance with what was observed by Clark & Dombrowski [36] and Dombrowski & Foumeny [54] and in a preliminary study we conducted earlier in this project [18]. Additionally, it could be observed that an increase in air pressure reduces the droplet size [15, 122, 175].

The most pronounced effect on the final spray droplet sizes is widely believed to come from the mean air velocity within the atomiser nozzle. A strongly exposed liquid surface combined with an increase in mean air velocity has been seen to result in increased aerodynamic forces that reduce the droplet sizes [14, 122, 181].

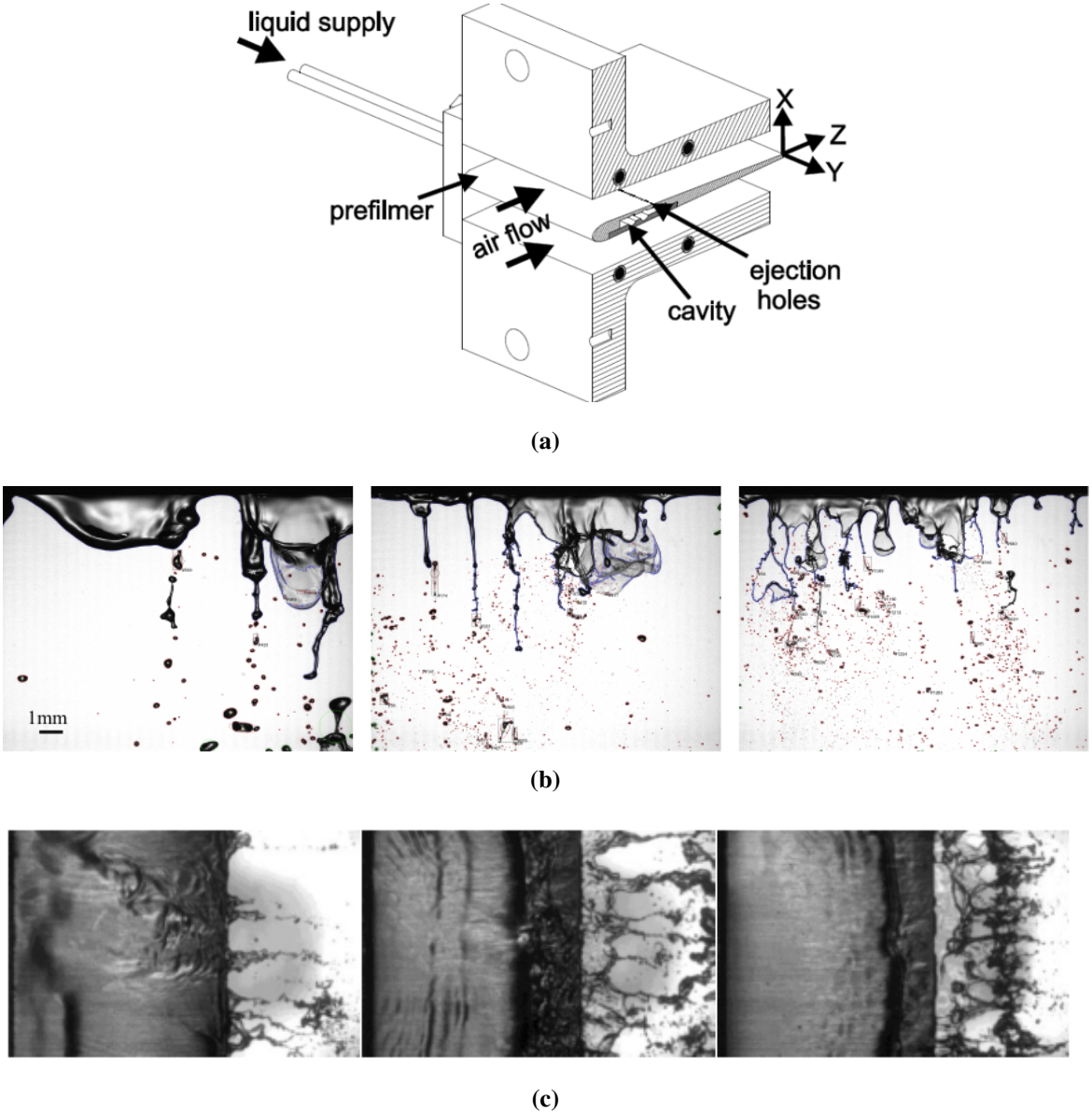

(a)

(b)

(c)

Fig. 2.11: **(a)** Schematic of the experimental set up of Gepperth et al. [72]. **(b)** Example of liquid accumulation undergoing stretched ligament breakup for a liquid loading of 25mm/s and mean air velocities of 20, 50 and 70 m/s [72]. **(c)** Example of liquid aspect on the prefilming zone for a mean air velocity of 50m/s and mean injection liquid velocities of 0.5, 1.5, 2.5 m/s in the experiments of Déjean et al. [48].

In the previous discussion it was supposed implicitly that all the liquid injected as a thin film reaches the prefilmer trailing edge. However, when a liquid film is subjected to high velocity flows, some droplets could detach from the liquid surface, and more specifically from the wave crests of the surface waves generated at the interface, in a process usually referred to as "wave stripping". An interesting investigation is the one performed by Bhayaraju & Hassa [15] where the stripping phenomenon over the prefilming surface of an airblast injector was experimentally studied. In severe operating conditions and for longer atomiser lengths, wave stripping could even lead to full atomisation before any of the liquid reaches the atomising edge [15]. Therefore, a non-negligible pre-vaporisation of the fuel before the prefilmer edge can be expected for higher air temperatures, which is something to be considered for injector and combustor design. However, for the engine conditions considered in a real injector as studied by Giusti [75], a value of stripped mass flow rate less than 3% of the total film mass flow rate was found at partial load conditions, whereas at conditions representative of full load operation a stripped mass of about 6% of the total liquid mass flow rate was predicted.

The significance of density on the breakup phenomenon performance is marginal as most liquids exhibit only minor differences in this property due to the incompressibility effect. However, an increase in liquid density equates to an increase in liquid momentum so that it is more difficult to destabilise. The most important liquid properties influencing atomisation are surface tension and viscosity. The importance of liquid viscosity stems from the fact that it hinders the development of any natural instabilities inside the injector, following the observations by Rizkalla & Lefebvre [176]. Thus, it has an adverse effect on atomisation because it opposes any change in liquid geometry and delays the onset of disintegration. The combined effect is to deteriorate the quality of atomisation by producing a less fine spray. However, Sattelmayer & Witting [181] came to a different conclusion while analysing their experimental data: a change in liquid viscosity had no effect on the droplet size, but affected the disintegration process of the ligaments. A related point to consider when discussing viscosity is that, in terms of hydrodynamic instabilities, the development of any instability is very sensitive to the details of the velocity (shear flow) profile. For a two-phase velocity profile with no point of inflection, an instability can still take place because of viscous action. Indeed, viscosity has a dual role: primarily a stabilising effect at low Reynolds numbers, but a destabilising effect at high Reynolds numbers [217].

In parallel, Rizkalla & Lefebvre [176] observed that a higher surface tension produces a more stable liquid film and an increase in droplet sizes, in particular for low liquid flow rates and low values of surface tension. In addition, the effect of varying the liquid flow rate while

maintaining the air flow constant was investigated. An increase in liquid flow rate markedly reduces the atomisation quality especially with liquids of high viscosity. An increase in liquid velocity provides the liquid mass with energy which opposes aerodynamic forces and therefore opposes destabilisation [176]. Nevertheless, according to the experiments of Sattelmayer & Witting [181] the droplet sizes were shown to be independent of the liquid flow rate.

A still controversial parameter is the liquid film thickness. Some researchers observed that an increase in liquid film thickness is accompanied by an increase in the mean drop size [122]. Other investigations could not identify this behaviour and reported that a change in the film thickness has no effect on the droplet size [73, 181]. This is due to a decoupling of the film disintegration process and the liquid film loading at the atomising edge. The reason is an observed accumulation of the liquid film at the tip and in the wake of the prefilmer prior to the primary atomisation of this liquid reservoir, recently observed by Gepperth et al. [72] for planar geometries and by Gepperth et al. [70] in 3-D realistic annular configurations. Films that are thin compared to the prefilmer edge height wrap around the atomiser lip, stay hooked in the wake region and therefore exhibit a storage mechanism, similar to the capillary effect that retains the liquid at a needle tip. A higher atomising edge leads to an increase in the liquid structures that develop there and hence an increase in the observed droplet sizes [22, 73]. The authors observed that the crest of the surface waves is blown by the gas stream, leading to the formation of a bubble framed by a thicker rim of liquid at the atomiser edge, which they call a “bag”. Liquid bags are blown by the gas and finally burst into smaller droplets. The remaining rim is stretched and splits into ligaments. The ligament structures exhibit a vortex-like motion, which is solely affected by the air velocity, and fragment into larger drops. The experimental data of several other researchers also exhibit the formation of a liquid reservoir at the atomiser lip [e.g. 95, 181]. Their results support the hypothesis that the film thickness has thus no direct effect on the droplet size. The recently published experimental data of Inamura et al. [95] on a planar airblast atomiser with prefilmer indicate that even under higher liquid flow rate conditions (see Table 2.1) a reservoir is formed at the atomising edge, but it might not be as pronounced as in the experiments presented by Gepperth et al. [73] at lower liquid flow rates. The observations of Gepperth et al. [73] and Inamura et al. [95] clearly identify the need for more detailed experimental investigations to fully identify the role of the film height and atomising edge thickness on the disintegration process at industrial relevant test conditions.

A question has recently been raised [135] about the possible mechanism that could trigger the initial longitudinal perturbation that is later amplified (“flag effect”, Section 2.1.1.1),

promoting the liquid film breakup. An explanation could relate to the air vortex shedding from the prefilmer lip, similarly to the unforced vortex shedding past a solid cylinder of from a backward-facing step, i.e. the typical Kármán vortex street. As the Kelvin–Helmholtz instability induces longitudinal waves, this instability has been clearly identified to be controlled by the gas boundary layer δ. Indeed, one of the most notable results presented by Raynal [167] and Lozano & Barreras [135] is the dependency of the wavenumber of the most amplified mode of the axial instability on the gas flow vorticity thickness.

Finally, Lean Premixed Pre-vaporised (LPP) combustion, introduced in Chapter 1, is prone to thermo-acoustic instabilities [55], which originate from an unsteady interaction between acoustics and heat release. Since the fuel is delivered by the injector into the combustion chamber, a feedback loop between thermo-acoustic instabilities and the atomisation process has been observed experimentally by Bärow et al. [10] and numerically by Chaussonnet et al. [33] to affect typical spray characteristics such as the droplet size distribution. Fluctuating ambient flow conditions are thus another physical aspect that appears to present the merit of further investigation.

2.2 State-of-the-art numerical methods in multiphase flows and atomisation research

The purpose of this section is to outline the current trends in atomisation modelling and to present a broad overview of the state-of-the-art numerical methods available to simulate multiphase flows and liquid disintegration. The number of works that can be found in the scientific literature is large, particularly since the introduction of commercial simulation codes, and the development of new promising interface-tracking techniques to capture the spatio-temporal evolution of the phase interface. We do not intend to give a comprehensive review of the current body of work, but only focus on some of the researches among whom atomisation of liquid jets and liquid sheets have been conducted. Comprehensive reviews on the subject of multiphase flows modelling can be found in Tryggvason et al. [220] and Gorokhovski & Herrmann [77].

One of the main difficulties of modelling the whole atomisation process comes from the breadth of length and time scales involved in the governing physical phenomena. This requirement is particularly challenging for Direct Numerical Simulation (DNS) studies aiming to reduce the uncertainty in the physics by resolving all the length and time scales of the flow. The smallest scale in flow turbulence should be resolved, let alone the resolution

requirements for representing the smallest liquid structure in the case of a topology change. However, the interface thickness – comparable to the molecular scale – can never be resolved even when using pure DNS, nor can a "zero-sized connecting ligament at the very instance of the breakup" [77].

DNS studies are limited on both the maximum Weber and Reynolds achievable in a simulation (see Section 2.3.1 for a description of non-dimensional numbers). More precisely, increasing the Weber or the Reynolds number generally leads to a more complex flow field with the production of smaller droplets and the generation of smaller vortices. It follows that the resolution required to achieve a reasonable accuracy is unaffordable for the simulation of the atomisation process in an aero-engine injector. In fact, most of the simulations of atomisation presented in the literature are actually "under-resolved DNS". DNS is too resources-consuming to be applied in industry to complex geometrical configurations. In fact, "combustion chamber-scale" studies have to be conducted using multi-physics codes with coarse grids and calibrated sub-grid models [41].

On another note, the addition of compressibility effects in multiphase flows schemes has been considered by very few authors, for instance Ireland & Desjardins [96], Dahms & Oefelein [43]. The generation of an efficient compressible multiphase solver remains to this day a great numerical challenge.

Despite all these challenges, some successful DNS results of atomisation have been obtained with various interface description techniques. In particular, two existing interface description methods, the Volume of Fluid (VoF) and Level Set (LS) methods, and their means of handling the interface singularity – principally the Continuum Surface Force method (CSF) and the Ghost Fluid Method (GFM) – have attracted significant attention for their development and have become contemporary standards as excellent numerical approaches for interface capturing to simulate multiphase flows involving extensive topology changes. These will be introduced in detail in Chapter 3, and will be the subject of a comparative study in Chapter 5.

The VoF SURFER code developed over the years by Zaleski and co-authors [117] is an example of DNS state-of-the-art on various atomisation phenomena, from droplet splashing to atomisation of liquid jets and liquid sheets. Kim et al. [110] successfully reproduced numerically the round jet in co-flow of the experiments of Marmottant & Villermaux [141] by combining the refined level-set grid (RLSG) method of Herrmann [86] with Lagrangian tracking of the small spherical droplets. Finally, the embedded DNS (e-DNS) concept with VoF treatment of the interface, developed by Sauer et al. [183], aims to use the consuming DNS resources only in the relevant primary breakup region. On the other hand, a recent study

by Warncke et al. [229] points out the high dependence of the qualitative and quantitative results on the diffusivity of the interface as a limitation of the e-DNS technique despite the significant numerical resources used: their conclusion is that a sharp interface technique is required.

In parallel, hybrid methods have been proposed to combine the advantages of the VoF method in terms of mass conservation even on coarse meshes and the LS method in terms of accuracy of the interface contour and a smoothly differentiable field for the calculation of the surface tension forces. Hybrid methods are thus particularly suited for the simulation of atomisation, as they minimise the mass loss thanks to the VoF correction and retain an accurate description of the interface geometry, due to the level-set formulation. A fully coupled CLSVOF method was proposed by Sussman & Puckett [204] and has been implemented by a number of researchers since. On the Diesel jet configuration it is worth mentioning the simulations of Ménard et al. [144] on cartesian orthogonal meshes; and the work of Yokoi [237] on the problem of droplet splashing and on the Rayleigh–Taylor instability. A recent development by Arienti & Sussman [7] has reformulated the CLSVOF method to adaptive cartesian meshes. In addition, some recent works have applied CLSVOF on unstructured meshes [52, 65].

Also, on Diesel jet atomisation, Desjardins [50] applied the modified LS method, the conservative level-set (CLS) of Olsson & Kreiss [150] with Ghost Fluid Method treatment of the singularities. This method maintains satisfactory mass conservation required for the stability of the calculation and the accuracy of the results at a much lower computational cost than the CLSVOF method of Ménard et al. [144]. We note that the CLS numerical framework is the subject of the present work. Pringuey [158] developed a novel version of the CLS numerical method – the Robust Conservative Level-Set (RCLS) method – coupled with a CSF numerical technique, which will be described in Chapter 3.

On one hand, DNS studies and high-fidelity simulations of the near-nozzle region with interface capturing methods have allowed a better understanding of atomisation, but they consume significant computational resources and do not allow one to study extended domains or combustion at the same time. Some alternative methods have been developed in order to work around the difficulty of running pure DNS on this problem in order to maintain affordable CPU requirements.

For this purpose, adaptive mesh refinement (AMR) techniques have been developed and utilised in multiphase flow DNS studies to scale the simulation with respect to the relevant quantities and deal with the breath of scales involved in primary breakup and therefore reduce the cost of computation [2, 69]. In AMR, a fine mesh is used only in the regions that require

a higher resolution, such as near the interface and in shear layers. These methods allow for accurate simulation of the liquid atomisation whilst embedding the complex geometry of the injector. A good example is the successful application of the VoF multiphase flow solver Gerris developed by Popinet [156] on Diesel injection [220], or the CLSVOF solver of Zuzio et al. [244] on liquid sheet atomisation.

In addition, Large Eddy Simulation (LES) studies have been used as an industry-friendly alternative to DNS for atomisation modelling. Such frameworks allow one to compute flows at Reynolds number not feasible in DNS, or at the same Reynolds numbers but at a considerable smaller expense. In particular, the simulations of Diesel jet atomisation run by de Villiers et al. [45] are based on an LES formulation. Pringuey & Cant [160] performed a three-dimensional quasi-DNS/Large Eddy Simulation to prove the applicability of the RCLS method on unstructured meshes to primary breakup of a flat liquid sheet of kerosene in coflowing gas at relevant aero-engine conditions. This approach provides an effective and efficient method, is low-CPU-time-consuming and highly accurate for industrial purposes. However, in the context of an industry-friendly LES formulation, a certain level of modelling has to be introduced to handle the resolution requirements for representing the smallest liquid structure (sub-grid scale modelling). Indeed, the main authors have identified the need for models for the sub-grid interface-turbulence interaction and sub-grid contribution of the interface (droplet pinch-off, ligament breakup) as essential to produce numerical simulation of atomisation that carries high physical significance [77, 220]. However, most of the simulations of atomisation presented in the literature are actually neglecting the sub-grid scale contribution of surface tension and turbulence at the interface.

Finally, the difficulty of developing efficient new ways of describing the interface and the complexity involved in the improvement of the existing interface-capturing techniques have led many researchers to consider transforming methods developed in other fields of science. For instance, the Smoothed Particle Hydrodynamics (SPH) method, a meshless approach, originally developed for astrophysics calculations [74], attracts some interest nowadays as a fresh perspective on primary breakup modelling. The spatial discretisation of a computational domain is done via Lagrangian particles, which represent a certain volume of the fluid. These particles move within the computational domain with the actual fluid velocity. However, by nature SPH presents a high computational cost. It was recently successfully applied by Braun et al. [22] on the simulation of liquid film primary breakup, in the same context as the present work. Braun et al. [22] focused his work on the investigation of the role of the atomising edge thickness in the breakup process as the experiments of Gepperth et al. [70] highlighted the possible influence of the latter on the decoupling of the breakup process from

the liquid film evolution along the prefilming surface (see Section 2.1.5). In addition, a recent numerical study by Chaussonnet et al. [32] validated their SPH method to simulate axial liquid jet fragmentation by a coflowing high-speed air in a pressurised atmosphere against in-house experiments.

To describe the full atomisation process, including the multi-scale liquid structure sizes of primary and secondary breakup, the coupling of an Eulerian multiphase solver with Lagrangian Point-Particle (LPP) tracking is another active field of research. Eventually, in a so-called Eulerian–Lagrangian simulation, the macro-scale fluid flow is resolved in an Eulerian framework and the dispersed phase point-particles are evolved in a Lagrangian framework. In recent years, several pioneering efforts have been made to couple the LPP model with interface-capturing schemes, such as LS [87] and VoF [75, 216]. For example, the PARIS Simulator code of Zaleski has recently been applied to the simulation of droplet formation in a gas-liquid mixing layer using DNS [131]. The results are encouraging and show the potential of this multi-scale approach for accurate large-scale simulations of atomisation and coupling with dispersion and evaporation models for subsequent spray combustion modelling [75]. In Chapter 4, our own version of dispersed phase point-particle method will be presented, as implemented within the RCLS method in the Eulerian multiphase flow solver *RCLSFoam* of Pringuey [158].

Following the mechanism described in Section 2.1.1.3, droplet formation is related to the growth and instability of liquid structures. Based on the experimental observations of Gepperth et al. [72, 73], Chaussonnet [31] proposed a novel phenomenological model to simulate the apparition of transverse waves following the Rayleigh–Taylor instability, as given in the model by Hong [92]. His Lagrangian film model is implemented into an LES formulation and coupled to a Lagrangian droplet tracking scheme as well as a model for secondary atomisation to simulate the spray generation at the prefilming injector outlet. To take into account transfers between the liquid phase solver and gaseous phase solver, an inter-phase momentum exchange term is added to the filtered compressible Navier–Stokes equations to account for the action of the gas onto the liquid film only. Following the conclusions drawn by Gepperth et al. [72], Chaussonnet [31] forces the Lagrangian liquid particles into an accumulation mechanism at the atomising edge and expresses the drop size Probability Density Function (PDF) of the spray in the form of a Rosin–Rammler distribution whose parameters depend on the flow conditions. In this formulation, the distribution of droplets downstream of the atomising edge is thus described without simulating the atomisation process. However, without detailed numerical investigations it is impossible to identify the responsible physical mechanisms for atomisation in prefilming airblast atomisers.

Such an approach is only useful for combustion, where the purpose is not to understand atomisation, but rather to reproduce the main characteristics of the spray that have an impact on the flame. Indeed, the low CPU cost and memory requirement of this kind of approach makes it suitable for industrial LES studies of the whole combustion chamber [31].

2.3 Latest endeavours in regime classification

Based on the experimental investigations described herein, morphological classifications of the atomisation process have been proposed, whether in the case of an injector with [e.g. 64, 139, 202] or without a prefilmer zone [15]. These regime classifications are based on different dimensionless numbers, which points to major shortcomings in the complete understanding of primary atomisation due to the absence of a universal consensus on which dimensionless numbers should be used to characterise the atomisation of an airblasted liquid sheet. In addition, these regime classifications continue to evolve with more recent works [46, 137]. An example of a regime classification was already given in Section 2.1.2 for the secondary breakup process of spherical liquid droplets, based on the drop Weber number. It is also important to emphasise that the various studies use injector nozzles with different geometries. Geometrical discrepancies are certainly a factor in the diversity of the results obtained in morphological regime classification studies. This section is aimed at presenting three families of attempts at mapping atomisation regimes: axial liquid jets, non-prefilming liquid sheets, and an overview of the recent work on prefilming liquid film atomisation classification.

2.3.1 Non-dimensional groups in multiphase flows

According to the above discussion, during liquid film evolution and spray formation, we note the dependence of the physical mechanisms behind the performance of atomisation on numerous parameters for a given geometrical and flow configuration. To characterise the breakup phenomenon, in many cases it is useful to perform an order of magnitude analysis in order to determine what are the prevailing interactions between the liquid and gas phases and express the relative importance of two or more physical processes. Such an analysis allows us to introduce some non-dimensional groups. In addition to the properties of the gaseous medium into which the liquid stream is discharged, quantities related to the liquid phase should also be considered since they have a great importance on the breakup process. To date, there is a lack of consensus over the choice of non-dimensional numbers, which

highlights the absence of a comprehensive understanding of primary atomisation. We herein identify a set of relevant dimensionless groups, developed over the past decades in an attempt to establish universal laws for atomisation behaviour.

As previously discussed, crucial factors influencing atomisation in configurations typical of airblast atomisers are the density ratio $\rho_{\mathrm{gas}}/\rho_{\mathrm{liq}}$ and viscosity ratio $\mu_{\mathrm{gas}}/\mu_{\mathrm{liq}}$. In addition, the relative velocity between the liquid flow and the gas phase $\bar{u}_{\mathrm{gas}}/\bar{u}_{\mathrm{liq}}$ has a significant impact. A way to combine the effect of density and velocity ratios is to introduce the momentum flux ratio MFR that reads:

$$\mathrm{MFR} = \frac{\rho_{\mathrm{gas}}\bar{\mathrm{u}}_{\mathrm{gas}}^2}{\rho_{\mathrm{liq}}\bar{\mathrm{u}}_{\mathrm{liq}}^2}. \tag{2.1}$$

The MFR is commonly used to characterise breakup regimes [48, 64, 131, 183], as shall be discussed in the next sections. Lozano et al. [136] identified the strong influence of the initial height of both fluid channels and suggested the use of the momentum ratio instead:

$$\mathrm{MR} = \frac{\rho_{\mathrm{gas}}\bar{\mathrm{u}}_{\mathrm{gas}}^2\mathrm{h}_{\mathrm{gas}}}{\rho_{\mathrm{liq}}\bar{\mathrm{u}}_{\mathrm{liq}}^2\mathrm{h}_{\mathrm{liq}}} \tag{2.2}$$

where h_{gas} and h_{liq} are the lengthscales for the gas and liquid, respectively.

An important dimensionless group is the Weber number which represents the ratio of the disruptive aerodynamic forces to the restoring surface tension forces:

$$\mathrm{We} = \frac{\rho_{\mathrm{gas}}\bar{\mathrm{u}}_{\mathrm{i}}^2\mathrm{h}}{\sigma} \tag{2.3}$$

where ρ_{gas} is the gas density, h is a lengthscale parameter, and u_i is either taken as the velocity of the gas $\bar{u}_{\mathrm{gas}}$ or defined by some authors as u_{rel}, the relative velocity between the liquid and the gas-phase [e.g. 183]. The length scale parameter h is often taken as a lengthscale based on a liquid phase scale [e.g. 15, 183]. It will be seen later that the Weber number has been used by several authors to classify the different regimes of the rupture of a jet.

It is useful to introduce the Reynolds number, expressed as the ratio between the aerodynamic forces and the viscous forces:

$$\mathrm{Re} = \frac{\rho_{\mathrm{gas}}\bar{\mathrm{u}}_{\mathrm{gas}}\mathrm{h}}{\mu_{\mathrm{gas}}}. \tag{2.4}$$

It seems reasonable to base the choice of the lengthscale h on the height of the liquid injection channel as done by Sauer et al. [183] and Ling et al. [131].

Another useful dimensionless number is the Ohnesorge number:

$$\mathrm{Oh} = \frac{\mu_{\mathrm{liq}}}{\rho_{\mathrm{liq}} \mathrm{h}_{\mathrm{liq}} \sigma^{1/2}} \tag{2.5}$$

which relates the internal viscous force to inertia and surface tension forces. This dimensionless group is generally used to describe the effects of liquid viscosity in the secondary atomisation process.

The Reynolds and Weber numbers may alternately be defined based not on a lengthscale depending on the liquid phase scale, but on the boundary layer size δ. Indeed, stability studies by Lozano et al. [136] have shown that the aerodynamic boundary layer thickness linked to the shear stress exerted by the gas on the liquid sheet had a strong influence on the growth rates and the frequencies of the hydrodynamic instabilities. Gepperth et al. [71, 72] when studying prefilming liquid sheet atomisation, and also Ling et al. [131] in the case of two-phase mixing layer, are using a definition of the lengthscale based on the developed gas boundary layer plate to characterise their aerodynamic Weber and Reynolds numbers. Other authors, such as Déjean et al. [48], adopt the vorticity thickness in their regime classification (see Section 2.3.4) defined by the following relation:

$$\delta_w = \frac{\bar{u}_{\mathrm{gas}} - \bar{u}_{\mathrm{liq}}}{\left(\frac{\partial u_{\mathrm{gas}}}{\partial y}\right)_{\Gamma}}. \tag{2.6}$$

These two thicknesses δ and δ_w are generally defined at the outlet of the injector, before the interaction between the two fluids, which will strongly modify their value [46].

2.3.2 Axial jet

This configuration consists in a cylindrical axial jet. The liquid is injected through a circular orifice. It can be divided into two categories, depending on the presence or not of an annular gas flow. If a co-axial airstream is present – air-assisted axial liquid jet – it is issued through a coaxial circular slit, separated by a thin wall. Reitz & Bracco [169] established predictions for jet breakup regimes in a quiescent atmosphere depending on the Reynolds, Weber and Ohnesorge numbers based on experimental observations. As shown in Fig. 2.12a, four main breakup regimes have been identified, corresponding to different combinations of liquid

inertia, surface tension and aerodynamic forces acting on the jet. These are the Rayleigh (We $>$ 8), first wind-induced (We $<$ 13), second wind-induced (We $<$ 40) and the atomisation regimes (We $>$ 40). For a more detailed quantitative description of these regimes, see Reitz & Bracco [169] and Lin & Reitz [128].

Farago & Chigier [62] distinguished three atomisation regimes for the disintegration of an axial jet in the presence of a high-speed coflowing gas stream: the Rayleigh-type breakup (We $<$ 25), the membrane-type breakup (25 $<$We $<$ 70) and the fiber-type breakup (100 $<$We$<$ 500). Later, Marmottant & Villermaux [141] identified the additional digitation-type regime. This regime was also investigated by Hong [92] as he suggested the transverse instability mechanism of Rayleigh–Taylor type leading to ligament formation, as described in Section 2.1.1.2.

Later, Lasheras & Hopfinger [120] emphasised the importance of the gas vorticity boundary layer thickness and the use of additional non-dimensional numbers to describe and separate the different regimes. The most influential numbers according to them are: the gas Reynolds number, the gas Weber number and the momentum flux ratio. The gas is thus believed to impose both the velocity and the lengthscale of the instability, and surface tension effects become negligible. Lasheras & Hopfinger [120] then proposed a scenario for the classification of the atomisation of a liquid jet in coaxial gas flow into regimes (Fig. 2.12b).

On the topic of axial jet atomisation, Dahms & Oefelein [43] proposed a regime diagram associated with Diesel engine injection and atomisation. For a shear-coaxial liquid-nitrogen-helium injector operating at supercritical pressures, the regime diagram of Dahms & Oefelein [43] shows a clear transition from exhibiting classical two-phase spray atomisation phenomena to single-phase diffusion-dominated mixing. This questions the classical view of spray atomisation for high-pressure diesel fuel injection phenomena.

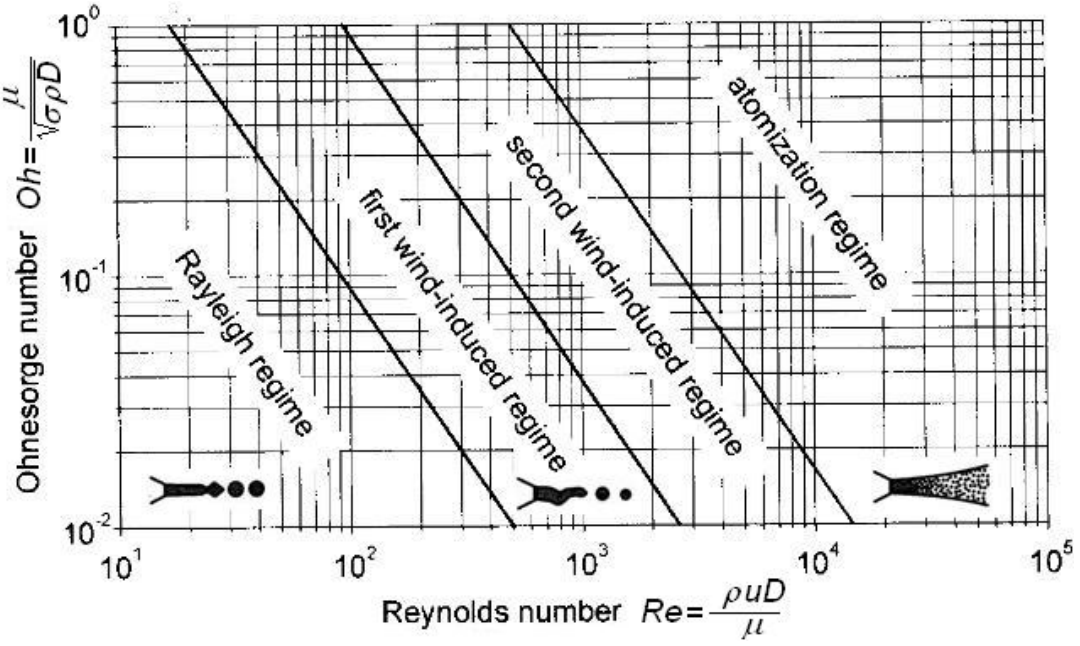

(a)

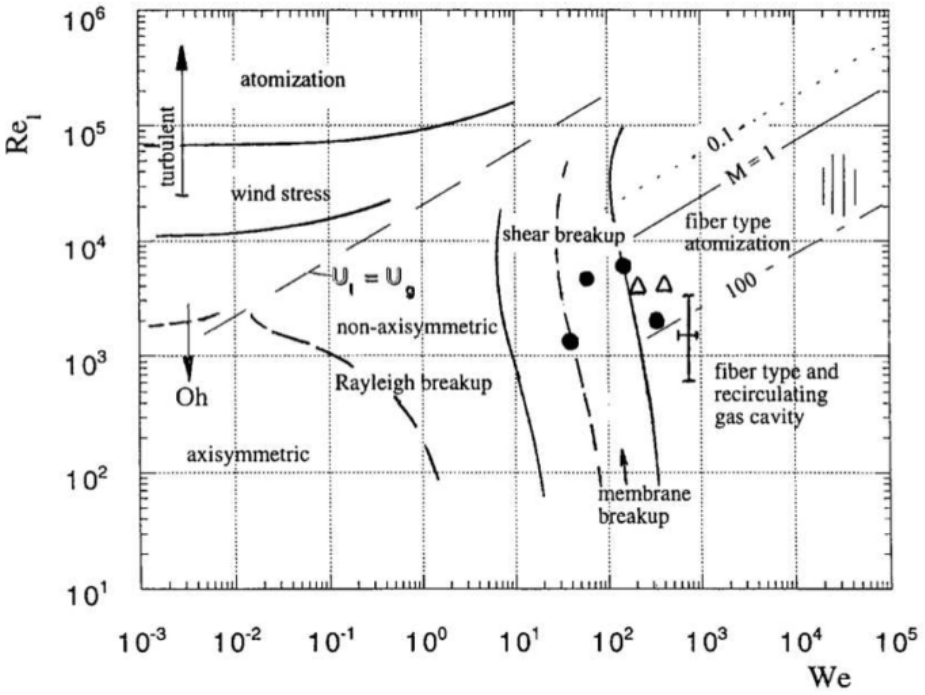

(b)

Fig. 2.12: **(a)** Classification of cylindrical axial jet breakup atomisation regimes in a quiescent atmosphere. Taken from Lefebvre [123]. **(b)** Map of the different breakup regimes in the air-assisted axial jet configuration from Lasheras & Hopfinger [120].

2.3.3 Liquid sheet configuration

This section is dedicated to the behaviour of liquid sheets bordered by two gas flows. In the investigations summarised in this section, both coflowing gas flows are identical in geometry and velocity. Within the last two decades, experiments by Stapper & Samuelsen [202], Mansour & Chigier [139] and Fernandez et al. [64], for instance, have allowed several classification of the macroscopic behaviours of liquid sheet disintegration to be established. The transition between those behaviours is believed to depend on the relative gas to liquid velocity.

A regime classification of the qualitative mechanisms observed in air-assisted liquid sheet configuration was proposed by Mansour & Chigier [139], who investigated the liquid velocity range $1.5 - 8.0$m/s and air velocity range of $0 - 145$m/s. Embracing the two types of liquid sheet oscillations introduced by the linear stability analysis of Hagerty & Shea [82] (Section 2.1.1.1), i.e. the sinuous and varicose modes of the liquid sheet interface, three distinct modes of breakup are distinguished by Mansour & Chigier [139]. They combined a linear stability analysis along with experimental observations to derive a relation between the liquid sheet oscillation frequencies as a function of the gas flow rate, for various liquid flow rates. For low liquid flow rates, the sinusoidal breakup mode is dominant. At intermediate liquid flow rates, both the sinusoidal and the dilatational modes are superimposed on the liquid sheet. With a further increase in liquid flow rate, the liquid sheet oscillations mainly become of the dilatational type. Lozano & Barreras [135] recovered with their own experiments these three breakup regimes, even though their experimental setup and flow configurations were different, questioning a little less the realism of the existence of these operating regimes.

In parallel, Stapper & Samuelsen [202] pioneered the advancement in the understanding of viscous liquid sheet fragmentation. Their liquid velocity range was $1 - 5$m/s and air velocity range, $0 - 60$m/s. They identified two atomisation regimes termed *cellular breakup* and *stretched streamwise ligament breakup* for airblast atomisation. Fig. 2.13 shows the schematic of the breakup mechanisms along with experimental photographs. *Cellular breakup* occurs when the ratio of gas to liquid velocity is high. The presence of streamwise waves, approximately equal in wavelength to the spanwise waves, generates a two-dimensional pattern involving the appearance of perforations, or cell-like structures, between the streamwise waves, as was described in Section 2.1.1.2. Eventually, these cells expand towards each other, coalesce and burst. The spanwise waves separate and finally lead to the formation of transverse ligaments (array of ribbons). The second mode, *stretched streamwise ligament breakup*, occurs at low liquid velocities, when the relative velocity increases. This mode is

characterised by a much faster growth of the transverse instability than the longitudinal one. Thus, ligaments formed in the flow direction predominate over the formation of spanwise ligaments. The sheet penetration is lower (shorter breakup length). It disintegrates closer to the injector exit.

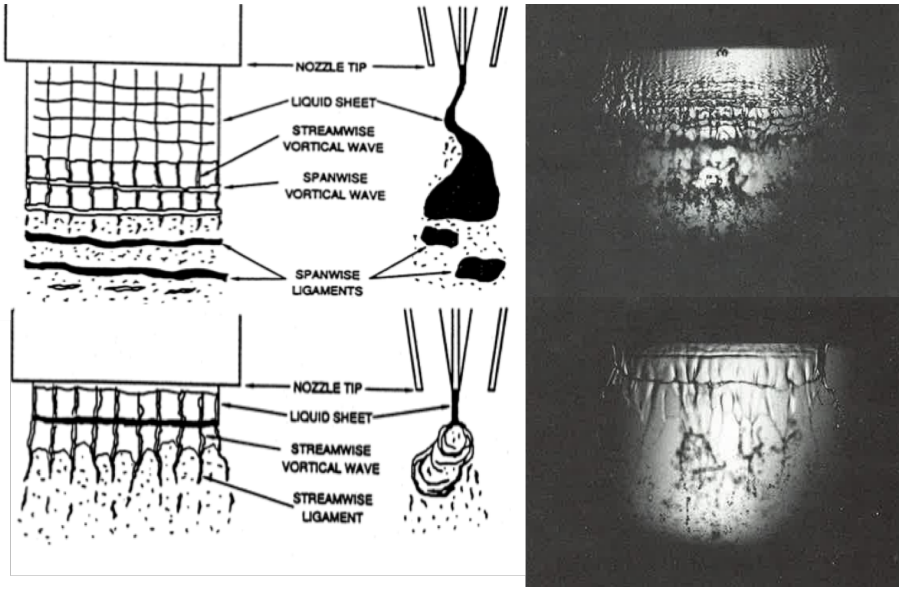

Fig. 2.13: The two liquid sheet breakup regimes observed by Stapper & Samuelsen [202]. Schematics and top view experimental photographs. *Top*: Cellular breakup; *Bottom*: Stretched streamwise ligament breakup.

Carvalho et al. [28] considered experimentally the disintegration of a flat liquid film, with a liquid velocity varied between 0.7 and 6.4m/s, surrounded by two air streams, up to an air velocity of 39m/s. A mapping exercise was conducted with experimental photos of the liquid disintegration process arranged as a function of the liquid velocity in the presence of different air flow velocities. They observed a transition of the liquid disintegration mode from dilatational to sinusoidal wave dominance at a momentum flux ratio of 0.5.

In his review on air-assisted liquid sheet atomisation regimes, Dumouchel [57] proposes a classification based on three breakup regimes based on the velocity ratio $\bar{u}_{\mathrm{gas}}/\bar{u}_{\mathrm{liq}}$, following the regime mapping study of Stapper & Samuelsen [202]. At low $\bar{u}_{\mathrm{gas}}/\bar{u}_{\mathrm{liq}}$, the sheet oscillates in a mixture of both spanwise and streamwise surface waves with low amplitude growth. The disintegration of the sheet is due to the growth of both spanwise and streamwise ligaments giving rise to liquid cellular structures. The liquid sheet penetration is high and the spray angle is small. This breakup mechanism is referred to as *cellular breakup* regime, named after the morphological classification of Stapper & Samuelsen [202]. When the relative

velocity increases (higher $\bar{u}_{\mathrm{gas}}/\bar{u}_{\mathrm{liq}}$), the streamwise instability predominates and ligaments are primarily formed in the flow direction. The stretching of streamwise ligaments mainly produces the droplets. This breakup mechanism is the *stretched streamwise ligament breakup regime* [202]. The "flag-effect" identified in Section 2.1.1.1 and characterised by the strong amplitude growth of the sinusoidal oscillation prior to the formation of the streamwise ligaments is likely to be a sub-mode of the stretched streamwise ligament breakup regime corresponding to lower gas velocity. For a further increase in $\bar{u}_{\mathrm{gas}}/\bar{u}_{\mathrm{liq}}$, no intact liquid sheet length is visible, the breakup of the streamwise ligaments occurs at the nozzle exit. This regime could be likened to the dripping regime of liquid jet of Lin & Reitz [128].

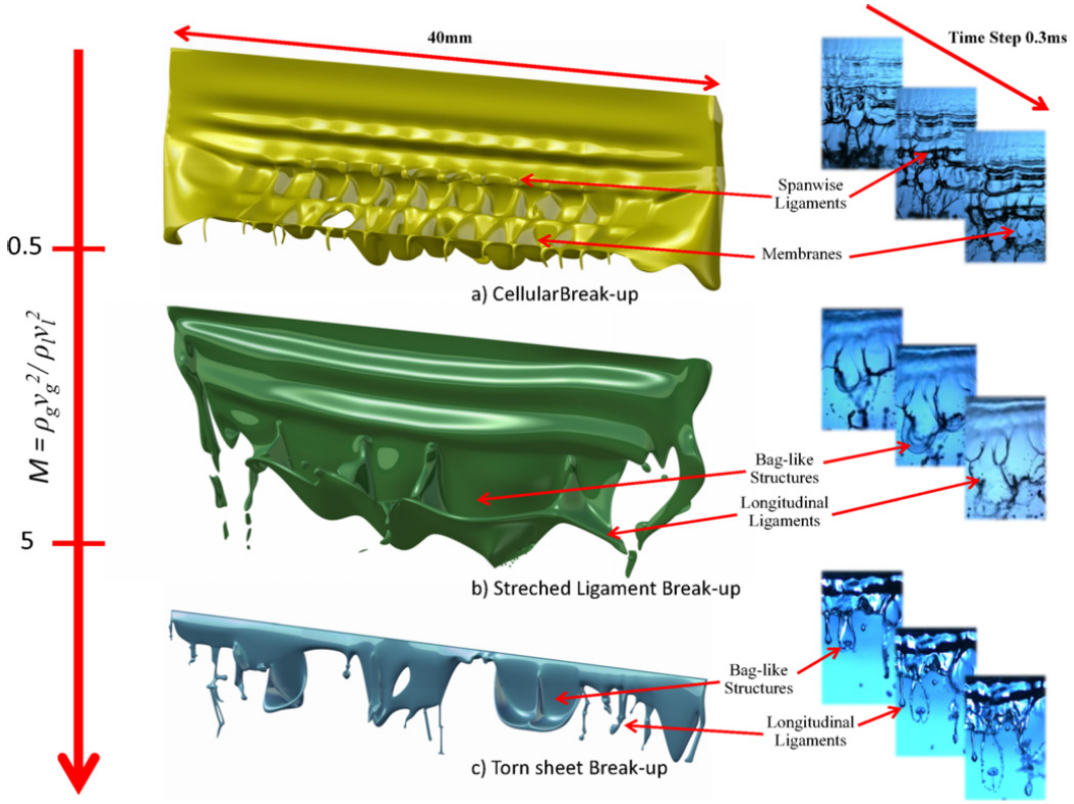

Fig. 2.14: Atomisation mechanisms evolution with momentum flux ratio as observed and classified by Fernandez et al. [64].

A more recent classification of atomisation regimes of a flat liquid sheet sheared on either side by a coflowing gas stream was proposed by Fernandez et al. [64] (Fig. 2.14). In their experimental analysis ($u_{\mathrm{liq}} \in [1; 2]$ m/s and $u_{\mathrm{gas}} \in [20; 70]$ m/s), the authors classify the regimes for primary breakup according to the momentum flux ratio MFR (Eq. 2.1). In particular, they identify three regimes of liquid sheet breakup. Up to a MFR of 0.5, Fernandez

et al. [64] identified the now-famous cellular breakup regime; and from MFR= 0.5 to MFR= 5, the stretched streamwise ligament breakup regime. One notes that the transitional value of 0.5 is equal to the one observed in the regime mapping by Carvalho et al. [28], outlined above. Above a MFR of 5, the torn-sheet breakup also produces droplets through the disintegration of membranes and via the fragmentation of streamwise ligaments and bags. These streamwise ligaments have highly irregular shapes and disintegrate through aerodynamic tearing rather than Plateau-Rayleigh instability. Increasing the MFR further, above 20, leads to what Fernandez et al. [64] refers to as a *membrane-sheet* type breakup where no clear pattern is visible. The breakup length is lower than in the previous regime.

2.3.4 Liquid film with prefilming zone

The study of liquid dynamics on prefilming zones is rather sporadic, as evident from the previous sections. In this section are outlined the experimental visualisations of the authors listed in Table 2.1, whose works constitute rare attempts at studying prefilming atomiser configurations. Their works highlight the influence of the prefilming zone on the classification of liquid evolution in regimes. The use of primary atomisation parameters based on the experimental conditions studied enables some atomisation cartographies to be proposed.

Fig. 2.15 presents the matrix of liquid film breakup phenomena proposed by Inamura et al. [95]. It shows the effect of a liquid flowrate and air velocity on the phenomenology observed, in a consistent manner, during primary breakup at the prefilmer edge. Their main conclusions are as follows. As the air velocity increases the breakup length of the liquid film shortens, and finer droplets are generated. In addition, the space between ligaments in the transverse direction narrows and ligaments diameter are thinning out. On the other hand, as the liquid flow rate increases the breakup length increases and coarser droplets are generated. However, the general mechanism by which the liquid film disintegrates is always the same. They observed the formation of three-dimensional surface waves on the liquid film surface. With the arrival of the liquid at the edge of the prefilmer plate, the liquid film deforms into bag-shaped liquid film structures, which consists of a thin liquid film attached to a thick rim. The thin liquid film disintegrates into numerous fine droplets, and thick ligaments attached to the trailing edge remain intact. Then, the thick ligaments disintegrate into bigger droplets.

Bhayaraju & Hassa [15] highlighted two atomisation regimes from their extensive visualisation experiments, depending on the Weber number $We_{gas,h_{liq}}$. The authors observed that for Weber numbers < 100, the liquid sheet breakup on the prefilming surface is similar to the non-prefilming surface breakup scenario (Section 2.3.3, Stapper & Samuelsen [202]).

Whereas for Weber numbers > 100, there exists a transition region to a surface stripping type of breakup in which detachment of mass from the liquid surface is observed (waves strip off from the liquid surface). Their study indicates that at higher Weber number conditions, the instantaneous topology of the liquid film on the prefilmer plate cannot be neglected.

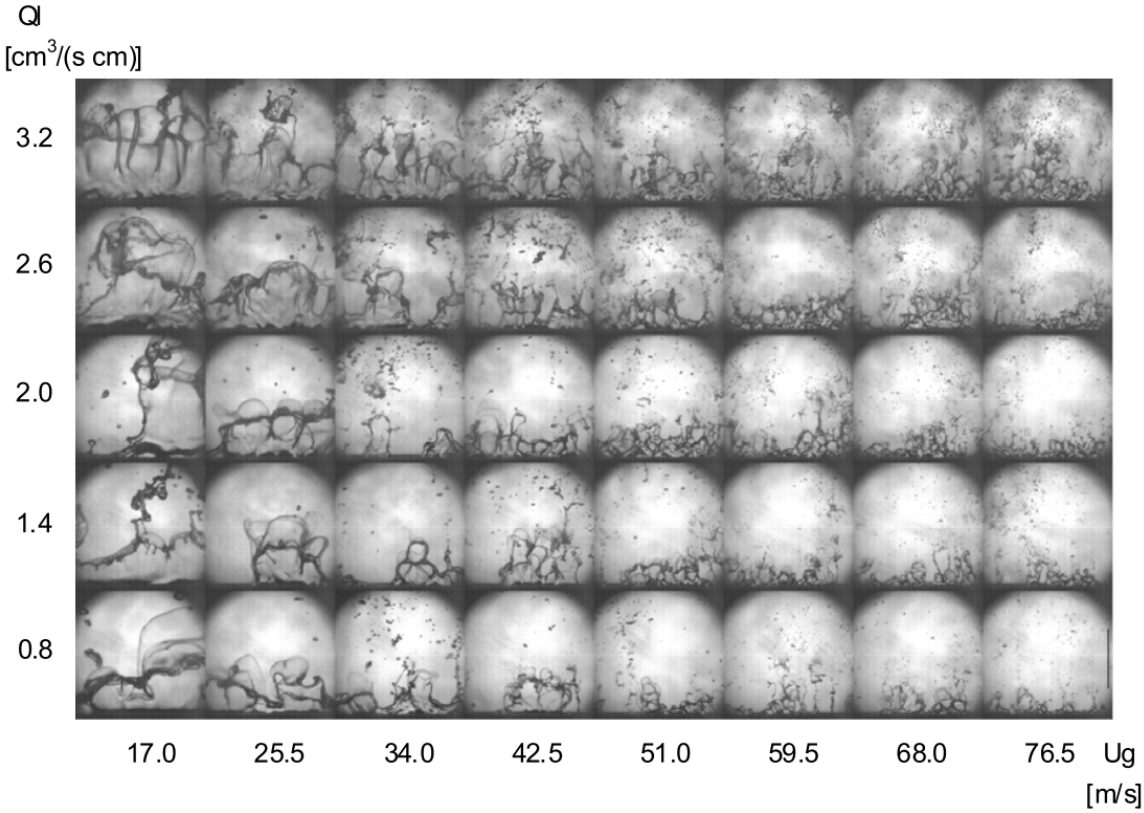

Fig. 2.15: Matrix of liquid film breakup phenomena as observed and classified by Inamura et al. [95]. The mean gas injection speed increases on the horizontal axis and the mean liquid injection speed on the vertical axis. The air and liquid flow from bottom to top in each photograph.

The recent experimental observations of Déjean et al. [48] enabled a regime classification into three distinct regimes: (i) a *smooth* regime for low velocity ratios, in which the thickness variation of the liquid film over the prefilmer is small although two-dimensional waves are visible; (ii) a *wave* regime for an increasing velocity ratio, where waves become three-dimensional and have a higher amplitude; (iii) for higher velocity ratios an *accumulation* regime is observed with periodic liquid release from the atomiser trailing edge. Based on the observation of these three different behaviours that depend on the flow parameters and injector geometry, a cartography based on two dimensionless numbers is established (Fig. 2.16). Given that these results are obtained for different liquid and air velocities and for

several prefilming zone lengths, these two non-dimensional groups are the MFR (Eq. 2.1) and the ratio between the length of the prefilmer (L_{pref}) and the vorticity thickness over the prefilmer plate δ_w (Eq. 2.6). Déjean et al. [48] further observed that the transition from the *smooth* to the *wave* regime only depends on the MFR. While the transition from the *accumulation* to the *wave* regime is due to a modification in prefilmer length and boundary layer thickness. Thus, Déjean et al. [48] highlights the influence of the prefilmer length on the atomisation process.

In contrast, the studies of Gepperth et al. [70, 71, 72] on the effect of the geometrical parameters, have shown the influence of the prefilmer trailing edge thickness only on the atomisation process. However, as was mentioned in Section 2.1.5, Gepperth et al. [70, 71, 72] visualised an accumulation-type of regime only, in which the liquid film evolution on the prefilmer plate is decoupled from the atomisation process at the prefilmer lip. The liquid sheet disintegration, under the influence of a vortex-like motion of the ligament structures at the prefilmer lip is solely affected by the air velocity. It is likely that in this regime only, the atomiser plate thickness plays a major role, but maybe not in the other regimes [48].

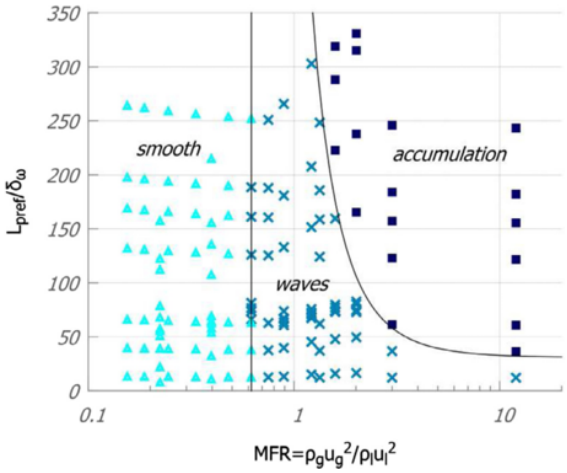

Fig. 2.16: Regime cartography of liquid atomisation for a prefilming airblast atomiser by Déjean et al. [48].

2.3.5 Final comments

This literature review has highlighted the complexity of liquid film dynamics and the atomisation process. A vast amount of literature has accumulated on the subject. In spite of this, there is a relatively limited understanding of these phenomena. Many aspects of spray formation are still poorly understood even at standard atmospheric conditions, let alone the requirement

for a deeper analysis of the mechanisms and processes involved at engine-relevant operating conditions. This chapter has demonstrated the necessity to take into account the geometry of the injector to predict the liquid dynamics, liquid atomisation and spray topology. There are some similarities in liquid evolution and fragmentation between jet atomisation and viscous liquid sheet/film atomisation. However, the details of the atomisation phenomenon must be asserted on a case-by-case basis. Liquid jet atomisation and non-prefilming liquid sheet disintegration have been the subject of an extended body of work. Although a few numerical and experimental studies have been performed on prefilming liquid sheet atomisation, a combined investigation considering the liquid wall film on top of the prefilmer and its subsequent disintegration is still a missing link, as pointed out by Warncke et al. [229]. The experimental approach is able to gather relevant qualitative information on the physical mechanisms controlling the primary breakup but still struggles to provide useful quantitative insight. Only recently, various experimental techniques have been developed in order to refine these measurements and extract quantitative liquid deformation characteristics on the prefilmer plate and downstream of the atomiser. Research studies suggest that a significant breakthrough in comprehension of atomisation could be achieved with the numerical approach. Much progress has been made towards the development of multiphase flow numerical methods. The smallest fundamental features identified during primary breakup are critical in the choice of a suitable numerical method to simulate the atomisation phenomenon. One of the main difficulties of modelling the whole atomisation process comes from the breadth of length and time scales involved in the governing physical phenomena and the resulting numerical requirements to achieve a reasonable accuracy in their representation.

Finally, some authors have attempted to categorise the breakup phenomena in terms of the operating conditions and geometrical features of the atomising device, with the aim of improving our understanding of the gas/liquid interaction in the near nozzle region and extrapolating breakup predictions to a multitude of operating conditions. This chapter allows to draw several conclusions about the description of the liquid phase in the dense spray region of prefilming airblast atomisers and approaches to classify them. Most authors agree on the critical influence of the relative liquid/gas velocity ratio on the atomisation process and recognise that all the atomisation mechanisms are connected with wave formation, wave development and wave disintegration. Nevertheless, there is no universal consensus among the scientific community regarding which additional flow parameters and geometrical parameters characterise the breakup process in liquid sheet and liquid film configurations. Hence, a common definition in non-dimensional groups is still lacking. The effects of the physical properties of the liquid and the gas outlined in this literature review seem to be strongly

regime dependent, highlighting the need to continue investigating the physics in several regime zones. This leaves the door open for a variety of useful investigations.

Chapter 3

Numerical Method

The involvement of complex interface movement in real flows requires robust but also efficient numerical techniques to handle topological changes of the fluid phases. This is especially the case in applications where hydrodynamic breakup is a dominant feature, for example in the near field of an atomising diesel jet [50, 195], or for micro-scale multiphase flows in porous media such as enhanced oil recovery or carbon dioxide storage in underground aquifers [162]. The simulation of these flows presents many numerical difficulties due to the necessity to track the exact location of the infinitely thin interface and the discontinuities in physical properties associated with it.

3.1 Numerical challenges in the modelling of two-phase flows

Numerical simulations of multiphase flows still challenge our capabilities in computing homogeneous flows using direct numerical simulations (DNS) – where the governing equations are solved using sufficiently fine grids so that all continuum time- and length-scales are fully resolved – which have become a standard tool in turbulence research [102]. From a mathematical point of view, multiphase flow problems are notoriously more challenging. Not only are the equations governing the fluid flow in both phases nonlinear, but considering that the position of the phase boundary must be calculated as part of the solution adds an extra level of difficulty to the numerical challenge.

3.1.1 Physical origin of surface tension

An interface is a surface delimiting two disjoint regions, two fluids, liquid and gas in this study. In each bulk phase, molecules or atoms attract one another. In the bulk liquid, intermolecular forces are responsible for the cohesion of the molecules. But at the interface with the gas medium, liquid molecules experience an uneven force since an imbalance arises due to the lack of – or the difference in – the attractive force from the gas beyond the phase boundary. Consequently the liquid particles located at the interface are pulled inwards by the molecules deeper in the same phase and cohere more strongly to the bulk liquid than they would otherwise. The latter translates into a surface force – surface tension – acting locally on the liquid particles, in both normal and tangential directions. Intermolecular forces between a liquid and a gas media associated with surface tension are given the special name of capillary forces. Surface tension depends on both media at an interface: for example, the surface tension of water surrounded by air is different than that of water surrounded by oil. It is generally calculated by experimental measurement techniques.

3.1.2 Accurate interface representation and advection

The interfacial treatment is, in the numerical representation of front propagating problems, probably the most challenging numerical problem among the diverse and complex physics involved. One must resolve the interface, i.e. account for its presence in the computational domain by transporting it and keeping track of its very frequent topology changes at any time, as the surfaces of the gas and liquid media merge and breakup. The interface thickness is comparable to the molecular scale. The difficulty of multiphase flow modelling thus comes with sharp interfaces that represent a continuous, but steep change of the material properties (density, viscosity, etc) of the two fluids, sometimes with density jumps of several orders of magnitude. Numerical schemes need to cope with the formation of these large gradients and preserve the sharpness of the interface.

Attempts to simulate flows involving extensive topology changes in multiphase CFD have resulted in a variety of numerical approaches. Among these, implicit interface-capturing methods – Volume of Fluid (VoF) and Level-Set (LS) – have attracted significant attention as good candidates for simulating flows involving extensive topology changes and high density ratios [8, 157, 171, 218].

Inherent to multiphase flow modelling is the numerical representation of the sharp interface location and its advection, as well as the effect of the surface tension forces, or capillary

forces. In the framework of all implicit interface-capturing methods, the interface is treated as a region of steep gradient in a scalar field. The interface location is known by defining its normal and curvature implicitly, from the underlying scalar field.

The VoF method captures the interface through the transport of a volume fraction scalar field γ in the computational domain [78, 90, 189]. The volume fraction – also known as indicator function – represents the volume in a 3-D computational cell (respectively the area in 2-D) occupied by one phase. Consequently, the indicator function takes values between 0 and 1 in the cells occupied by both fluids and either 0 or 1, depending on the phase, in the rest of the domain. Accurate knowledge of the interface topology is required for accurate determination of the interface curvature, needed for the calculation of the surface tension forces. An "interface reconstruction" algorithm is implemented in the VoF method, based on the liquid volume fraction γ. Following the reconstruction of the interface, the volume fraction is transported by the velocity field using an advection algorithm.

The level-set (LS) formulation, originally formulated in Osher & Sethian [152], Sussman et al. [205], is based itself on the transport of a continuous function $\phi(\mathbf{x},t)$ in the computational domain by the underlying velocity field. In this framework, the level-set of the interface is represented by $\phi_\Gamma = 0$ and ϕ takes values below zero in one fluid and above zero in the other. The function ϕ is generally taken as the signed distance function from the interface such that the Eikonal equation is satisfied: $|\nabla\phi| = 1$.

Like the VoF method, the LS technique handles topology changes naturally. However, the main advantage of the LS method is that it provides the precise front location directly (no interface reconstruction is needed). The interface topological changes are handled automatically in the computational mesh elements where the two fluids coexist. It inherently offers a sharp representation of the interface and accurate representation of the interfacial quantities such as the interface normal and curvature, needed for computing accurate surface tension forces. The major advantage of the VoF numerical method is that it is inherently mass-conservative, if a conservative numerical scheme is in use.

However, interface-capturing methods are associated with a number of disadvantageous numerical challenges, which limits their accuracy [189]. Intrinsic to the method is a rather excessive diffusion of the interface, highly-dependent on the mesh spacing. The reason behind the numerical diffusion of the interface is the advection of the underlying original discontinuous indicator function with no control over the interface thickness [157, 220]. Compression methods have been introduced to minimise this deficiency, using algebraic manipulations such as the CICSAM scheme of Ubbink & Issa [221] or the inter-gamma scheme *interFoam* of Jasak & Weller [101]. These methods are commonly observed to

smear the interface out due to numerical diffusion when low-order discretisation methods are used [76]. In the case of mesh under-resolution, with a radius of curvature of the order of the mesh spacing, the approximate interface reconstruction leads to an uncertainty in curvature calculation. This leads to inaccuracies in the calculation of the capillary forces. When using higher-order schemes, the solution is commonly found to produce numerical oscillations.

In level-set approaches, as opposed to VoF approaches, mass conservation is not embedded in their formulation. As a result, poorly resolved regions of the flow are susceptible to mass loss or mass gain. With the iterative "re-distancing" scheme proposed by [205] as a remedy, level-set methods have since then matured into a promising numerical technique for accurate simulation of multiphase flows. Although the implementation of an iterative re-initialisation algorithm partially corrects this issue, this method does not systematically re-distribute the mass appropriately where it was originally lost [150, 151] and therefore still does not satisfy mass conservation exactly [158].

An additional challenge to the modelling of multiphase flows follows directly from the above discussion. The choice of numerical schemes must be capable of limiting numerical artefacts present in the calculations because of errors in the curvature computation, thickness of the interface and stiffness induced by the additional capillary forces, as well as balance between surface tension forces and pressure gradients. The generation of unphysical flow at the interface – so-called spurious or parasitic currents – is due to a combination of numerical inadequacies between an inaccurate curvature calculation and lack of a discrete force balance [66]. For flows with large density ratios, the interfacial force imbalance is larger and parasitic currents are more significant [163, 220]. The numerical challenge of representing the surface tension force at the phase interface is present in both VoF and LS methods. For VoF methods that suffer from diffusion, it is difficult to achieve an accurate representation of interface curvature. For LS methods that provide a sharp interface, the effect of the volumetric surface force is confined to a narrow region around the interface and the calculation of the normal vector can be numerically unstable. Various methods have been developed to minimise spurious currents, such as (i) improvement of the curvature computation, (ii) achievement of discrete balance between surface tension and pressure gradient and (iii) use of an adaptive time integration scheme to tackle the stiffness induced by surface tension. It should be noted that the generation of spurious currents is not usually considered of great importance for inertia-dominated flows. However, it is detrimental in the computation of capillary flows and surface tension dominated flows, for example in hydrodynamic flows involving quasi-stationary flows (see Chapter 5) and pore-scale modelling [1].

Another difficulty lies in the design of a reconstruction operator to reconstruct the cell-face values, needed by the flux evaluation (so-called interpolation problem or Riemann problem) that would allow a high-order accuracy while avoiding the generation of spurious oscillations in the vicinity of discontinuities. Spurious currents create oscillations strong enough to destroy the interface. Artificial numerical wiggles must be damped to predict the physics of breakup accurately. Spurious currents in this region pose serious concerns in the computation of the atomisation process as the generation and evolution of capillary flows at the interface are directly characterising the small liquid structures detaching from the liquid bulk.

3.2 Solution of the incompressible Navier–Stokes equations and surface tension forces

We consider incompressible liquid-gas two-phase flows with constant densities ρ_{gas} and ρ_{liq} and viscosities μ_{gas} and μ_{liq}. Most primary atomisation applications involve low Mach number everywhere in the domain considered ($Ma << 1$), i.e. the speed of the flow is much lower than the speed of sound. Solving the Navier–Stokes equations [148] and the continuity equation in the incompressible limit is thus perceived as a valid assumption and is the approach chosen here.

If the multiphase flow domain was divided into sub-domains, and each fluid domain had its own set of Navier–Stokes equations according to which it evolved, the mathematical connection between the domains on the interface would be obtained through mass and momentum conservation, which leads to the formulation of jump conditions for quantities discontinuous across the interface as extra equations to solve for.

Instead, it is easier to express the governing equations a system of equations for both fluids, over the whole multiphase domain, and the jump conditions across the interface are effectively replaced through the singular capillary forces on the right-hand-side of the Navier–Stokes equations (Eq. 3.1). The conservative formulation of the incompressible Navier–Stokes equation in each phase is given by

$$\frac{\partial \rho \mathbf{u}}{\partial t} + \nabla \cdot (\rho \mathbf{u}\mathbf{u}) = \nabla \cdot \boldsymbol{\mathcal{T}} + \mathbf{f} \tag{3.1}$$

$$\nabla \cdot \mathbf{u} = 0$$

where $\mathbf{u}$ is the fluid velocity and ρ its density. The term $\nabla \cdot \boldsymbol{\mathcal{T}}$ is the viscous stress tensor. It comprises normal stresses (pressure p) and shear stresses for viscous fluids and reads: $\boldsymbol{\mathcal{T}} = -p\boldsymbol{\mathcal{I}} + \boldsymbol{\mathcal{S}}$, where $\boldsymbol{\mathcal{S}}$ is the shear stress tensor:

$$\boldsymbol{\mathcal{S}} = \mu \left(\frac{\partial u_i}{\partial x_j} + \frac{\partial u_j}{\partial x_i} \right)_{i,j=1,2,3} \tag{3.2}$$

We note that the shear stress tensor also comprises normal stresses when $i = j$. The term $\mathbf{f} = \mathbf{f_g} + \mathbf{f_c}$ corresponds to all the external forces, i.e. $\mathbf{f_g} = \rho \mathbf{g}$ is the gravitational force and $\mathbf{f_c}$ represents the singular capillary forces only present on the nearly infinitely thin interface:

$$\mathbf{f_c} = -\sigma(\nabla \cdot \hat{\mathbf{n}}_\Gamma)\hat{\mathbf{n}}_\Gamma \delta_\Gamma + \nabla_\Gamma \sigma. \tag{3.3}$$

The term δ_Γ denotes a distribution concentrated on the sharp interface Γ. We assume a constant surface tension coefficient σ along the interface, which gives rise to $\nabla_\Gamma \sigma = 0$, whereas across the interface, σ varies and is responsible for the curvature of this interface. The interface curvature is given by

$$\kappa = -(\nabla \cdot \hat{\mathbf{n}}_\Gamma) \tag{3.4}$$

where $\hat{\mathbf{n}}_\Gamma$ represents the unit interface normal

$$\hat{\mathbf{n}}_\Gamma = \frac{\nabla \psi}{|\nabla \psi|} \tag{3.5}$$

and ψ is the indicator function used to represent the amount of each fluid present in each cell, previously introduced in Section 3.1.2 as γ. The sharp interface Γ represents a discontinuous change of the properties of the two fluids.

As finite volume numerical methods can only handle volumetric forces, the surface tension forces have to be converted into volumetric forces (Nm^{-3}) before being incorporated as a source term in the Navier–Stokes equations (Eq. 3.1). Eq. 3.3 is transformed into a volumetric force by distributing its effects over a small volume in the vicinity of the interface. The pressure difference due to surface tension $\sigma\kappa$ (Nm^{-2}) is multiplied by the gradient of the indicator function $\nabla\psi$ (m^{-1}). This numerical method of obtaining the volumetric surface tension forces represents the Continuum Surface Force (CSF) model of Brackbill et al. [21]:

$$\mathbf{f_c} = \sigma\kappa\nabla\psi. \tag{3.6}$$

The localisation of the interface is thus available through the calculation of its curvature κ (Eq. 3.4) and non-zero gradient of the indicator function $\nabla\psi$. We note that the curvature is

thus calculated by two consecutive spatial derivatives of the indicator function field. The fact that this field is not smooth can cause large errors during the calculation of the second derivative, which can lead to inaccurate estimations of the surface tension forces and thus can cause unphysical spurious currents at the interface. The latter can become a limiting factor during the simulation of surface tension-dominated flows.

In terms of momentum conservation, and given the forces in play, the surface tension forces must balance the jump in the stress tensor $\mathcal{T}$ (normal and tangential components) along the fluid interface. For static fluid configurations (see Chapter 4, Section 4.1), for which the stress tensor reduces to the form $\mathcal{T} = -p\mathcal{I}$, and the dynamics of the interface are determined by the Young-Laplace balance condition

$$\Delta p = \sigma \kappa \tag{3.7}$$

where Δp is the pressure jump – normal pressure gradient – across the fluid interface, which must be balanced by the curvature pressure at the interface [9].

3.3 Computational framework for the RCLS method

The RCLS method is based on the conservative level-set method (CLS) of Olsson & Kreiss [150] and Olsson et al. [151] that transports the liquid-vapour interface accurately while conserving mass. The CLS method is based on an alternative definition of the level-set function introduced in Section 3.1.2. In the current formulation, instead of transporting a signed distance function ϕ, the method transports a hyperbolic tangent function ψ initialised with the signed distance function ϕ as follows:

$$\psi = \frac{1}{2}\left(\tanh\left[\frac{\phi}{2\varepsilon}\right] + 1\right). \tag{3.8}$$

The conservative level-set ψ goes smoothly from 0 (in the gas phase) to 1 (in the liquid phase). It takes values between 0 and 1 in the transition region. The approximate location of the interface is given by the level-set $\psi_\Gamma = 0.5$. Whereas the conservative level-set methods of Olsson & Kreiss [150] and Desjardins [50] treat the scalar field ψ as a level-set, we choose to consider it as a smeared out liquid volume fraction. In this manner, all the volume encompassed by the iso-surface $\psi_\Gamma = 0.5$ can be considered as being filled with liquid. The inner-most ($\psi = 0.95$) and outer-most ($\psi = 0.05$) contour lines gather 90% of the phase transition.

The representation of what is meant by the hyperbolic tangent of the level-set function in 3-D with respect to the computational domain discretisation is depicted in Fig. 3.1a. Both the interface and the level-set function are infinitely thin (the interface thickness is of the order of the molecular scale) and can never be resolved within one computational cell, in a pure DNS sense. One can imagine constructing in 3-D a $3 \times 3 \times 3$ stencil (27 cells, 9 cells in 2-D) in which the central cell contains the peak of the level-set function and the cells around it contain the rest of the interface, i.e. the tail of the function. This stencil is the best we can do to describe the level-set contour ($\psi = 0.5$) representing one droplet: a $3 \times 3 \times 3$ stencil box centred at the droplet centre, as shown in Fig. 3.1b. This is the absolute minimum over which we can resolve a liquid structure such as a droplet. Therefore, by design, the RCLS method makes more efficient use of cells, for the same accuracy, than VoF methods. The main parameter of the CLS method is the coefficient ε that controls the width of the hyperbolic tangent profile in Eq. 3.8. Therefore, ε effectively controls the resolution of the interface through the interfacial thickness. Stability studies by Olsson et al. [151] and Pringuey & Cant [160] recommend values of $\varepsilon > 0.5\overline{\Delta x}$, where $\overline{\Delta x}$ is the characteristic average mesh-element size.

Since a sharp interface provides a better representation of the physics, it is generally desirable to limit the spread of the phase transition as it is the locus of the capillary forces (Eq. 3.6, CSF formulation), and preferable to model the interface to be as thin as possible to minimise the effect of smearing of the material properties and surface tension forces.

Nevertheless, the interface needs to have a minimal thickness, so that the gradient of ψ (Section 3.5) and interface normal (Eq. 3.5) are accurately calculated. As a result of the CSF method, the material properties over the whole multiphase domain are given by:

$$\begin{aligned} \rho &= \rho_{\text{gas}} + (\rho_{\text{liq}} - \rho_{\text{gas}})\psi \\ \mu &= \mu_{\text{gas}} + (\mu_{\text{liq}} - \mu_{\text{gas}})\psi. \end{aligned} \tag{3.9}$$

The relative performance of the RCLS method with respect to established multiphase numerical methods such as OpenFoam multiphase flow solver *interFoam* [101] and the Accurate Conservative level-set (ACLS) method of Desjardins [50] was assessed and discussed in Pringuey & Cant [160]. From canonical numerical test cases, the RCLS method was shown to outperform the latter in terms of accuracy and robustness. As part of the present work, additional numerical test cases were conducted and presented in Section 3.9 of the present chapter and Chapter 4 and 5.

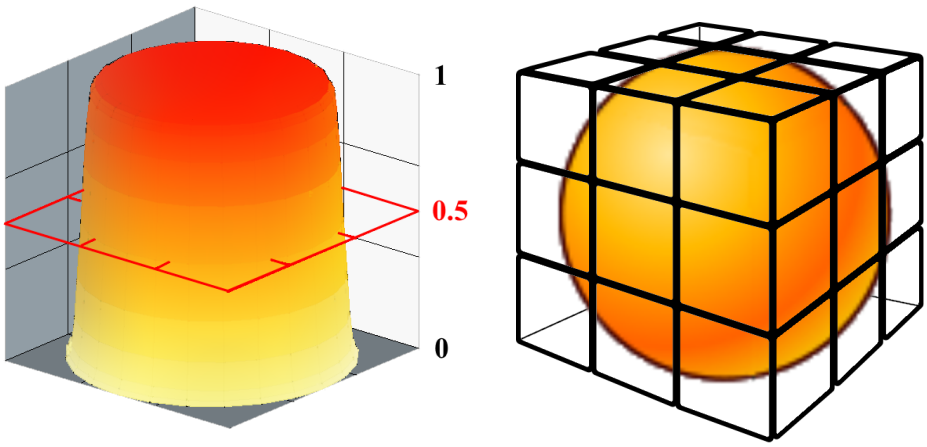

(a) 3-D hyperbolic tangent in a $3 \times 3 \times 3$ stencil **(b)** 3-D droplet in a $3 \times 3 \times 3$ stencil

Fig. 3.1: (a) Representation of the smooth conservative level-set function in 3-D with respect to the computational domain discretisation. The conservative level-set field ψ is bounded between 0 and 1. The phase boundary iso-contour is given by $\psi = 0.5$ (red); and **(b)** corresponding liquid droplet.

3.4 Weighted Essentially Non-Oscillatory (WENO) schemes

The function ψ in Eq. 3.8 is advected in a conservative manner, in a zero-divergence velocity field, with an arbitrarily high-order WENO scheme developed for three-dimensional mixed-element unstructured meshes by Pringuey [158] in order to handle complex real-world geometries:

$$\frac{\partial \psi}{\partial t} + \nabla \cdot (\mathbf{u}\psi) = 0. \tag{3.10}$$

WENO schemes were a mathematical tour de force first developed by Liu et al. [134]. They have the unique ability to preserve the required sharpness of the interface in front-propagating problems and to cope efficiently with the large gradients associated with jumps in material properties of several orders of magnitude, resulting from the presence of the phase boundary. As shown in Fuster et al. [69] for example, the accurate simulation of the atomisation process requires precise numerical representation of the geometry of the injection device. As a result, the focus of the work in Pringuey [158] has been placed on the development of a numerical approach specifically tailored for the transport of a scalar level-set on 3-D mixed-element unstructured meshes for application to incompressible two-phase flow problems, to achieve high-order accuracy and non-oscillatory properties near discontinuities such as phase

interfaces in complex real injector geometries. The WENO scheme is an essential building block of the RCLS method (Section 3.3) developed by Pringuey [158].

For each cell in the mesh – in which the point-wise values of the flow variables will be calculated – a set of computational cells is generated around it. This comprises a central stencil (Fig. 3.2a) and several sectorial stencils (Fig. 3.2b) covering all the direction of the space in the vicinity of the targeted cell are added around that cell. For each stencil of each targeted cell of the computational domain, a polynomial reconstruction procedure is performed that produces a polynomial $p(\mathbf{x},\mathbf{y},\mathbf{z},t)$ representing the flow variable, for example $\mathbf{u}(\mathbf{x},\mathbf{y},\mathbf{z},t)$, everywhere in the cell. This polynomial is reconstructed using the cell-averages of the variables in the cells of the associated stencil. For conservation, the integral of this polynomial over the targeted cell must equal the cell-average value of the variable in that same targeted cell.

Then, a WENO polynomial is reconstructed for each targeted cell upon combination of all the linear polynomials generated in the previous step. These are combined in a way that their respective smoothness contribution is weighted. The fact that the reconstruction procedure is not done with a single stencil, but multiple stencils, serves to ensure that only smooth solutions are interpolated. Hence, WENO schemes diminish the occurrence of numerical instabilities that can grow when connected with non-linear flow dynamics.

To time-advance the cell-averages of the flow variables in the context of the finite-volume scheme, the inter-cell fluxes need to be computed. The reconstructed solution of the flow variable in the targeted cell and the reconstructed solution in the neighbouring cells are used for flux calculation. An inter-cell flux is associated with a given cell and with a given face of that cell. There are as many inter-cell fluxes per cell as there are faces encapsulating that cell. Pringuey & Cant [159] chose to use an exact Riemann solver to express the numerical fluxes, for both Eq. 3.10 and Eq. 3.11.

A final central aspect of the present WENO scheme is the generality of the method: the polynomial reconstruction is performed in a reference space $\xi = (\xi,\eta,\zeta)$, as opposed to a physical space $x = (x,y,z)$, where scaling effects do not apply [159]. A mapping is created $x = x(\xi,\eta,\zeta)$ to relate the physical coordinates to the reference coordinates. For each cell in the mesh, the inverse of this cell-dependent mapping: $\xi = \xi(x,y,z)$ is applied to the targeted cell and its stencil to undertake the reconstruction in the reference space.

Although the WENO numerical scheme can formally reach arbitrarily high-order in space, in this demonstration of the modelling capability we limit ourselves to a third-order polynomial reconstruction, $r = 3$, with r denoting the order of the linear polynomial reconstruction.

This typically leads to a fourth-order accurate scheme for the transport of the liquid volume fraction with a WENO-treatment reconstruction [158].

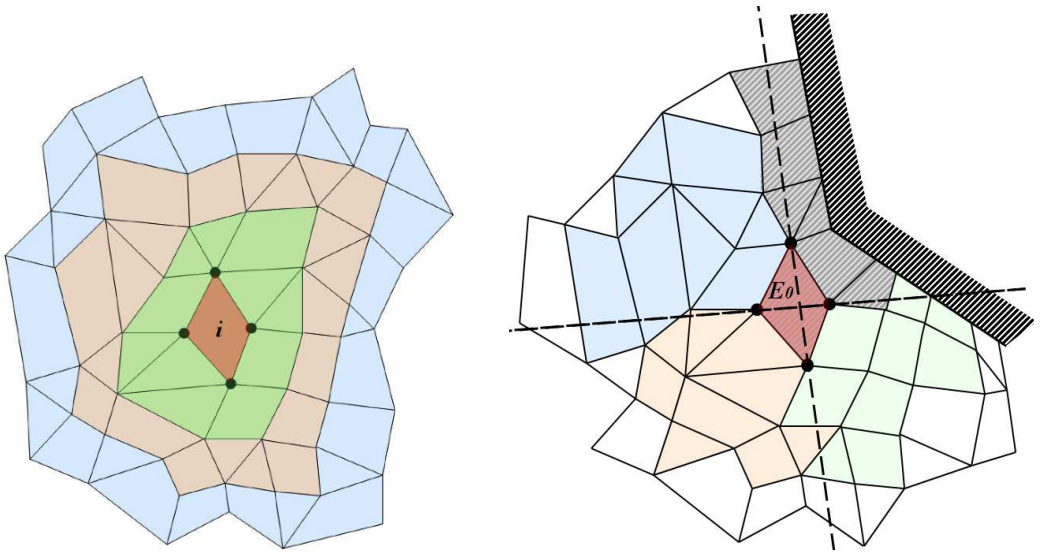

Fig. 3.2: **(a)** Central stencil and **(b)** sectorial stencils. Layers of cells added to each cell in the mesh for polynomial interpolation. Taken from Pringuey [158].

3.5 Calculation of gradient

It is known that the quality of the gradient field calculation is important to avoid spurious oscillations, as expressed in Desjardins [50]. To resolve this issue, Pringuey [158] took advantage of the polynomial reconstruction of the scalar field ψ performed by the WENO scheme (Section 3.4). The WENO polynomial embeds both the essentially non-oscillatory properties required to avoid the spurious oscillations and high-order approximation of the face-averaged gradient $\overline{\nabla\psi}$, which is required for the non-linear flux calculation with the exact Riemann solver, the calculation of the interface normal (Eq. 3.5) and surface tension forces (Eq. 3.6).

3.6 Re-initialisation equation

Once again, as the surface tension is applied in the region of the phase transition, it is desirable to limit the spread of the interface, and not to lose small-scale liquid structures

because of mass conservation issues. However, even high-order numerics such as the WENO scheme will eventually diffuse the interface. As a result, there is a need to re-initialise the level-set profile ψ to maintain the interface thickness at a constant value. In order to achieve that, a re-initialisation algorithm is applied [160]. The formulation presented is combining the simplicity and generality of the original re-initialisation equation by Sussman et al. [205] in terms of high-order standard discretisation and the accuracy of the constrained re-initialisation scheme in terms of interface displacement. The technique ensures mass-conservation to machine accuracy. The re-initialisation equation reads

$$\frac{\partial \psi}{\partial \tau} + \nabla \cdot (\psi(1-\psi)\hat{\mathbf{n}}_\Gamma) - \varepsilon \nabla \cdot (\nabla \psi) = 0 \tag{3.11}$$

where $\hat{\mathbf{n}}_\Gamma$ is the normal to the interface, ε was introduced in Section 3.3 as the CLS coefficient, and τ is the artificial time in which the equation is solved until the initial level-set profile is recovered. As the temporal discretisation of the re-initialisation equation is performed with an explicit Runge–Kutta (RK) scheme, it is necessary to consider the stability restrictions associated with the numerical solution of Eq. 3.11. Olsson et al. [151] identified the viscous term in Eq. 3.11 as the driver of numerical instabilities and suggested the following condition:

$$\Delta\tau \leq K \frac{(\Delta x)^2}{\varepsilon}. \tag{3.12}$$

From numerical experiments, Olsson et al. [151] established that stability is typically obtained with $K = \frac{1}{4}$; and the iteration stops when

$$\frac{||\psi^{n+1} - \psi^n||}{\Delta\tau} < \delta \tag{3.13}$$

for some small δ.

A compression flux is introduced in the re-initialisation equation (Eq. 3.11). It is applied in the transition region in the direction normal to the interface to maintain a sharp interfacial profile of constant thickness. Because the compressive flux alone would reduce the interface thickness to nearly zero, leading to a less robust method, a diffusion term is also introduced to stabilise the CLS method, in the direction normal to the interface. With our numerical formulation – conservative finite volume WENO scheme and exact Riemann solver – only numerical simulations involving very large density ratios (of the order of 1000) require the diffusion term to be stabilised.

Desjardins et al. [51] introduced an extra parameter for CLS methods, the periodicity of the re-initialisation N_S, i.e. the periodicity over which Eq. 3.11 is solved. An optimum value for N_S can be found and tuned. Indeed, it is clear that re-sharpening the hyperbolic tangent

profile via Eq. 3.11 will move the interface front. As a result, despite this shortcoming, it is of primary importance to ensure that the conservative re-initialisation equation is used without deteriorating the level-set transport itself. Desjardins et al. [51] found that increasing the periodicity N_S of the re-initialisation step could improve the ability of the method to capture thin ligaments and droplets: if the re-initialisation equation is applied too frequently the solution worsens; it is detrimental to the predicted level-sets, which become convoluted. Provided we perform the conservative re-initialisation step every five time steps or less, the quality of the level-set profile appears satisfactory [51, 158].

3.7 Implementation in OpenFoam in parallel

The numerical approach described is implemented in parallel and in C++ within the framework provided by the open-source CFD Toolkit OpenFoam of Weller et al. [231]. In this instance, the pressure-velocity coupling in the Navier–Stokes equations is handled with the readily-implemented Pressure-Implicit with Splitting of Operators (PISO) method. Since the numerical framework is geared towards industry application as the complex geometries of modern aero-engine fuel injectors must be faithfully represented [158], the RCLS method with WENO treatment of the discontinuities runs on 3-D mixed-element unstructured meshes consisting of general convex polyhedra. Since OpenFoam uses finite-volume discretisation for the solution of the two-phase flow equations, the implementation of unstructured grids is easier than with finite-difference schemes.

The parallelisation of the code is based on conventional domain decomposition techniques using MPI. However, in addition, a n-halo parallelisation method has been implemented in OpenFoam to perform the computations at the expected order of accuracy [158]. Using a high-order WENO scheme with a lower-order-accurate flux exchange at the inter-processor boundaries (0-halo approach), leads to non-physical behaviour of the interface near those boundaries [158]. In order to reach the appropriate level of accuracy in parallel, the size of the halo surrounding each processor subdomain varies with the order of the WENO polynomial reconstruction. We note that the pressure solvers GAMG and PCG have, as of yet, not been parallelised with the n-halo approach. This may lead to a small mass error in parallel [158]. However, we did not notice any effect in our calculations.

3.8 MULES flux limiter

The third-order Total Variation Diminishing (TVD) RK scheme of Shu & Osher [197] is used for higher order accuracy in the temporal discretisation, for both the advection (Eq. 3.10) and re-initialisation (Eq. 3.11) steps. However, WENO schemes are not necessarily Total Variation Bounded (TVB), even when coupled with TVD Runge–Kutta time integration. Non-physical values of ψ such that $\psi < 0$ or $\psi > 1$ cannot be tolerated.

As a result, the Multidimensional Universal Limiter with Explicit Solution (MULES) of Weller et al. [231] is employed to maintain the boundedness of the liquid volume fraction profile. A mathematical description of the MULES method is given in Pringuey & Cant [160] and Deshpande et al. [49]. The MULES limiter is based on the Flux Corrected Transport scheme of Zalesak [242] to guarantee boundedness in the solution of hyperbolic problems. The addition of the flux limiter, specific to VoF methods, ensures that the CLS field ψ remains strictly bounded.

3.9 Dynamic contact angle modelling at wall boundaries

Yarin [234] reformulated a statement by Edgerton & Killian (1954), "*in the land of splashes, what the scientist knows as Inertia and Surface Tension are the sculptors in liquids, and fashions from them delicate shapes none the less beautiful because they are too ephemeral for any eye but that of the high-speed camera*".

Drop impacts on solid and liquid surfaces are a key element of a wide variety of natural phenomena but the topic of wetting has also received tremendous interest from an industrial point of view. The numerical simulation of dynamic wetting processes is of critical importance for a number of industrial applications, such as: ink-jet printing, spray-painting, crop spraying, oil-recovery, rapid spray cooling of hot surfaces (e.g. semiconductor chips), surface cleaning, lubrication and liquid coating [203, 234, 241]. Other applications include ice accumulation on power lines and aircraft, which also involve drop impacts and wetting dynamics. Even more surprisingly, the collision of meteoroids with planetary surfaces can be considered as a droplet impact [234]. Finally, the subject of this work – liquid atomisation for application to internal combustion engines – is an additional industrial application involving the fascinating phenomenon of drop impact [60], and for which the wetting behaviour of the liquid film on the solid substrate is of utmost importance. Understanding the accompanying physical phenomena of drop impact is of paramount importance in formulating reliable

boundary conditions in numerical codes for spray simulation and spray/wall interaction. For instance, in some injection systems the spray impacts inner walls, leading to rebound, splashing, filming or sticking [34].

Drop impact dynamics is a very broad field of research due to the occurrence of extremely diverse and involved accompanying physical non-stationary phenomena. The process is rich in fundamental hydrodynamics and physics. The outcome of a droplet impact depends on its shape: a drop may be spherical or elliptical (due to oscillations) at the moment of impact. It may impact perpendicularly or obliquely, on the free surface of a liquid in a deep pool, on a thin liquid film or on a dry solid surface, in a coflowing air or in vacuum. The impacted target may be soft or hard, smooth or rough, which will affect the drop deformation and its spreading. It may also be porous, flat or curved, at a temperature different from that of the drop or the same. The liquid of the droplet and bottom pool/film may be miscible or immiscible, Newtonian or non-Newtonian. Attempts to understanding the above-mentioned topics are then considered and investigated in their experimental [e.g. 172, 177, 198], theoretical [e.g. 111, 207], and computational aspects [e.g. 104, 146]. This section begins with an introduction to the fundamental science behind wetting and contact angle phenomena, followed by the numerical model we have chosen to implement in our numerical capability to account for the liquid-film wetting and contact angle at the walls.

3.9.1 Wetting phenomena

Ideally, the shape of a liquid droplet is determined by the surface tension of the liquid, as was introduced in Section 3.1.1. On a flat solid surface however, the surface tension σ_{ls} between the liquid drop and the solid is a fundamental ingredient in the behaviour of that droplet. Macroscopically, surface tension can be seen as a force acting along the interface. In Yuan & Lee [241], a thorough physical description of the microscopic origin of surface tension is given. A microscopic interpretation of wetting lies in the intricate intermolecular interactions and thermal effects in the vicinity of the contact line, where the liquid-vapour interface meets the solid substrate.

When considering a liquid drop resting on a flat, horizontal solid surface, the static contact angle is defined as the angle formed by the intersection of the liquid-solid interface and the liquid-vapour interface. The interface where solid, liquid, and vapour co-exist is referred to as the “three-phase contact line”. It is a mathematical line, not a material line, that marks the separation between wetted and dry parts of the solid. Geometrically the contact angle is acquired by applying a tangent line from the contact point along the liquid-vapour interface

in the droplet profile (Fig.3.3). When a small contact angle is observed ($< 90°$), it indicates high wettability, the liquid will spread over a large area on the solid substrate. By contrast, a contact angle greater than $90°$ generally implies low wettability, i.e. poor spreading of the liquid. The fluid will minimise its contact with the surface in order to minimise its surface energy and form a compact liquid droplet. Complete wetting occurs when the contact angle is zero.

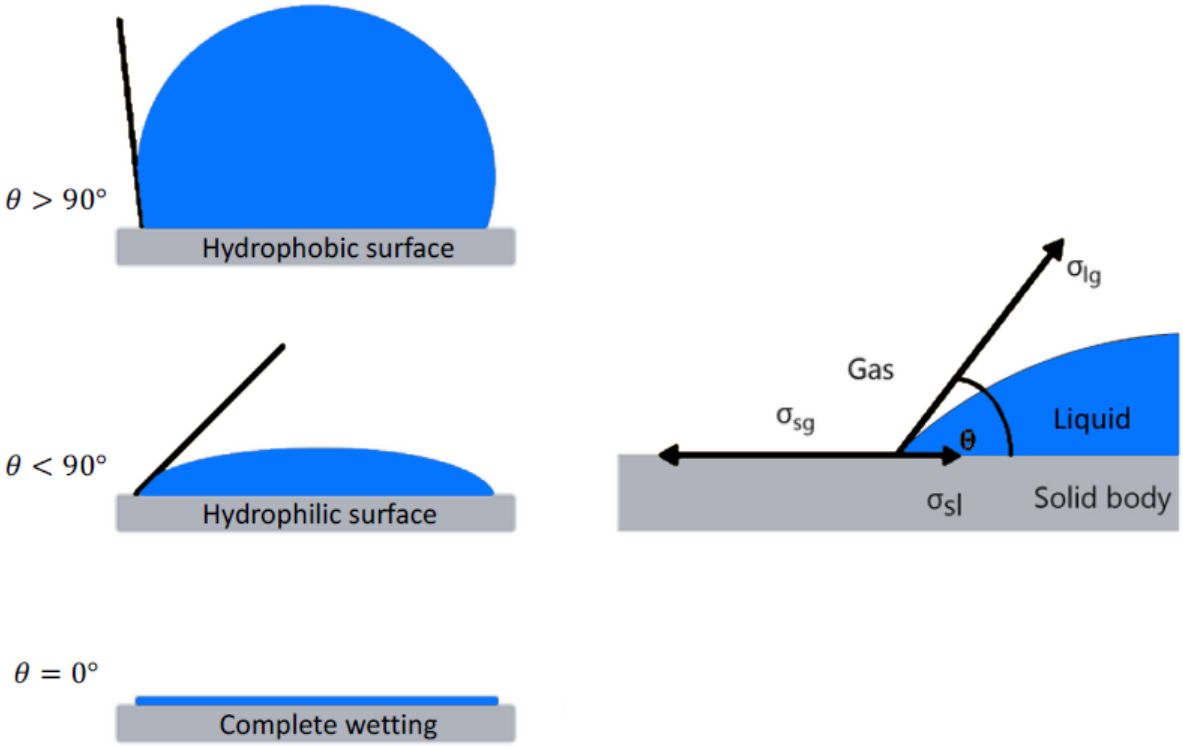

Fig. 3.3: Illustration of the definition of the static contact angle at a triple solid-liquid-gaseous contact line and how a droplet is affected by hydrophobic and hydrophilic surfaces. Adapted from Krüss GmbH [114].

3.9.2 Equilibrium contact angle and Young's law

The static – or equilibrium – contact angle θ_{eq} is a quantitative measure of wetting of a solid by a liquid. It is a characteristic for a given solid-liquid system in a specific ambient environment. As first described by Thomas Young [240] in 1805, the contact angle of a liquid drop on an ideal solid surface is governed by Young's equation (Eq. 3.14), which is satisfied in mechanical equilibrium of the drop at the three phase contact of solid-liquid and

vapour:

$$0 = \sigma_{sg} - \sigma_{sl} - \sigma_{lg}\cos\theta_{eq} \tag{3.14}$$

where σ_{lg}, σ_{sg} and σ_{sl} represent the liquid-gas, solid-gas, and solid-liquid interfacial tensions, respectively, and θ_{eq} is the static equilibrium contact angle. Applied to a specific liquid-solid system, Young's equation and the interfacial tensions determine a single and unique equilibrium contact angle of wetting. The two possibilities that exist – partial wetting or total wetting – depend on the surface energies of the three interfaces [241].

3.9.3 Contact angle hysteresis

Static contact angles are measured when the liquid droplet is standing on the surface and the three phase boundary is not moving. However, the phenomenon of wetting is more than just a static state. When the liquid moves, the measurement of a single static contact angle to characterise the wetting behaviour is no longer adequate. If the three-phase contact line is in actual motion, the contact angle produced is called a dynamic contact angle. Imagine filling a liquid drop slowly with a syringe. The drop is initially at rest in equilibrium with $\theta = \theta_{eq}$. It follows that θ will increase progressively until attaining θ_{adv}, the so-called limiting advancing contact angle. Conversely, when draining a drop, θ decreases progressively until attaining θ_{rec}, the limiting receding contact angle, at which point the contact line retreats. This is illustrated in Fig. 3.4.

In other words, when there is a relative motion of the droplet over a solid substrate, a different contact angle than the equilibrium contact angle will be measured. The former depends on the direction of the previous motion, advancing or receding, of the interface. The advancing and receding contact angles give the maximum and minimum values the static contact angle can have on that substrate. One defines the contact angle hysteresis as the difference between the advancing and receding contact angles.

The impact of contact angle hysteresis has been investigated experimentally by Rioboo et al. [172], Šikalo et al. [198], Roisman et al. [177] for example. The general conclusion seems to be leading to micro-scale surface topography (roughness and/or heterogeneity) playing a role in generating hysteresis. The actual non-homogeneity of the solid surface (either chemical or textural) and microscopic variations of the slope on the surface creates barriers to the motion of the contact line and alter the macroscopic contact angle. For surfaces that are not homogeneous, the impurities on the solid substrate present an energetic impediment to the contact line motion. This is because the increased interfacial area seen by the liquid is energetically costly. The contact line motion is thus resisted. On ideal solid surfaces, there is

no contact angle hysteresis, and the experimentally observed contact angle is Young's contact angle θ_{eq}.

In liquid atomisation, interpreting liquid filming might be misleading if the numerically-solved equations and/or boundary conditions fail to consider surface topography, as there is, as yet, no general understanding of how the contact angle may impact the atomisation process.

For drop impact especially at low impact velocities (low Weber numbers), the effects of surface tension and wettability are foreseen to be significant. The study by Šikalo et al. [198] has clearly shown the importance of the accurate estimation of the contact line speed and of the use of a reliable model for the dynamic contact angle, especially for the prediction of the receding phase of a drop impact.

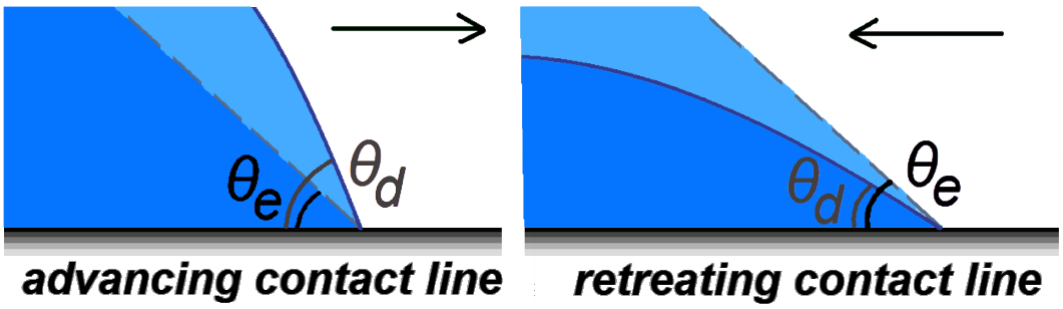

Fig. 3.4: Illustration of the definition of the advancing and receding contact angles.

3.9.4 Numerical challenges in the modelling of triple contact lines

In two-phase flows, with a further difficulty that stems from the presence of a moving contact line, the entire flow might often be driven by the latter or be so strongly coupled with the conditions at the moving contact line that changing them can result in different flow regimes. Indeed, the flow in the immediate vicinity of the contact line is intertwined with the flow on a larger scale. Well-grounded physical modelling of moving contact lines is therefore required for the numerical simulation of such flow systems. Detailed reviews of the wettability phenomena and modelling can be found in Kistler [111], Shikhmurzaev [193], Sui et al. [203]. The numerical challenge that constitutes the simulation of two-phase flows and the rich physics governing the statics and dynamics of contact lines, has resulted in few attempts in modelling the conditions in the vicinity of moving contact lines. This is due to two fundamental difficulties which constitute the so-called "moving-contact line problem".

Firstly, the classical theory of continuum fluid mechanics (i.e. the Navier–Stokes equations with no-slip boundary condition at the wall for velocity) predicts a shear stress singularity at the moving contact line. As fluid particles on the free surface reach the moving contact line, they experience an infinite acceleration in order to adjust to the velocity of the wall. Therefore, it becomes difficult to model a moving contact line with dynamic contact angle less than 180° without violating the assumption of fluid continuity [177]. The motion of the contact line across the surface implies a contradiction with the no-slip boundary condition.

The second difficulty is the modelling of the contact angle which is usually required as a boundary condition and determines the shape of the free surface at the contact line. Within our two-phase modelling capability (Section 3.3), a correct implementation of the contact angle is necessary as a boundary condition for the conservative level-set function ψ for the computation of curvature.

As discussed in Sui et al. [203] and Šikalo et al. [198], to fully capture all the physics involved would require resolving a very wide range of scales with a very high mesh resolution, much higher even than the typical mesh resolution required for a DNS calculation of turbulent flow. In order to simulate all the details of the flow near the contact line the size of the mesh in this region should be of the order of the "slip length". This length is comparable with the intermolecular distances. Any mesh of size larger than this will lead to mesh size dependent results. For practical situations this will be prohibitively expensive.

The alternative approach is to specify a macroscopic contact angle. In this approach the "apparent" contact angle observed at the scale of the mesh resolution is applied as a boundary condition. Interface tracking methods can be easily coupled with such moving contact lines macro-scale model. This approach allows the inclusion of surface properties in the calculation by making the macroscopic contact angle a function of the surface and liquid properties as well as the contact line velocity. In practice, a slip condition is normally readily implemented, with the implicit assumption that there is a slip length smaller than the near wall cell. This is the method that is adopted in the present work, whereby the macroscopic contact angle is specified as a wall boundary condition, rather than attempting to predict the contact angle as part of the simulation, which result in a new Neumann boundary condition for the liquid volume fraction.

This macroscopic contact angle approach has been applied in several previous studies to include surface contact physics into the simulations: Yokoi et al. [238] elaborated a dynamic contact angle model and presented numerical results obtained with a CLSVOF method – compared against his own experiments – and more recently Dianat et al. [52] and Renardy et al. [170] with the VoF method, as well as Michael & Margrit [146] using a level-set

method with high-order numerical schemes. These works show that with the correct contact angle specified, very good agreement with experiments can be obtained; the correct droplet dynamics can be reproduced using this macroscopic approach. However, the contact angle model by Yokoi et al. [238], used in the numerical studies of Dianat et al. [52] and Michael & Margrit [146] lacks a thorough underlying mathematical theory [146]. It was developed for and based on a single droplet impact experiment, as a prescription of contact angle values which fit well with a specific practical experiment. A straightforward application of this model to any wetting calculation is difficult as there are no experimental data available.

3.9.5 The Kistler dynamic contact angle model

An approach to the problem of the modelling of contact-lines and dynamic contact angles has been based on experimental observations [40, 91, 207]. An empirical correlation for θ_{dyn} in such cases was obtained by Hoffman [91], Voinov [226], Tanner [207] known as the Hoffman–Voinov–Tanner relationship [111], in which θ_{dyn} depends primarily on the capillary number Ca. A later formula was proposed by Cox [40], the Cox-Voinov model.

One of the most recent and accurate contact angle models is the Kistler model [111], derived following the experimental measurements by Hoffman [91]. This dynamic contact angle model applies a varying contact angle, which depends on instantaneous flow parameters. The Kistler model has been observed to yield good overall agreement in comparison with experimental data [12, 81, 177, 198] The dynamic contact angle θ_{dyn} is evaluated at each time step as follows

$$\theta_{\text{dyn}} = f_{\text{Hoff}}\Big[\text{Ca} + f_{\text{Hoff}}^{-1}(\theta_{\text{adv,rec}})\Big] \tag{3.15}$$

where $\theta_{\text{adv,rec}}$ is the advancing or receding contact angle based on the local contact line motion; and where the Hoffman function f_{Hoff} is defined as:

$$f_{\text{Hoff}} = \cos^{-1}\left[1 - 2\tanh\left[5.16\left[\frac{\text{Ca}}{1+1.31\text{Ca}^{0.99}}\right]^{0.706}\right]\right]. \tag{3.16}$$

The inverse Hoffman function appearing in Eq. 3.15 is determined from the following expression:

$$(f_{\text{Hoff}}^{-1})^{0.706} - \left[1 + 1.31(f_{\text{Hoff}}^{-1})^{0.99}\right]^{0.706} \frac{1}{5.16}\tanh^{-1}\frac{1-\cos\theta_{\text{adv,rec}}}{2} = 0 \tag{3.17}$$

where $\theta_{\text{adv,rec}}$ is again chosen by the algorithm based on the local contact line motion; and is calculated iteratively using a Regula-Falsi root-finding algorithm. The local capillary number,

Ca, is built according to

$$\mathrm{Ca} = \frac{\mu |u_{\mathrm{CL}}|}{\sigma} \tag{3.18}$$

where $|u_{\mathrm{CL}}|$, μ and σ are the velocity of the contact line, the dynamic viscosity of the liquid and the surface tension of liquid and gas phase, respectively. The local capillary number at the wall boundary is estimated based on the contact-line velocity:

$$u_{\mathrm{CL}} = \left[\frac{\mathbf{n}_{\mathrm{wall}} - (\hat{\mathbf{n}}_\Gamma \cdot \mathbf{n}_{\mathrm{wall}})\hat{\mathbf{n}}_\Gamma}{|\mathbf{n}_{\mathrm{wall}} - (\hat{\mathbf{n}}_\Gamma \cdot \mathbf{n}_{\mathrm{wall}})\hat{\mathbf{n}}_\Gamma|} \right] \cdot \left[\mathbf{U}_{\mathrm{P}} - (\mathbf{n}_{\mathbf{wall}} \cdot \mathbf{U}_{\mathrm{P}})\mathbf{n}_{\mathrm{wall}} \right] \tag{3.19}$$

where $\hat{\mathbf{n}}_\Gamma$ is the unit normal interface vector and $\mathbf{n}_{\mathrm{wall}}$ is the face normal at the wall. The velocity of the contact line is calculated based on the interfacial velocity in the first computational point above the wall ($\mathbf{U}_{\mathrm{P}}$), i.e. the velocity component normal to the contact line and tangential to the wall. It is defined so that it points towards the liquid. Thus, u_{CL} is negative for an advancing motion and positive for a receding motion.

The contact angle $\theta_{\mathrm{adv,rec}}$ in Eq. 3.15 and Eq. 3.17 is replaced by either the advancing contact angle θ_{adv} or the receding contact angle θ_{rec} depending on the sign of the velocity vector at the contact line u_{CL} from Eq. 3.19. The system properties are summarised in Table 3.1. They depend on the solid substrate chemical and physical nature as well as on the liquid properties, interfacial properties and atmospheric conditions.

Table 3.1: Angles

Equilibrium contact angle	θ_{eq}
Dynamic contact angle velocity scale	u_{CL}
Limiting advancing contact angle	θ_{adv}
Limiting receding contact angle	θ_{rec}

3.9.6 Implementation in OpenFoam

The implementation of the Kistler dynamic contact angle boundary condition into the RCLS formulation is here discussed. This is done by following the method already available for a generic contact angle model in OpenFoam. The unit interface normal vector field $\hat{\mathbf{n}}_\Gamma$ obtained via Eq. 3.5, and herewith the local orientation of the liquid-vapour interface does not necessarily fulfill the local wall contact angle condition, as discussed in Section 3.9.1–3.9.4. In Section 3.9.5, we introduced the dynamic contact angle model that was implemented within our numerical capability. In the following, we outline the procedure by which the

Kistler dynamic contact angle model is used within the OpenFoam framework to correct locally the interface normal vector in a face f at a wall boundary. The current contact angle between the unit interface normal vector and the normal vector to the wall can be calculated from the inner product of these vectors (Fig. 3.4)

$$\cos(\theta_0) = \hat{\mathbf{n}}_{\Gamma,0} \cdot \hat{\mathbf{n}}_{\text{wall}} \tag{3.20}$$

where θ_0 is the current contact angle at the wall and $\hat{\mathbf{n}}_{\text{wall}}$ is the normal vector to the wall. The target interface normal vector $\hat{\mathbf{n}}_{\Gamma,0}$ will be corrected to $\hat{\mathbf{n}}_{\Gamma,\text{corrected}}$ which will satisfy:

$$\cos(\theta_{\text{dyn}}) = \hat{\mathbf{n}}_{\Gamma,\text{corrected}} \cdot \hat{\mathbf{n}}_{\text{wall}} \tag{3.21}$$

The following describes how $\hat{\mathbf{n}}_{\Gamma,\text{corrected}}$ is obtained. It must lie in the plane that is spanned by the current normal vector $\hat{\mathbf{n}}_{\Gamma,0}$ and the normal vector of the wall $\hat{\mathbf{n}}_{\text{wall}}$:

$$\hat{\mathbf{n}}_{\Gamma,\text{corrected}} = a\hat{\mathbf{n}}_{\text{wall}} + b\hat{\mathbf{n}}_{\Gamma,0} \tag{3.22}$$

where

$$\left.\begin{aligned} a &= \frac{\cos\theta_{\text{dyn}} - \cos\theta_0 \cos(\theta_0 - \theta_{\text{dyn}})}{1 - \cos^2\theta_0} \\ b &= \frac{\cos(\theta_0 - \theta_{\text{dyn}}) - \cos\theta_0 \cos\theta_{\text{dyn}}}{1 - \cos^2\theta_0} \end{aligned}\right\} \tag{3.23}$$

In Eq. 3.23, θ_0 is the un-corrected wall boundary contact angle, while θ_{dyn} is the (corrected) dynamic contact angle calculated via the Kistler model, as indicated in Section 1.10.6 through Eq. 3.15.

This new contact angle is then used to reset the interface unit normal $\hat{\mathbf{n}}_\Gamma$ using Eq. 3.22. This means that any difference between the un-corrected interface normal and the corrected interface normal vectors leads to a local surface tension force $\mathbf{f_c}$ (Eq. 3.6). This local surface tension force adjusts the local interface curvature (Eq. 3.4) to match the target contact angle θ_{dyn}.

3.9.7 Two-dimensional investigation of drop impact on a dry hydrophobic surface

In order to validate the full implementation of the RCLS method with the momentum solver and Kistler contact angle model, the experimental data set of Šikalo et al. [198, Table 2, Expt. 7] for the behaviour of a droplet impacting on a dry surface was used. In addition,

Šikalo et al. [198] validated their experimental data against a set of numerical simulations using the Kistler dynamic contact angle model [198, Fig. 10, Fig. 11]. In this experiment a spherical water drop of 2.45mm diameter impacts a solid surface with an impact speed U_0 of 1.64m/s and spreads onto it, as described in Fig. 3.6. The substrate is made of wax with a surface roughness height of 16.3μm. The surface tension is 0.073 N/m, the air and liquid densities are 996 kg/m^3 and 1.25 kg/m^3 respectively and the dynamic viscosities of air and liquid are 1.18×10^{-5} kg/m.s and 1×10^{-3} kg/m.s. The impact Weber and Reynolds numbers based on the initial drop diameter D_0 and impact speed U_0 are defined as:

$$\mathrm{We} = \frac{\rho_{\mathrm{liq}} U_0^2 D_0}{\sigma}; \quad \mathrm{Re} = \frac{\rho_{\mathrm{liq}} U_0 D_0}{\mu_{\mathrm{liq}}}. \tag{3.24}$$

The Weber number of the impact is thus 90 and the Reynolds number is 4010. The flow in both phases is assumed to be laminar. Detailed measurements are available for the dynamic advancing (105°) and receding (95°) contact angles. Both fluids are assumed to be incompressible and Newtonian with constant properties (density, viscosity and surface tension). The impact parameters are summarised in Table. 3.2. The reason for choosing this specific set of experimental conditions is because it lies in the complete rebound regime, as classified by Rioboo et al. [172] (Fig. 3.5) for a similar set of experimental conditions: water on wax, $U_0 = 1.18$m/s [172, Table 1, Column 1].

Solutions were first obtained using a two-dimensional Cartesian orthogonal mesh. The solution domain is 10mm$\times$4mm in the x and y directions respectively. The mesh used is a hexahedral mesh of 400×400 cells in the corresponding directions being uniform but refined near the bottom wall in the vertical direction with an expansion ratio of 1.02. The numerical calculation has been performed using a mesh size of 100 cells/drop diameter. This optimal mesh size has been chosen based on the discussion on mesh sensitivity analysis in Roisman et al. [177] and Guo et al. [81] for who the wetted surface diameter converged when a minimum of 60 computational cells per the initial drop diameter was used. A constant pressure is imposed on the top plane which allows inflow and outflow. At this boundary a zero gradient is assumed for the conservative level-set field. Elsewhere wall boundary conditions are applied with no-slip boundary condition for velocity and zero gradient for pressure.

The computational results for the simulation of a two-dimensional water droplet impacting a wax substrate is shown in Fig. 3.7.

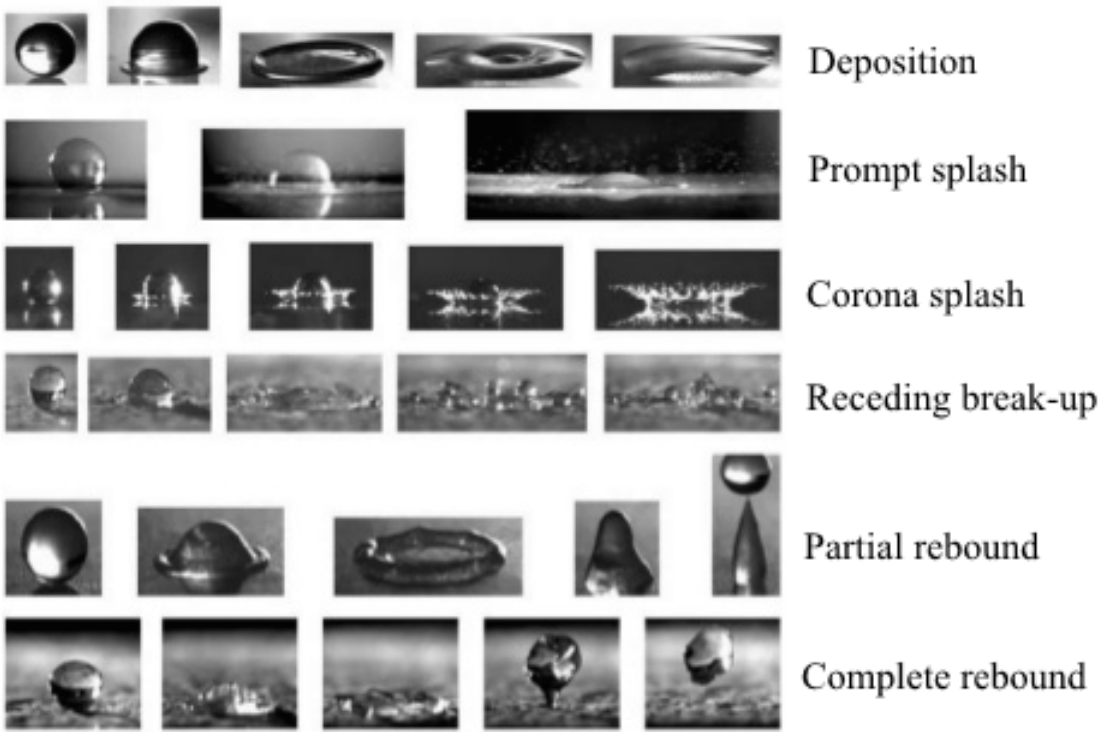

Fig. 3.5: The modes from drop impact on a dry solid surface: spreading, splashing and bouncing, as observed and classified by Rioboo et al. [172].

The numerical algorithm predicts well the shape of the spreading drop during the time instants when the drop deformation and its spreading on the solid wall are governed by inertial forces (Fig. 3.7a–c). The prediction of the receding phase however, which is governed mainly by the capillarity and contact-line forces has not been as successful. The water drop does not recoil fully, even beyond a computational time of $t = 50$ms. The flow in the liquid corner and the corresponding stresses determine the value of the dynamic contact angle. We postulate that due to the choice of a 2-D non-axisymmetric computational domain and boundary conditions, the curvature calculation and subsequent surface tension force calculation do not allow for the correct computation of the receding dynamic contact angle acting to recoil the droplet.

3.9.8 Three-dimensional drop dynamics after impact on a solid wall

The advantage of the present contact angle algorithm lies in the possibility to generalise it to the more general 3-D non-axisymmetric droplet impact case. In Fig. 3.8 we present the spreading phase results of the three-dimensional simulation of a water droplet impacting a

wax substrate for the same simulation parameters as the ones used in Section 3.9.7 (Table 3.2) for the 2-D case. The phase interface is coloured by impact velocity.

Table 3.2: List of impact parameters, properties of the liquids and wettability of the surface corresponding to the experiments of Šikalo et al. [198, Table 2, Expt. 7].

Liquid	Water
Substrate	Wax
Impact velocity [m/s]	1.64
Initial diameter [mm]	2.45
Advancing angle (θ_{adv})	105°
Receding angle (θ_{rec})	95°
Weber number	90
Reynolds number	4010

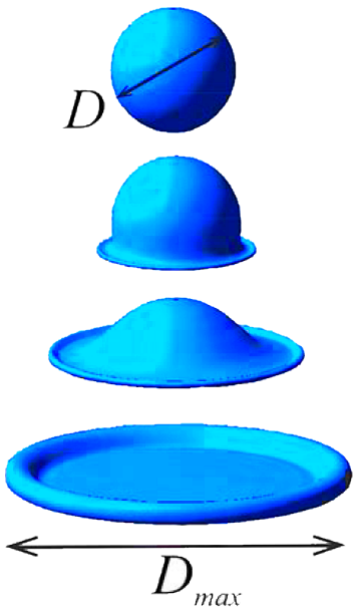

Fig. 3.6: Sketch of the numerical simulation set up for the impact of a spherical droplet of diameter D and velocity U_0 onto a dry solid substrate. The droplet reaches a maximum spreading diameter D_{max}. Adapted from Visser et al. [225].

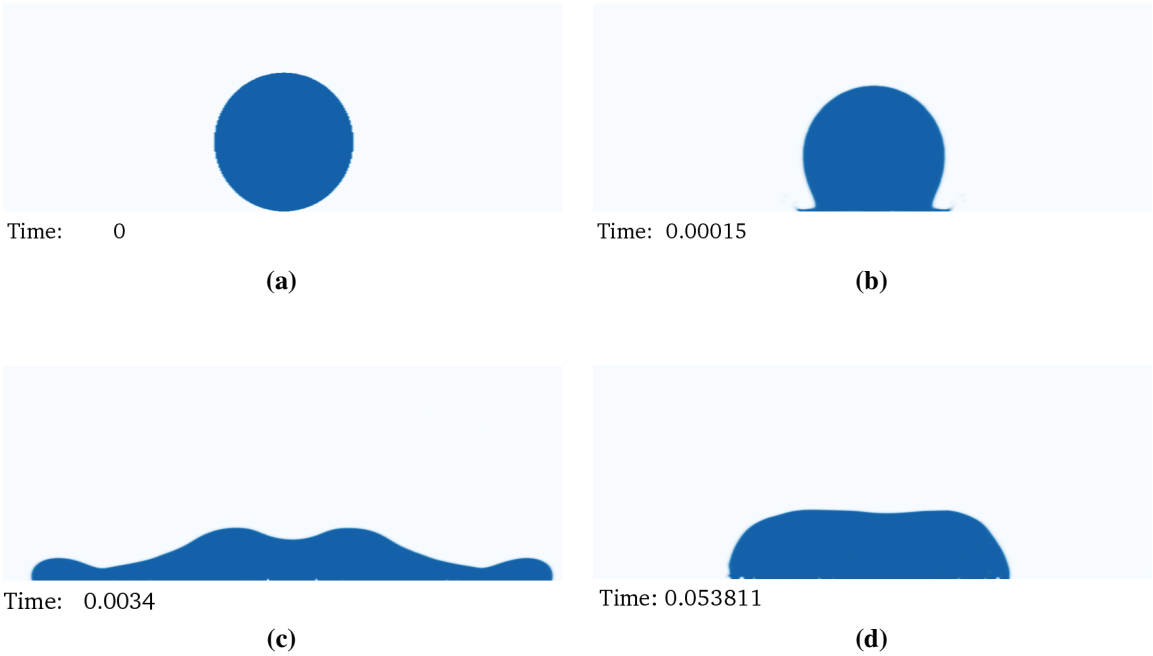

Fig. 3.7: Overview of the different stages of two-dimensional droplet impact. A droplet with initial diameter D and impact velocity U_0 is impacting onto a flat dry solid surface. During its spreading a lamella and rim form (spreading phase), before the drop rebounds on the surface under the effect of surface tension (receding phase). All times are in seconds.

In addition, we conducted an alternative water droplet impact calculation on a dry wax substrate in the partial rebound regime. This time a spherical water drop of 0.2mm diameter impacts the solid surface with an impact speed of 5m/s from a height h_0 of 0.8mm above the solid substrate. We expect the initial gas layer aspect ratio h_0/D_0 to be irrelevant if: (i) the air flow has as little effect on the droplet as possible during its fall, which should be verified if the gas Weber number, $\mathrm{We}_{\mathrm{gas}} = \rho_{\mathrm{gas}} U_0^2 D_0/\sigma$, and the Froude number quantifying gravity, $\mathrm{Fr} = U_0^2/gD_0$, are small; and (ii) if we assume that the oscillations of the droplet shape caused by the droplet release mechanism are as small as possible. Here $\mathrm{We}_{\mathrm{gas}} < 1$ and $\mathrm{Fr} < 1$. In addition, we did not observe any oscillations in the droplet shape during the free-falling phase. The impact parameters are summarised in Table. 3.3.

The solution domain is $1 \times 1 \times 1$mm in the x, y and z directions respectively. The mesh used is a hexahedral mesh of $100 \times 100 \times 100$ cells in the corresponding directions. The numerical simulation shown in Fig. 3.9 has been performed using a mesh size of 20 cells/drop diameter. The mesh resolution near the wall is such that there are respectively 1 and 3 cells across

the thinnest and the thickest part of the film when the drop attains its maximum spreading diameter at $t = 0.237$ms.

Table 3.3: List of impact parameters, properties of the liquids and wettability of the surface corresponding to the experiments of of Šikalo et al. [198, Table 2, Expt. 7].

Liquid	Water
Substrate	Wax
Impact velocity [m/s]	5.0
Initial diameter [mm]	0.2
Initial height above substrate [mm]	0.8
Advancing angle (θ_{adv})	105°
Receding angle (θ_{rec})	95°
Impact Weber number	70
Reynolds number	990

This does not fully correspond to the resolution criterion that is needed with the RCLS method, for which typically 3–5 control volumes must be contained in the region between two free surfaces, such as in the case of the spreading lamella. However, despite a rather coarse mesh resolution the predicted droplet motion agrees well with qualitative experimental observations of droplet behaviour of Rioboo et al. [172] in the compelte rebound regime, for both the advancing and receding phases of the impact process. The time sequence of the spreading phase and receding phase is shown in Fig. 3.9a. The time sequence of the recoiling lamella and rim are highlighted in Fig. 3.9b. After contact is made with the solid substrate, the lower part of the droplet compresses and deforms. A liquid sheet lamella spreads over the solid surface ($t = 0.237$ms). In parallel, liquid accumulates at the edge, or rim, of the lamella due to surface tension effects, and its thickness increases with time. Finally, when the maximum spreading diameter is reached ($D_{\text{max}} = 0.6$mm at $t = 0.237$ms) the major driving forces become capillary forces and the droplet begins to retract under the action of the receding contact angle as the surface is hydrophobic. The liquid from the lamella pulls into the outer rim under the action of surface tension forces ($t = 0.407$ms). The liquid is now concentrated along the thick rim, which grows in thickness and recoils ($t = 0.497$ms). The evolution of such a doughnut-like drop [177] with a thickening and retracting rim is determined by the rim motion, a scenario that resembles the Taylor–Culick instability outlined in Chapter 2, Section 2.1.1.2. At $t = 0.667$ms and subsequent times, at the end of the receding phase, the liquid drop detaches from the surface, and complete rebound is attained ($t = 0.867$ms).

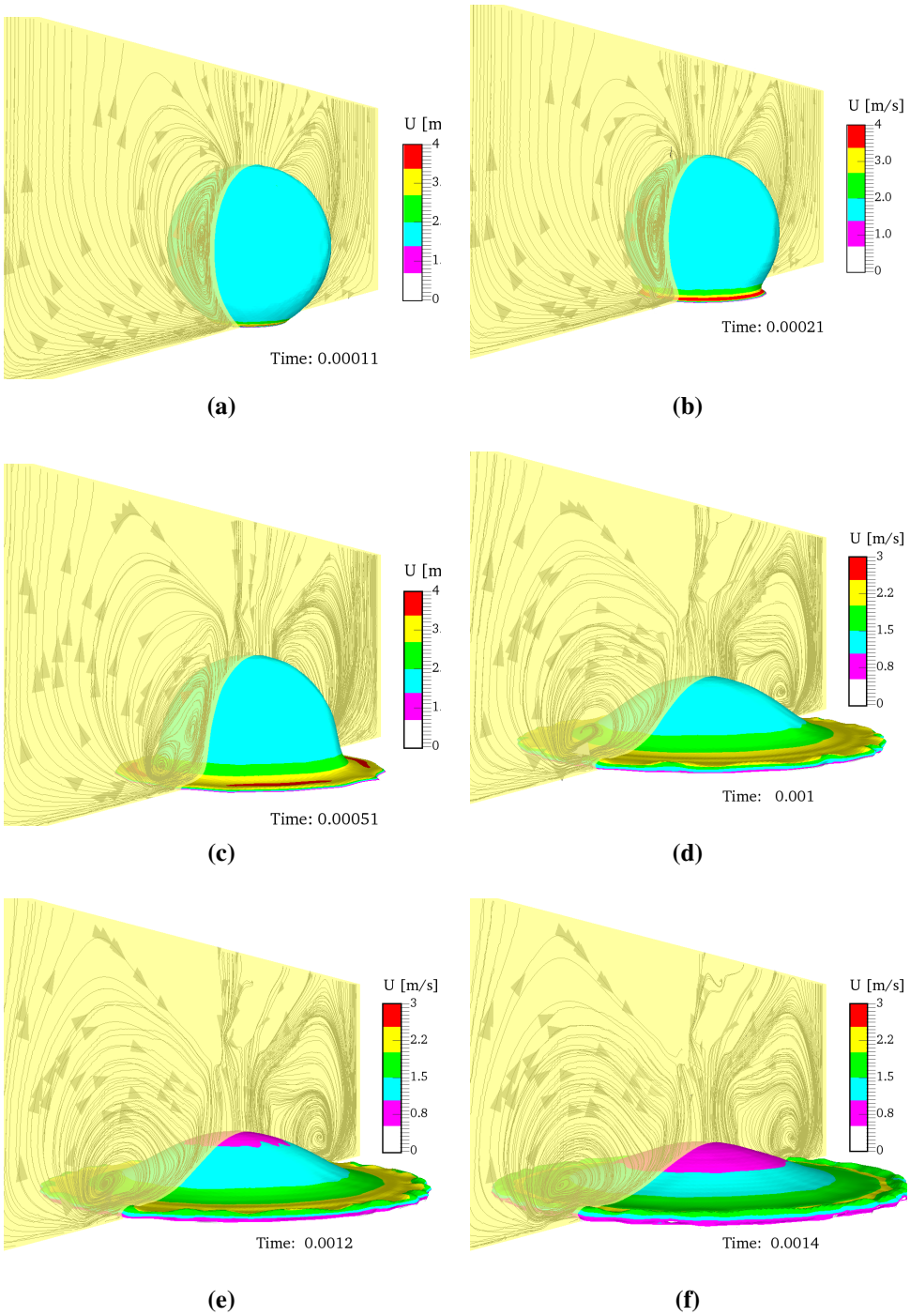

Fig. 3.8: Velocity field for the three-dimensional simulation of a water droplet impacting a wax substrate for the simulation parameters given in Table 3.2.

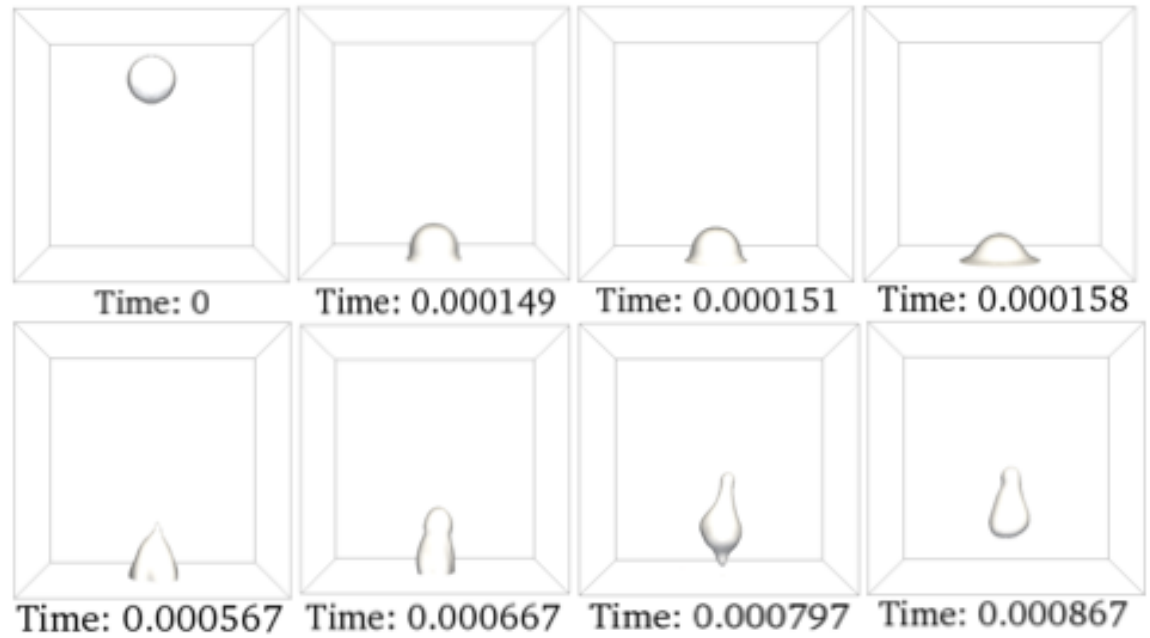

(a)

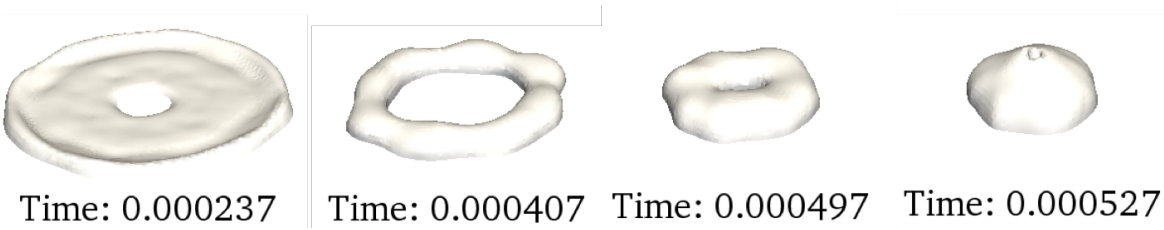

(b)

Fig. 3.9: (a) Three-dimensional simulation of a water droplet impacting a wax substrate with spreading and receding phase. The recoiling lamella and rim are highlighted in **(b)**. The impact parameters are summarised in Table. 3.3.

3.10 Final comments

The interface description technique, the robust conservative level-set method, as implemented in the multiphase flow solver *RCLSFoam* of Pringuey [158] was presented. In the further development of the numerical tool, the main focus has been placed on the inclusion of a dynamic contact angle model. Realistic liquid/wall and spray/wall interactions are a combination of liquid wetting behaviours and energetic impact dynamics. Influential parameters are (i) the presence or not of a liquid film on the surface (see Chapter 4 for impacts on wetted walls), (ii) the surface roughness and (iii) the wettability of the liquid/solid/gas system. The

later types allow insights into the basic mechanisms of wetting and dewetting and constitutes a first step towards gaining knowledge on liquid film wetting behaviours on solid substrates for the application to prefilming airblast atomisers. A parameter not taken into account in the present study but of interest in the context of combustion chamber studies is the wall surface temperature, which influences the impact through liquid vaporisation and film boiling effects [31]. This study has clearly shown the importance of the addition of a reliable model for the accurate estimation of the contact-line forces, especially for the prediction of droplet splashing on dry rough surfaces and the receding phase of the drop splash dynamics.

Chapter 4

Droplet Formation and Recognition: A Droplet Tracking Algorithm for Primary Breakup Modelling

The need for droplet detection and transfer arises from the computational modelling of atomisation, which generally involves two stages: primary breakup where drops are detaching from the liquid core and secondary breakup where the droplets produced at the previous stage further disintegrate into smaller droplets, that will later evaporate inside the combustion chamber. The faithful prediction of the spray requires the simulation of both primary and secondary breakup droplets. Under aero-engine conditions, the atomisation process produces a large amount of droplets, whose size can reduce to very small values, and even smaller values after secondary breakup. Within the context of DNS of atomisation, as the detailed simulation of all the spatial and temporal scales remains very expensive, the mesh refinement required to resolve the very small liquid structures following secondary atomisation becomes impossible with a level-set formulation. A droplet tracking method thus appears interesting for the smallest particles generated following primary breakup, albeit the body of work on cost-effective numerical techniques for droplet tracking during primary breakup is rather scarce. The present chapter details the dispersed phase formulation implemented by Pringuey [158] to describe the evolution of the spray following the intrinsic modelling of primary breakup using the RCLS interface-capturing method (Chapter 3, Section 3.3). The overall procedure is tested on two-phase numerical benchmark problems.

4.1 Outline of the numerical method

Kim et al. [110] introduced a novel procedure to take small spherical liquid structures out of the level-set formulation in order to transfer them into a Lagrangian stochastic spray model for the subsequent simulation of secondary breakup. The transfer of droplets into a Lagrangian spray model saves computational time while retaining an accurate description of the liquid phase during primary breakup.

Pringuey [158] built upon this formulation and implemented a droplet tracking algorithm into the RCLS method in which the droplets generated are then identified, removed from the level-set formulation, and stored for further analysis including the calculation of geometrical and physical parameters. The level-set field associated with the removed droplets is stored into a *Drops* field. This is the level-set field gathering all the drops produced between t^{n-1} and t^n in the state in which they were at t^n.

First, the algorithm detects liquid blobs. Blobs are considered as liquid structures of arbitrary shapes, sizes, positions and velocities. For a liquid blob to be detected, the surrounding cells need to have a CLS liquid volume fraction ψ less than a chosen threshold value to be considered as "gas". Then, suitable droplets are identified for transfer based on a few numerical criteria, of which their size and shape. For a liquid blob to be considered as a droplet, it needs to contain at least one cell with $\psi_i \geq \psi_{\text{threshold}}$, where $\psi_{\text{threshold}}$ is the liquid volume fraction threshold defined by the user as representative of liquid. Based on the definition of the conservative level-set ψ (Section 3.3), the value of 0.5 is a good choice.

In addition, the droplets selected and transferred are chosen to be assumed to be spherical and isolated. This is particularly important since during primary breakup various irregularly-shaped liquid structures can separate from the main liquid bulk – i.e. the maximum radius of the drop must follow:

$$r_{\max} = \max_{E_i \in \mathscr{D}} (|\overrightarrow{C_i C_{\mathscr{D}}}|) \leq D_{\text{eq},\mathscr{D}} \tag{4.1}$$

and

$$D_{\text{eq},\mathscr{D}} \leq D_{\max} \tag{4.2}$$

where $C_{\mathscr{D}}$ is the centre of mass of the drop, C_i is the cell centre of a cell belonging to that drop, $D_{\max}$ is a maximum diameter chosen by the user, and introducing $D_{\text{eq},\mathscr{D}}$, the equivalent diameter defined as

$$D_{\text{eq},\mathscr{D}} = \sqrt[3]{\frac{6V_{\mathscr{D}}}{\pi}} \tag{4.3}$$

where $V_{\mathscr{D}}$ is the volume of the droplet. From a purely representational standpoint this does not pose difficulties even for regions of the spray where the liquid phase is present as non-spherical elements, rather than as fully dispersed droplets, as sphericity is an optional criterion set by the user in the numerical method. When this criteria is de-activated, the information concerning the shape of the non-spherical liquid element is lost in the process. As long as the volume of such liquid elements can be defined, one can always associate with each liquid element a characteristic length scale which is the radius of a spherical droplet of the same volume. Indeed, injected droplets accounted for in most Lagrangian stochastic spray model have to be spheres for secondary breakup modelling [80]. The model assumption to regard droplets as spherical is questionable, in particular near the nozzle in the dense spray region. Past a certain downstream location, all droplets should have become nearly spherical under the action of surface tension. Therefore, the assumption of fully dispersed spherical droplets can be justified, and a consistent solution obtained.

Table 4.1: Stored characteristics of the droplets extracted by the drop tracking algorithm. A cell E_i contains a liquid fraction of ψ_i.

Volume	$V_{\mathscr{D}} = \sum_{i=1}^{N_{\mathscr{D}}} \lvert E_i \rvert \psi_i$
Mass	$m_{\mathscr{D}} = \rho_{\mathrm{liq}} V_{\mathscr{D}}$
Centre of mass	$\overrightarrow{OC_{\mathscr{D}}} = \frac{1}{V_{\mathscr{D}}} \sum_{i=1}^{N_{\mathscr{D}}} \lvert E_i \rvert \psi_i \overrightarrow{OC_i}$
Equivalent diameter	$D_{\mathrm{eq},\mathscr{D}} = \sqrt[3]{\frac{6V_{\mathscr{D}}}{\pi}}$
Mass-averaged velocity vector	$\mathbf{u}_{\mathscr{D}} = \frac{1}{V_{\mathscr{D}}} \sum_{i=1}^{N_{\mathscr{D}}} \lvert E_i \rvert \psi_i \mathbf{u}_i$
Mass-averaged momentum vector	$\mathbf{p}_{\mathscr{D}} = m_{\mathscr{D}} \mathbf{u}_D$

A further direction criterion test is performed, where we account for droplets re-entering the bulk of the liquid. The droplet characteristics calculated and stored by the algorithm are given in Table 4.1. Droplet characteristics are calculated from the amount of liquid in each cell of the droplet. This drop removal technique further allows the modelling capability to export these droplets as boundary conditions into a Lagrangian tracking framework, equipped with an appropriate secondary breakup model, to simulate the final fine spray formation, prior to spray combustion modelling. After the droplet removal the conservative level-set field ψ is re-initialised (in a conservative manner via Eq. 3.11), such that the hyperbolic tangent profile

is recovered. It is crucial to account for liquid volume fraction actually removed in order to maintain mass conservation all the way through the calculation.

We note that droplet transfer conserves the momentum of the pinched-off liquid droplets. Once the droplets are extracted and transferred as Lagrangian drops they do not return to the level-set representation. This type of framework is a one-way coupling between the level-set representation and the Lagrangian particles [110]. In the future, this Lagrangian particle tracking algorithm will require a two-way coupling between the Lagrangian particles and the fluid to incorporate the loss or gain of momentum in the fluid because of the presence of particles, as done by Tomar et al. [216] and Ireland & Desjardins [97] for example. This requirement is due to the significant amount of mass loss that atomisation simulations with many topology changes can incur. This translates to a momentum source term in the Navier–Stokes equation, a two-way inter-phase coupling force.

4.2 Modification to the droplet transfer algorithm

As discussed previously, because the droplets and the fluid are two-way coupled, not only does the fluid exert a fluid-dynamic force on the droplets, but this force is also exerted back to the fluid with an opposite sign. Typically, the calculation of this coupling force requires the knowledge of the undisturbed fluid velocity at the droplet location. In the present numerical configuration, the particle tracking algorithm does not incorporate such a two-way coupling. Therefore, upon droplet removal from the level-set field, the undisturbed flow field is not reconstructed (i.e. the fluid velocity without the local perturbation induced by the droplet), as described in Ling et al. [132]. To anticipate potential numerical errors, the droplet tracking algorithm of Pringuey [158] is modified to account for droplet detection but without removing them from the level-set field. The identified liquid drops are gathered in the *Drops* field and are kept in the *CLS* field. The *Drops* field is now the level-set field gathering all the drops produced between the start of the simulation and t^n in the state in which they are at t^n. Fig. 4.1 gives a schematic description of the differences in the *CLS* and *Drops* fields at times t^n, t^{n+1}, t^{n+2} and t^{n+3} between the original algorithm of Pringuey [158] and our modified version. Broken-off drops in the level-set representation are identified and replaced with Lagrangian drops having the same mass and momentum.

In addition, we have implemented a selection criterion for the droplets to be finally extracted from the *CLS* field and the *Drops* field once their centre of mass has passed a user-defined outlet plane at a given downstream location. The sampling plane should be placed sufficiently

downstream to avoid significant mass or momentum loss in the system. The droplets physical properties are then stored for subsequent quantitative analysis. In the case of the two-dimensional Rayleigh–Taylor instability, as described in detail in Section 3.3.1, the outlet sampling plane is placed at a given y-location as the droplets are advected upwards (Fig. 4.2). At $t = 1.35$s, drops are identified, then, at $t = 1.40$s, the droplets whose centre of mass was beyond the sampling plane location at $t = 1.35$s have been removed from the level-set field and from the Lagrangian drop field. Finally, liquid structures that were identified as droplets at $t = 1.35$s and added to the *Drops* field have been advected upwards, until they themselves cross the sampling plane (not shown in Fig. 4.2). For an atomisation simulation, the outlet sampling plane would be placed at a chosen x-location downstream of the injector nozzle.

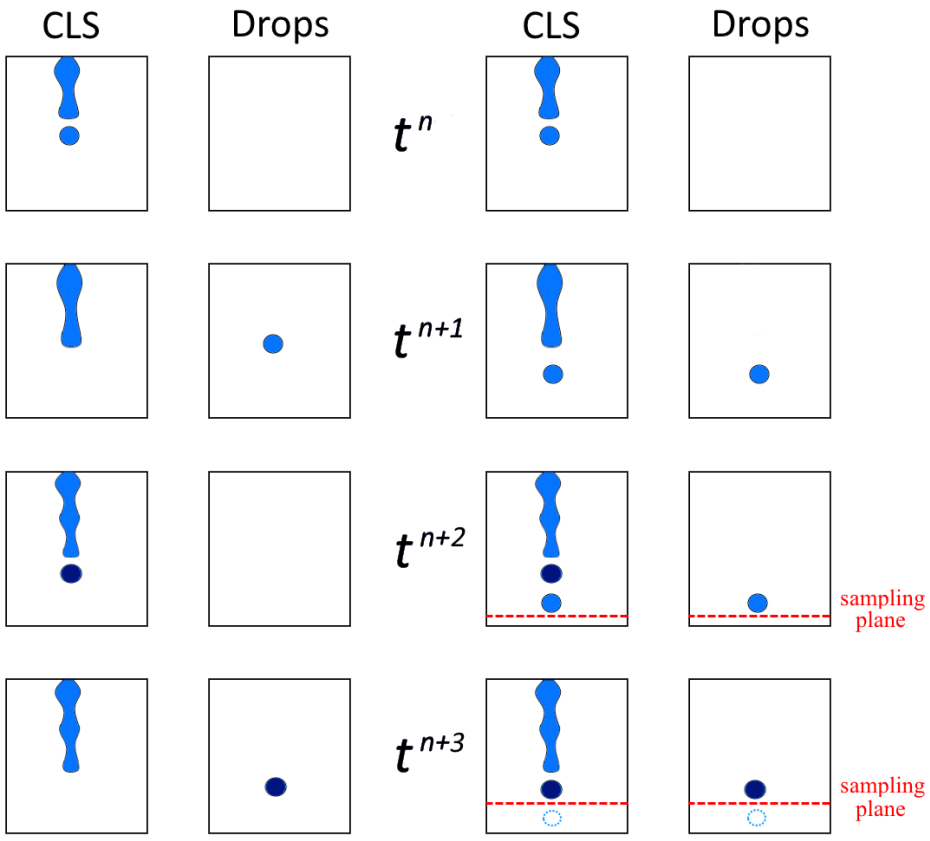

Fig. 4.1: *CLS* and *Drops* fields at times t^n, t^{n+1}, t^{n+2} and t^{n+3} between the original algorithm of Pringuey [158] (*left panels*) and our modified version (*right panels*). Droplets past the outlet sampling plane location (*red*) are extracted from the *CLS* and *Drops* fields.

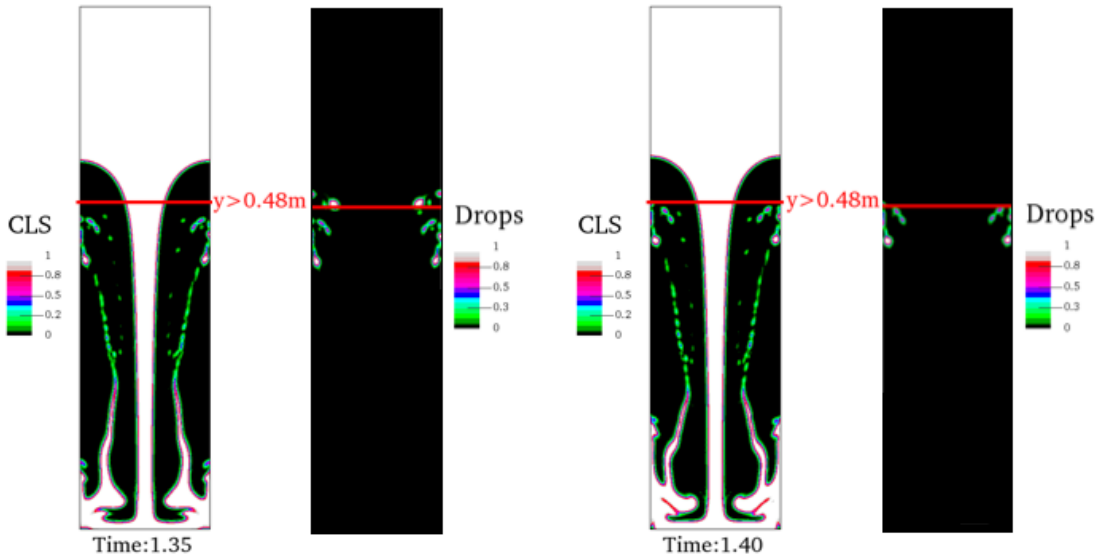

Fig. 4.2: *CLS* and *Drops* fields for the 2-D Rayleigh–Taylor instability after modification of the droplet transfer algorithm. The red line indicates the location of the outlet sampling plane at $y = 0.48$ metres.

4.3 Validation of the droplet transfer algorithm

The validation exercises presented in the following sections are based on the droplet tracking algorithm as implemented by Pringuey [158] and described in Section 4.1.

4.3.1 Rayleigh–Taylor instability

The Rayleigh–Taylor instability (RTI) is an instability of an interface between two stratified fluid layers of different densities which occurs when the lighter fluid is pushing the heavier fluid. The numerical demonstration of the RTI is a common test case when examining the numerical convergence and the capability of a solver to capture the interface physics in the presence of high density ratio and surface tension. It will be the subject of a thorough investigation as part of Chapter 5. In this section, we only highlight the functioning of the droplet tracking algorithm.

In Fig. 4.3 and Fig. 4.4, we present the results obtained for times $t = 1.45$s through $t = 1.60$s, during which generated liquid droplets are identified and extracted from the computational domain. It becomes apparent that following the extraction of liquid droplets at $t = 1.45$s, they are no longer present as part of the *CLS* field at $t = 1.5$s. For a liquid blob to be considered as a spherical droplet it needs to satisfy a few criteria (see Section 4.1). It needs to contain at least one computational cell with $\psi_{\text{threshold}} = 0.5$ (pink in Fig. 4.4) to be identified as enclosing liquid. In addition, its surroundings need to have a liquid volume fraction $\psi_{\text{threshold}}$ less than a chosen threshold value (in this case 0.01, black in Fig. 4.4) to be considered as "gas". The droplet characteristics stored by the algorithm (Table 4.1) were further analysed using a MATLAB® post-processing method developed during the course of this work. An example of such a quantitative analysis is given in Fig. 4.5. This graph shows the droplet data obtained with 1.5 seconds of simulated time of a 2-D simulation of the RTI. Droplet locations are plotted against their velocity (third axis).

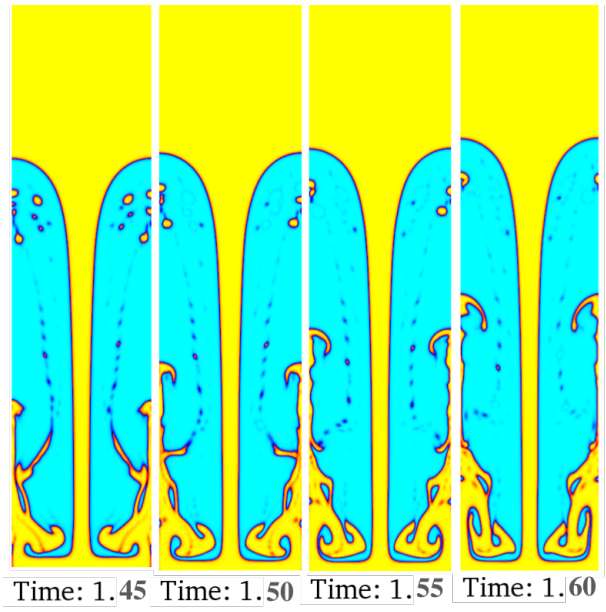

Fig. 4.3: Droplet tracking algorithm applied to the Rayleigh–Taylor instability. At $t = 1.45$s, the generated liquid droplets are all present in the *CLS* field. At $t = 1.5$s and subsequent times, individual liquid drops satisfying the algorithm criteria have been removed from the *CLS* field.

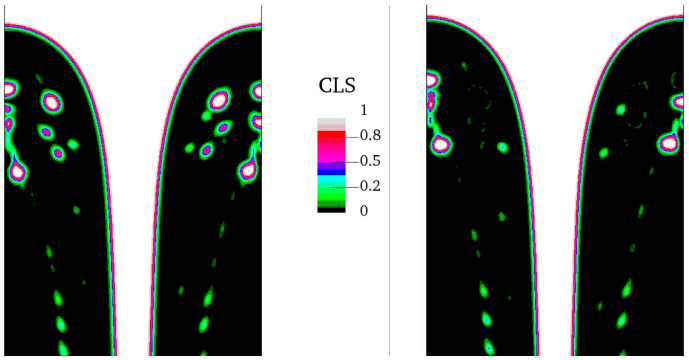

Fig. 4.4: A close-up view of the droplet tracking algorithm applied to the Rayleigh–Taylor instability for times $t = 1.45$s (*left*) and $t = 1.5$s (*right*). It is clearly apparent that only droplets surrounded by gas (ψ threshold of 0.01, *black*) get extracted. Liquid structures that remain attached to each other are not counted as individual droplets. Also, a minimum value of $\psi = 0.5$ (*pink*) is needed for a fluid structure to be considered as liquid.

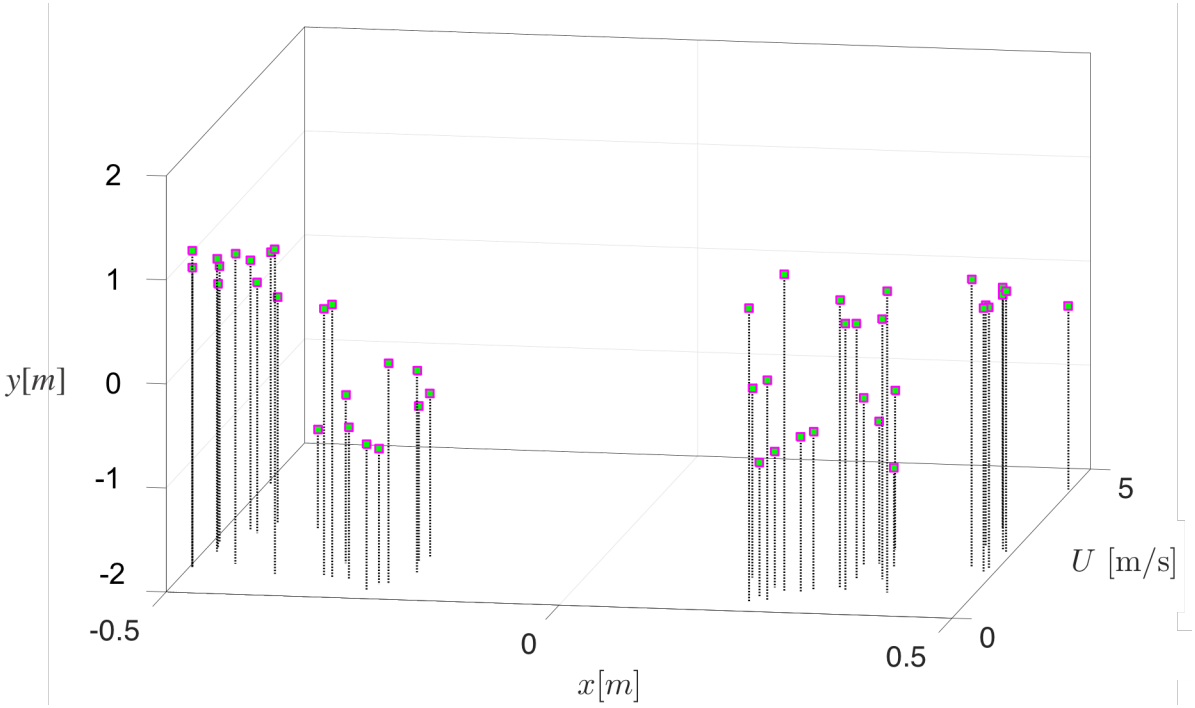

Fig. 4.5: Three-dimensional view of the spatial repartition of identified liquid droplets in the rectangular domain as time progresses. The third axis represents the droplets' velocity magnitude.

4.3.2 Breaking of a dam

Dam-break flows, which are represented by the sudden release of a fluid contained in a reservoir behind a vertical barrier, are both of practical and fundamental importance in fluid mechanics and engineering. In spite of their simplicity, these problems embed several features related to practical hydrodynamic circumstances, e.g. in marine, coastal and offshore engineering applications, such as wave breaking, wave impact on structures, and sloshing [129, 130]. They have also played a crucial role in underpinning simple models for a number of natural and catastrophic events such as break-out floods. Dam-break flows are of an interesting nature in the present numerical investigation of multiphase flow and atomisation as they represent the complex evolution of a free surface, accompanied by splashing and liquid breakup into smaller structures.

We discuss the flow originated by the break of a dam in two dimensions and the impact of the liquid front against a fixed vertical obstacle, located downstream of the dam. The geometry and the initial setup are shown in Fig. 4.6. Given our interest in high-density ratio two-phase flows throughout this work, the density ratio is here 1000:1, the setup consists of a column of water at rest surrounded by air. At time $t = 0$s, gravity is left to take over and the column of water collapses. During the collapse, the water impacts an obstacle at the bottom of the tank and creates a highly distorted interface and complex flow structure (Fig. 4.7).

The dam-break problem is dynamically challenging, exhibiting a complex interaction between shear-induced wave formation, mixing and splashing (Fig. 4.7). On that account, it is of utmost importance in the context of the present work to be in a position to track water droplets produced during these physical phenomena. A Kelvin–Helmholtz-type instability (KH) rapidly develops along the underside of the interface where KH rollers grow (Fig. 4.8b). This instability results from the entrainment of the ambient air by the moving water front and the shearing action between the two fluids. Gradually, individual KH waves break up into droplets. As the liquid front splashed against the right wall, the nature of the mixing and atomisation becomes more and more complex.

As the column of water begins to fall under gravity, a backward moving wave folds over, forming a closed loop of entrapped air (Fig. 4.9). Air entrainment due to wave breaking during this downward motion has been reported in several studies, recently in the numerical study of Lind et al. [129]. Fig. 4.9 shows the flow field to the left of the obstacle as the tip of the plunging-water column impinges upon the top part of the interface, trapping air beneath it, forming a small air pocket.

Fig. 4.10 shows a snapshot in time of the *CLS* field along with the corresponding *Drops* field into which the identified droplets have been transferred between two subsequent timesteps. Droplet sampling is conducted every timestep. The droplet statistics are then collected during domain reconstruction and post-processed with an external post-processing routine. Subsequent quantitative analysis of the identified primary breakup droplets properties lead to the spectrum of droplets shown in Fig. 4.11, a droplet size histogram representing the droplet size distribution in the breaking of a dam. The set of droplet sizes produced by a given spray can be subdivided into statistical bins, where each bin consists of a drop whose size is within some diameter range. By counting the number of drops in each bin, it is possible to construct a histogram of the frequency of occurrence of a given bin. The continuous version of the histogram is the probability density function (PDF) of the drop size, or the (number) drop size distribution function.

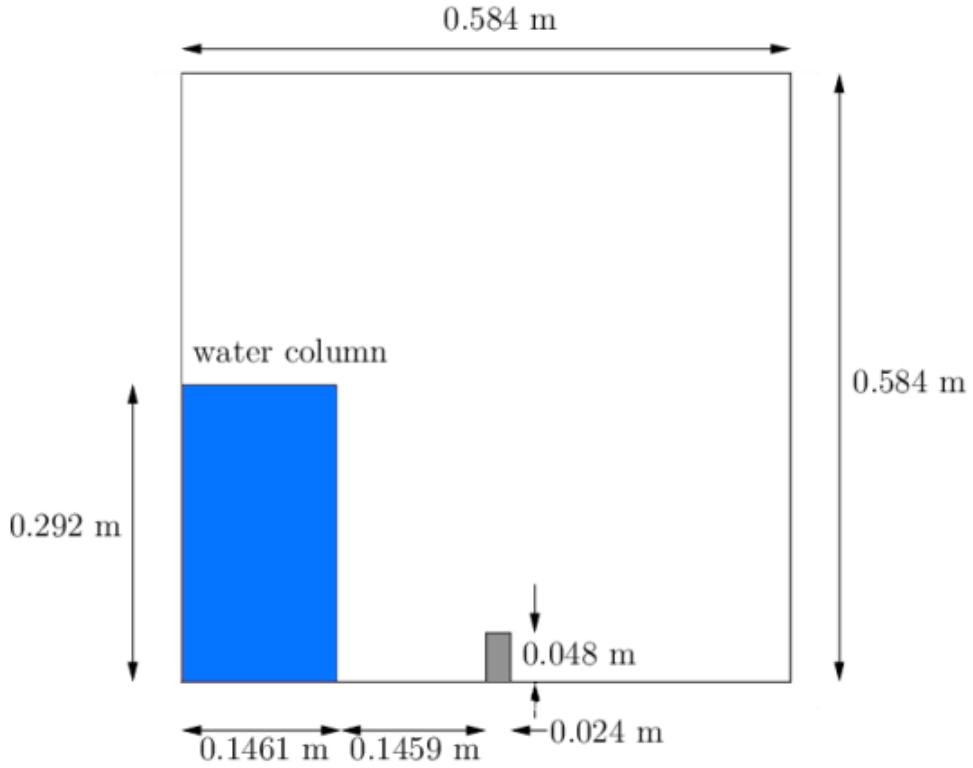

Fig. 4.6: Computational domain and initial setup for the breaking of a dam in two dimensions.

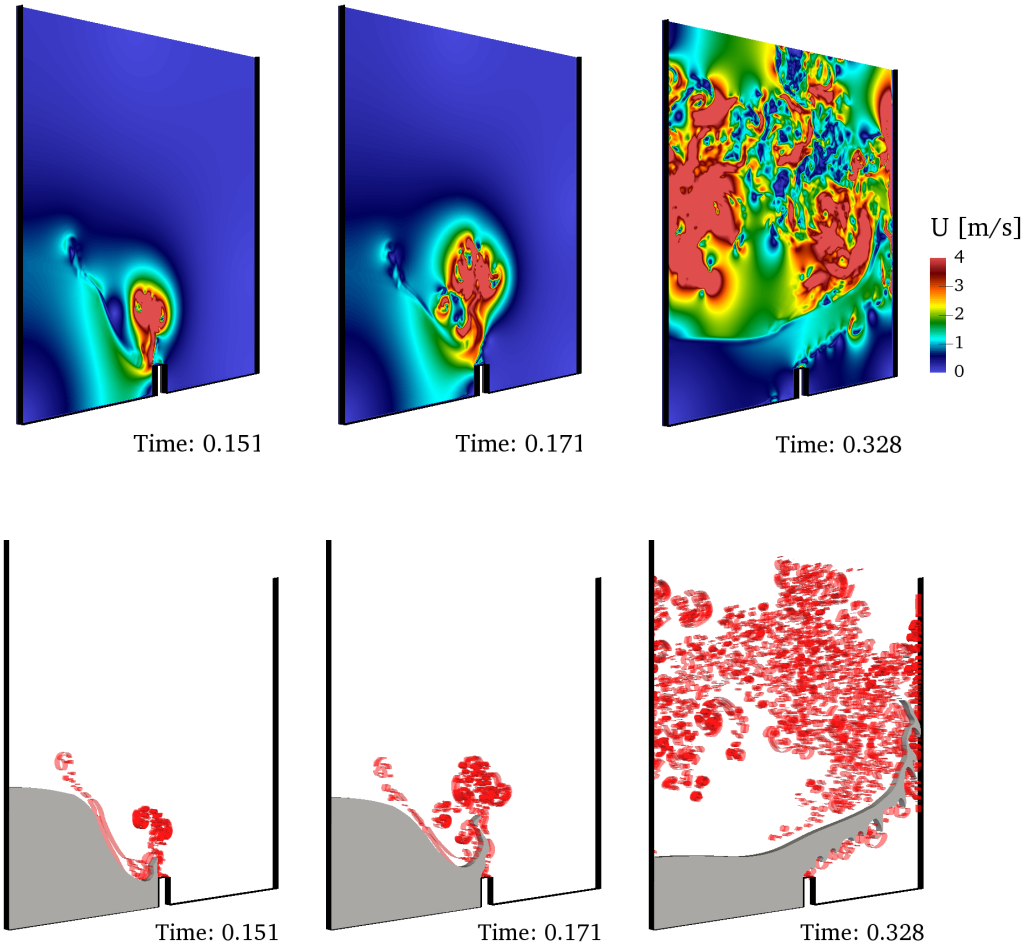

Fig. 4.7: Breaking of a dam under a gravitational acceleration of 9.8m/s^2. *Top row*: Total velocity field; *bottom row*: Liquid phase in grey and iso-surface of Q-criterion in transparent red. All times are in seconds.

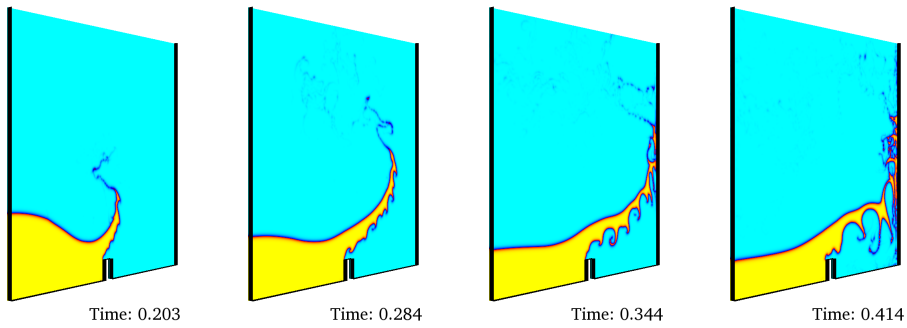

Fig. 4.8: Free-surface flow generated by the break of a dam and formation of shearing instabilities. All times are in seconds.

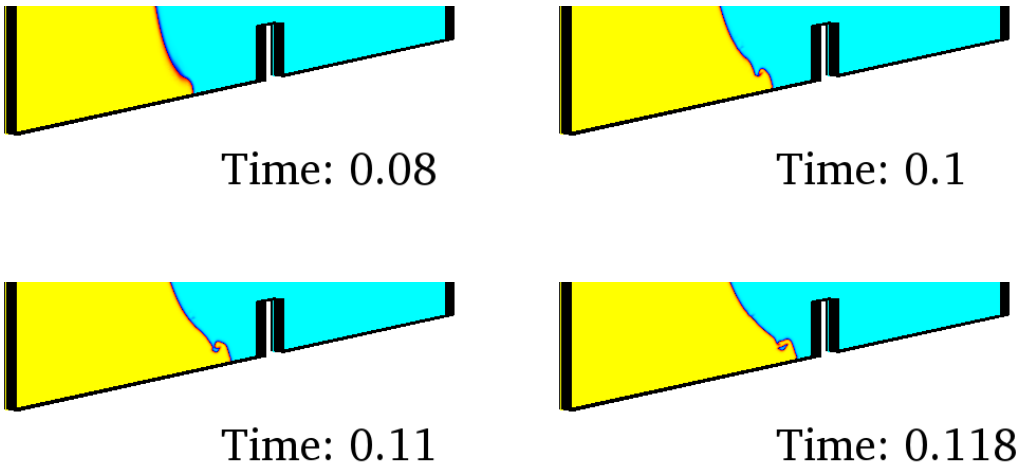

Fig. 4.9: Close-up view of the free-surface flow generated by the breaking of a dam. At $t = 0.118$s a trapped air pocket is visible in the water column front.

The spectrum of droplet sizes that can be found in sprays can vary depending on the particular atomising process. Depending on the applications, the drop size distribution must have a particular form for optimal operation. Knowledge of the effect of variations in fluid physical properties, atomiser geometry, and atomiser operating parameters on drop size distribution is crucial for effective control of the resulting distribution. Droplet size distributions give not only an indication of how heterogeneous the spray droplets are, but also of the relative atomisation performance of various nozzle designs and how these nozzles perform with changing operating conditions. The classical method of modelling drop size distributions is empirical: a curve is fit to the data collected for a wide range of atomiser nozzles and operating conditions. Curves appearing most frequently become the basis for 'standard' empirical distributions. The Rosin-Rammler distribution or log-normal distribution are frequently used for representing droplet size distributions in sprays. Then, as mentioned in Chapter 1, Section 1.2.4, the present state-of-the-art is to empirically optimise fuel injectors. For spray combustion modelling, such a 'standard' droplet size distribution is usually assigned as a boundary condition for the spray, and injected inside the combustion chamber as a droplet population assumed to have been generated by primary breakup [35, 75, 98], thereby treating the atomisation process as a black-box model. The problem with the empirical approach in modelling drop size distributions is the difficulty of extrapolating the data to operating regimes outside the experimental range given the impracticality or prohibitive cost of additional experimentation. The result in Fig. 4.11 constitutes a rare attempt at computing on-the-fly a drop size distribution following primary breakup, which makes us

come closer to simulating atomisation and spray combustion without the need to resort to current black-box primary breakup models. The mean of the present drop size distribution is $2,700\mu$m. The histogram data is fitted with a distribution of log-normal type. As the droplet size distribution is sensitive to the sample number, and for shorter simulations the sample number is also smaller, this leads to an overall distribution trend that exhibits some fluctuations. An alternative insight into droplet properties is obtained by the scatter plot of the droplet diameter and velocity in Fig. 4.12. No particular trend is emerging, especially given the small data sample.

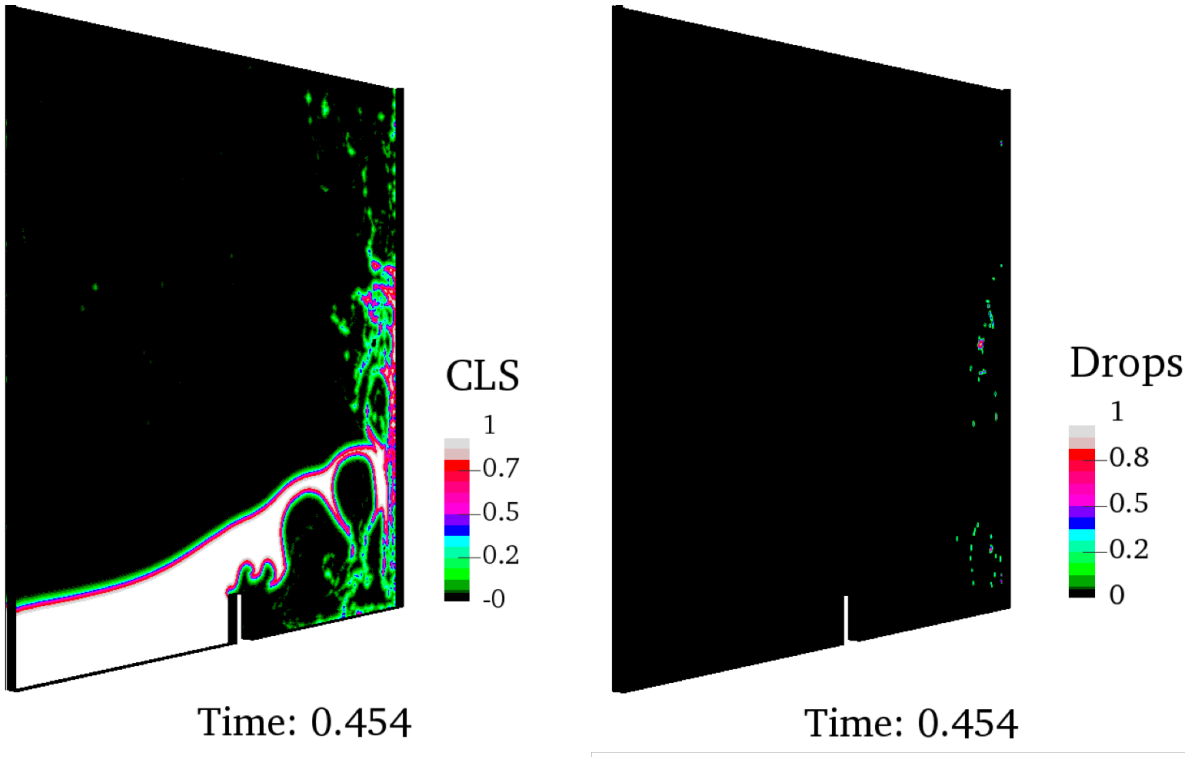

Fig. 4.10: Snapshot example of liquid droplets having been extracted from the CLS formulation during the breaking of a dam.

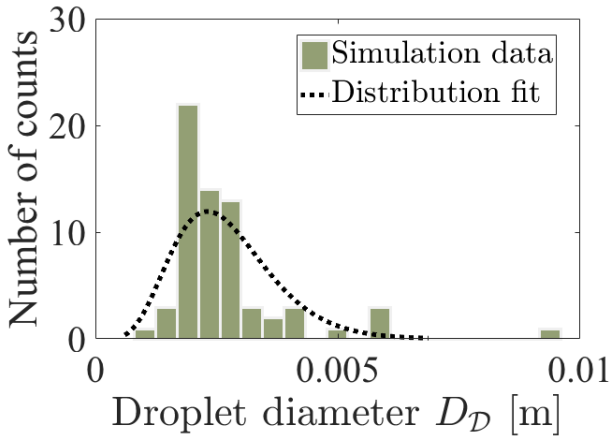

Fig. 4.11: Droplet size distribution of the droplets generated during the primary breakup of the breaking of a dam. Droplets sampled between times $t = 0.45$s and $t = 0.48$s.

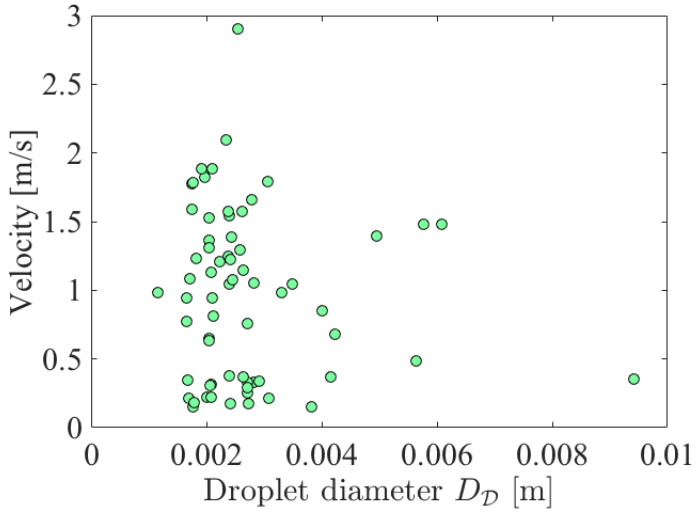

Fig. 4.12: Velocity scatter plot for the droplet size distribution in Fig. 4.11.

4.3.3 Droplet impact on a thin liquid layer

Droplet impacts and splashing are iconic multiphase flow problems for large enough Weber and Reynolds numbers, as introduced in Chapter 3, Section 3.9. The impacting droplet (mother drop) fragments into a myriad of smaller droplets (daughter droplets) which are ejected away from the zone of impact. Since the pioneering work of Worthington (Fig. 1.2), many experimental, theoretical, and numerical works have been performed. Nevertheless, the dynamics of droplet impact is complex and an overall understanding of the whole process

is still lacking. For a comprehensive review see Yarin [234]. The control of the outcome of impact is crucial for applications in which the present work is beneficial. For instance, spreading is desirable for coating of solid substrates (see Section 3.9.1), while splashing may improve the efficiency of evaporation and mixing in combustion chambers. As a result, the dynamics of drop impact on a thin liquid film is investigated in order to assess the RCLS framework performance in identifying the mechanisms of splash formation and atomisation at the heart of the splash. High-fidelity numerical simulations are performed with the RCLS method (WENO3, $\varepsilon = 0.5\overline{\Delta_x}$) of both 2-D and 3-D incompressible Newtonian two-phase droplet impacts. In the theory of droplet impact on thin films, the moving contact line problem (Section 3.9.1) is circumvented by assuming that the surface is already covered by a thin film of fluid.

Numerical set up We consider a water-like liquid droplet of diameter D impacting on a thin pre-existing layer of the same liquid of thickness e with a downward impact velocity U_0, as shown in Fig. 4.13, and following the numerical set up of Josserand et al. [104] as a benchmark state-of-the-art comparison. The droplet is initially at rest. Impact velocities resulting in compressibility effects are outside the scope of the present work. The velocity range is confined to $2-4$m/s, at which compressibility effects in typical liquids are negligible. The liquid (glycerinated water) and gas (air) have densities ρ_{liq} and ρ_{gas} and dynamical viscosities μ_{liq} and μ_{gas}, respectively. The surface tension is σ. These physical properties are summarised in Table 4.2.

Splash dynamics depends on many physical parameters, the most important being the impact velocity U_0. For high impact velocities, splashing is promoted, while at low velocities the droplet spreads more gently (deposition). The latter depends mostly on the balance in the liquid between inertial forces and viscous forces [105], characterised by the impact Reynolds and Weber numbers given by Eq. 3.24. The main dimensionless groups governing the present investigated drop impact are summarised in Table 4.2.

Droplet impact is produced by the release of the drop at some height h_0 above the liquid film, falling under gravity g. We note, however, that in the phenomena accompanying drop impact, gravity effects are typically not important. The Froude number that quantifies the influence of gravity is high (see Table 4.2), indicating that gravity has only a small effect on the dynamics. At very short times and scales, it is clear that gravity has an even smaller effect.

The droplet is assumed to be spherical, which is a valid assumption if the air flow has as a little effect as possible on the droplet shape (small Weber number) and if the oscillations of

the droplet during its free-fall are negligible. If those conditions are satisfied, the initial gas layer aspect ratio h_0/D (see Table 4.2) is irrelevant [104]. Another important dimensionless number in this study is the aspect ratio between the liquid film and the droplet, e/D. Finally, the computational domain is a rectangular box of 10mm$\times$3mm, meshed with 192,000 hexahedral elements.

Table 4.2: Dimensionless values of the parameters and dimensional values of the main parameters for the first simulation reported in Fig. 4.13. Individual parameters will be varied in subsequent sections.

We	Fr	Re	ρ_{liq}/ρ_{gas}	e/D	h_0/D
500	815	2000	826.4	0.2	1/30
U_0[m/s]	D [mm]	μ_{liq}[kg/m.s]	μ_{gas}[kg/m.s]	σ[kg/s^2]	e [mm]
4	2	4×10^{-3}	18×10^{-6}	64×10^{-3}	0.4

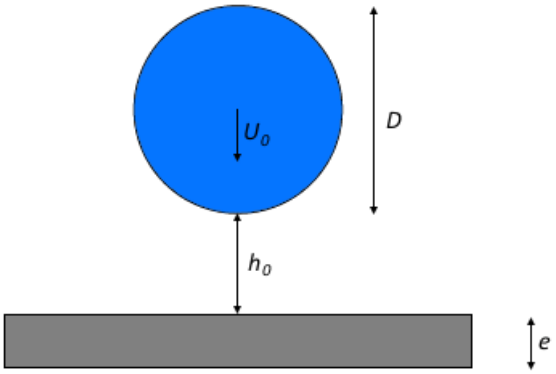

Fig. 4.13: Sketch of the numerical simulation set up for the impact of a spherical droplet of diameter D and velocity U_0 onto a thin liquid layer of thickness e. The droplet is initially sitting at a distance h_0 from the liquid film. Adapted from Josserand et al. [104].

Droplet impacting on a thin liquid film for the parameters in Table 4.2 The splash is the result of the collision between the spreading drop and the liquid layer at rest. Almost immediately after the impact, in a small "impact neck" region at the intersection between the almost spherical drop and the upper boundary of the liquid layer, ligament-like structures form on either side of the drop. This is called the ejecta sheet, or corolla, witnessed in experiments [214] and numerical simulations [44, 83, 230]. The ejecta sheets move rapidly radially outwards ($t = 5\times10^{-05}$s in Fig. 4.14) and grow into a vertical expanding lamella before disintegrating eventually into droplets, as seen in Fig. 4.14 at $t = 0.0005$s.

The ejecta sheet is commonly accompanied by the ejection of a thin liquid jet. The thin liquid jet is believed to emerge due to the large pressure peak in the reconnection zone when the droplet and the liquid layer have connected [2]. To capture such a fast and small-scale phenomenon, the mesh needs to adapt to the smallest existing length scales: the thickness of the gas layer and the thickness of the jet, and the radius of curvature of the interface. The ability to capture these small-scale phenomena in numerical simulations remain a challenge based on the level of grid refinement [83]. The small length scales associated with the additional observation of the ejection of a thin liquid jet have been numerically achieved only in 2-D with adaptive mesh refinement [2, 3, 104, 105].

The inertial dynamics of the splash are in part due to the cushioning effect of the gas underneath the droplet front, although the effect of the surrounding air has been shown not to be as dramatic as for impacts on solid surfaces [104]. The air layer beneath the droplet between the two liquid regions evolves to a very small thickness. The connection between the droplet and the liquid layer is eventually made – the contact occurs along a ring enclosing a thin disk of air. If the thin gas layer cannot retract fast enough and cannot be expelled, a sequence of air bubbles may become entrapped by the impact dynamics, clearly visible in Fig. 4.15. These have been noted both experimentally and numerically [104, 213, 215]. Thoroddsen et al. [215] studied the dynamics of this air sheet as it contracts due to surface tension. Their experiments revealed that during the contraction of the air disk an azimuthal undulation resembling a pearl necklace develops along its edge, in a similar manner to that observed in Fig. 4.15. The contraction speed of the sheet was accurately described by a balance between inertia and surface tension [149, 215]. A potential interplay between the bubble entrapment and the ejecta sheet still needs to be elucidated [104], which is why numerically the small thickness of the gas layer needs to be resolved [2].

At the time of reconnection between the impacting drop and the target liquid surface, i.e. during the first instances after impact, it is not possible to capture the smallest length scales at which molecular forces act and trigger reconnection, as the curvature becomes infinite at that point. Molecular forces would also most certainly affect the motion of the interfaces in reality [105]. It is argued that the situation just after reconnection offers a realistic starting point for our simulations as the RCLS method is based on the precise resolution of the momentum balance and the mass conservation equation.

Hsiao et al. [93] predicted that vortex ring formation underneath the free surface of the liquid layer is possible as a result of the initial drop impact. Agbaglah et al. [3] characterised precisely the vortex shedding in the neck of the impact. They created a phase diagram in Weber and Reynolds numbers space and defined a with-or-without vortex shedding regime

transition through a constant capillary number. In a 2-D simulation with similar Weber and Reynolds numbers to our computation (We = 292, Re = 2042), Agbaglah et al. [3] noticed that the ejecta sheet was accompanied by vortex separation leading to a separate roll jet, in a manner similar to the liquid structures we observe at the root of the lamellas in Fig. 4.14 at $t = 0.00025$s.

Fig. 4.16a shows the instantaneous velocity vector field and vorticity field (Fig. 4.16b) at $t = 0.0001$s. The colour scale shows high clockwise vorticity regions (red), and corresponding velocity field in light colours. We observe that the vorticity in the gas phase is concentrated near the neck of the drop and forms two counter-rotating vortex rings due to the interaction of the ejected liquid structures with the surrounding fluid.

Finally, we observe that the initial symmetry is lost when the droplet impacts the liquid pool. Indeed, at short times only, before instabilities can develop and particularly before the ejecta sheet and droplets form, we can consider the physical problem to be symmetric. Because of axi-symmetry, the lamellas seen in Fig. 4.14 are actually toroidal. Further three-dimensional calculations are needed to account properly for the evolution of the crown once non-axisymmetric perturbations grow. This will be the subject of our investigation in the final part of this chapter.

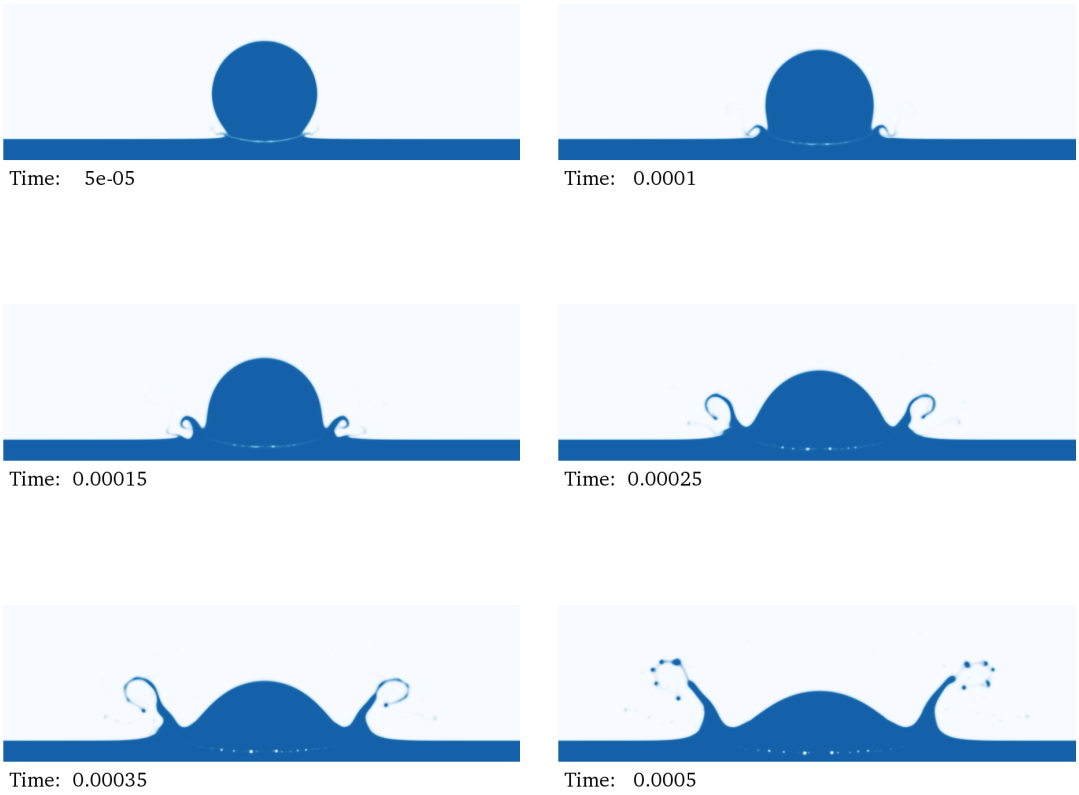

Fig. 4.14: Snapshots of a droplet impacting on a thin liquid film for the parameters in Table 4.2, i.e. We=500, Re=2000.

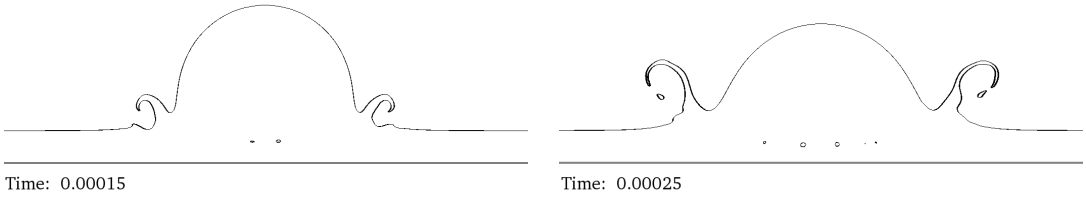

Fig. 4.15: CLS contour ($\psi = 0.5$) of a droplet impacting on a thin liquid film for the parameters in Table 4.2, i.e. We=500, Re=2000. Interface shapes near the neck of the impact. A jet is observed coming out of the neck.

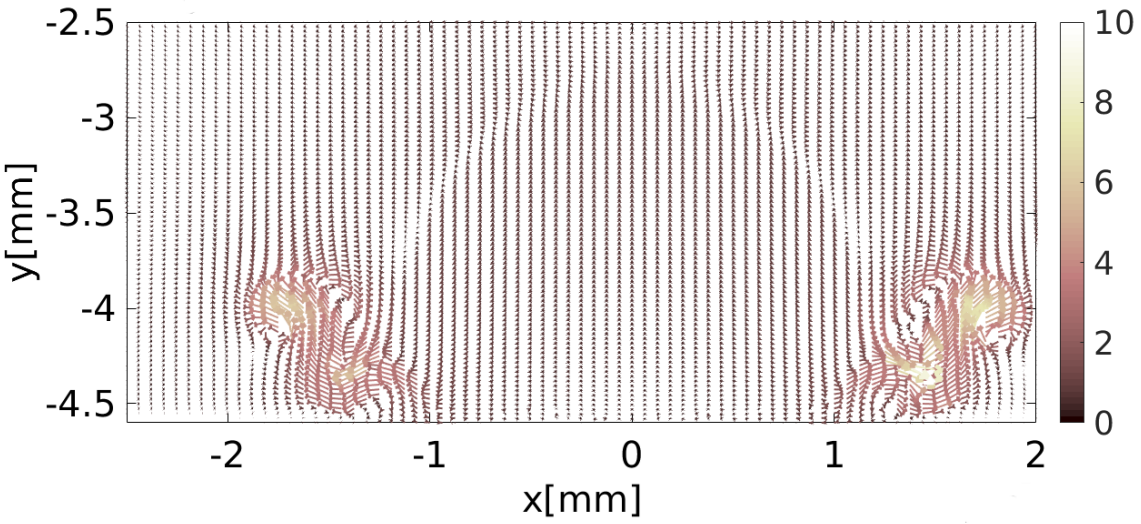

(a)

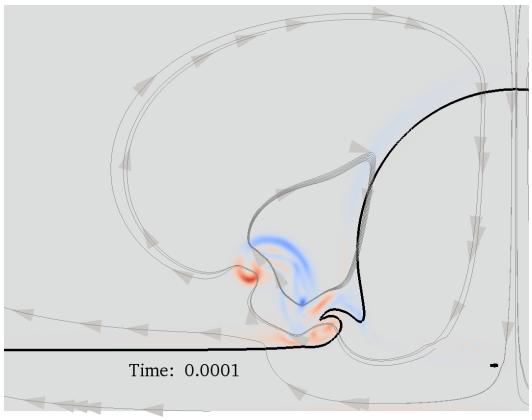

(b)

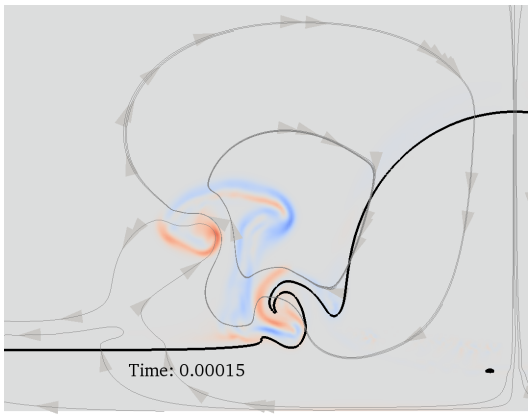

(c)

Fig. 4.16: Instantaneous velocity vector field at $t = 0.0001$s **(a)** and vorticity field **(b–c)** at times $t = 0.0001$s and $t = 0.00153$s of a droplet impacting on a thin liquid film for We=500, Re=2000. The colour indicates vorticity, with blue/red representing counterclockwise/clockwise rotation, also visible through the velocity vectors in **(a)**.

Reduction in impact speed The same computation was performed while halving the impact speed of the drop. The impact velocity is now $U_0 = 2$m/s and the corresponding non-dimensional numbers are Re=1000 and We=120. In Fig. 4.17, one can see that the impact dynamics is different. The droplet spreads more gently on the surface. The impact creates a radially expanding lamella, consistent with the observations by Josserand & Zaleski

[105]. The figure also illustrates the relatively straight outer rims compared to the inward bending of the outer rims for the simulation at Re = 2000. Indeed the lamellas are relatively horizontal and stay as such until the end of the simulated time. They subsequently break up into droplets, as can be seen at $t = 0.00033$s. As the lamellas are smaller in diameter, the drops are smaller too as a result. We do not observe an additional roll jet below the ejecta due to vortex shedding as for the simulation at Re = 2000. The ejecta leads solely to the growth of the lamellas. This was also noted by Agbaglah et al. [3] for their simulation with We= 292 and Re= 1000. We note, however, that in order to compare thoroughly simulations with different impact speeds ($U_0 = 4$m/s and $U_0 = 2$m/s), it would be necessary to normalise the time by a characteristic time of impact, a delay time of impact due to the air cushioning, defined for example as $\tau = D/U_0$ by Josserand & Zaleski [105].

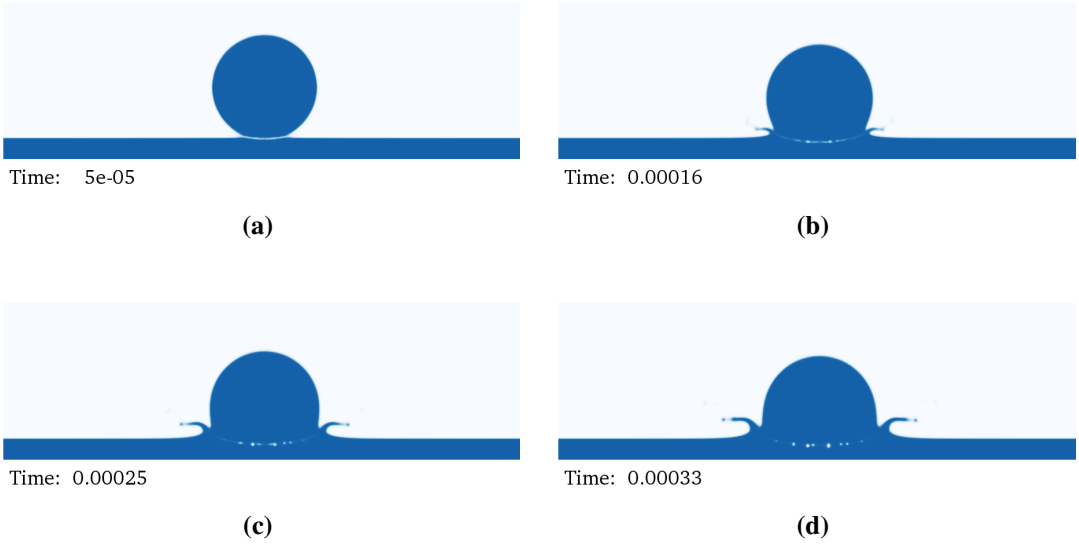

Fig. 4.17: Snapshots of a droplet impacting on a thin liquid film for a lower impacting speed, i.e. We=120, Re=1000.

Reduction in liquid pool height For drop impact on a liquid layer, the thickness of the liquid film is crucial and controls partly the impact dynamics. We performed the same computation as detailed in Table. 4.2 but this time while varying the liquid pool height and as a result changing the initial gas layer aspect ratio h_0/D, which might affect the air cushioning during the falling phase. We here have $e/D = 0.05$ where $e = 0.1$mm and $h_0/D = 2/15$. In Fig. 4.18, at $t = 0.00035$s, a shallow water wave travels on the liquid pool on either side of the impact point and away from it. We postulate that the liquid pool being less deep, the surface wave is affected by the bottom wall before becoming a breaking wave. At $t = 0.0005$s, the

ejecta sheets on the outer rim of the drop are forced to bend downwards and plunge into the liquid pool due to the ratio between the wave height and the water depth (depth-induced wave breaking), which echoes the spiralling corolla observed by Thoroddsen [214]. The bent corolla finally forms closed liquid loops with entrapped air pockets. This is a similar wave breaking mechanism and air entrapment to the one observed in the breaking of a dam in Section 4.3.2. It would be necessary in a follow-up study to keep the initial gas layer aspect ratio h_0/D constant while varying the liquid pool height for a more direct comparison to the benchmark case of Table 4.2.

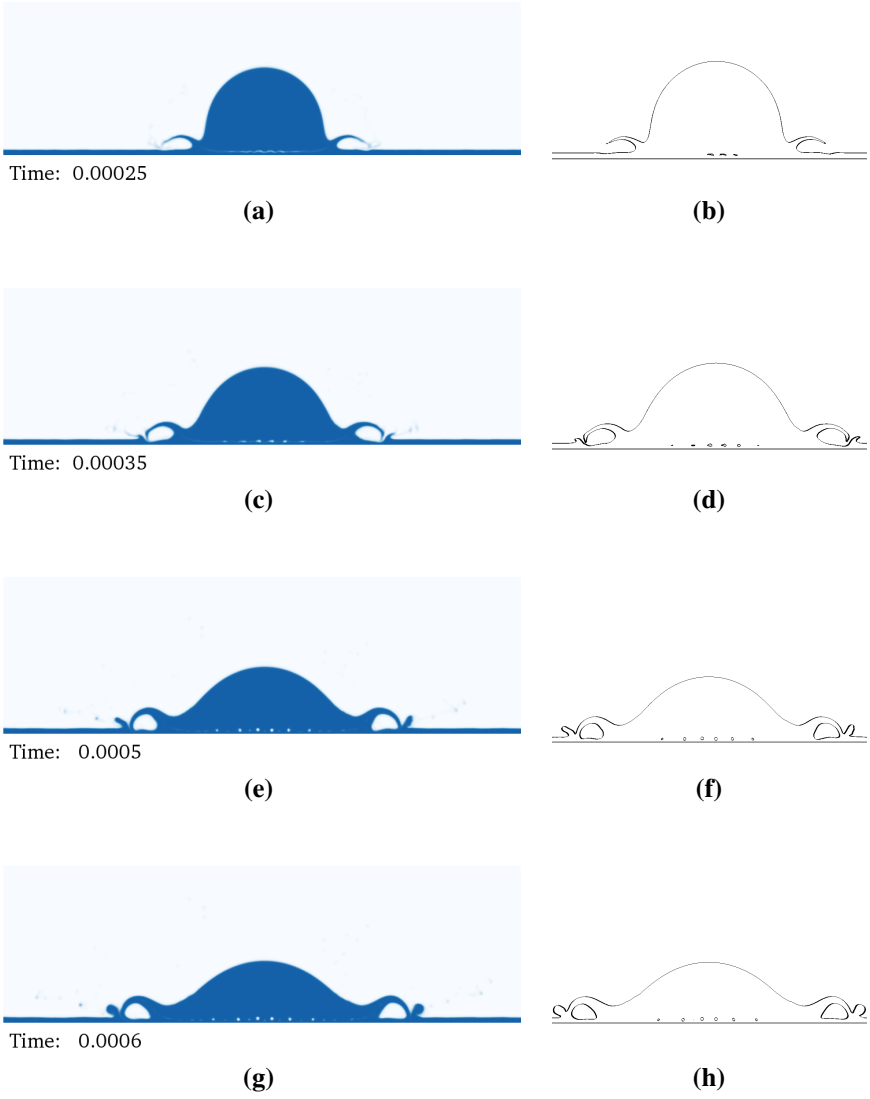

Fig. 4.18: Snapshots of a droplet impacting on a thinner liquid pool where $e/D = 0.05$ and $h_0/D = 2/15$ (We=500, Re=2000) (*left panels*) and corresponding $\psi = 0.5$ iso-contour (*right panels*).

Three-dimensional droplet impacting a liquid pool State-of-the-art two-dimensional computations [3, 104, 105] allow for a precision that cannot be reached in realistic three-dimensional calculations. The general 3-D problem remains a significant numerical challenge because of the large range of scales involved, despite some recent excellent numerical results [2, 51, 236]. In order to evaluate further the ability of the RCLS methodology to handle realistic 3-D splashing problems with topology changes and large density ratios, we carry out a three-dimensional calculation of a liquid droplet impacting a liquid pool following the parameters listed in Table 4.2, i.e. We=500, Re=2000. The computational domain has dimensions $10 \times 10 \times 3$mm, and is meshed with 4 millions hexahedral elements. The computational results in Fig. 4.19 show the complexity of such dynamics. The impact of a liquid drop on a liquid film is capable of pushing apart a significant liquid mass. An obvious manifestation following the splash of the drop is thus the formation of a crater – with a larger diameter than the initial drop diameter – in the middle of the liquid pool where the drop impacted (Fig. 4.19c). The liquid rises around the impact point through a circular, approximately vertical and expanding sheet, the "corolla" (Fig. 4.19d). The corolla grows vertically and propagates radially around the droplet, ending in a circular rim that destabilises into fingers, or ligaments (Fig. 4.19e). In addition to the rim-to-finger formation mechanism at the tip of the corolla, hole formation in the corolla, or membrane puncturing, is also visible (Fig. 4.20) and destabilises the corolla at the late stage of crown formation. Recent experimental photographs have indeed shown corollas with holes [220]. The ligaments eventually break up into small droplets by a Rayleigh–Plateau-like instability [105] (Fig. 4.19f). For higher impact speeds, an uprising central jet would be generated at the centre of the impact location. It is a consequence of air entrainment by the impinging droplet. This whole process has been described in numerous experimental papers, for instance see the review by Yarin [234], and is generally called "corona" or "crown" splash named after the celebrated Worthington-Edgerton crown (Fig. 1.2). For a similar Weber and Reynolds numbers regime, the present simulation is qualitatively in accordance with the numerical results by Yokoi [236].

A point of interest recently investigated by researchers is the shape of the emerging ejecta sheet as it evolves in the neck region [4, 104]. The shape depends on the angle of ejection of the ejecta sheet, the location and time of appearance of the ejecta sheet and the width of the associated rim. Knowledge of these different elements would provide a better ability to compute its stability against perturbations and understanding of the long-standing problem of crown formation.

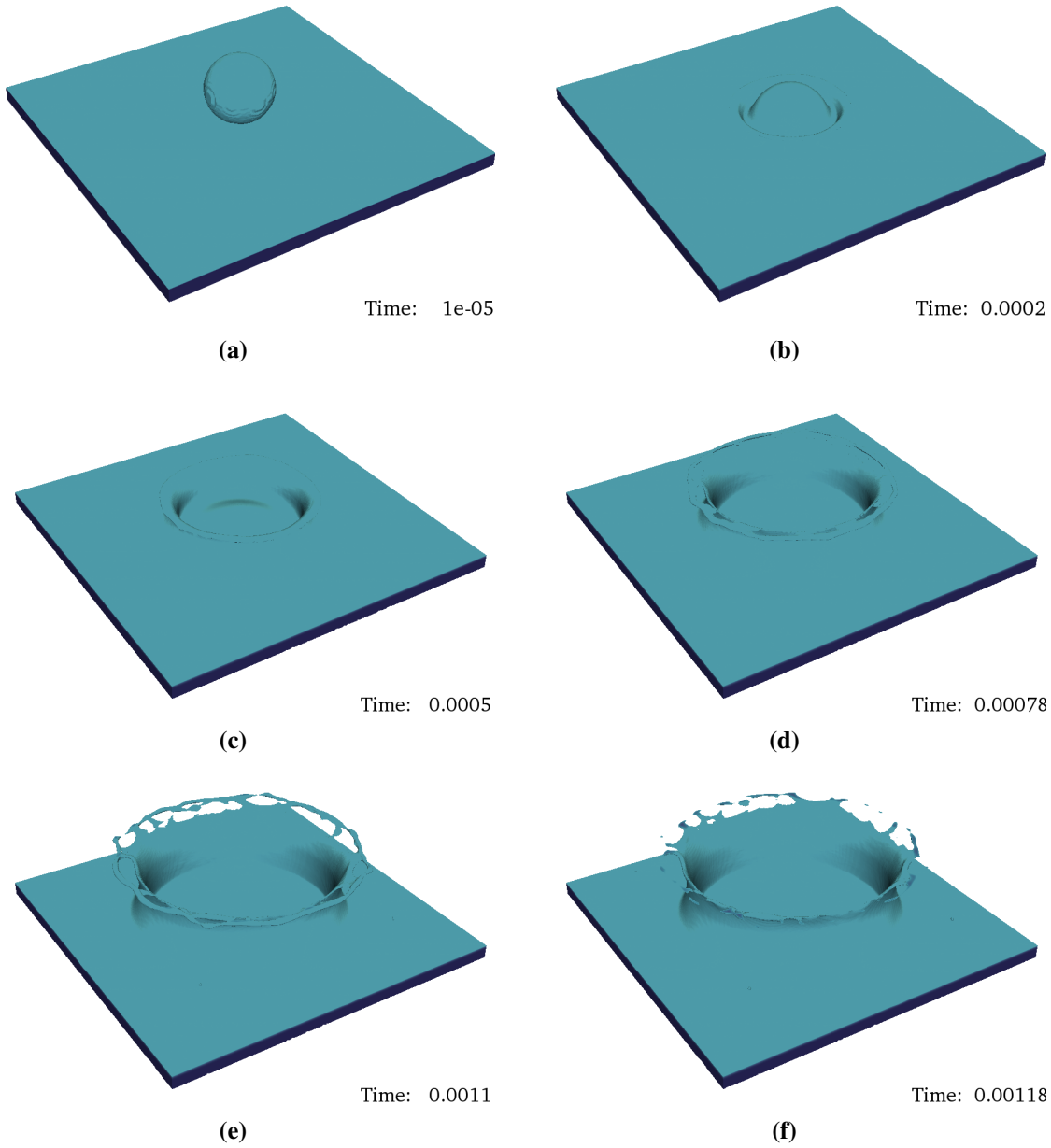

Fig. 4.19: Snapshots of a three-dimensional droplet impacting on a thin liquid film for the same parameters as in the 2-D case listed in Table 4.2, i.e. We=500, Re=2000.

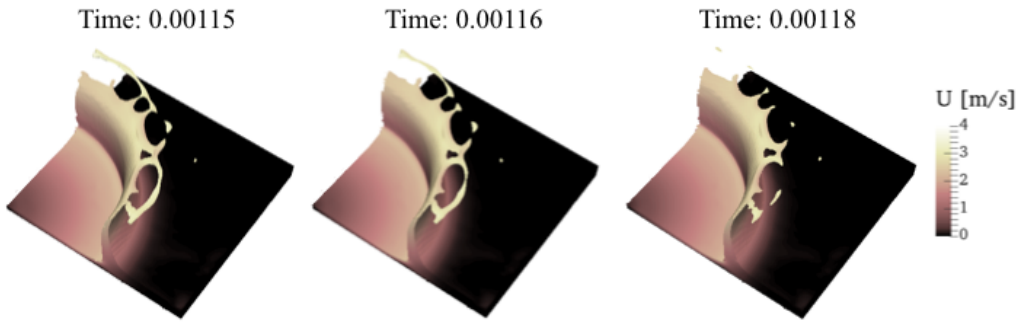

Fig. 4.20: Velocity field of the three-dimensional droplet impacting on a thin liquid film. Membrane puncturing, ligament formation and droplet pinch-off.

Droplet transfer during splashing Fig. 4.21 shows the application of the droplet transfer algorithm on the droplet impacting a thin liquid film for the parameters listed in Table 4.2. At $t = 0.0008$s, liquid structures on the left hand side are still attached to each other and therefore are not extracted as individual droplets from the CLS formulation. They are extracted in the next timestep, at $t = 0.00085$s.

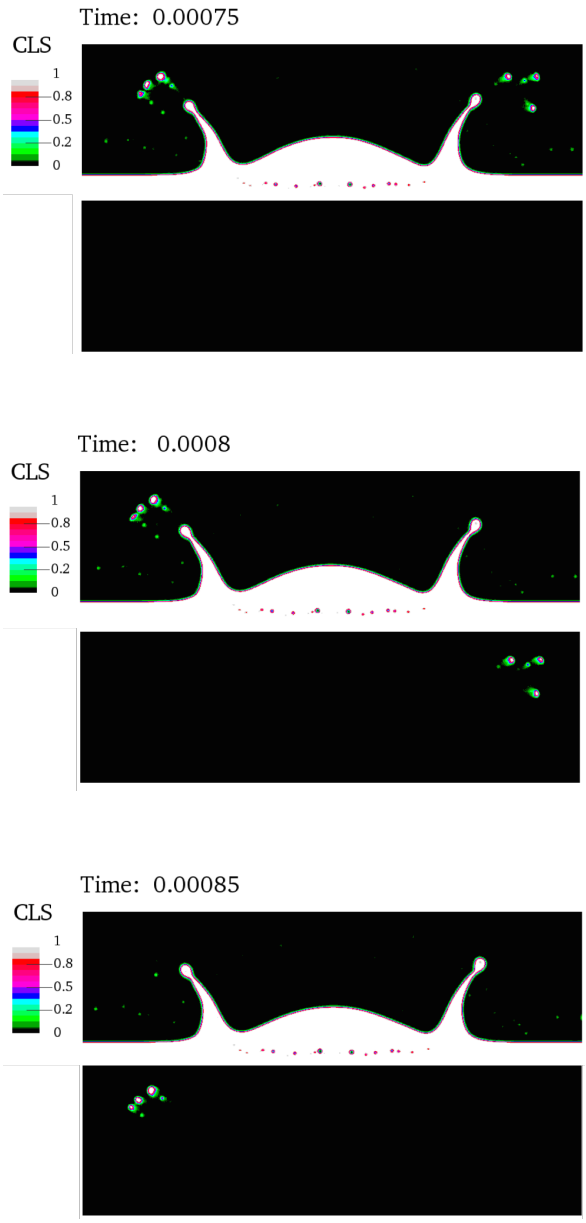

Fig. 4.21: Droplet tracking algorithm applied to a liquid drop impacting a liquid film. Top panels represent the *CLS* field. Bottom panels show the droplets that have been extracted from the *CLS* field.

4.4 Final comments

Droplet impacts are so spectacular that they have come to symbolise the beauty and fascination of fluid mechanics. In the present chapter, the splashing regime of droplet impacts

on wetted surfaces has been investigated. When the impact velocity is high enough, droplet impact yields characteristic phenomena. The liquid rises around the impact point through an expanding "corolla", which sprouts fingers at its tip leading to crown formation. Finally, droplets may be ejected from the crown. The splashing regime is complex, underlying several instability mechanisms and fragmentation of the liquid bulk, making it an interesting candidate to asses the numerical capability of the RCLS method in capturing the expected theoretical hydrodynamics and atomisation scenario.

A vast number of drops can be generated in an atomisation process. Thus, it becomes prohibitively expensive to resolve every drop by the conservative level-set scalar ψ. Instead, Lagrangian spray models are more adequate to describe small-scale liquid drops having simple geometry. Computing the primary breakup drop size distribution is thus of paramount importance for its transfer to a Lagrangian stochastic spray model in order to describe the secondary breakup process. In this study, broken small liquid drops are identified during primary breakup following a set of criteria, removed from the level-set representation for further insertion into a Lagrangian stochastic spray model, preserving their mass, centre of mass, and momentum.

This chapter has highlighted the accurate operation of the droplet tracking algorithm on primary breakup modelling as implemented in the RCLS formulation. In particular, the interface-capturing numerical approach has demonstrated its ability to capture accurately, on several test cases with different challenging physical and numerical requirements, the dynamics of the phase interface and to achieve a good and cost-effective performance on droplet recognition, tracking and transfer. The results indicate that the RCLS method with droplet tracking is able to work well across a broad range of operating conditions. In Chapter 7, we will submit the droplet tracking algorithm to conditions relevant to the atomisation of liquid kerosene in jet engines.

Chapter 5

Stationary and Non-stationary Interfacial Dynamics

Two principal methods have become commonplace to simulate the evolution of two-phase immiscible flows of liquid and gas separated by a sharp interface and to deal with the large jumps in physical properties associated with it. These are the Level-Set (LS) method and the Volume of Fluid (VoF) method, introduced in Section 2.2. As discussed in Chapter 2, both methods have their own strengths and weaknesses. For example, the VoF method is known to be prone to excessive numerical diffusion, while a rudimentary LS method has some difficulty in conserving mass. However, each of these methods can now reach a high level of physical accuracy, having been paid particular attention in the past decades by different research groups who worked towards remedying these deficiencies. It now remains unclear what are the remaining advantages and drawbacks of each method relative to the other. The key message lies in the fact that these newly improved numerical methods have been developed by different groups, using different codes and most importantly fine tuned to tackle different applications. Therefore, we are in a position to question what might be the optimal way to unify them.

In an attempt to subject the RCLS method to a pair of benchmark test cases to examine a) the accuracy of curvature and surface tension forces representation, b) its ability to minimise non-physical interfacial velocities and c) the ability to tackle fluids with very different densities, as well as to answer the aforementioned question, we performed a direct comparison of two current state-of-the-art variations of these methods in collaboration with City University London and the University of Brighton (LS: *RCLSFoam* and VoF: *interPore*) and implemented in the same code (OpenFoam). This chapter is a result from this collaborative effort.

We shall give a brief introduction to the *interPore* solver in the following. The reader is referred to Chapter 3 for a presentation of *RCLSFoam*. The VoF two-phase incompressible flow solver *interPore* [1] is based on a compressive/smoothing treatment of the phase interface, in which the indicator function γ (introduced in Section 3.1.2) is used to represent the liquid volume fraction in each computational cell. The objective of Aboukhedr et al. [1] was to implement an improved interface capturing framework in an effort to capture droplet impact dynamics and penetration even in regions where capillary effects are dominant, such as flows through porous media at very low capillary numbers. In this effort, they introduced a new methodology implemented into the OpenFoam framework in order to address the aforementioned challenges. Their numerical formulation allows for correcting the capillary forces at the interface and hence avoid non-physical velocities. The scalar compression factor C_{comp} – as implemented in the default multiphase flow solver *interFoam* in OpenFoam [101] – is applied for limiting the artificial compression velocity. An additional procedure is implemented in order to maintain the interface sharpness: a sharpening function controlled with the sharpening coefficient C_{sh}. For $C_{\text{sh}} = 0$ the original VoF formulation is recovered. As C_{sh} approaches 1, the interface becomes sharper, hence the estimation of capillary forces becomes more accurate. Finally, a filtering coefficient U_f is used to filter out the capillary flux components of the capillary forces that result in non-physical (spurious) currents parallel to the fluid interface. The reader is referred to Aboukhedr et al. [1] and Bilger et al. [17] for more information.

This chapter is organised as follows. The first test case, consisting of a three-dimensional stationary spherical droplet in equilibrium, is discussed in Section 5.1. Results are compared in terms of the development of spurious currents at steady state. A further discussion on the nonlinear oscillation of the droplet during relaxation is given. The second test case involves a developing Rayleigh–Taylor instability (Section 5.2). The evolution of the instability is tracked and the solvers are compared in terms of their numerical and physical performance in capturing the interface dynamics including the production of small droplets.

5.1 Stationary deformation of a spherical droplet in equilibrium

When a cubic droplet of high density fluid is immersed in a low density fluid, the forces of surface tension cause it to deform and relax to a spherical shape, as shown in Fig. 5.1. In theory, the spherical interface should then remain at rest, with the pressure jump at the

interface exactly balancing the surface-tension force, as described by Laplace's balance law, provided the shape of the interface is given enough time to relax to its equilibrium shape [21]. However, depending on the numerical discretisation method used, and accuracy of the representation of the surface tension forces and pressure gradient, an exact numerical balance is very difficult to obtain. Non-physical vortex-like velocities (spurious currents thereafter) may appear, triggered by this imbalance, further limiting severely the accuracy of the standard CSF method [84]. The interface geometry is rather benign, however because of the low inertia environment in which it is evolving, it is particularly challenging to pick up the flow field for methods *a priori* not designed for this situation.

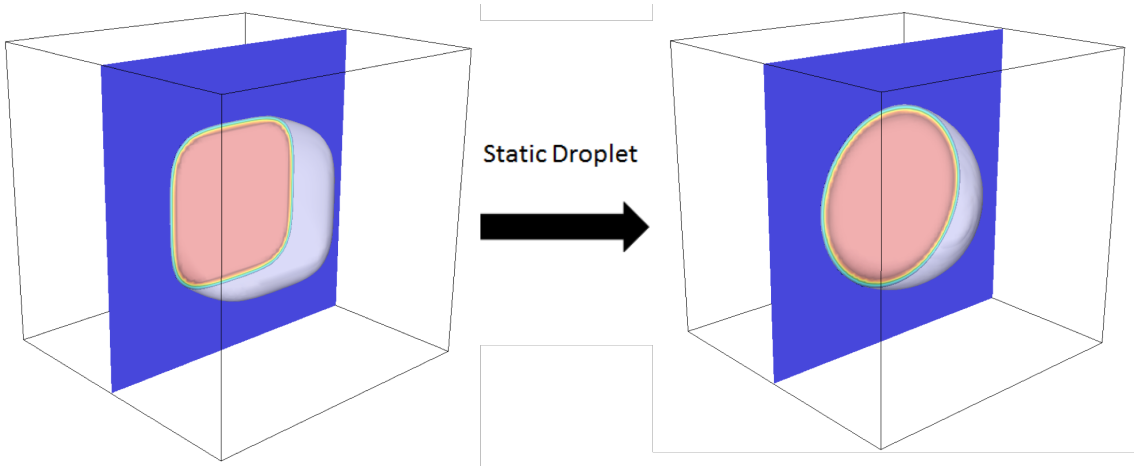

Fig. 5.1: Solution domain for modelling the static droplet. *Left*: initial condition, a cube of size 600 μm; and *right*: static shape of droplet at $t = 0.01$s.

5.1.1 Numerical set-up

We model the relaxation process of an initially cubic-shaped oil droplet of diameter D_0= 300 μm in water at static equilibrium in the absence of gravity. The fluid properties are as follows: the background (water) density ρ is 998 kg/m^3, and the viscosity ν is 1.004×10^{-6} m^2/s, while the droplet (oil) density ρ is 806.6 kg/m^3, and its viscosity ν is 2.1×10^{-6} m^2/s. The surface tension coefficient is fixed to 0.02 N/m. Computational boundaries are modelled as no-slip walls and the domain is discretised using a uniform cartesian mesh of $60 \times 60 \times 60$ hexahedral elements. The cubic droplet is allowed to relax to a static spherical shape, as described in Fig. 5.1. The force balance should converge to a correct solution of zero velocity everywhere and predict a pressure jump from a constant value p_0 outside the droplet to a value of $p_0 + 4\sigma/D_0$ inside the droplet. In the opposite case, spurious currents will develop at the interface and result in the destabilisation of the droplet interface [21]. In Table 5.1 we

tabulate the numerical parameters examined for each method to demonstrate the efficiency of the two solvers. The numerical parameters of the RCLS method are further discussed in Section 3.3 and those of the *interPore* solver have been introduced in the introductory section of this chapter.

Table 5.1: Table of varied numerical parameters for the static droplet simulation.

	RCLSFoam			***interPore***			***interFoam***
Case 1	WENO3	$N_S = 5$	$\varepsilon = 0.5\overline{\Delta x}$	$C_{\text{comp}} = 0$	$C_{\text{sh}} = 0.1$	$U_f = 0.1$	$C_{\text{comp}} = 1$
Case 2	WENO3	$N_S = 5$	$\varepsilon = 1.0\overline{\Delta x}$	$C_{\text{comp}} = 0$	$C_{\text{sh}} = 0.5$	$U_f = 0.1$	$C_{\text{comp}} = 2$
Case 3	WENO3	$N_S = 5$	$\varepsilon = 2.0\overline{\Delta x}$	$C_{\text{comp}} = 1$	$C_{\text{sh}} = 0.1$	$U_f = 0.5$	

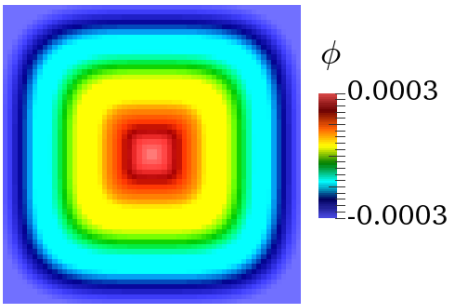

Analytical solution to the initialisation of the signed distance function ϕ – three-dimensional superquadric.

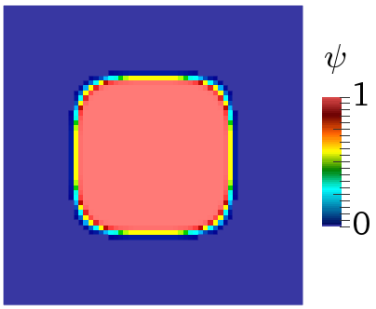

Initialisation of the conservative level set field ψ.

Fig. 5.2: The function used to initialise ϕ is the implicit equation for a three-dimensional superquadric. The initial ψ field of the RCLS method is derived by re-initialising it to steady state.

Different methods are used for the liquid volume fraction initialisation for each solver. At $t = 0$, the liquid volume fraction α in *interPore* is initialised by setting $\alpha = 0$ in the cells containing water and $\alpha = 1$ in the cells containing oil, forming an initially cubic-shaped drop. In the RCLS method, the initialisation is not so straightforward. At $t = 0$, the signed distance function from the interface ϕ is calculated analytically. The function used to initialise ϕ is the implicit equation for a three-dimensional superquadric:

$$|x|^r + |y|^r + |z|^r = R^4. \tag{5.1}$$

In the limit of large r a cube is recovered. With this initialisation method, the phase interface is smeared over approximately 4 cells and remains constant during the simulation. The initial

conservative level set field ψ of the RCLS method is then easily derived by applying Eq. 3.11. This allows ψ to vary from 0 (oil) to 1 (water) smoothly, with no interface corner discontinuity at initialisation. Indeed, as pointed out by Amat & Ruiz [5], when the smoothness indicators of the WENO interpolation (see Section 3.4) work very well for jump discontinuities – as WENO schemes were originally designed in the context of conservation laws in order to deal with problems that contain shocks – they do not provide an appropriate performance for corner discontinuities.

5.1.2 Accuracy of the velocity field

The maximum velocity in the domain resulting from spurious currents was recorded for both solvers is shown over a simulation time of 0.01s in Fig. 5.3. Then the performance of both numerical capabilities were compared to the standard *interFoam* solver. Spurious currents are expected to be limited by the transient inertia term during the initial relaxation phase.

During the relaxation period, the maximum velocity magnitude observed with *interFoam* (Fig. 5.3, *red lines*) remains fairly small. As the relaxation process progresses, the compression term in the advection equation alone is not capable of restricting interface diffusion and the interface thickens. This has a stabilising effect in terms of spurious currents. In return, as we shall discuss later in Section 5.1.3, this creates a large error in the prediction of capillary pressure.

The *interPore* solver (Fig. 5.3, *blue lines*) provides the lowest spurious currents, almost two orders of magnitude difference. By contrast, for *RCLSFoam* (Fig. 5.3, *black lines*) the spurious currents are comparable with those of *interFoam*. It is worth mentioning that the maximum velocity magnitude recorded by *RCLSFoam* is sensitive to the value of the interface thickness parameter ε. For higher values of ε, hence for a more diffused interface, spurious velocities are reduced with minimal overshoots during the relaxation. On the other hand, *interPore* is found to reduce the maximum velocity down to minimal values, regardless of the controlling numerical parameters. This is because, by design in *interPore*, the interface capillary forces are filtered for the spurious currents to remain weak, even with sharp interfaces. This feature of the method is essential for the simulation of multiphase flows at low capillary numbers. However, this reduction happens over a longer period of time. Indeed, the results demonstrate that the RCLS method more quickly diminishes the spurious currents compared to *interPore*.

We now turn our focus to the analysis of interface thickness, capillary pressure and the instantaneous velocity field. The results for *RCLSFoam* and *interPore* are compared in

Fig. 5.4 and Fig. 5.5. For *RCLSFoam*, the value of ε shows a direct impact on the interface thickness (Fig. 5.4, *left column*), as expected. This affects the pressure and the velocity of the surrounding field. In Case 3 with $\varepsilon = 2.0\overline{\Delta x}$ (Fig. 5.4, *bottom row*), the spurious currents become very low with in counterpart an increase in interface diffusion. From Fig. 5.5 one can see that the magnitude of the spurious currents is also sensitive to the interface thickness in *interPore* (see Case 1 and 3 in Fig. 5.5, *top row* and *bottom row*). Both solvers show an order of magnitude difference between their sharpest interface run and their most diffused interface run (see also Fig. 5.3).

The influence of the sharp interface-tracking methodologies used in both solvers is shown in Fig. 5.6b, where the indicator function (α for *interPore* and ψ for *RCLSFoam*) is plotted across the x-axis of the droplet, after relaxation. When a low value of ε is used for the RCLS method, the results confirm the findings discussed around Fig. 5.3. For an increase in interface sharpness, the spurious currents are increased. With the *interPore* solver (Fig. 5.5), the magnitude of the spurious currents is reduced by two orders of magnitude compared to the standard *interFoam* solver when less sharpening is applied (Case 1). Moreover, the magnitude of the spurious currents consistently decreases when increasing the filtering threshold value (U_f) as shown in Fig. 5.3 (Case 3).

It is interesting to note that the spurious currents tend to form distinctive patterns that are similar for both numerical capabilities, as shown in the third column of Fig. 5.4 and Fig. 5.5. The patterns tend to emphasise the coordinate axes where the alignment between the mesh and the interface is at its best, and also the diagonals where the alignment is at its worst. Weak spurious vortices are formed in between these principal directions.

5.1.3 Accuracy of the pressure jump across the droplet

Once equilibrium has been reached, the now spherical oil droplet should sit in a quiescent water fluid, where all fluid velocities should tend to zero. In this instance, the curvature everywhere on the interface surrounding the droplet should be uniform and the interface normal should be directed everywhere in the radial direction. The pressure should be uniform both inside and outside the droplet but undergo a step change across the interface. In sum, as the oil droplet statics is concerned with the balance of forces which stabilises its positioning at the centre of the computational domain, the surface tension force should be balanced precisely by the pressure gradient and the pressure jump should be equivalent to the theoretical Laplace pressure of a droplet of that given diameter, as defined in Section 5.1.1.

The pressure distributions across the centre of the droplet are shown in Fig. 5.6a. The numerical results differ from the exact physical force balance. This is because small numerical errors occur when calculating the interface normal. This results in the interface normal vector not being precisely aligned with the radial direction. The interface curvature will therefore vary slightly from its exact physical value, and the droplet density will also vary due to the variations in the interface location (CSF model). Finally, the interface volume force will include a non-physical rotational component. The surface tension forces, which cannot reach a force balance with this irrotational pressure gradient, end up instead balancing the inertia forces. These transient inertial effects associated with non-zero velocities give rise to spurious currents and cause errors in the calculated pressure field. Fig. 5.6a shows the numerically predicted pressure difference between the relaxed spherical droplet and the ambient liquid along the droplet diameter axis for each of the 6 cases, in comparison with the theoretical value predicted from the Laplace equation [233]. The pressure calculation illustrates that both methods produce a pressure consistent with the Laplace jump prediction.

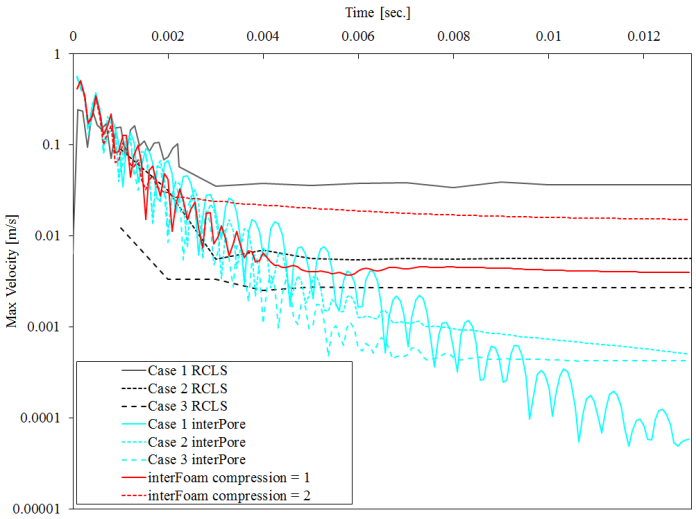

Fig. 5.3: Comparison between the numerical predictions for spurious currents by the standard *interFoam* solver, the modified VoF solver (*interPore*) and the Conservative Level-Set solver (*RCLSFoam*).

The results show that *interPore* (Fig. 5.6a, *blue lines*) seems to provide a consistent prediction of the theoretical pressure difference regardless of interface thickness. However, *RCLSFoam* (Fig. 5.6a, *black lines*), for low ε values (Case 1 and 2), achieves a pressure jump almost identical to the theoretical one (Fig. 5.6a, *red line*). However, it fails to predict the correct pressure jump for Case 3 due to the higher interface diffusion, which leads to an amplified imbalance of the surface tension forces with the pressure forces.

Another measure of the relative error between the theoretical and computed pressure drop is conferred in terms of the error in the predicted pressure, Error(P), defined as follows:

$$\text{Error(P)} = \frac{\text{P} - \text{P}_{\text{theoretical}}}{\text{P}_{\text{theoretical}}} \tag{5.2}$$

The results from Eq. 5.2 are tabulated in Table 5.2. The calculated pressures converge to the theoretical solution subject to interface sharpness. When the interface curvature is obtained from a sharper indicator function as in Case 1 and 2 with *RCLSFoam*, it is clear that we can achieve a very low error, less than 1.5%. Comparison of the error norms indicate that the RCLS method is in good agreement – within $\sim$1.5% – with the analytical pressure, while *interPore* predicts a relatively constant, but higher, error in the calculated pressure jump across all three cases. This is due to the precise calculation of curvature and liquid volume fraction gradient at the interface (as showcased in Section 3.5). By contrast, the standard *interFoam* solver cannot achieve the desired theoretical pressure jump, and the average error goes up to 12%. The method's inability to capture such a precise estimation of the interface orientation manifests itself in the resulting pressure distribution.

Table 5.2: Errors in the predicted pressure

	RCLSFoam	***interPore***	***interFoam***
Case 1	Error(P) = 0.01499	Error(P) = 0.03868	Error(P) = 0.109605263
Case 2	Error(P) = 0.00921	Error(P) = 0.03556	Error(P) = 0.131954887
Case 3	Error(P) = 0.05359	Error(P) = 0.04311	

It is clear that both solvers accurately reproduce the dynamics of a static cubic droplet relaxing in a quiescent environment, provided the numerical parameters of each method are carefully chosen. The *interPore* solver, designed for applications with very low capillary numbers, offers good predictions of the physical solution with very low spurious currents. On the other hand, *RCLSFoam*, despite being designed for high inertia applications, offers better agreement with theoretical values for the pressure jump across the droplet at the end of the relaxation period. The magnitude of spurious currents is however higher. An additional small and expected disadvantage that both solvers exhibit is a sensitivity to the numerical control parameters and in particular, the diffusivity of the interface. A sharply resolved interface instils an enhancement in the magnitude of the spurious currents. This enhancement however does not affect the physical representation of the two-phase flow simulation. We observe no off-centre displacement of the droplet, nor distortion of the droplet's interface, two

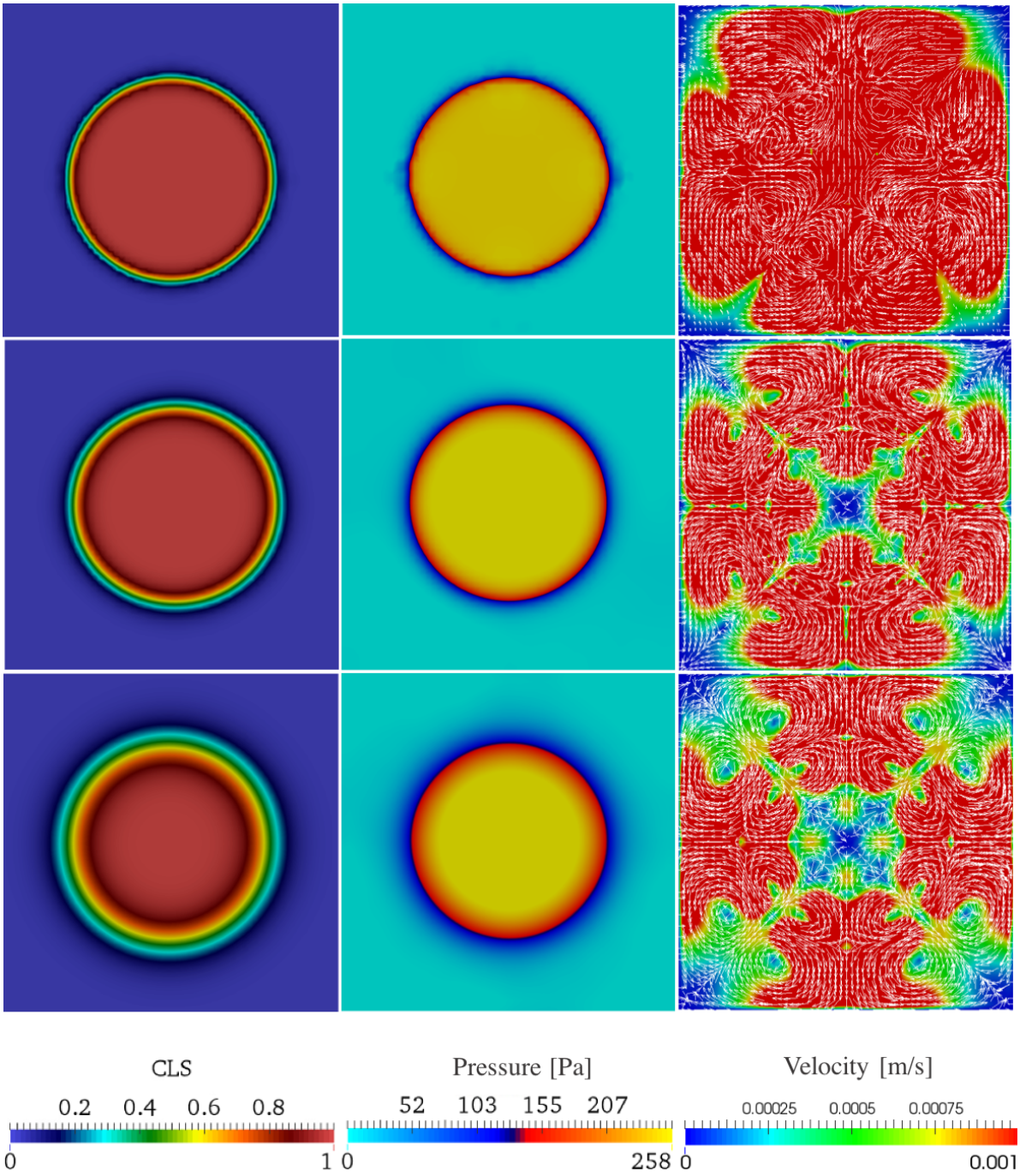

Fig. 5.4: Results predicted by *RCLSFoam* for the static droplet at $t = 0.013$s. Top to bottom: Case 1, Case 2, Case 3. From left to right: indicator function, pressure field and velocity vector field.

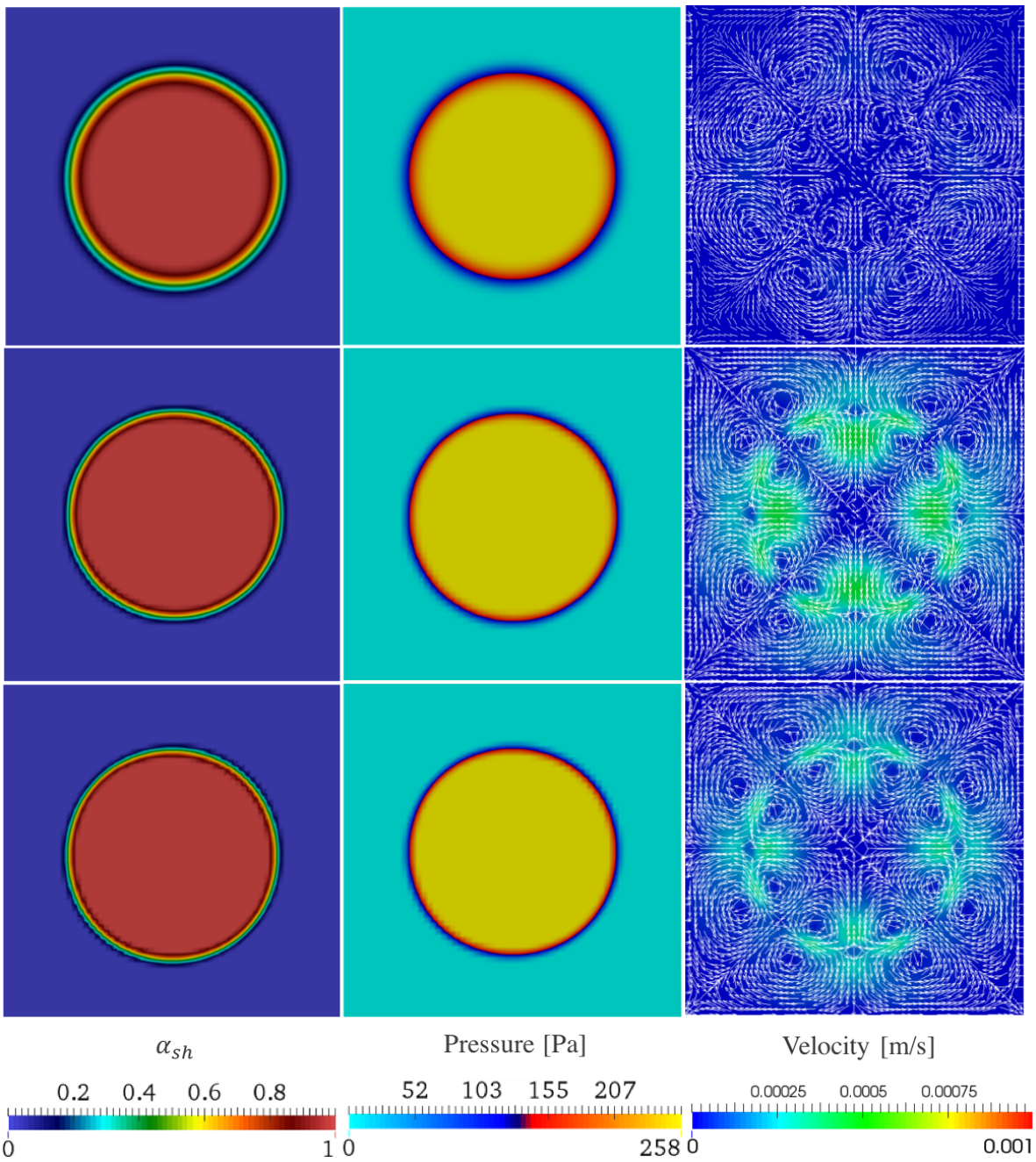

Fig. 5.5: Results predicted by *interPore* for the static droplet at $t = 0.013$s. Top to bottom: Case 1, Case 2, Case 3. From left to right: indicator function, pressure field and velocity vector field.

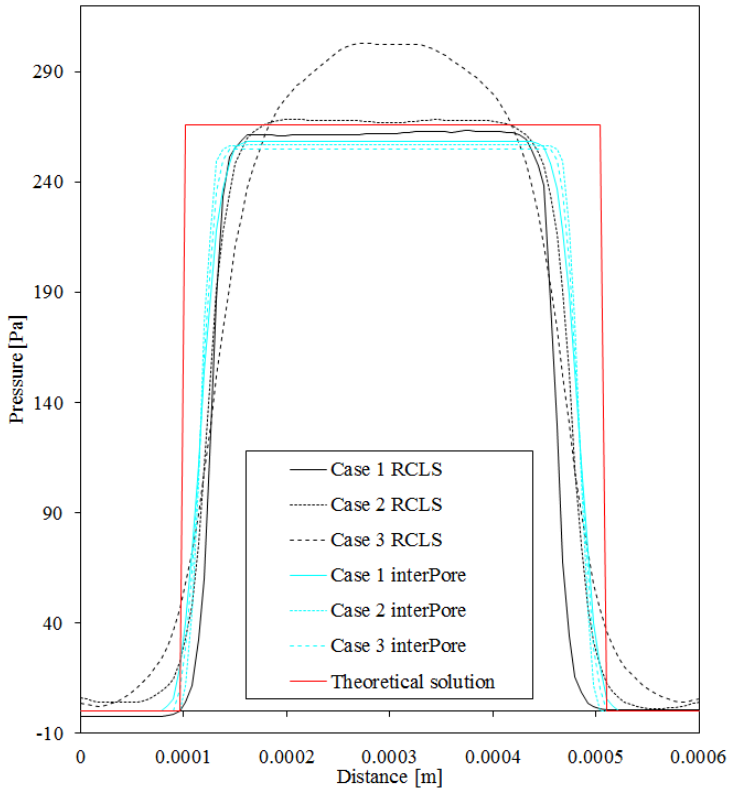

(a) Laplace pressure jump across the droplet interface

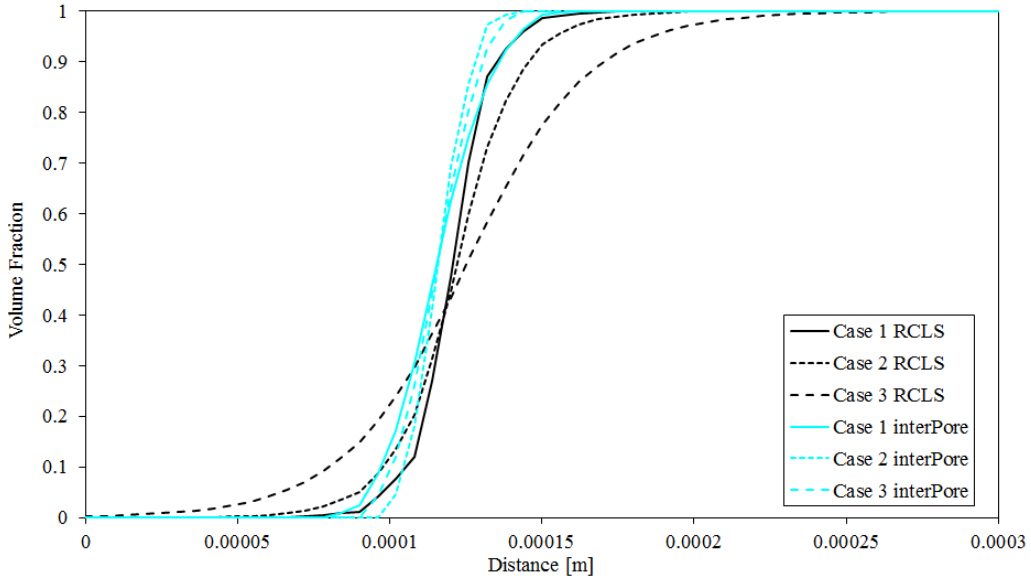

(b) Indicator function profile across the droplet interface

Fig. 5.6: Comparison between the numerical predictions of both solvers showing **(a)** the Laplace pressure jump across the droplet interface, and **(b)** the liquid volume fraction profile.

peculiarities of this challenging system with inadequate numerical capabilities. Neither the magnitude of the spurious currents nor our inability to capture the sub-grid curvature prevent our methods from modelling accurately the present physical phenomenon.

5.1.4 A discussion on nonlinear oscillations

Here a mesh convergence study has been conducted on the droplet relaxation case with the RCLS method on a grid of $100 \times 100 \times 100$ elements with $\Delta x = \Delta y = \Delta z = 6\mu$m. The method is found to produce mesh independent solutions at the mesh element sizes used for the results shown below (Fig. 5.7 and Fig. 5.8).

Large unsupported liquid drops in zero gravity will tend to form spherical drops to minimise their surface energy, as introduced in Section 5.1. The relaxation of an initially square drop is a response to unbalanced surface tension forces, the initial numerical setup of the volume fraction produces a non-physical interface distribution that the surface tension forces work to redistribute. Very strong surface tension forces at the high-curvature corners set the drop into deformation, capillary waves are induced that causes the drop surface to oscillate about its equilibrium shape. The physical nonlinear capillary oscillations of the interface of the relaxing static droplet are well captured. During the time sequence presented in Fig. 5.9, the oscillations of the surface of the drop are apparent. The problem of oscillating fluids was first considered by Kelvin [109] and Rayleigh [166] who calculated the linearised solution for small “vibrations of a globule”. Lamb [119] later treated the more general case of two fluids, in which one of them is enclosed by the other one. In his linear analysis, he identified the eigen-modes of the system to be spherical harmonics characterised by mode numbers. Lamb [119] then derived the natural frequencies of these eigen-modes, related to the equilibrium radius of the drop under consideration. Overall, the drop motion is found to be dominated by spherical harmonic perturbations of typical fourth-mode shapes (hexadecapole mode), as visible in Fig. 5.9. According to Brackbill et al. [21], small displacements of the phase boundary cause discontinuous changes in the location and orientation of the interface. These occur in phase with the oscillations of the interface and provide a small impulse through the surface tension to sustain the oscillations. Physical dissipative effects, in addition to presumably some numerical dissipation, eventually damp the oscillations causing the drop to approach an equilibrium spherical shape.

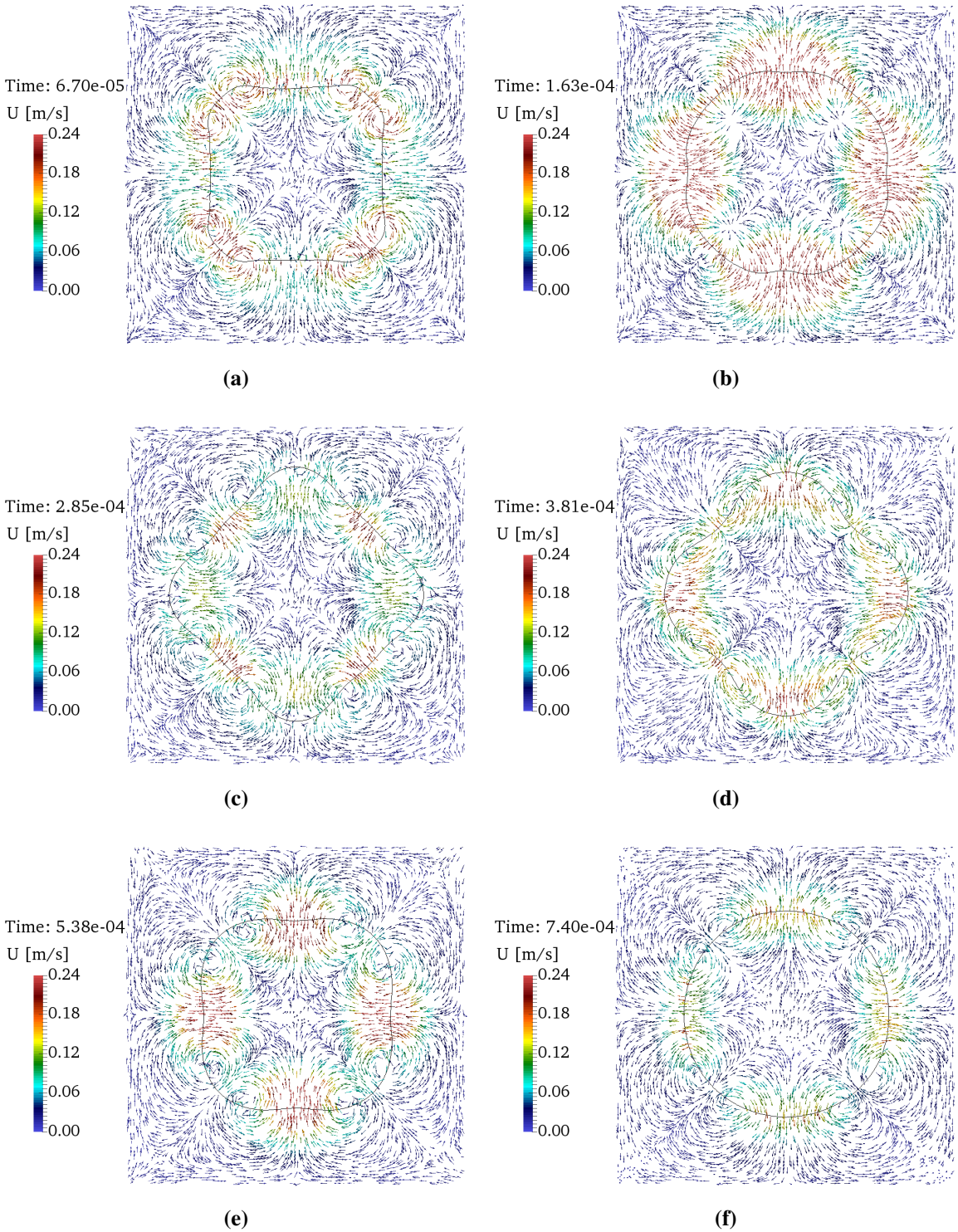

Fig. 5.7: Stationary deformation of a cube into a spherical droplet in equilibrium. Slice through the computational domain showing the velocity vector field. Initial cube size of 600μm discretised uniformly with 1 million mesh elements.

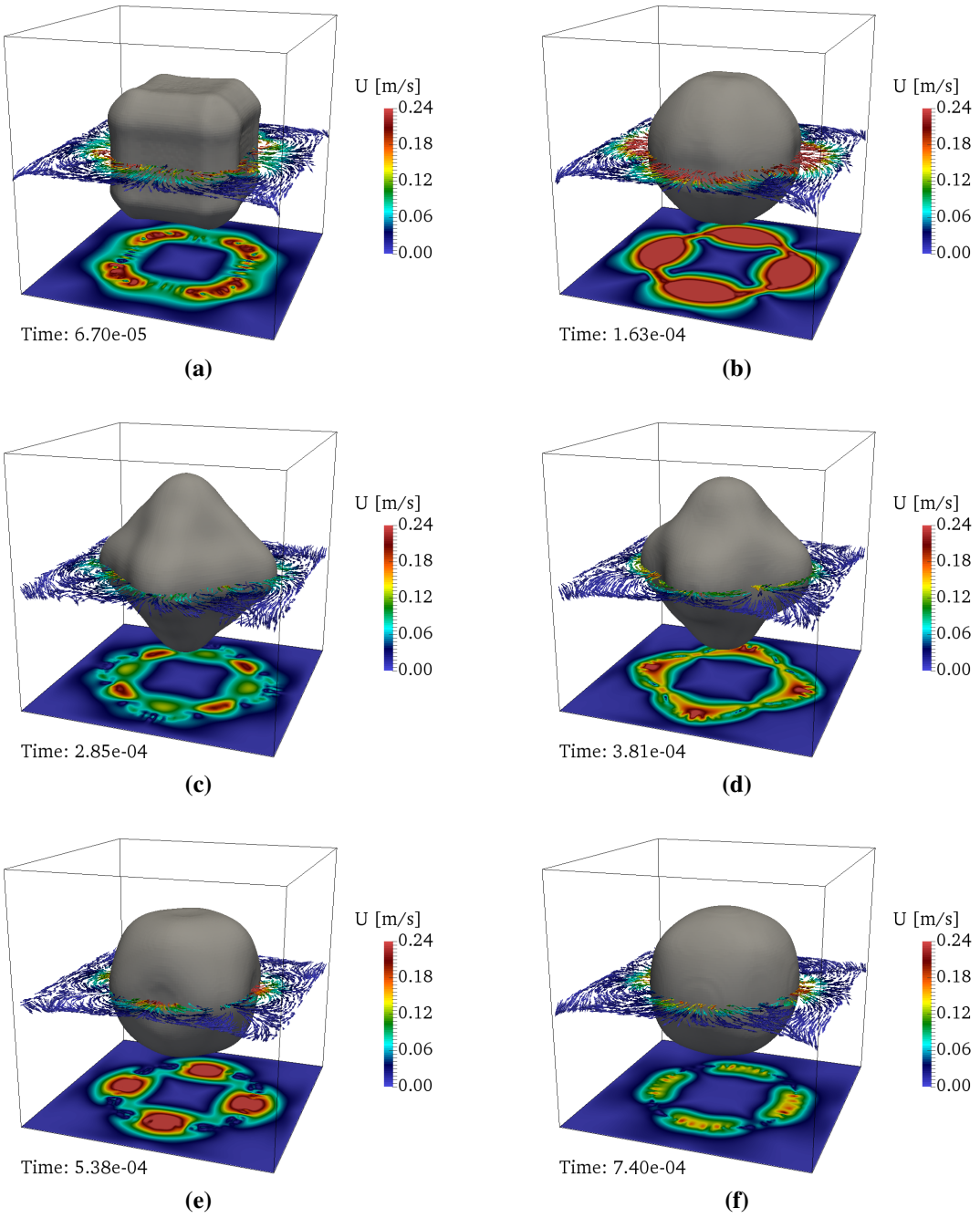

Fig. 5.8: Stationary deformation of a cube into a spherical droplet in equilibrium. Interface contour $\psi = 0.5$ (in grey) and velocity vector field.

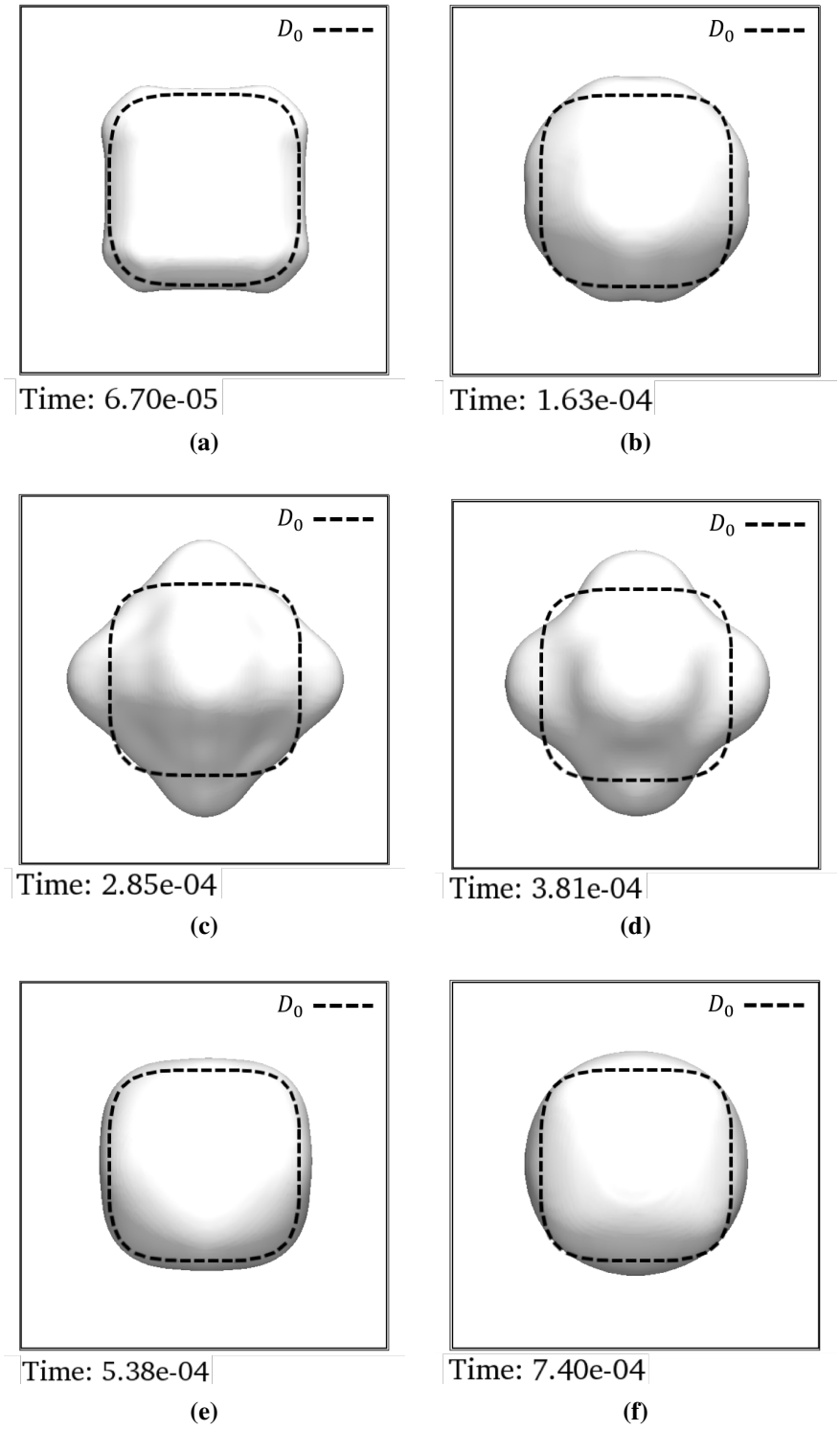

Fig. 5.9: Nonlinear oscillations or capillary waves on the surface of an initially-square oil drop.

5.2 Rayleigh–Taylor instability with surface tension

The second test configuration consists of a Rayleigh–Taylor problem with homogeneous layers of a high-density fluid penetrating into a low-density fluid under the influence of gravity alone, as shown experimentally in Fig. 5.10. The Rayleigh–Taylor instability (RTI) is of great fundamental interest in physics and fluid mechanics. For example, in spray atomisation, it partly drives the breakup of liquids due to aerodynamic forces on the phase interface (see Chapter 2, Section 2.1.1.2). In geological flows, it can represent situations where water is suspended above oil.

A hydrodynamically-unstable interface is formed between the stratified laminar immiscible fluid layers, initially at rest. Infinitesimally small perturbations of the interface will grow with time due to the continuous generation of vorticity that leads to a pattern of bubbles of light fluid penetrating the heavy fluid (upwards), and spikes of heavy fluid penetrating the light fluid (downwards). This process may lead to the formation of a turbulent mixing layer. The RTI was initially investigated by Lord Rayleigh in 1883 [164] and later theoretically studied by Taylor [210]. An overview of the subject has been given by Sharp [192].

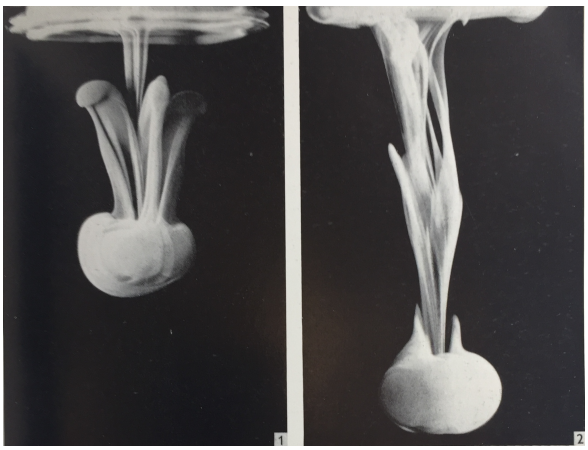

Fig. 5.10: Photographs of two stages of the Rayleigh–Taylor instability. Taken from Van Dyke [222].

The numerical demonstration of the RTI is a common test case when examining the numerical convergence and the capability of a solver to capture the interface physics in the presence of high density ratio and surface tension. In the following sections the capability of the VoF method as implemented in the *interPore* solver is evaluated along with the conservative LS method as implemented in the RCLS solver, for the modelling of a single 2-D “finger”, “spike” or “stem”, of the RTI with surface tension.

5.2.1 Numerical set-up

The two adjacent fluids are initially quiescent but the sharp horizontal density mismatch induces a density gradient (upwards) opposite to the pressure field and gravitational field (downwards). The acceleration due to gravity is set as $g = (0, -9.8\text{m/s}^2, 0)$. The interface is hydrodynamically accelerated by the pressure gradient [192]. The gravitational forces act to destabilise the interface, while the surface tension forces act to stabilise it. The two isothermal fluids are at ambient temperature and pressure. The viscosities are assumed equal, so that there is no jump in viscosity at the interface and thus no jump in the velocity gradient, as viscosity controls the shear stress. The physical parameters for the fluids are $\rho_{\text{light}} = 0.1694\text{kg/m}^3$, $\mu_{\text{light}} = 3.13 \times 10^{-3}\text{kg/m.s}$ and $\rho_{\text{heavy}} = 1.255\text{kg/m}^3$, $\mu_{\text{heavy}} = 3.13 \times 10^{-3}\text{kg/m.s}$ (density ratio of 7.4), with a constant surface tension of $\sigma = 0.01\text{N/m}$. The present set of simulations for comparison and validation are based on the numerical settings for RTI given in Popinet & Zaleski [157] and Puckett et al. [161] on a comparatively coarse mesh of 64×224 hexahedral elements. The two-dimensional domain is $[-0.5, -2] \times [0.5, 2]$ m. An initial surface perturbation is applied with a wave number of 2π and wavelength of 1 m. The initial disturbance in the free surface is given by the expression:

$$y = -0.05\cos(2\pi x). \tag{5.3}$$

The numerical resolution of the initial perturbation is thus $\lambda/\overline{\Delta x} = 60$. The resulting initial computational domain is shown in Fig. 5.11. For the liquid volume fraction, a homogeneous Neumann boundary condition was set at the bottom boundary of the domain and symmetry conditions were set at both sides. The same boundary conditions were set for the pressure field. Finally, the boundary conditions for the velocity were set as no-slip walls for the top and bottom boundaries and symmetry planes at both sides. The chosen set of simulation parameters for both solvers is summarised in Table 5.3.

Table 5.3: Table of numerical parameters for the Raleigh–Taylor simulation for two different mesh sizes.

RCLS			***interPore***			60×224	128×512
WENO3	$N_S = 5$	$\varepsilon = 0.5\overline{\Delta x}$	$C_{\text{comp}} = 0$	$C_{\text{sh}} = 0.1$	$U_f = 0.1$	Case 1	Case 4
WENO3	$N_S = 5$	$\varepsilon = 1.0\overline{\Delta x}$	$C_{\text{comp}} = 0$	$C_{\text{sh}} = 0.5$	$U_f = 0.1$	Case 2	Case 5
WENO3	$N_S = 5$	$\varepsilon = 2.0\overline{\Delta x}$	$C_{\text{comp}} = 1$	$C_{\text{sh}} = 0.1$	$U_f = 0.5$	Case 3	Case 6

5.2.2 Qualitative Description

Fig. 5.13 and Fig. 5.14 show the interfacial history obtained by the two solvers on the same rectangular mesh of 60×224 cells, for eight different times in the interval $[0; 1.3]$ seconds. The complex phenomenology associated with the evolution of a RT unstable interface is reproduced reasonably well here by both solvers and compares very well with reference numerical solutions by Popinet & Zaleski [157] and Puckett et al. [161]. The light fluid moves into the heavy fluid in the form of rising round bubbles on either side of the domain, while the heavy fluid sinks into the light fluid under gravity, between the bubbles, building up a central falling spike (Fig. 5.13, $t = 0.55$s). The heavy fluid entering the spike region from the troughs of the initial instability feeds the RTI.

A mushroom-shaped structure develops at $t = 0.7$s. Then, the mushroom is stretched and filaments start to detach, forming isolated liquid structures (at $t = 0.95$s). Towards $t = 1.3$s, a settling process begins in which the denser fluid falls back down as droplets. Finally, the less dense fluid blobs trapped in the bottom layer escape by buoyancy as bubbles (see Fig. 5.12). The two numerical methods appear to provide the same interface topology for most of the simulation. Yet, differences are noticeable in terms of interface thickness, penetration rate and secondary structure formation (filaments, droplets, etc.). We shall discuss the later in the following sections.

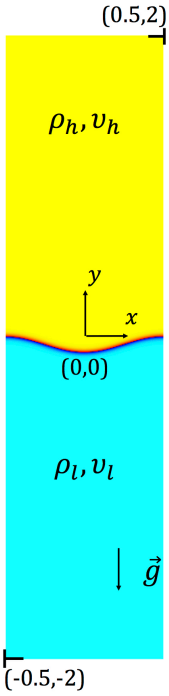

Fig. 5.11: Computation domain for the simulation of the RTI.

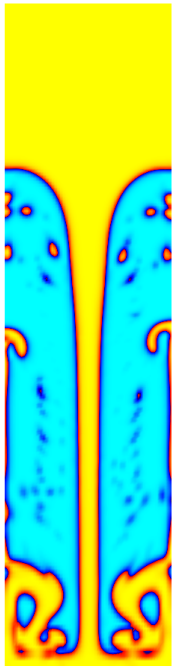

Fig. 5.12: Volume fractions predicted by *RCLSFoam* at $t = 1.65$s.

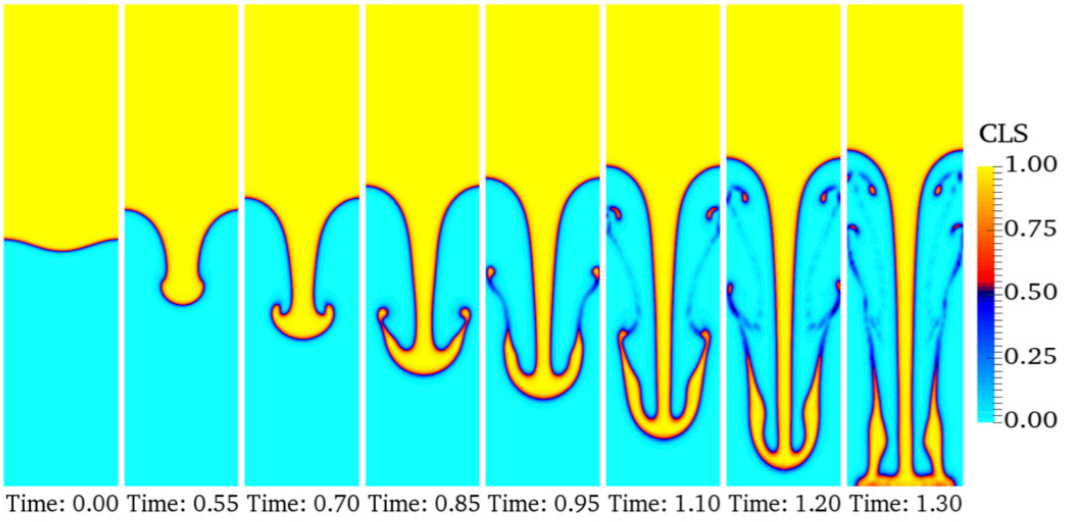

(i) Case 1

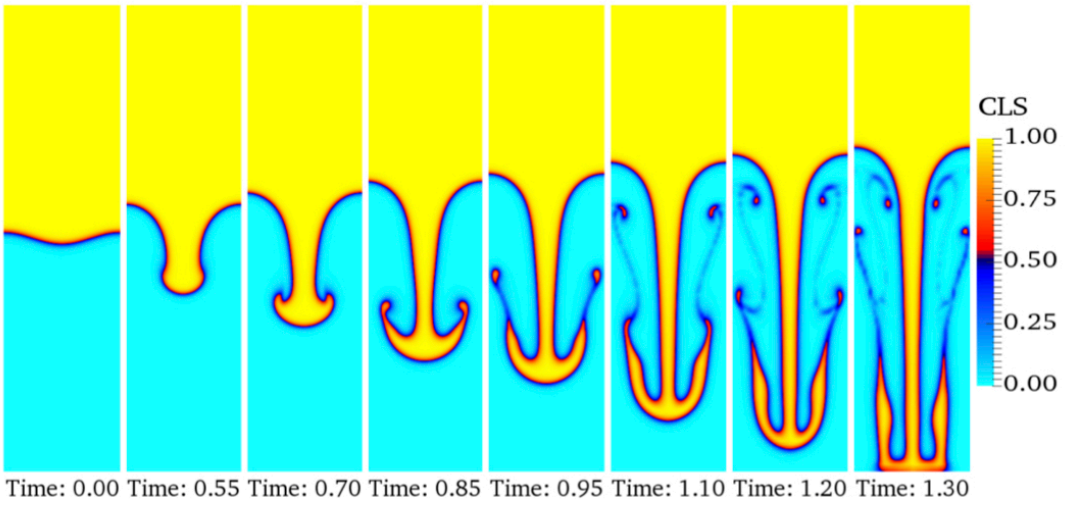

(ii) Case 2

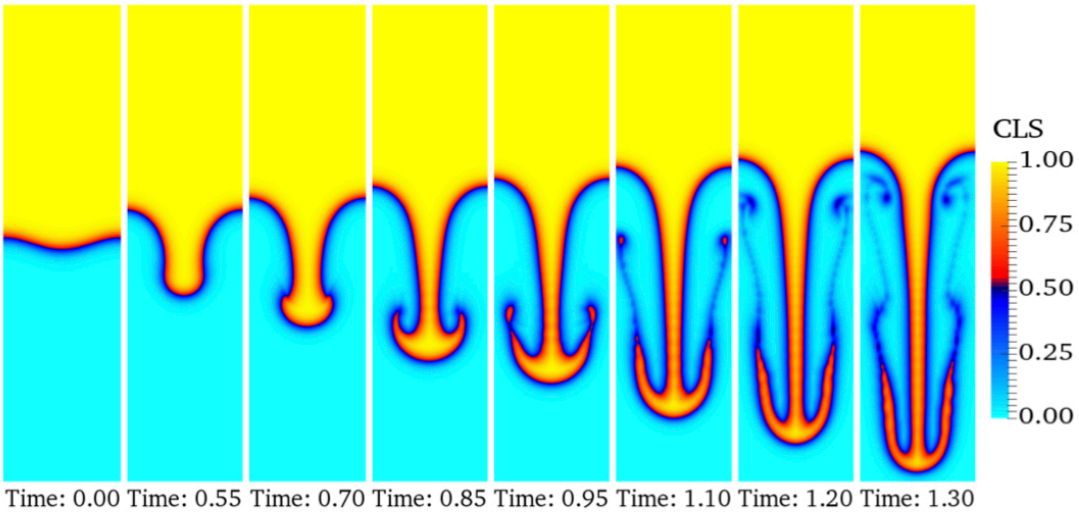

(iii) Case 3

Fig. 5.13: Volume fractions predicted by *RCLSFoam* for the Rayleigh–Taylor instability with 60×224 mesh elements.

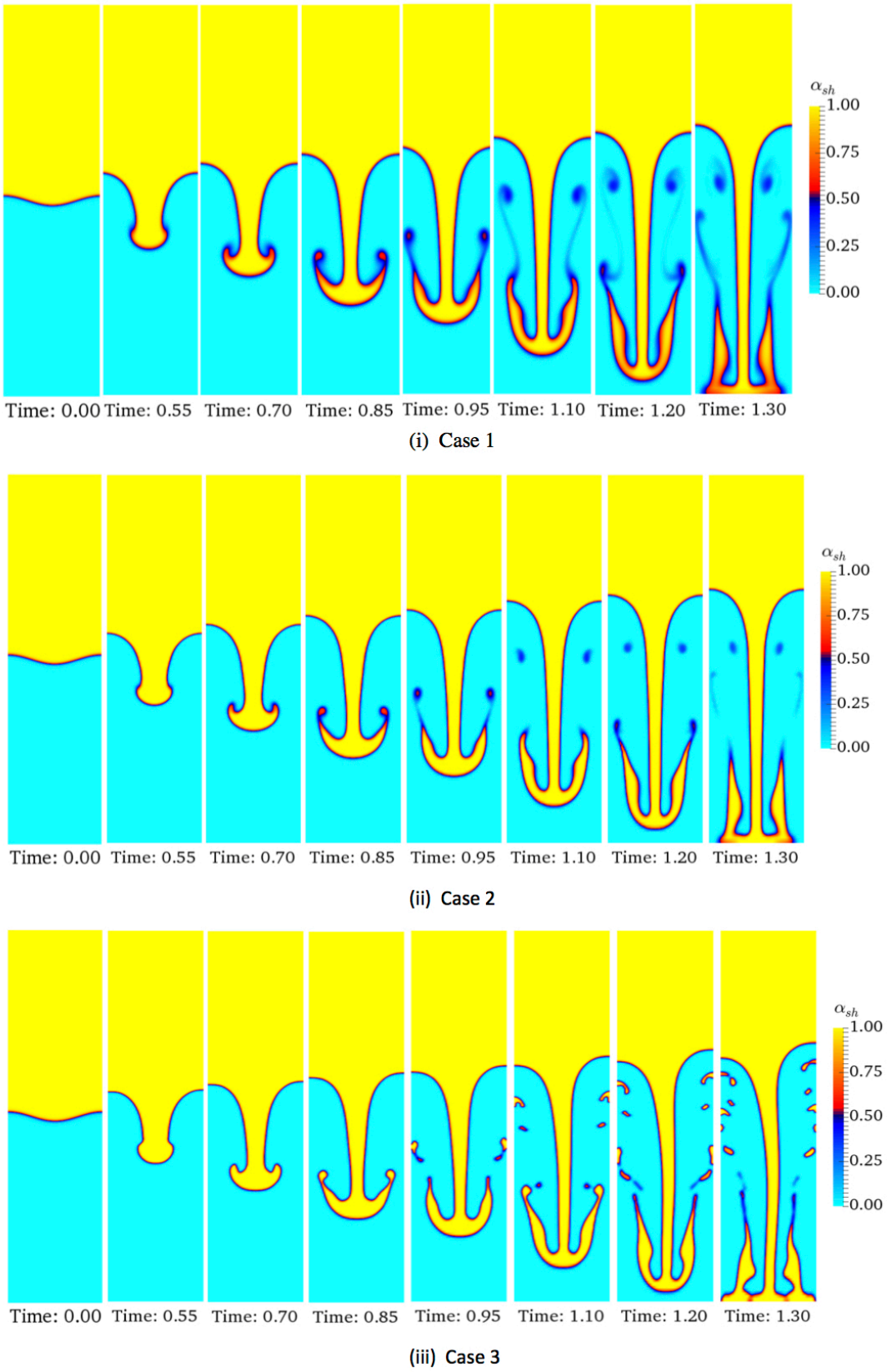

Fig. 5.14: Volume fractions predicted by *interPore* for the Rayleigh–Taylor instability with 60×224 mesh elements.

5.2.2.1 Interface capture and sharpness

The sharpness of the phase boundary between the two fluids is an indication of the numerical diffusion of the scheme used. Also, the amount of individual resolved fine-scale structures is sensitive to how well the algorithm preserves the sharpness of the interface, as will be discussed in Section 5.2.2.5. From Fig. 5.13 and Fig. 5.14, both numerical methods are able to maintain a sharply resolved interface and capture thin liquid structures. Overall the comparison of the interface predicted by the two solvers for the first four times ($t = 0.55, 0.70, 0.85, 0.95$ seconds) demonstrates the similar performance of both simulation methods.

With *interPore*, a higher interface sharpening with no numerical compression (Fig. 5.14 (ii)) is able to capture a sharper interfacial jump than with no sharpening. When numerical compression is added (Fig. 5.14 (iii)) the interface is even sharper. With the RCLS method, as the interface thickens (ε is increased from $0.5\overline{\Delta x}$ to $2\overline{\Delta x}$), the interface becomes smeared and we suffer a loss of sharp numerical resolution of very small secondary liquid structures (compare Case 1 to Case 3 in Fig. 5.13). The re-initialisation procedure integrated into *RCLSFoam* (see Section 3.6) helps in capturing correctly the formation of droplets. The RCLS method on the other hand seems to be better able to treat the small-scale inclusions of one phase into the other regardless of the ε parameter. For times beyond $t = 0.95$s, i.e. at $t = 1.10$s, $t = 1.20$s, and $t = 1.30$s, small differences in the solution can be perceived between the two methods. With the *interPore* solver the interface sharpening algorithm with no compression is able to capture droplets up to a time of 0.95s. After that, filaments continue to detach from the mushroom but fragment into liquid structures that are not trackable, and get diffused numerically (Case 1 and Case 2 in Fig. 5.14). Fig. 5.15 emphasises the values of $\nabla\psi$ that are local to the fluid interface and thus the importance of a sharply defined $\nabla\psi$ in the locus of the interface to localise the surface tension forces as per Eq. 3.6.

5.2.2.2 Stem symmetry and numerical convection

The symmetry of the flow structure is well captured with *RCLSFoam*. With *interPore* however, the interface obtained for the central stem is slightly asymmetrical when using numerical compression (Case 3 in Fig. 5.14). This may be due to the compression scheme in OpenFoam [231]. As a result, *interPore* does not fully recover the physical solution published in the literature [157, 161] after a time $t = 0.95$s. On the other hand, the non-physical wiggles usually seen with VoF solvers [76] in the neck of the stem close to the mushroom-shaped structure have disappeared for all *interPore* runs with compression factors $C_{\text{comp}} = 0$ and

with $C_{\text{comp}} = 1$ (Fig. 5.14). These non-physical wiggles formed by the penetration of the denser phase into the lighter phase are believed to be due to the compression flux added in the VoF formulation of *interFoam* to maintain a sharp interface, as discussed in Pringuey [158].

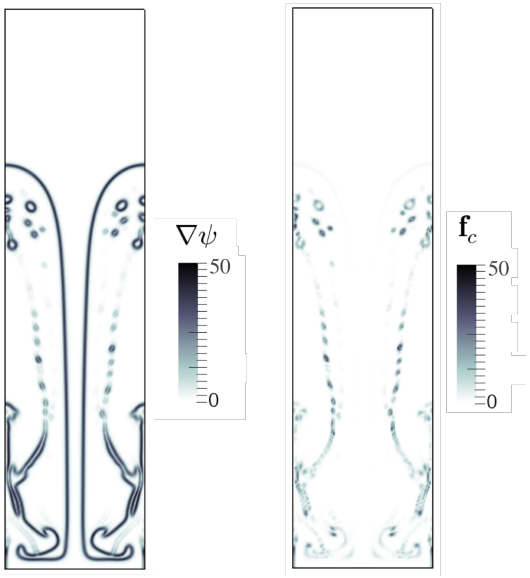

Fig. 5.15: Locus of the gradient of the CLS field (*left*) and of the interfacial capillary forces (*right*), at $t = 1.45$s.

5.2.2.3 Rate of penetration of the heavy phase into the light phase

The dense phase penetrates into the light phase at a rate that is in accordance with the simulations of Popinet & Zaleski [157]. As ε is increased from $0.5\overline{\Delta x}$ to $2\overline{\Delta x}$ in the RCLS formulation, the start of the instability is marginally delayed at $t = 0.70$s. As a result, the rate of penetration of the spike is reduced overall. For Case 3, at $t = 1.3$s, the mushroom tip does not yet touch the bottom wall (Fig. 5.13 (iii)). On the other hand, the penetration rate does not seem to be altered when varying the numerical parameters of *interPore*.

5.2.2.4 Mushroom-shaped structure development

Fig. 5.16 (i) shows the interface contour along with the corresponding velocity field (Fig. 5.16 (ii)) at a number of discrete time intervals. The RTI spike has a positive velocity downwards, consistent with the direction of acceleration it experiences from the pressure gradient. There is a stagnation point on the lower tip of the spike (zero velocity field (*black*) in Fig. 5.16).

There is evidence of interfacial shearing instabilities associated with the formation of a mushroom-shaped structure (Fig. 5.16 (iii)). It is believed that the Kelvin–Helmholtz instability is the reason for the development of the mushroom cap at the tip of the spike [192]. The development of this structure is arising mainly due to the velocity shear between the two fluid layers. Counter-rotating vortices are always observed at the roll-up sites. Once the mushroom cap has formed, and is being accelerated downwards, the effect of drag forces on the spike is increased. Upstream of the mushroom cap, there is a low velocity region, consistent with a high-pressure region. According to the dynamic behaviours observed in their recent numerical study, Liu et al. [133] noted that the pressure is maximum at the root of the spike in the region around the interface; and that below that maximum pressure location, the motion of the spike is dynamically de-coupled from the motion of the rest of the fluid bulk. The highest velocities are located on either side of the mushroom cap, extending along and at the tip of the ejected fluid ligaments. The light fluid is thus accelerated faster upwards than the spike downwards. This is clearly visible in Fig. 5.16a (iii) where the two ligaments tip exhibit a strong upward velocity right before droplet separation.

As ε is increased from $0.5\overline{\Delta x}$ to $2\overline{\Delta x}$ in the RCLS numerical formulation, the mushroom cap opens less (Fig. 5.16a). With the modified VoF method *interPore*, a change in the sharpening coefficient does not seem to alter the openness of the mushroom cap, but adding numerical compression does widen it (Fig. 5.16b (iii)). At $t = 0.70$s, the roll-up of the edges of the mushroom cap under the shearing instability is predicted similarly by both solvers (Fig. 5.16 (iii)). At $t = 0.85$s however, droplets have already detached from the two ligaments in the *interPore* solution (Fig. 5.16b (i)), causing a noticeable difference in the development of the shearing instability compared to the RCLS formulation.

5.2.2.5 Ligament breakup into droplets

The works of Popinet & Zaleski [157] and Puckett et al. [161] suggested that the correct capture of the thin ligaments has a strong influence on the overall simulation results in terms of penetration of the dense phase and opening of the mushroom cap. For all the runs with the RCLS method, at $t = 0.95$s, the filaments elongated on either side of the mushroom have not yet fragmented into droplets, in accordance with Popinet & Zaleski [157]. This is true also for Case 1 and Case 3 simulated with *interPore* (Fig. 5.14 (i and iii)). However, in *interPore* Case 2, at $t = 0.95$s, the two droplets have already detached from the end of the filaments (see Fig. 5.14 (i)). This is most probably due to the extra sharpening algorithm employed with this solver in Case 2.

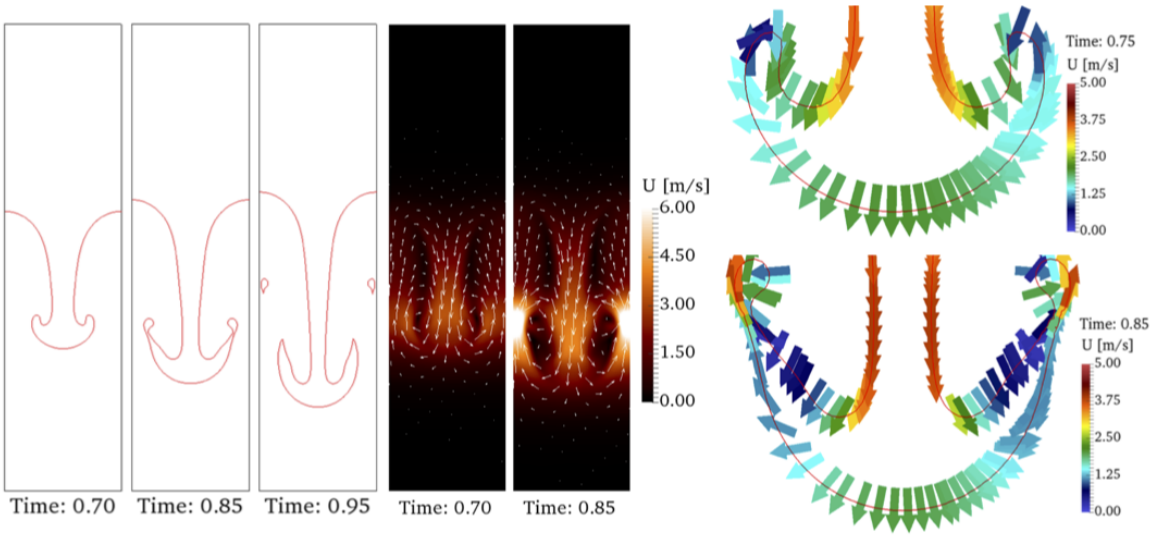

(a) *RCLSFoam*, Case 1

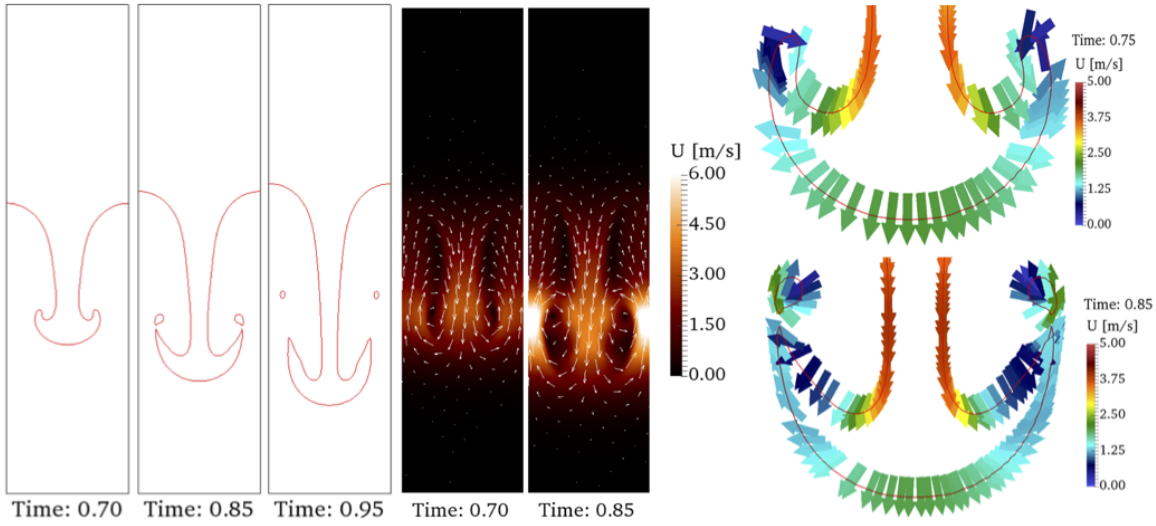

(b) *interPore*, Case 2

Fig. 5.16: Interface (0.5 iso-contour of both indicator functions) predicted by both solvers for the Rayleigh–Taylor instability with 60×224 mesh elements, velocity field and velocity vectors overlaying the interface contour.

5.2.2.6 Mesh refinement to 128×512 cells

Again, we are concerned with providing a mesh independence study for this benchmark test case. Fig. 5.17 presents the volume fractions and interface predicted by *RCLSFoam* and *interPore* on a refined mesh of 128×512 cells. The flow solution with the RCLS method with $\varepsilon = 0.5\overline{\Delta x}$ is grid independent. The interface appears sharper but the same number of liquid structures are resolved as with the previous coarser mesh (Fig. 5.17). We conclude that the RCLS numerical scheme makes very efficient use of the computational cells on a coarser mesh, without loss in physical accuracy of the solution, which further highlightes the relevance of this numerical capability. On the other hand, mesh refinement does improve the performance of the modified VoF method *interPore*, with extra droplet capture at later times (see Case 5 in Fig. 5.17 versus Case 2 in Fig. 5.14 (ii)). This behaviour is to be expected. While LS methods provide interface sharpness inherently, VoF methods require an additional mesh refinement treatment to limit diffusion. When compression is added (Case 6 in Fig. 5.17), ligaments and ligament breakup become well resolved, however, numerical wiggles start forming along the stem and mushroom cap. There appears to be an optimal numerical set-up for the *interPore* solver in which the traditional OpenFoam numerical compression scheme is not used, but in which the interface sharpening algorithm provides good physical accuracy and resolution of the interface (Case 2 and Case 5), similarly to the conservative level-set method with $\varepsilon = 0.5\overline{\Delta x}$ (Case 1 and Case 4).

5.2.3 Quantitative Results and Discussion

When the perturbation amplitude η is small compared to its wavelength λ, the early stages in the growth of the instability can be analysed using the linearised equations of motion. Small initial amplitude perturbations increase in magnitude exponentially with time [192]. However, substantial deviations from linear theory are observed when nonlinear effects begin to appear. Their development is strongly influenced by three-dimensional effects such as the formation of well-known structures discussed in the previous sections: spikes, bubbles and mushroom caps. At even later times, not computed in this study, spikes and bubbles develop their own mushroom-shaped structures at their tips, which eventually interact and merge. At this stage, nonlinear effects can no longer be ignored. The system enters a regime of turbulent mixing of the two fluids. In order to describe the aforementioned linear evolution stages, a more quantitative description of the RTI is given through the comparison of the calculated amplitude growth rates against their theoretical prediction.

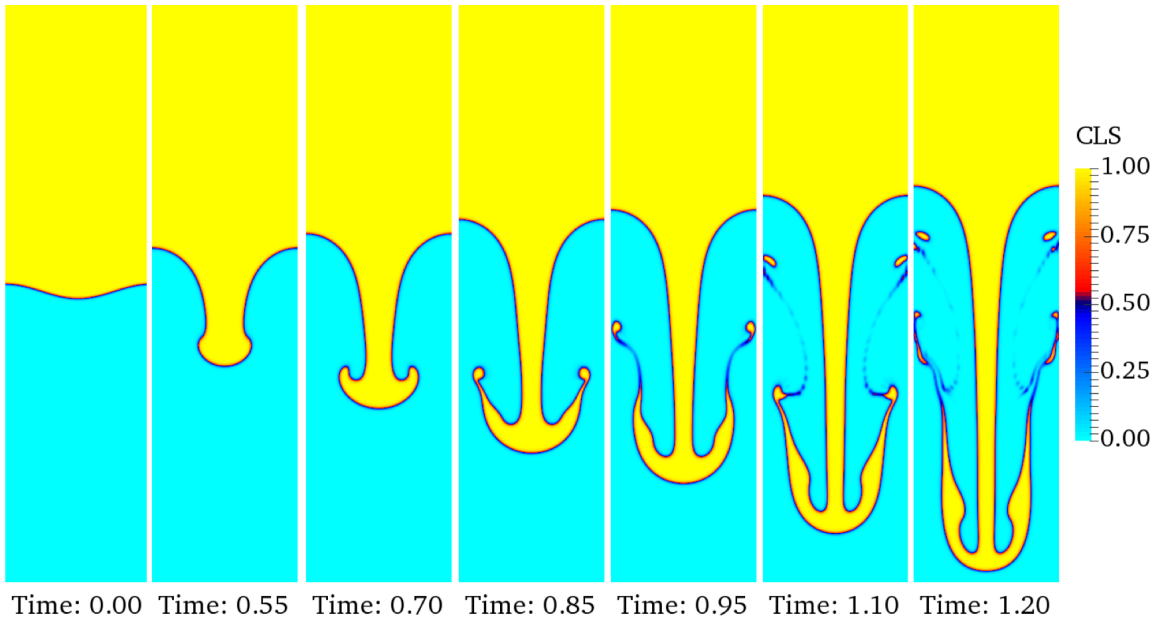

(a) *RCLSFoam*, Case 4

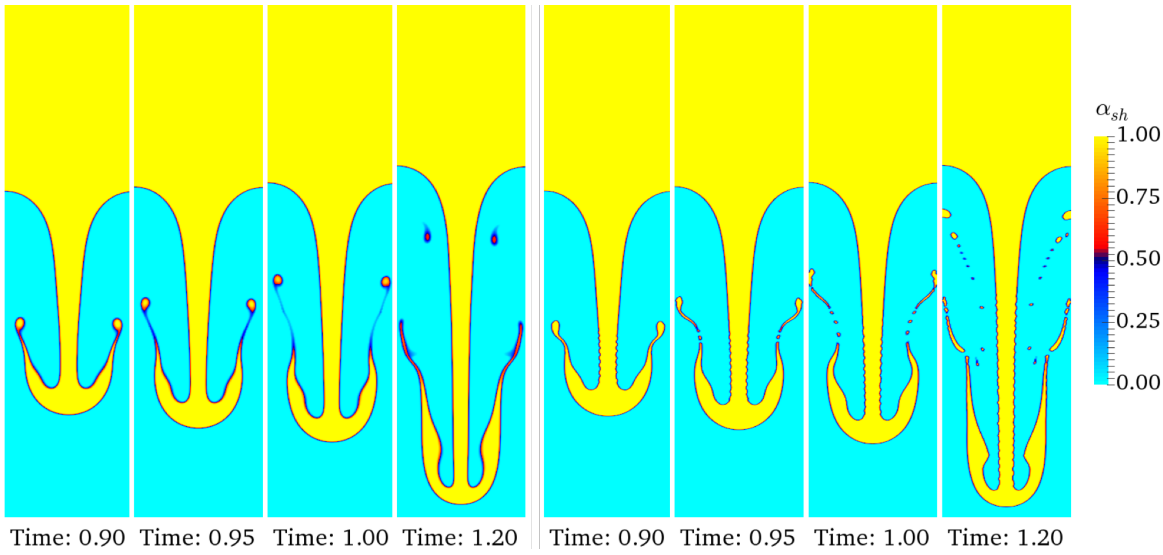

(b) *interPore*, Case 5 (*left*) and Case 6 (*right*)

Fig. 5.17: Volume fractions predicted by both solvers for the Rayleigh–Taylor instability with 128×512 mesh elements.

5.2.3.1 Amplitude growth rate

The initial growth rate of small amplitude perturbations can be affected by various physical properties including viscosity and surface tension. In linear theory, viscosity tends to reduce

the growth rate appreciably, whereas surface tension stabilises wavelengths shorter than a critical wavelength.

Inviscid linear theory Lord Rayleigh [164] first considered the linear stability problem of inviscid fluids with various stratification profiles. He examined the stability of small perturbations in the form of normal modes, where the linearised form of the equations of fluid dynamics can be used. Considering only the very simplest case of two incompressible immiscible fluids in a two-dimensional set-up with an interface between two fluids, one of density ρ_{heavy} that occupies the region $y > 0$ acted on by gravity with constant acceleration g in the y-direction; and the second fluid of density ρ_{light} in the region $y < 0$. If $\rho_{\text{heavy}} > \rho_{\text{light}}$, then a statically displaced small-amplitude interfacial perturbation of wavenumber k is unstable:

$$y(x,t) = \eta(t)\cos(kx) \tag{5.4}$$

with amplitude η, such that $\eta << \lambda$ (where $\lambda = 2\pi/k$ is the wavelength of the initial perturbation). The inviscid linear stability theory of Rayleigh [164] then predicts that n, the growth rate of the instability, will satisfy the following ordinary differential equation

$$\ddot{\eta}(t) - kAg\eta(t) = 0 \tag{5.5}$$

where g is the constant gravitational acceleration and A the Atwood number defined as,

$$A = \frac{\rho_{\text{heavy}} - \rho_{\text{light}}}{\rho_{\text{heavy}} + \rho_{\text{light}}} \tag{5.6}$$

with ρ_{light} and ρ_{heavy} being the densities of the light and heavy fluids, respectively. The ordinary differential equation Eq. 5.5 leads to the following dispersion relation:

$$\eta(t) = \eta(0) + e^{\sqrt{Agkt}} \tag{5.7}$$

with initial amplitude $\eta(0)$. Thus, the initial linear instability growth rate is exponential, i.e. the interface disturbance with wave number k will increase exponentially in amplitude. The linearisation used to formulate Eq. 5.7 strictly applies only for $k\eta << 1$. The literature reveals that the exponential growth persists until $k\eta \approx 1$ [145], which implies that nonlinearity begins when the amplitude satisfies $\eta \approx \lambda/2\pi$. In the present RTI configuration, $k\eta = 1$ when $\eta = 0.15$m. Taylor [210] later observed that the nature of instability of a heavy fluid on top of a lighter one is identical to the problem of an interface accelerated towards the heavy fluid. Lewis [126] performed several such experiments, confirming Taylor's and Rayleigh's theoretical predictions for the linear stage.

Inviscid linear theory with surface tension The stability analysis of Rayleigh [164] and Taylor [210] on RTI has been extended in various directions to include additional physical effects such as, for instance, surface tension and viscosity [192]. The work of Chandrasekhar [29, Chapter 10] sought to extend the inviscid linear theory and has led to a comprehensive understanding of RTI in incompressible viscous fluids with surface tension. At time t, a fluid element of cross section $dydx$ displaced a distance $\eta(t)$ below $y = 0$, feels a downwards force due to gravity and a downward force from surface tension. The fluid element net downward acceleration is therefore given by:

$$g\frac{\rho_{\text{heavy}} - \rho_{\text{light}}}{\rho_{\text{heavy}} + \rho_{\text{light}}} - \frac{\sigma}{\rho_{\text{heavy}} + \rho_{\text{light}}}k^2. \tag{5.8}$$

The simple harmonic solution is

$$\ddot{\eta} - \alpha^2(k)\eta = 0 \tag{5.9}$$

where

$$\alpha^2(k) = gk\frac{\rho_{\text{heavy}} - \rho_{\text{light}}}{\rho_{\text{heavy}} + \rho_{\text{light}}} - \frac{\sigma}{\rho_{\text{heavy}} + \rho_{\text{light}}}k^3. \tag{5.10}$$

Eq. 5.9 is the well-known dispersion equation for interfacial waves of wavenumber k when viscosity is neglected. As expected, the interface is now unstable, and the solution to Eq. 5.9 for fluids initially at rest is

$$\eta(t) = \eta(0)\cosh(\alpha t) \tag{5.11}$$

where $\eta(0)$ is the perturbation amplitude at $t = 0$. The interfacial wave amplitude grows like $e^{\alpha t}$. The linear treatment of this instability is, of course, valid only so long as the amplitude remains small. We note from Eq. 5.10 that surface tension can prevent the instability from growing for sufficiently small wavelengths. To take into account viscosity, Chandrasekhar also applied normal mode analysis to the linearised Navier–Stokes equations to derive an implicit fourth-order ODE for the amplitude of the y-velocity component. The latter is a viscous eigenvalue problem that needs to be solved numerically.

Viscous linear theory Plesset & Whipple [155] developed a simple, physical approximation for the effect of viscous damping of unstable interfacial waves with negligible dynamic effect. The downward velocity of the stem gets reduced as viscosity increases. To simplify their physical discussion, the term arising from surface tension is dropped in the following; its effects can always be included in the way that was described in the previous section. In the long wavelength-limit where viscous damping is small, i.e. viscous effects are small and

$\nu k^2 << \alpha$, where α is given by Eq. 5.10. The growth rate n varies according to the following simple harmonic equation:

$$n^2 + 4\nu k^2 n - \alpha^2 = 0 \tag{5.12}$$

where

$$\nu = \frac{\nu_{\text{heavy}} + \nu_{\text{light}}}{2} \tag{5.13}$$

according to Plesset & Whipple [155, Equation 15]. Solving for the quadratic equation Eq. 5.12 in n, and keeping only the positive root, as before, we get

$$\eta(t) = \eta(0)\exp(nt). \tag{5.14}$$

Fig. 5.18 shows the results of the three linear stability analyses discussed above as well as some of our computational results. The numerical solutions reproduce accurately the theoretical prediction of Chandrasekhar [29] at early times, when the system is still behaving linearly. Without surface tension in the linear theory of Rayleigh [164], the predicted growth rate is faster. The perturbation amplitude temporal evolution by Plesset & Whipple [155] predicts a faster growth rate than Chandrasekhar [29]. *RCLSFoam* (Case 1) and *interPore* (Case 2) perform equally well. We also ran an additional case with the RCLS formulation and a reduced dynamic viscosity by two orders of magnitude, which does not seem to affect the amplitude growth of the instability.

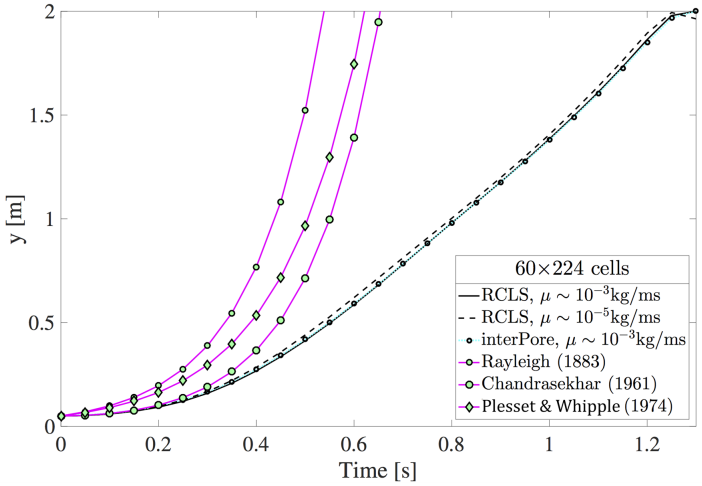

Fig. 5.18: Amplitude growth for the Rayleigh–Taylor instability in the 60×224 computational domain compared to the theoretically predicted growth rates of *RCLSFoam* (Case1) and *interPore* (Case 2).

5.2.3.2 Volume fraction profiles

Fig. 5.19 shows volume fraction profiles along the y-direction centreline of the computational domain at $t = 0.2$s and for our two mesh resolutions along with the theoretical perturbation amplitude predicted by Chandrasekhar [29].

At $t = 0.2$s, and for the 60×224 mesh size, both solvers marginally under-predict the theoretical amplitude, at a liquid phase fraction of 0.5. As Chandrasekhar's linear theory does not take into account viscosity, we postulate that this is the reason for the under-prediction of the perturbation amplitude compared to the estimated theoretical value (grey vertical line). Over the range of coefficients ε tested for the RCLS method, as ε is increased the amplitude at the 0.5 iso-contour diminishes in magnitude, i.e. departs from the theoretical value, in accordance with a less sharply defined interface location. Indeed, the interface needs to have a minimal thickness, so that the gradient of ψ and the interface normal are accurately calculated.

For the 128×512 mesh size, the 0.5 volume fraction iso-contour of the perturbation amplitude is slightly under-predicted for both solvers, probably for the same reason described in the paragraph above. For the VoF solver with interface sharpening *interPore*, a refined mesh does not change the calculated amplitude of the perturbation. However, *RCLSFoam* predicts an amplitude very slightly closer to the theoretical value.

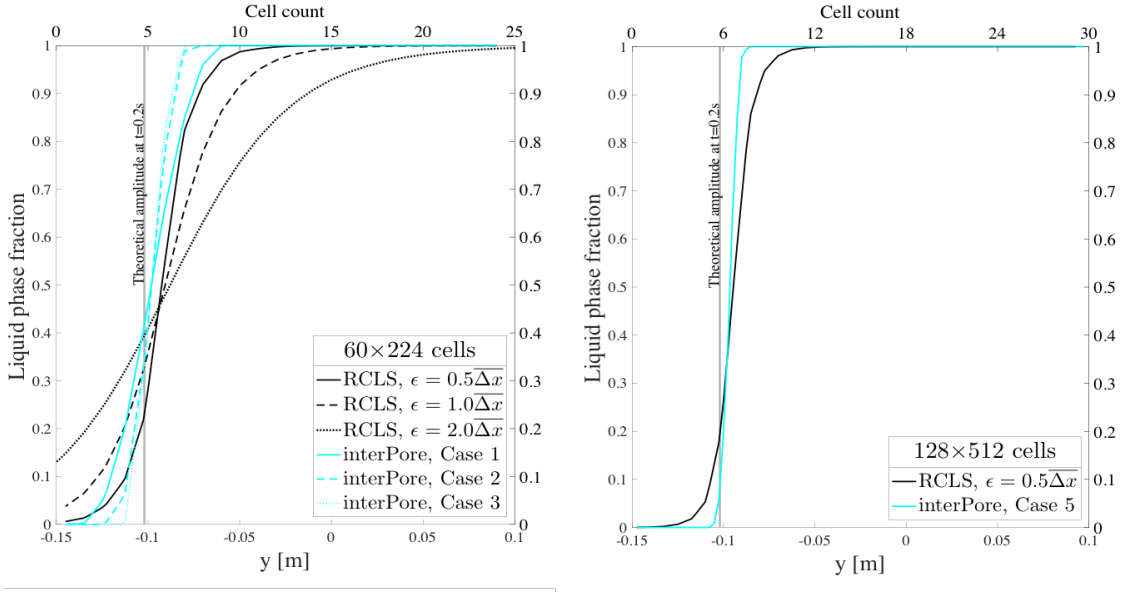

Fig. 5.19: Indicator functions smeared over cell count and y-location at $t = 0.2$s for two mesh sizes (60×224 and 128×512 mesh elements) along with the theoretical amplitude predicted by the linear stability theory of Chandrasekhar [29] (grey vertical line).

5.2.3.3 Self-similarity solution

The RTI marks only the onset of a complex interpenetration process, leading ultimately to the growth of mixing regions between neighbouring fluids [115]. At later times, once the instability has become fully nonlinear, it is difficult to make quantitative comparisons. However, the flow may enter a self-similar growth phase [63]. In the present case, self-similarity can be described by the following equation:

$$\frac{dh}{dt} = 2\sqrt{\alpha A g h} \tag{5.15}$$

where h is the height of the mixing region and α is a dimensionless growth parameter [173]. The parameter α is the subject of extensive research [53, 106, 173]. The physical solution to Eq. 5.15 is

$$h(t) = h(0) + \sqrt{\alpha A g h(0)}t + \alpha A g t^2 \tag{5.16}$$

taking $t = 0$ as the moment in time when the flow first achieves self-similarity, where $h(0)$ corresponds to the thickness of the mixing region at that instant. The last term clearly dominates the right-hand side of Eq. 5.16. We can therefore simplify the equation for mixing thickness such that

$$h(t) \sim \alpha A g t^2. \tag{5.17}$$

We argue that the RTI system becomes self-similar from the very early stages of the instability. Fig. 5.20 shows the numerically calculated mixing height versus time, as well as the predicted mixing height (Eq. 5.17) for two different numerical values of the parameter α. A numerical value of α between 0.19 and 0.17 appears to match very well with the numerical results. For $t = 0.4 - 0.8$s, both solvers present a similar behaviour, slightly under-predicting the two theoretical curves, while for $t \geq 0.9$s, our numerical predictions fall in-between the two theoretical curves.

As viscosity is not taken into account by the present self-similarity model [173], an additional case was run with *RCLSFoam* in which the dynamic viscosity was reduced artificially by two orders of magnitude. This reduction in viscosity did result in a change of the amplitude growth of the instability.

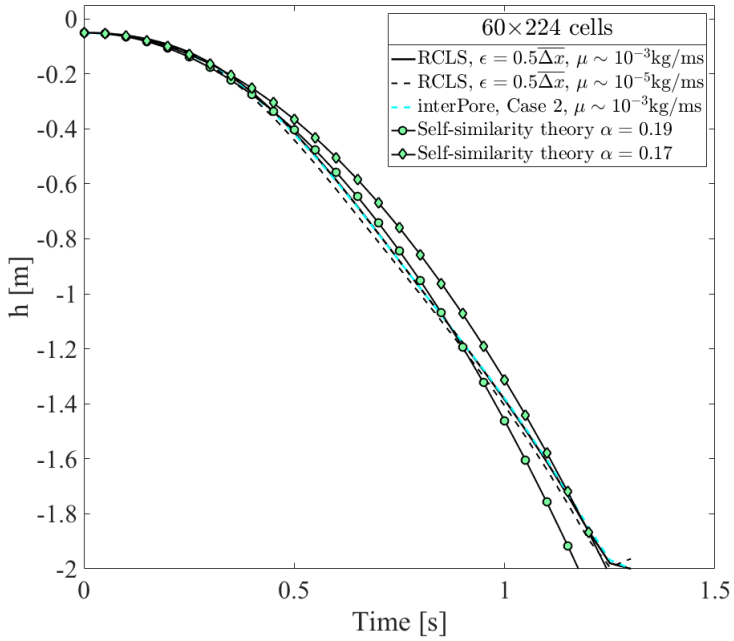

Fig. 5.20: Theoretically predicted self-similar solution for the Rayleigh–Taylor instability against our numerically predicted solutions.

5.2.4 Three-dimensional Rayleigh–Taylor instability

We ran a curiosity-driven three-dimensional version of the case set-up outlined in Section 5.2.1 with *RCLSFoam*. A mesh of $64 \times 224 \times 64$ hexahedral elements is used. The three-dimensional domain is a rectangular box with a square horizontal cross section. It extends in the x–direction and in the z–direction from -0.5 to 0.5, and from -2 to 2 in the y–direction. The same initial surface perturbation is applied with a wave number of 2π and wavelength of 1 m. The instability develops from the imposed single-mode initial perturbation:

$$y = -0.05\cos(2\pi x)\cos(2\pi z). \tag{5.18}$$

The evolution of the fluid interface in the three-dimensional RTI is shown in Fig. 5.21. Presented in the Figure are views of the interface from the heavy-fluid side. As expected, the heavy and light fluids penetrate into each other as time increases. The light fluid rises to form bubbles and the heavy fluid falls to generate spikes. These results are in agreement, at least qualitatively, with the numerical studies published in the literature [85, 121, 219]. There is an additional landmark that distinguishes the interface from that observed in a two-dimensional RTI, which is the existence of four saddle points in the function of the initial disturbance. An

interesting study by He et al. [85] investigated the evolution of the interface around these saddle points. In the nonlinear growth stage, due to the Kelvin–Helmholtz instability (see Section 5.2.2.4), the heavy fluid tends to roll up at both the saddle point and the spike tip. The roll-up of the heavy fluid at the saddle points does not occur in the 2-D case, and is a unique feature of the three-dimensional single-mode RTI.

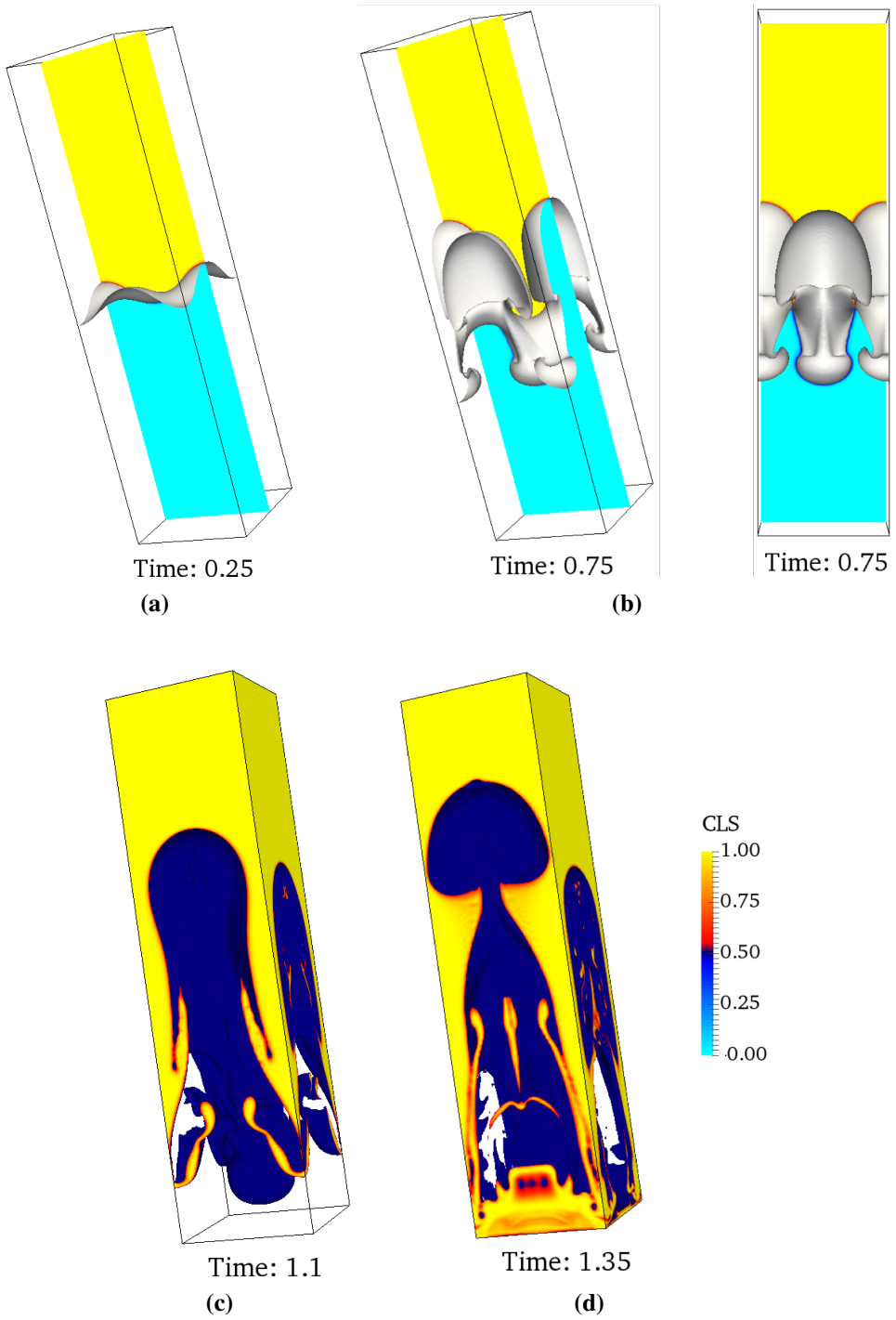

Fig. 5.21: Three-dimensional Rayleigh–Taylor instability. Iso-contour of the interface, viewed from both the heavy-fluid side (*top panel*) and light-fluid side (*bottom panel*). All times are in seconds.

5.3 Discussion

Two different numerical methods for the solution of two-phase flow problems have been compared in detail on two different test cases, chosen specifically to highlight the strengths and weaknesses of each method. In a static droplet test case, both methods are able to minimise the development of spurious currents, and achieve a good representation of surface tension effects. The RCLS numerical method exhibits higher magnitude in spurious currents. However, its ability to minimise the latter with no off-centre displacement of the droplet, nor distortion of the droplet's interface, in a low capillary number environment, although it was not designed with this intention, further demonstrates its robustness and accuracy. In a Rayleigh–Taylor test case, both methods are able to capture the development of the interface perturbation, with *RCLSFoam* showing a significantly better ability to capture droplet pinch-off, symmetry of the system and absence of numerical wiggles on the interface, in accordance with the numerical state-of-the-art reference in the literature [157]. Improving on interface tracking methods to resolve the interface until it becomes grid independent assures us of resolving thoroughly the rest of the solution. Nevertheless, sub-grid scale models to take into account the unresolved surface tension forces, combined with Adaptive Mesh Refinement techniques (AMR) are becoming imperatives in the simulation of two-phase flows.

This collaborative work was intended to overcome a natural tendency to evaluate numerical methods using only test cases close to the specific application for which they were designed in the first place. In the present context, methods based on achieving optimum interface sharpness at higher Ca numbers were believed to be more prone to spurious currents at low Ca numbers. By the same token, methods that are more resistant to interface artefacts may well be less accurate in terms of sharpness. Our results indicate that a well-tuned implementation of either the LS or the VoF method is able to work well across a broad range of relevant conditions, and that the underlying techniques for interface capture have many features in common.

Chapter 6

From High-Fidelity Numerical Simulations of a Liquid Film Atomisation to a Regime Classification

The breakup of a liquid phase is the process whereby a mass of liquid, accelerated through an ambient gaseous flow, is dynamically broken up into a large number of small droplets. The complexity of the problem is due to the chain of physical processes involved in parallel and/or in sequence. A vast amount of literature has accumulated on the subject (see Chapter 2). Much progress has been made towards high-order numerical schemes, computational power, and experimental visualisations. In spite of this, many aspects of spray formation are still poorly understood. Some recent publications have attempted to categorise the breakup phenomena in terms of the operating conditions [e.g. 48, 57]. Most authors agree on the critical influence of the relative liquid/gas velocity ratio on the atomisation process and recognise that all the atomisation mechanisms are connected with wave formation, wave development and wave disintegration. The question remains as to whether the onset of shear-driven instabilities and surface waves development have an effect on atomisation for every operating conditions. This chapter is a systematic fundamental investigation of the physics involved during the atomisation of a prefilming airblasted liquid film, described herein. We perform high-fidelity transient three dimensional calculations, providing detailed information on the processes and structures in the near nozzle region, the primary breakup region. This work was published in Bilger & Cant [20] and Bilger & Cant [19].

6.1 Operational range

The operational range of an aircraft engine covers six different operating points: start, idle, take-off, cruise, landing and high-altitude relight conditions. Table 6.1 illustrates some of these operating regimes. All operating points were measured at the German National Aeronautics and Space Research Centre (DLR) in Cologne, Germany [11]. Noting the extensive variety of Reynolds and Weber numbers regimes, from take-off to cruise condition at high altitude, consequently the injection regime will vary accordingly. As DNS simulations are constrained by the resolution of the smallest turbulent lengthscales, computations applying a DNS formulation are therefore limited to rather small Reynolds numbers. For the computation of primary breakup, the resolution of the smallest droplets represents yet another numerical challenge in terms of grid resolution. Due to these limitations in grid resolution, DNS computations of the high-load operating points such as start and take-off seem unrealistic at this time.

Table 6.1: Typical aircraft engine operating points from the experimental test rigs of Behrendt [11]. Adapted from Sauer [182]. The Reynolds number is defined using the channel half height. The Weber number is defined using the height of the liquid inlet slit.

	p_{gas} [bar]	T_{gas} [K]	$\overline{u}_{\text{gas}}$ [m/s]	ρ_{gas} [kg/m^3]	ν_{gas} [m^2/s]	σ [N/m]	Re_{gas}	$\text{We}_{\text{gas,h}_{\text{liq}}}$
Start	36	850	98	14.76	2.7×10^{-6}	2.32×10^{-3}	364,200	18,327
Idle	4.8	477	74	3.51	7.7×10^{-6}	1.88×10^{-2}	95,470	305
Take-off	29.6	809	96.8	12.75	3×10^{-6}	4.48×10^{-3}	320,000	7,994
Cruise	14.7	759	93.3	6.75	5.5×10^{-6}	1.05×10^{-2}	169,700	1,678

Furthermore, at take-off, when the pressure of the working fluid exceeds the thermodynamic critical pressure of the liquid phase, the presence of discrete two-phase flow processes becomes diminished. A well-defined molecular interface no longer exists. Both a vanishing surface tension and locally diminishing gas-liquid interface essentially result in the disappearance of the interface. These are called supercritical mixture states, in which the classical view of spray atomisation is no longer valid and our numerical modelling capability is no longer adequate. For take-off design points, the liquid fuel is in its supercritical state (Fig. 6.1) and requires a special numerical treatment for the simulation of atomisation [43]. It is not the subject of the present work to apply the RCLS formulation over the full range of pressures and temperatures relevant to modern propulsion systems and be able to replicate the injection and atomisation regimes at these high-load operating points. The present approach rather constitutes a fundamental study of atomisation. We present the results

of laminar flow calculations and demonstrate the capability of the RCLS method to delve into the fundamental physics behind the atomisation phenomenon. In this demonstration exercise, the evolution of the liquid film over time is investigated, in a systematic manner, to characterise the primary breakup mechanisms and the dominating liquid deformations. The study has been substantiated numerically for a parametric range of fuel and oxidiser injection velocities.

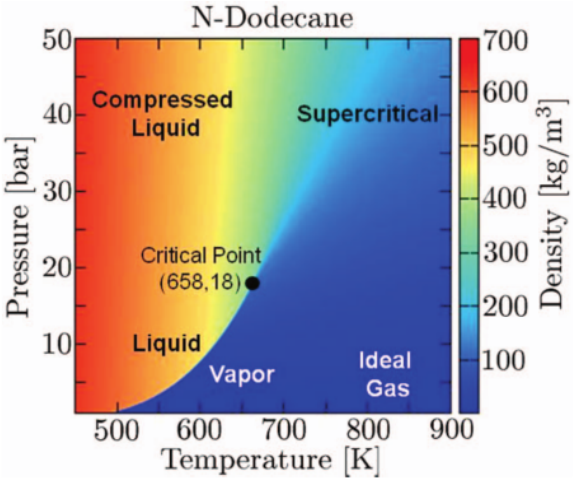

Fig. 6.1: Density contours of pure n-dodecane showing the saturation line, key thermodynamic regimes and critical point. Taken from Dahms & Oefelein [43].

6.2 Settings of the computation

This section details the computational settings employed in the simulation of the atomisation of a prefilming airblasted liquid film. In particular, the mechanical and physical boundary and initial conditions are given throughout Section 6.2.1 to Section 6.2.4. In Section 6.2.5 we present our choice of numerical parameters for the computations. Finally, in Section 6.2.6 and 6.2.7 we discuss briefly the implications of our choice of numerical resolution in terms of the physical realism we can hope to extract from our computations.

6.2.1 Computational domain and boundary conditions

In order to reduce the complexity of the computational configuration in this parametric study, the realistic annular geometry of most airblast commercial atomisers (Fig. 1.5) is simplified into a three-dimensional planar geometry (Fig. 6.2b), where the liquid is injected as a thin

planar sheet. Our choice for the design of our computational domain is partly driven by experimental studies [15, 46, 72] (see Section 2.1.5), in order to demonstrate the performance of the RCLS modelling capability on a geometry reproducing the original experimental design and validate our numerical results against observed experimental evidence. Indeed, whereas realistic fuel injectors are in general annular, the planar design is becoming increasingly popular as a benchmark flow to study primary atomisation among experimentalists, particularly due to the relative simplicity of experimental visualisation. The similarity in the physical phenomena observed between the annular liquid sheet and the planar liquid sheet has been studied experimentally by Berthoumieu & Lavergne [13]. They concluded that the basic atomisation mechanisms are the same in both axisymmetric and planar configurations and that this similarity is achieved when the ratio between the radius of the annular injector and the liquid sheet thickness is well above 1. For the liquid film thickness of 100μm considered in the present work, and for an annular injector to behave in a similar way to the planar liquid film, it would need to be of a minimum diameter of 4mm. In addition, to be certain that the planar liquid film is not affected by the walls on either side, we need to impose a big enough ratio between the liquid thickness and its width. In our study this ratio is equal to 40, which is of the same order of magnitude as the ratios employed by Déjean [46] in his experimental work. Of course, despite our precautions, the similarity between the annular and planar injectors will not be perfect. In view of the limited knowledge on primary breakup, the decision to neglect some aspects to focus on a simplified liquid film study seems sufficient to highlight and identify the principal physical mechanisms.

The geometrical details of the injection configuration are as follows (Fig. 6.2). The x-direction corresponds to the streamwise direction, the y-direction is upward and the z-direction is spanwise. Our computational domain is a cuboid of $16 \times 11 \times 4$ mm^3, where the prefilmer is a flat solid plate of 4mm in width, 8mm in length and of 1mm thickness. We resolve a length downstream of the prefilmer of 8mm. As the emphasis of this numerical study is placed on the mechanisms driving the primary breakup, the computational domain is limited to the close vicinity of the injection plane. Despite basing our choice for dimensions on commonly-used geometries of the injector for experimental studies of prefilming airblast atomisation, our choice has also been driven by how large the amplitude modifications of the liquid film are expected to be, and by limiting interference with the flow over the prefilmer with the top and bottom wall (no-slip) domain boundaries. The front and back planes, respectively defined by $z = 2$mm and $z = -2$mm, are set as cyclic boundary conditions. This implies that the cell faces situated on these boundaries are treated as “virtually" connected in terms of discretisation and domain decomposition for parallel computations. The rest of the domain boundaries are defined as inlet/outlet boundary conditions, fixed mass inflow and fixed back

pressure. In case reverse flows are observed at the exit plane, which would then destabilise the computation, a specific set of velocity and pressure boundary conditions can be used to prevent this effect.

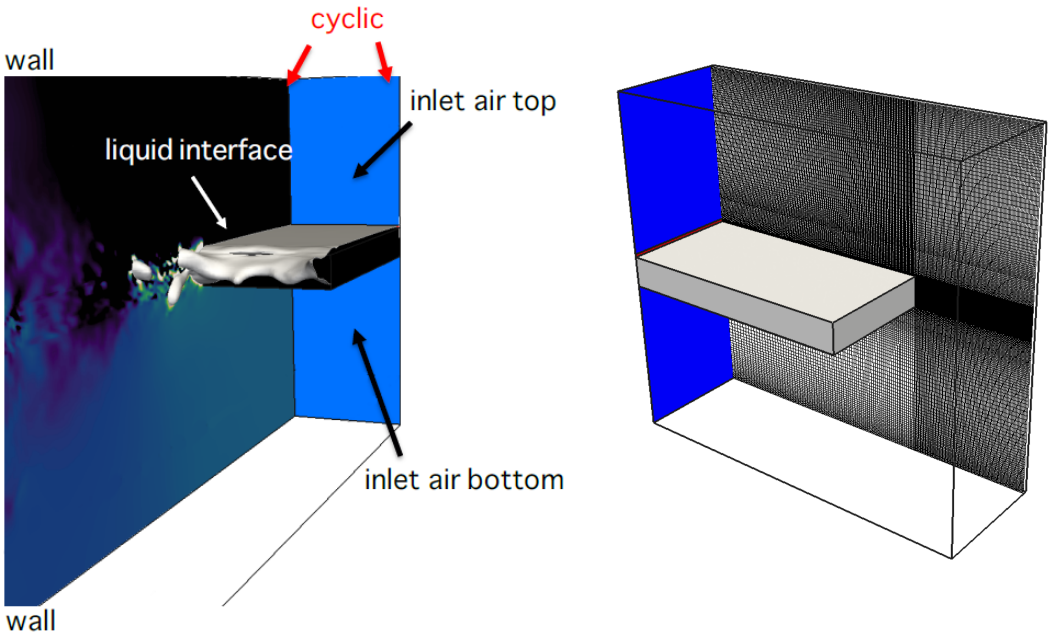

Fig. 6.2: **(a)** View of the computational domain with the liquid interface shown in grey, the gas inlet planes in blue and the prefilmer (rectangular parallelepiped) in black; **(b)** Mid-plane cut of the mesh with the liquid rectangular inlet slit shown in red, the gas inlet planes in blue and the prefilmer (rectangular parallelepiped) in grey.

For an outflow, a von Neumann boundary condition is used for velocity (zero gradient specification of the normal component) and the back pressure is set as a fixed value. In case of an inflowing velocity, the set of boundary conditions is interchanged: the velocity is set to zero via a Dirichlet boundary condition, while the pressure is instead initialised by a zero gradient von Neumann boundary condition. Using this approach mass conservation is assured.

The thickness of the solid prefilmer plate is resolved, which is a feature that has proven to be of significant importance in the numerical simulation of primary breakup [69]. The RCLS method is designed to run on hybrid meshes. However, to improve the accuracy in representing the atomisation process, the entire computational domain is meshed with 2.47×10^6 hexahedral elements.

In multiphase flow dynamics, the timestep must be small enough to resolve the propagation of the capillary waves that develop at the interface [21]. Here we keep the maximum Courant number in the domain under 0.5.

6.2.2 Two-phase velocity injection profiles

Previous numerical and experimental studies of atomisation have highlighted the sensitivity of computations to boundary conditions on the liquid atomisation. In particular, it is believed that the accurate application of both velocity profiles (boundary layers in liquid and gas phases) are critical to predict the onset of the breakup and the growth of perturbations at the interface [107, 135, 141]. The liquid and the gas are both entering the simulation domain at the inlet plane, with different heights $h_{\text{liq}} = 0.1\text{mm}$ and $h_{\text{gas,top}} = h_{\text{gas,bottom}} = 5\text{mm}$; and at different mean velocities $\overline{u}_{\text{liq}}$ and $\overline{u}_{\text{gas}}$. In a first attempt to describe numerically the injection of the liquid and the gas as a two-phase flow in the top injection channels, there seems to be a practical significance in applying a two-phase Poiseuille flow profile, to avoid the extra computational cost of an extended domain to let the velocity profiles develop. The two-phase Poiseuille flow is a simple interfacial flow that allows an accurate estimation of a fully-developed two-phase channel flow: a no-slip boundary condition must be satisfied at the top wall boundary and on the prefilmer plate, and the velocity of the two fluids must match at the interface. However, as detailed in Appendix A, one cannot freely choose the thickness of both injection channels as well as the physical properties of the two fluids and their average speeds: the mathematical system of equations for the determination of the mean injection liquid and gaseous speeds is over-determined, as discussed in Johnson et al. [103], Miehe [147]. One way of bypassing this issue would be to relax the upper wall no-slip boundary condition and apply a two-phase Poiseuille flow with a slip wall boundary condition (see Appendix A). Nevertheless, we decided to go forward with a no-slip top wall boundary condition, which is a more definite boundary condition to use. We outline our method in what follows.

A continuous laminar airflow (conservative level-set $\psi = 0$) with no swirl is supplied at the inlet plane. The air emerging is split into two streams that pass the prefilmer on each side. The gas enters the domain with a parabolic velocity profile in order to account as much as possible for upstream flow development in the air supply channels. Its mean speed is varied parametrically between 5 and 50m/s. The parabolic gas velocity profiles are derived mathematically based on the geometry of the domain (Fig. 6.3). This leads to, in the top

injection gas channel,

$$\begin{cases} u(e) & = 0 \\ u(e+d) & = 0 \\ u(e+\frac{d}{2}) & = u_{\max} \\ u(y) & = \dfrac{4u_{\max}}{d^2}\Big(-y^2+(2e+d)y-e^2-(ed)\Big) \end{cases}$$

and in the bottom injection air channel,

$$\begin{cases} u(-c,-2a) & = 0 \\ u(-c,-2a-b) & = 0 \\ u(-c,-2a-\frac{b}{2}) & = u_{\max} \\ u(y) & = \dfrac{u_{\max}}{-b^2/4}\Big(y^2+(4a+b)y+4a^2+2ab\Big) \end{cases}$$

where a, b, c, d, e, and f represent the geometrical lengthscales as schematically described in Fig. 6.3 and $u_{\max}$ is the centreline velocity of the parabolic profiles.

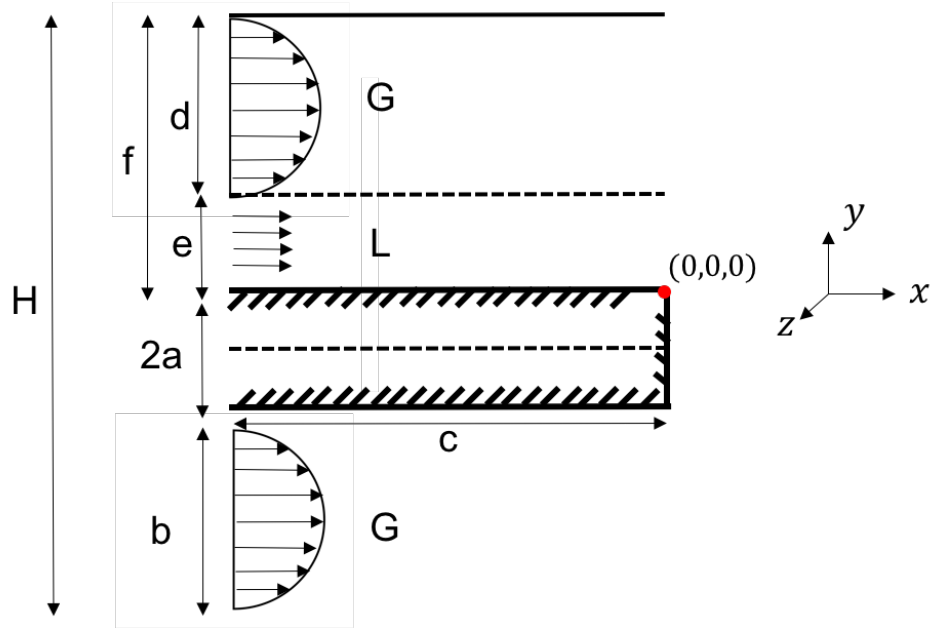

Fig. 6.3: Representation of the fluid channels – around the prefilmer – for the derivation of the parabolic velocity profiles applied at the inlet of the top and bottom gas channels.

The liquid ($\psi = 1$) is continuously fed onto the prefilmer plate through an injector slit of 4mm×0.1mm with a uniform velocity profile and mean speed varied parametrically between 0.5 and 10m/s. The liquid forms a thin film travelling downstream.

We assign a small-amplitude velocity fluctuation to the liquid inlet plane. This boundary condition generates a fluctuating inlet condition by adding a random component to the mean velocity field, defined as a fraction of the mean velocity, based on a chosen intensity. In this study, the random generator interval is between -1% and $+1\%$ of the inlet velocity. The reader is referred to the OpenFoam user-guide for more information [231]. The objective behind the use of such a boundary condition is to avoid perturbations of the surface in the first instants of the injection being triggered purely by numerical noise.

The liquid stream and top gas stream rapidly develop into a two-phase Poiseuille flow profile, with a point of inflection, as expected, over the course of a few mesh elements (Fig. 6.4). Indeed, after a few timesteps, the restraining influence of the wall spreads further into the fluid. The central portion of the velocity profile is adjusting until at a certain time when all parts of the fluid are subject to the effect of the wall and the shape of the velocity profile ceases to change.

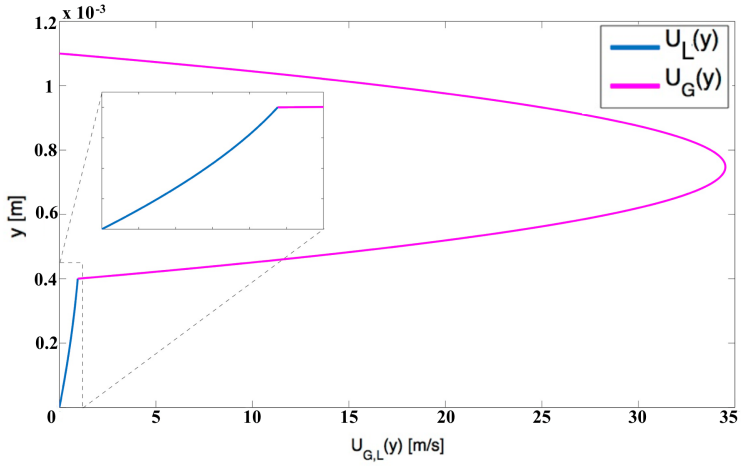

Fig. 6.4: Example of one of the inflow axial velocity profiles for the top inlet channels, above the prefilmer plate. The liquid velocity is shown in blue and the gas velocity in pink.

6.2.3 Material properties

The flow conditions chosen for this study are listed in Table 6.2. Although the material properties chosen for this study differ slightly from those of an aero-engine, the physical quantities remain similar and of the same order of magnitude. All numerical simulations use atmospheric conditions for pressure and temperature.

We note that in the application of airblast atomisation in aircraft engines, the variation in liquid temperature is immense: from 240K in the fuel tank to approximately 600K after

injection into the combustion chamber. Thus the difference in liquid density and viscosity and also surface tension are bound to change the atomisation mechanism.

Gravity is ignored in the context of primary atomisation as it has no effect over the length-scales and timescales involved. Indeed, given the flow velocities at play, the Froude number (given by Eq. 6.1) is always much greater than 1,

$$Fr = \frac{u^2}{gh} \tag{6.1}$$

for any characteristic velocity scale (u) and lengthscale (h) of the gaseous or liquid phase. In addition, ignoring evaporation is reasonable because the dense-spray region of combusting sprays generally involves relatively cool portions of the flow where rates of heat and mass transfer are modest [61]. Downstream however, in the dilute-spray region, the spray widens due to turbulent dispersion and gas entrainment whereby the liquid volume fraction decreases. The surface to volume ratio of droplets and the free distance between them become larger. Evaporation thus becomes significant.

No dynamic contact angle modelling is used in the present chapter. For a demonstration of the dynamic contact angle model as implemented in *RCLSFoam*, the reader is referred to Chapter 3.

Table 6.2: Material properties for the simulation of atomisation

Phase	ρ [kg/m^3]	μ [kg/m.s]	$\overline{u}$ [m/s]	σ [N/m]
Gas	1.2	1.18×10^{-5}	5–50	
Liquid	998	1.0×10^{-3}	0.5–10	0.0283

6.2.4 Non-dimensional numbers

The order of magnitude of the non-dimensional numbers associated with the flows simulated are given in Table 6.3. The non-dimensional numbers were introduced in Section 2.3.1. We recall that there is a lack of consensus over the choice of non-dimensional numbers, which highlights the absence of a comprehensive understanding of primary atomisation. The present choice is driven by the studies of Déjean [46], Sauer [182] and Ling et al. [132].

Table 6.3: Non-dimensional numbers investigated in this study. The ranges given correspond to the lowest and highest relative velocity between the two fluids.

ρ_{liq}/ρ_{gas}	μ_{liq}/μ_{gas}	MFR	MR	Oh	$We_{gas,h_{liq}}$	$Re_{gas,h_{liq}}$
830	80	0.0075–12	0.37–600	0.0595	0.038–10.39	500–4990

Another additional Weber number to be considered in this study is the turbulent Weber number in the liquid phase defined as:

$$We_{turb} = \frac{\rho_{liq} u'^2 h_{liq}}{\sigma}. \tag{6.2}$$

Som & Aggarwal [200] discusses the topic of turbulence induced breakup in which turbulent fluctuations in the liquid are responsible for perturbations on the liquid surface in the form of turbulent eddies emerging from the liquid bulk and through its surface. Assuming a velocity fluctuation of 6% in the liquid phase flowing at 10m/s, and assuming the highest possible eddy size to be of the order of the liquid channel height h_{liq}, this gives $We_{turb} \sim 1$. The liquid turbulence is therefore unlikely to have an impact on breakup.

In addition, the liquid Reynolds number, defined as,

$$Re_{liq} = \frac{\rho_{liq} \bar{u}_{liq} h_{liq}}{\mu_{liq}} \tag{6.3}$$

is found to be of the order of 990. Given the liquid Reynolds number at play, the liquid flow can be viewed laminar, as the critical Reynolds number corresponding to the transition between the laminar and turbulent regime is considered to be of the order of 2,500 [46]. Turbulence is unlikely to play an important role within the thin and viscous liquid film region. A further discussion on turbulence will be given in Section 6.2.7.

6.2.5 Choice of RCLS settings and OpenFoam discretisation schemes and solvers

In the interest of robustness and because atomisation problems involve large density ratios, we use a WENO high-order numerical scheme for the treatment of discontinuities (see Section 3.4). The parameters of the RCLS numerical method have been chosen to reach a trade-off in terms of performance, stability of the method and compliance with the physics of the atomisation. The chosen set of RCLS parameters – discussed in Section 3.3 – is

recapitulated in Table 6.4. In addition, Table 6.5 recapitulates the choice of discretisation schemes and solvers as well as convergence criteria chosen as part of the numerical framework of OpenFoam. The reader is referred to the OpenFoam user-guide for more information [231].

Table 6.4: RCLS parameters for the simulation of atomisation

Order of the polynomial reconstruction:	$r = 3$
Numerical scheme:	WENO
CLS coefficient:	$\varepsilon = 0.5\overline{\Delta x}$
Periodicity of re-initialisation:	$N_S = 5$

Table 6.5: Details of the discretisation schemes, solvers and convergence criteria adopted for the simulations of atomisation. The acronyms are described in the Nomenclature.

$\frac{\partial \psi}{\partial t}$	Runge–Kutta, TVD, third order implicit
$\frac{\partial \rho \mathbf{u}}{\partial t}$	Pure Crank–Nicholson, second order implicit
$\vec{\nabla}(\psi \mathbf{u})$	WENO, third order
$\vec{\nabla} \cdot (\rho \mathbf{u}\mathbf{u})$	Gauss LimitedLinear, TVD, second order
$\vec{\nabla}$	Gauss linear
∇^2	Central difference with explicit non-orthogonal correction
p–**u** coupling	PISO (3 corrections)
Pressure solver	PCG+DIC or PCG+GAMG
Velocity solver	PBiCG + DILU or smoothSolver + GaussSeidel
Convergence criteria:	**u**: Residual $< 10^{-6}$; p: Residual $< 10^{-7}$

6.2.6 A discussion on grid resolution

In the resulting mesh, the smallest edge length is $\Delta x_{\text{min}} = 10\mu$m and the average characteristic length scale of the grid, defined as

$$\overline{\Delta x} = \frac{1}{N_\Omega} \sum_{f=1}^{N_\Omega} |\overrightarrow{O_f N_f}| \tag{6.4}$$

is $\overline{\Delta x} = 40\mu$m. In Eq. 6.4, N_Ω is the number of internal faces of the mesh, and O_f and N_f are the cell centres of the owner and neighbour cells of a given internal face f, respectively. Eq. 6.4 is a representation of the average characteristic length scale of the grid, i.e. an average of the cell-to-cell (centres) distance, with an orthogonality correction.

The focus of the present study did not lie in the need to resolve the smallest lengthscales of the flow, but to conduct a wide parametric study with the most affordable mesh to accurately resolve the interface geometrical properties and surface tension forces. Real systems with relatively complex flows provide challenges that still limit the range of situations that can be simulated with DNS. The problem is, as one might expect, one of scale. We are limited by the need to resolve processes taking place on an enormous range of length- and timescales. Generally, the smallest lengthscale of the flow has to be resolved and is the limiting factor. As the number of computational grid points available cost-effectively increases, the range of scales that can be resolved goes up.

The Kolmogorov scale is the smallest scale in turbulence. Thus, in DNS of turbulence, the Kolmogorov scale is the most limiting factor in grid resolution. Lately, our capabilities to address large, transient and multi-physics problems with DNS have been promoted by the development of High Performance Computing (HPC), which has considerably improved our ability to produce robust and reliable solutions to complex problems.

However, in multiphase flows, resolving the interface in a given mesh element, which is of the order of the molecular scale in thickness, is impractical. Only a quasi-DNS numerical approach is available. The more refined the mesh, the more accurate the resolution of interfacial geometrical properties such as curvature and unit normal. Numerical techniques are being developed to refine the interface: for instance sharpening in VoF methods or level-set techniques (see Section 2.2). Even with these techniques, evidence suggests that the sub-grid contributions of the smallest liquid structures and of the interface to the flow field must be treated [116, 158]; especially given the fact that turbulence is believed to play a strong role in the onset of the breakup [61]. The creation of sub-grid scale models for the turbulence-interface interaction should therefore become a priority with the need for closure of the unresolved surface tension term [88]. A further discussion on the topic of turbulence resolution for the atomisation of liquids appears in Section 6.2.7.

One of the smallest lengthscales associated with the flow field that we aim to resolve is the estimated maximum droplet diameter produced resulting from primary breakup, prior to secondary breakup. The finest grid size should therefore be calibrated to capture those liquid structures as the smallest drop size captured will always depend on the smallest grid size used in the computational modelling of multiphase flows. A liquid blob moving in a gaseous phase is subjected to aerodynamic forces, which could lead to its deformation and fragmentation into smaller and smaller droplets. The breakup of a droplet into smaller entities is usually referred to as secondary atomisation. An overview was given on secondary atomisation in Section 2.1.2. From droplet stability studies, the critical condition for drop breakup is

reached when the aerodynamic force exerted on the drop is equal to the surface tension force [123]. In inertia-dominated flow fields, the critical Weber number is an appropriate criterion for the prediction of the initiation of droplet breakup:

$$\mathrm{We_c} = \frac{\rho_{\mathrm{gas}} u_{\mathrm{rel}}^2 D_{\mathscr{D}}}{\sigma}. \tag{6.5}$$

where $D_{\mathscr{D}}$ is the droplet diameter. Eq. 6.5 is relevant only for low-viscosity fuels, i.e. for very low Ohnesorge numbers (Oh<0.1). In this respect, the critical Weber number for breakup has been reported to be around 12 by different experimental studies [80, 123]. Having found a critical Weber number, this allows us to estimate the maximum diameter of stable droplets in a given spray that can be observed right after primary breakup:

$$D_{\mathscr{D},\mathrm{max}} = \frac{\mathrm{We_c}\sigma}{\rho_{\mathrm{gas}} u_{\mathrm{rel}}^2}. \tag{6.6}$$

The latter means that secondary breakup will happen for droplets with a diameter larger than $D_{\mathscr{D},\mathrm{max}}$. We note that turbulence will also affect the value of the critical Weber number. Experiments by Guildenbecher et al. [80] indicate that the breakup of droplets in turbulent flows requires a lower Weber number compared with that in laminar flows. Numerical results by Jain et al. [99] also indicate that the value of the critical Weber number for droplet breakup decreases with increasing turbulence intensity. In our computations, for $\mathrm{W}_c = 12$ and for the highest relative velocity investigated between the two fluid phases, $D_{\mathscr{D},\mathrm{max}} = 100\mu\mathrm{m}$. Considering that a given length scale L is resolved if $L \geq 2\overline{\Delta_x}$ [158], it can be seen that the maximum droplet diameter resulting from primary breakup is properly resolved by our mesh, which suggests that the mesh can resolve the smallest liquid structures produced. This further highlights our ability to make an efficient use of grid cells with the RCLS method.

6.2.7 A discussion on turbulence

Turbulence is very likely to be generated inside the liquid phase because of the velocity shear between the gas and liquid mediums and resulting boundary layer development. Indeed, past studies of pressure-atomised sprays have clearly established that one of the criteria for the development of interfacial structures and the onset of breakup is the degree of flow development and the presence of turbulence at the jet exit [61]. The so-called turbulent primary breakup along the liquid surface is associated with the presence of turbulent boundary layers along the injector passage walls near the exit, suggesting the absence of breakup in

the absence of liquid vorticity, i.e. for conditions where the liquid velocity distribution is uniform and no turbulence is present.

In those phenomenological atomisation models that consider turbulence in the liquid flow as a driving force for disintegration, the liquid jet starts to disintegrate when the liquid turbulent boundary layer reaches its free surface. Turbulent eddies with sufficient kinetic energy to overcome the liquid surface tension are able to deform and disrupt the interface, as described in Som & Aggarwal [200]. Correspondingly, the smallest drops are then either comparable to the Kolmogorov lengthscale, or to the smallest turbulent eddy with sufficient kinetic energy, whichever is larger [200].

The computational diesel spray atomisation simulations of Bianchi et al. [16] and de Villiers et al. [45] have highlighted the sensitivity of computations to turbulent boundary conditions on liquid atomisation. They suggest that the breakup is fundamentally three dimensional and strongly coupled (spatially and temporally) to the upstream liquid turbulence of the liquid jet generated in the injection nozzle. Their results indicate that the inclusion of turbulence enhances primary breakup, leading to, in part, smaller droplet sizes. In the case of non-prefilming liquid film primary breakup, Fuster et al. [69] observed vortices produced in the injection channels, similar to the turbulent eddies formed in the injector channel of the pressure-atomiser nozzle of Som & Aggarwal [200]. These vortices appeared to affect significantly the primary breakup process and interact strongly with the droplets generated. According to Fuster et al. [69], it is therefore necessary to model the injection channels.

Therefore, not only is the accurate application of both the velocity profiles important – boundary layers in liquid and gas phases [107, 135, 141] – but the inlet turbulence is critical to predict the onset of the breakup and the growth of perturbations at the interface. To prescribe the inlet turbulent conditions, two types of methodologies have emerged: some authors simulate the flow in the injector channels and let it develop [69] whereas others have created specific numerical procedures to avoid the extra computational cost of an extended domain [112, 183].

Turbulence is undoubtedly created during prefilming liquid film primary breakup, simply due to the atomisation dynamics themselves. However its feedback on those same dynamics is poorly understood as a systematic study of this effect has yet to be undertaken. The presence and properties of turbulent boundary layers and level of turbulence along the passage walls are rarely quantified in experimental data on prefilming atomisation, because of their difficult nature in being assessed by measurements. However, as novel experimental visualisation techniques are emerging, this suggests that turbulent atomisation characterisation will become easier. One cannot strictly affirm if turbulence will play a significant (positive or negative) role

in the process of atomisation of liquid films. The question remains whether turbulence in the two-phase system provokes, enhances or suppresses atomisation and if a laminar environment accompanied by hydrodynamic instabilities is sufficient to result in primary breakup. While some authors acknowledge the importance of turbulence [16, 45, 141], certain older classical primary breakup theories by Taylor [209] and Levich [125] showed that aerodynamic forces could contribute solely to the breakup of a (non-turbulent) liquid bulk. As pointed out by Faeth et al. [61] and more recently by Desjardins [50], these theories merit additional study. Therefore, we decided to move away from the more conventional way of thinking in which simulating turbulence is a prerequisite to obtain a better understanding and description of the physics involved during primary breakup. Our computational domain and initial conditions do not account for turbulence. This facilitates our aim to distinguish the shearing action and growth of perturbations at the interface away from the turbulence action. This methodology allows for a comprehensive separate examination of non-turbulence-related influences on the breakup process. By factoring out turbulence, we can provide a detailed picture of the hydrodynamic mechanisms that govern spray formation. Therefore, the injected parabolic velocity profile of the gaseous phase is laminar.

6.3 Results and Discussion

6.3.1 Regimes of liquid film development and atomisation

Several excellent graphical classifications of regimes for two-phase flow dynamics have been reported in the literature based on numerical and experimental observations: these cover for example secondary atomisation of liquid drops [80], jet breakup based on the Weber number [62], as well as the non-prefilming liquid sheet atomisation classification of Fernandez et al. [64] based on the momentum flux ratio and the more recent cartography established by Déjean et al. [48] on prefilming liquid sheet atomisation. A more complete review of regime classifications can be found in Chapter 2, Section 2.3 of this work.

Inspired by the recently published works of Bhayaraju & Hassa [15], Déjean et al. [48], Inamura et al. [95], which have helped in building towards a formulation of regime classification for prefilming atomisation of planar liquid films, the present study sets out to study the phenomenology observed during primary breakup of an airblasted planar liquid film with a set of high-fidelity numerical simulations. Using the results, we propose a mapping for prefilming liquid film atomisation in velocity space.

6.3.1.1 Regime mapping

A preliminary regime diagram is built based on the key findings presented in the following sections that quantifies under what velocity conditions a liquid film will atomise following a certain interfacial behaviour. A representative map is given in Fig. 6.5, which shows the results of the set of high-fidelity numerical simulations that were conducted at ambient pressure and temperature. Because the prefilmer geometry is fixed as well as the thermodynamic state of the fluids, we have explicitly chosen not to use non-dimensional numbers for the characterisation of the boundaries of these regimes. In any case, as discussed in Section 2.3.5, it is not yet clear what those non-dimensional numbers should be. In addition, we considered it convenient in the first instance to present these results in a dimensional space to facilitate comparisons with experimental results, where generally variables such as liquid and gas loading rather than non-dimensional groups are controlled.

Our velocity matrix suggests that the smallest-droplets spray phenomenon does not occur simply due to an increase in gas velocity. Instead, for a fixed liquid injection speed and increasing gas injection speed, the liquid suffers a diminished sinusoidal interfacial structure in the streamwise direction; only transverse wave modes are visible, in which surface tension forces dominate over aerodynamical forces leading to a "ligament merging" behaviour. The droplets generated in this instance are rather big. Interestingly, there seems to be a stronger change in the atomisation mechanism going along the vertical axis of increasing liquid injection velocity. Only under higher liquid speeds does there appear to be an atomisation scenario with an overall sheet-to-small drop transition that takes place. This casts no doubt on the fact that the best atomisation characteristics seem to occur in the uppermost section of the matrix, with a dominant longitudinal oscillation of the liquid film and rapid development of perpendicular transverse waves. The observed regime was named "3D wave modes". However, in this atomisation scenario, breakup does not occur in the vicinity of the prefilmer lip, which is essential for aircraft engine combustion applications, but further downstream. Nevertheless, the liquid drops generated are rather small ($\sim 100\mu$m). For very low liquid flow rates, liquid accumulates at the atomising edge and experiences deformation by which an intermittent liquid release occurs. The liquid structures and droplets generated are rather big (~ 0.6mm). This is because the liquid entrained into the vortex at the prefilmer lip is rather slow and thick. The gas stream is not fast enough to empty the liquid reservoir in a way to promote fine atomisation. We call this regime "accumulation". Finally, for very low liquid flow rates and very high gas flow rates, relevant to the injection conditions of the industry [89], a combination of liquid accumulation at the lip and thick rim-driven retraction of the film is observed.

These observations are summarised into a schematic regime map of atomisation, as shown in Fig. 6.6. We have here attempted to place the liquid film breakup phenomena in an organised perspective. There seems to be a few breakup regimes which reflect the action of the different forces on the liquid film causing changes in film appearance. The visual evidence of variations in the behaviour of liquid films as the test conditions were changed are analysed in the light of previous numerical and experimental studies on the subject. These variations are elaborated upon in the following sections and their implications on the atomisation mechanism are discussed.

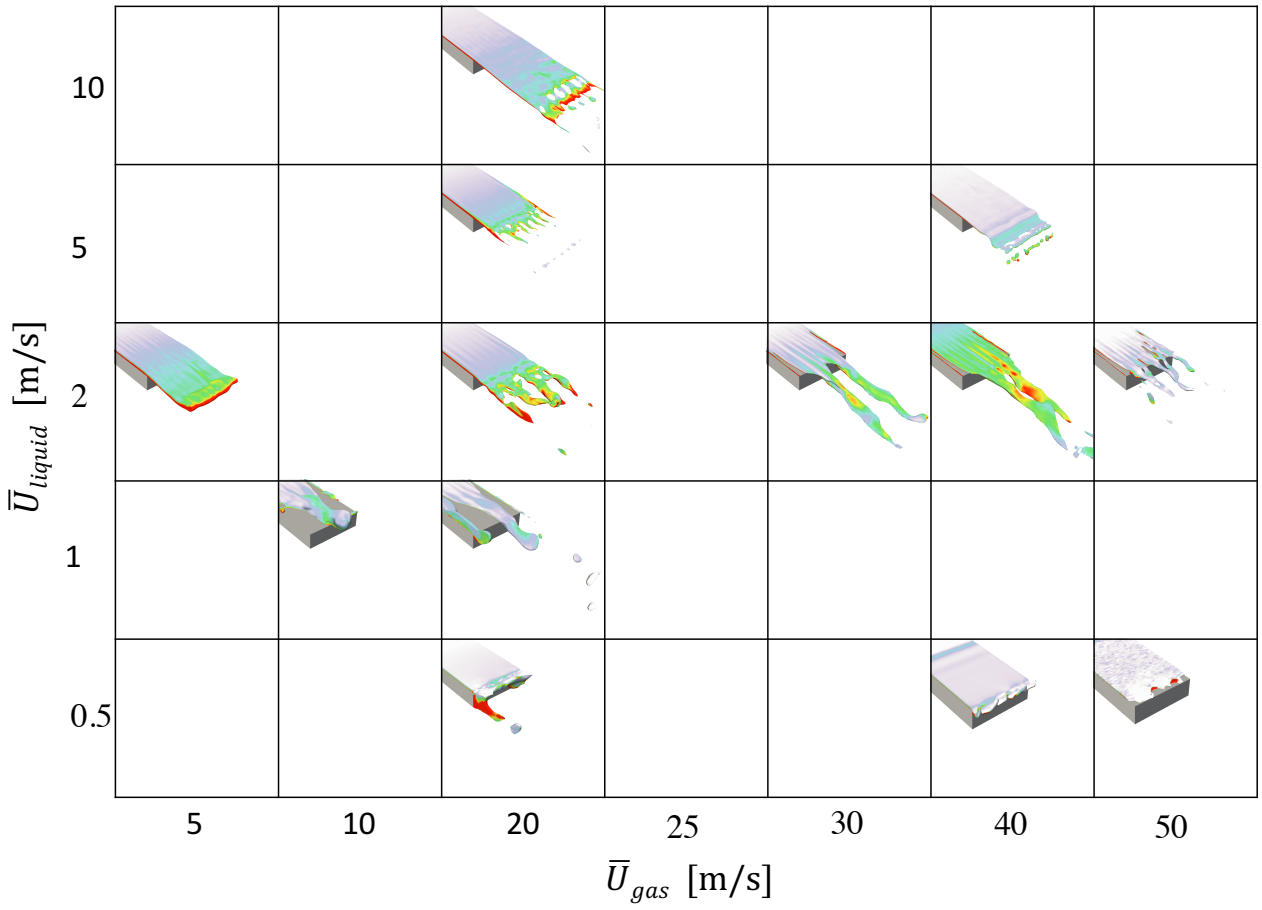

Fig. 6.5: Matrix representation of the observed liquid film breakup phenomena over our velocity parametric space.

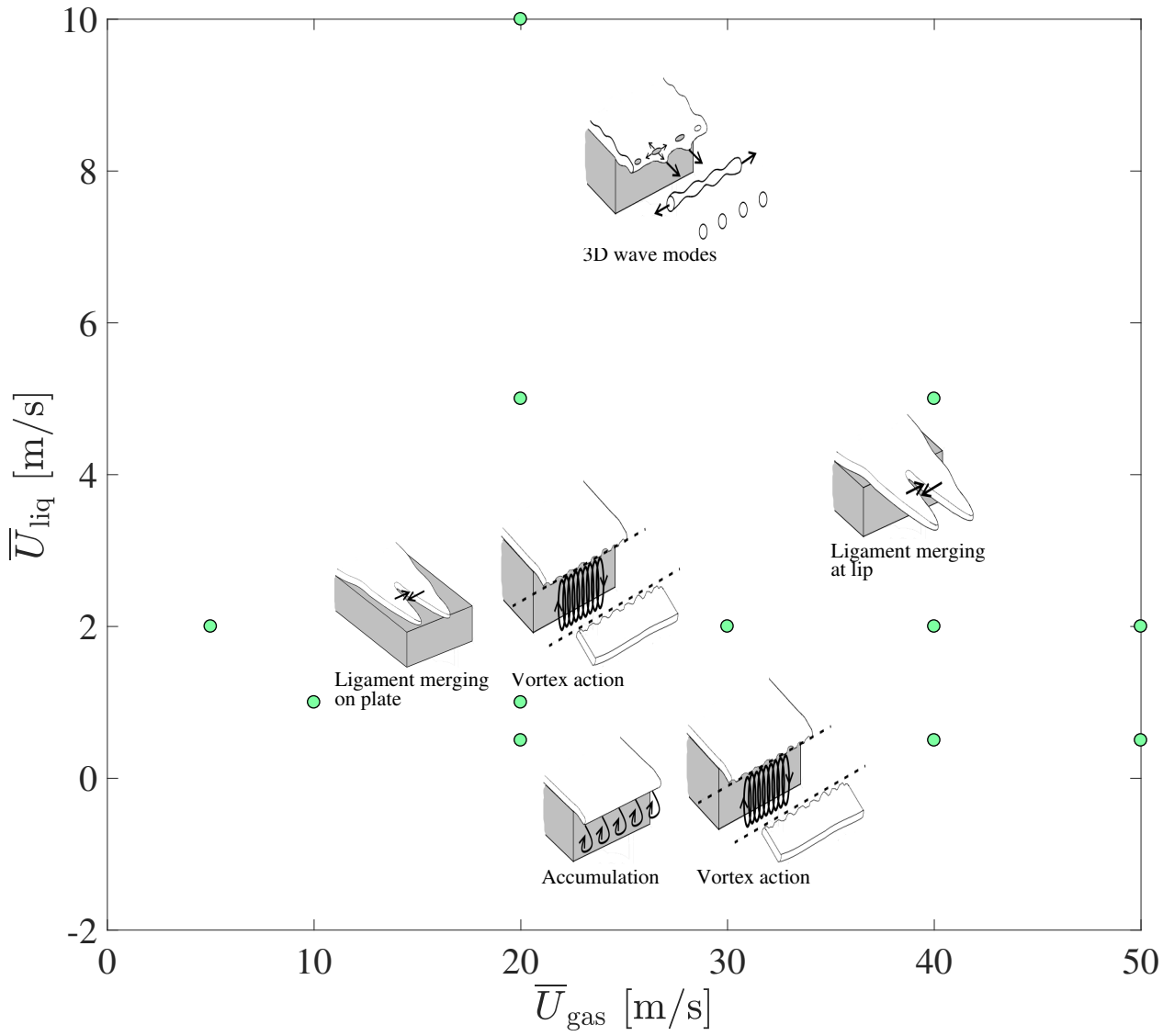

Fig. 6.6: Regime map obtained from our numerical simulation operating points (*green dots*) for prefilming liquid film atomisation.

6.3.1.2 Mechanisms of atomisation

6.3.1.2.1 Atomisation by accumulation

For liquid flow rate as low as 0.5m/s, the bulk liquid accumulates close to the atomising edge, as previously witnessed in the experiments of Gepperth et al. [72], Inamura et al. [95] and Déjean et al. [48]. Here, surface tension effects oppose any wave growth via inertial forces. As a consequence, this type of atomisation seem to be decoupled from any wave development appearing on the liquid film surface. A very similar breakup phenomenon was observed by Gepperth et al. [70] in annular airblast injectors, suggesting its relevance to real atomisers, as well as by Sauer et al. [183] and Warncke et al. [229] who numerically studied this mechanism. Fig. 6.7 shows a series of snapshots for the liquid film evolution with a bulk gas velocity of $\overline{u}_{\text{gas}} = 20\text{m/s}$ and $\overline{u}_{\text{liq}} = 0.5\text{m/s}$. Prior to breakup, at 14ms (Fig. 6.7a), an initial cell-like structure in the sheet – or membrane – is visible. This membrane is a result of the thickness modulations on the liquid film, whose amplitude grows until it becomes of the order of the liquid film thickness and the film perforates, as witnessed in the earlier experimental works of Bremond et al. [24] for example. This membrane grows in time before bursting, building the onset of primary breakup at 15ms (Fig. 6.7b). This is an indication of the surface tension effect, as well as the shearing action of the gas on the liquid at the lip. We also note that the pinch-off of membranes at the troughs creates regions of very low velocity and non-wetting of the plate. The bursting of this membrane is accompanied by the creation of a streamwise ligament that remains attached to the rim of the liquid bulk, which facilitates the pinch-off events through aerodynamic tearing. At 27ms (Fig. 6.7c), a large ligament stretches away from the liquid core rim in the streamwise direction and pinches off into a droplet that is accelerated into the air. Then, the liquid reservoir at the lip is refilled and the whole process starts again (Fig. 6.7d-f). From a qualitative point of view, this configuration has the advantage to limit atomisation in a small and controlled area. However, overall, this yields to the generation of droplets whose diameter exceed the initial liquid film thickness. The difference between the velocity of the observed large drop and the gas (Fig. 6.7c) can be attributed to the poor response properties of larger droplets [61].

The liquid attachment at the prefilmer lip via a meniscus [127] is an important physical and chemical aspect to be considered in substrate wetting properties. The liquid wetting behaviour might change depending on the chosen substrate. For example, Gepperth et al. [72] and Gepperth et al. [70] who only observed a liquid accumulation type of breakup, use a prefilmer made of acrylic plastic in order to enable visualisation of the liquid film by their shadowgraphy measurement technique. But they do not report on the level of hydrophobicity

of that surface. They identify however the effect of the thickness of the trailing edge as a parameter influencing spray characteristics, in which for prefilmer heights smaller than the average film thickness, the impact of the trailing edge seems to be reduced. Braun et al. [23] numerically addressed the question how the trailing edge thickness does affect the atomisation and at which scales a further reduction of the trailing edge height no longer has an influence. It was shown that for trailing edge heights below 100μm, a further height reduction does not significantly alter the breakup mechanism. Therefore, there appears to be a necessary scope to evaluate the impact of a change in prefilmer geometry as well as liquid wetting behaviour comprising contact angle hysteresis relevant to the manufactured injection nozzles.

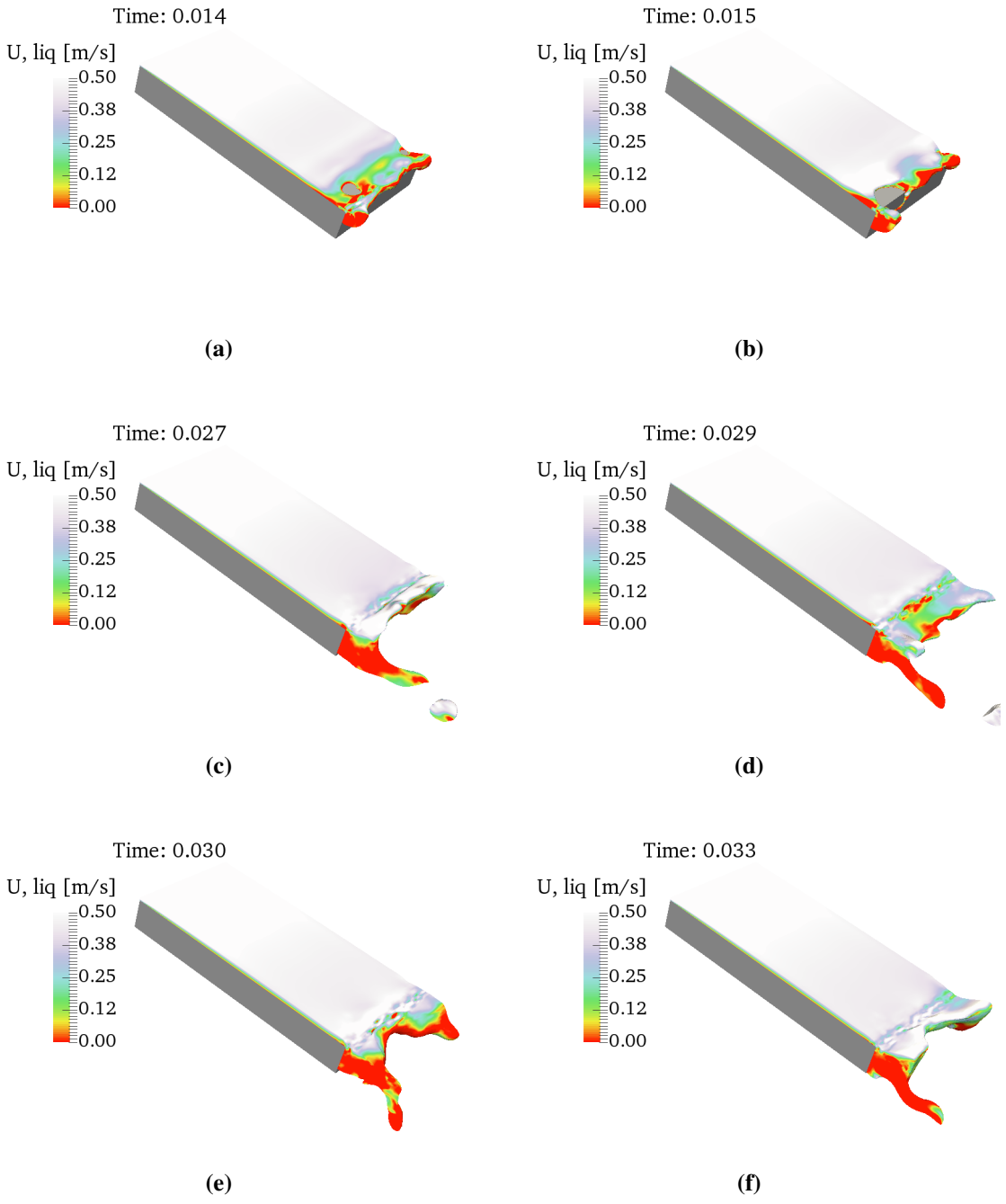

Fig. 6.7: Iso-surface of $\phi_\Gamma = 0.5$ coloured by liquid velocity for $\overline{u}_{\text{gas}} = 20\text{m/s}$ and $\overline{u}_{\text{liq}} = 0.5\text{m/s}$ showing the effect accumulation at the prefilmer trailing edge. Development of a membrane puncturing the liquid film **(a)** which breaks up **(b)** into a streamwise ligament that elongates and sheds a droplet into the air stream **(c-d)** before the liquid reservoir at the lip is refilled and the whole process starts again **(e-f)**.

6.3.1.2.2 Atomisation by hydrodynamic instabilities

For a mean liquid injection speed greater than 2m/s, the simulations picked up a clear surface wrinkling due to the growth of linear instabilities at the interface location: these include longitudinal instabilities as well as transverse instabilities and the development of both spanwise and streamwise ligaments disintegrating into smaller liquid structures. Instantaneous snapshots in Fig. 6.8 and Fig. 6.9 illustrate this behaviour. We will go into more detail on the wavy-surface mechanism with three-dimensional perpendicular wave modes in Section 6.3.2.

Here, droplet formation results therefore from the unstable growth of short wavelength surface waves on the surface, due to the relative motion of the liquid film and ambient gas. The droplets produced from the liquid surface have decreased significantly in size from the former "accumulation" atomisation regime. Indeed, for a fixed gas velocity at $\overline{u}_{\text{gas}} = 20$m/s, an increasing liquid velocity from $\overline{u}_{\text{liq}} = 0.5$m/s to 10m/s induces a higher inter-phase shearing ratio. The ligaments formed are small in size, which leads to small drops being generated. As the mean gas velocity is increased from 20m/s (Fig. 6.8) to 40m/s (Fig. 6.9) – with $\overline{u}_{\text{liq}}$ held constant at 5m/s – a higher amplitude sinuous mode develops on the liquid film and travels downstream, helping promote atomisation.

The tangential shearing forces at play act on the ligaments and cause them to be destabilised over rather short time periods and thus lead to early fragmentation. This is conducive to better atomisation in terms of timescales. However, since the liquid phase is so fast, the liquid core rim has had time to reach the end of the prefilmer before the first atomisation events take place; the liquid film "shoots-off" the prefilmer trailing edge and atomisation happens many film thicknesses downstream. This spatial delay in the onset of atomisation is problematic with regards to jet-engine combustion. It would be interesting to investigate on the impact a longer prefilmer would have on this regime: would the hydrodynamic instabilities occur at the same location downstream of the injection point when supported underneath by the solid plate? A preliminary study we conducted points in that direction [18]. However, the length of the prefilmer has been reported by Déjean et al. [48] to have an impact on the atomisation process: an increase in the prefilming length induces first a decrease in the breakup length up to an optimal length, while conversely, longer plates will induce an increase in the breakup length.

6.3.1.2.3 Ligament-merging regime

For a fixed liquid injection velocity of 2m/s, the mean gas velocity was varied spanning a range from 5m/s to 50m/s, which correspond to a parabolic profile centreline velocity

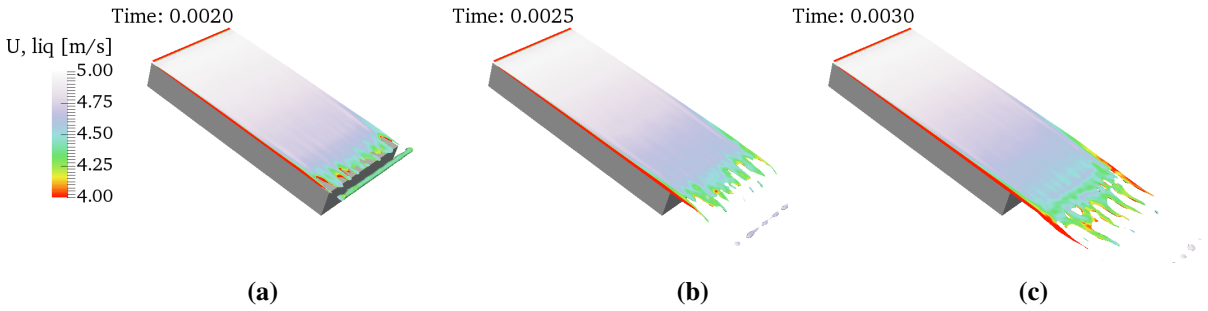

Fig. 6.8: Interface location coloured by liquid velocity for $\overline{u}_{\text{gas}} = 20\text{m/s}$, $\overline{u}_{\text{liq}} = 5\text{m/s}$. First, a transverse roll ruptures into drops under capillary breakup, followed by the formation and elongation of longitudinal ligaments and their pinch-off.

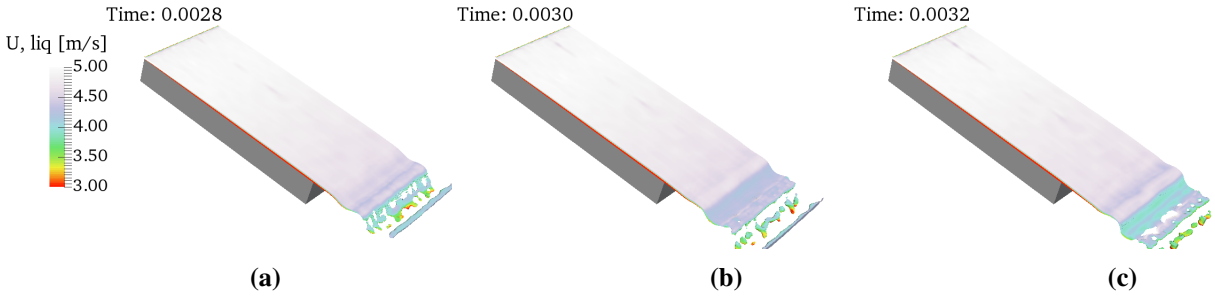

Fig. 6.9: Interface location coloured by liquid velocity for $\overline{u}_{\text{gas}} = 40\text{m/s}$, $\overline{u}_{\text{liq}} = 5\text{m/s}$. Membrane puncturing and formation of transverse ligaments that rupture into drops under capillary breakup.

of 10m/s to 100m/s. In every flow configuration, transverse ripples dominate the thickness modulation of the liquid film and exhibit higher wavelengths than longitudinal ripples. The high-speed gas co-flow seems to constrain the growth of sinusoidal longitudinal waves, a comment also made by Lozano & Barreras [135]. Indeed, longitudinal instabilities seem not to have an impact on the thickness modulation of the liquid film. They can be seen only through highlighting the velocity field mapped on to the liquid/vapour interface contour (Fig. 6.10). Transverse waves on the other hand do induce thickness modulations from which liquid structures elongated in the streamwise direction emerge. The liquid is drawn out from the atomising lip in the form of long streamwise ligaments. As more liquid is injected, it feeds the growth of these ligaments, which merge and pair up over time, as depicted in Fig. 6.11 through Fig. 6.13. As the ligaments reach for the prefilmer lip, they remain attach to it and break up by pinching off the remaining liquid bulk. The result from such an atomisation regime in which the surface tension forces dominate over the inertia forces is that droplet

sizes tend to be bigger. A similar ligament-merging behaviour occurs for smaller mean gas velocities and a fixed liquid injection velocity of 1m/s (Fig. 6.14). Considering that the liquid stream is not fully wetting the prefilmer as the ligaments develop and merge with one another, sometimes quite early onto the prefilmer plate, these results might be of high relevance for other applications such as the surface treatment of substrates, in which wetting with washing or etching liquids is critical [234]. The accurate application of the dynamic contact angle outlined in Chapter 3, Section 3.9 would be particularly relevant in the present case in order to account for the complex liquid wetting behaviour observed.

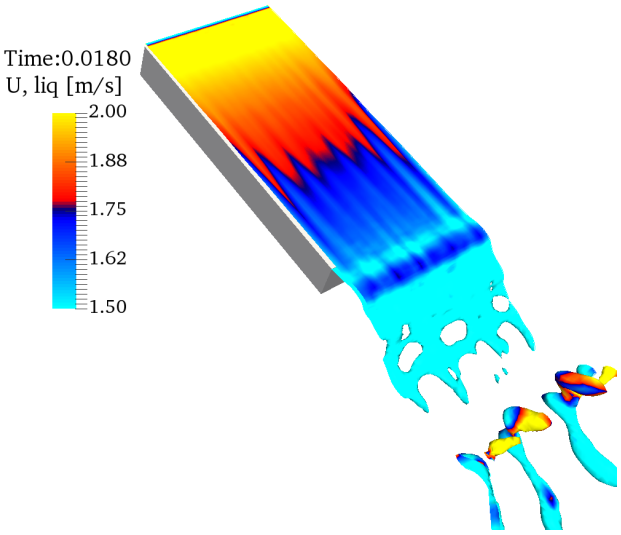

Fig. 6.10: Interface location coloured by liquid velocity for $\overline{u}_{\text{gas}} = 20\text{m/s}$ and $\overline{u}_{\text{liq}} = 2\text{m/s}$ showing the longitudinal wavelengths.

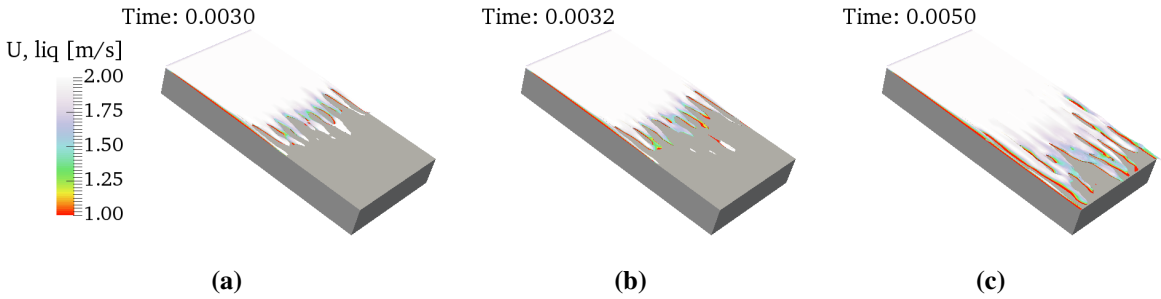

Fig. 6.11: Interface location coloured by liquid velocity for $\overline{u}_{\text{gas}} = 50\text{m/s}$ and $\overline{u}_{\text{liq}} = 2\text{m/s}$ showing the ligament-merging dynamics as they evolve on the prefilmer plate.

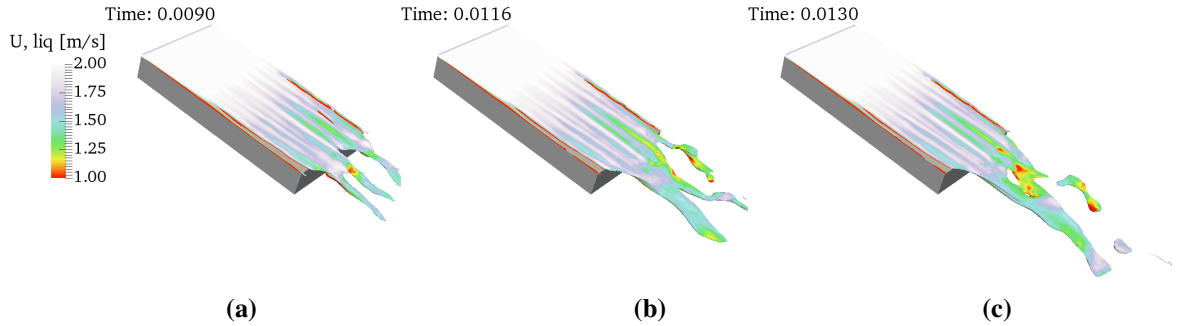

Fig. 6.12: Interface location coloured by liquid velocity for $\overline{u}_{\text{gas}} = 40\text{m/s}$ and $\overline{u}_{\text{liq}} = 2\text{m/s}$ showing the ligament-merging dynamics encountered for an increasing gas injection velocity at the prefilmer lip.

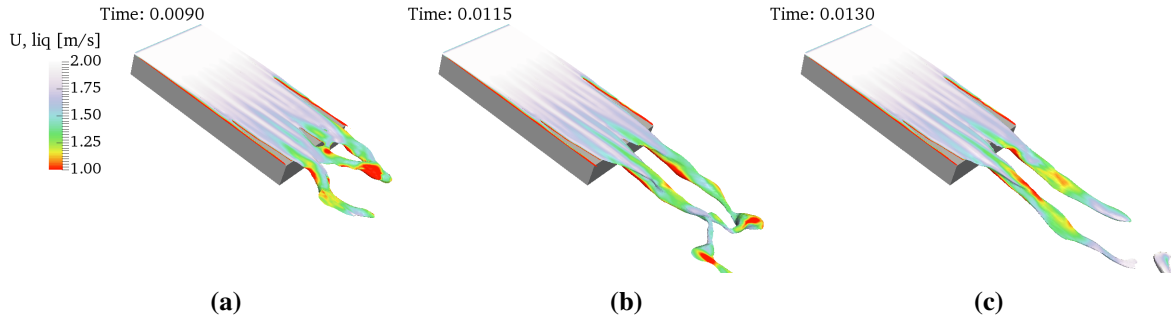

Fig. 6.13: Interface location coloured by liquid velocity for $\overline{u}_{\text{gas}} = 30\text{m/s}$ and $\overline{u}_{\text{liq}} = 2\text{m/s}$ showing the ligament-merging dynamics encountered for an increasing gas injection velocity at the prefilmer lip.

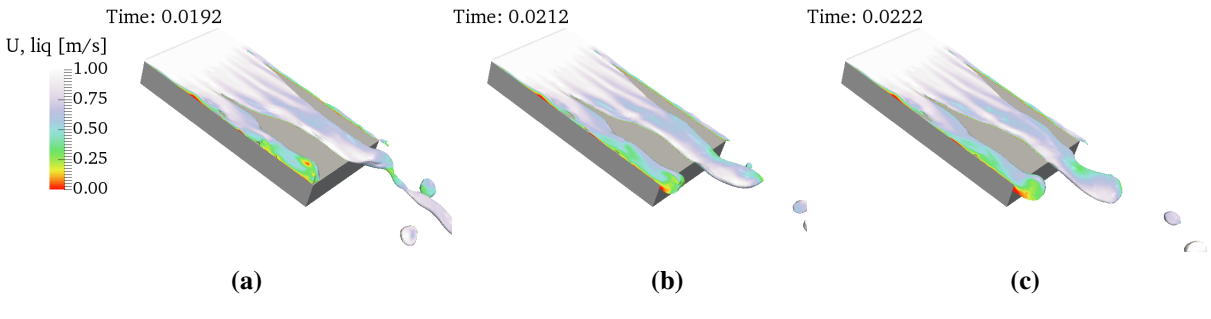

Fig. 6.14: Interface location coloured by liquid velocity for $\overline{u}_{\text{gas}} = 20\text{m/s}$ and $\overline{u}_{\text{liq}} = 1\text{m/s}$ showing the ligament-merging dynamics encountered on the prefilmer plate for a lower liquid velocity.

6.3.1.2.4 Atomisation by vortex action

The liquid film is a thin and flexible membrane that flutters like a flag in the longitudinal direction. Although this flapping mode is commonly understood to originate from the Kelvin–Helmholtz instability growth downstream (see Section 2.1.1.1), it also appears that the vortices in the gas stream are interacting with the flapping interface. As a result, vortex action in the gas stream is also a vehicle for atomisation. For example, for a mean gas velocity of $\overline{u}_{\text{gas}} = 20\text{m/s}$ and liquid injection velocity of $\overline{u}_{\text{liq}} = 2\text{m/s}$, once the liquid film has passed the atomiser lip and is supported by the two gas-streams, vortex rotation is influencing the underside of the liquid surface, as apparent on Fig. 6.15. When the liquid film bends upwards, pushed by the underneath vortex core, and obstructs the gas stream (Fig. 6.15b), it is exposed to relatively high aerodynamic forces, which promote primary breakup (Fig. 6.15c). Agbaglah et al. [4] and Fuster et al. [69] also noted the intense and extended gas vortices generated that interact with the liquid bulk, and indicated that the fluctuations in the gas stream play an important role in the breakup of the liquid. Similarly, for an equivalent mean gas velocity but a smaller liquid injection speed of $\overline{u}_{\text{liq}} = 0.5\text{m/s}$, gas vortices also help in tearing the liquid bulk apart, as can be seen in Fig. 6.16. As opposed to originating from the recirculation zone underneath the liquid film as discussed previously, here a gas vortex is formed from the top gas channel thus affecting the upper side of the sheet and causing the tip of the liquid film to bend upward and the trough of the wave downwards – before the entire structure is separated from the remaining liquid stream. We named this wavy sheet atomisation mechanism, “vortex action”. It has been witnessed by several experimentalists for both non-prefilming [68, 224] and prefilming configurations [15].

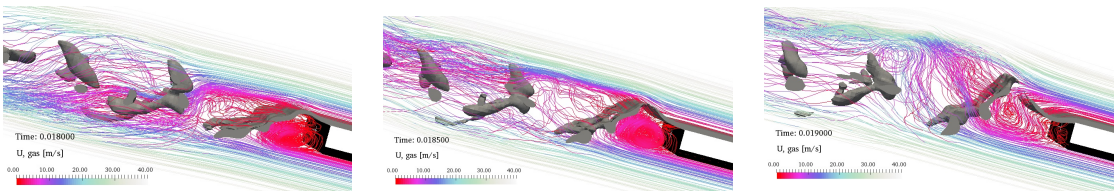

(a) **(b)** **(c)**

Fig. 6.15: Air streamlines revolving around the liquid bulk. Flapping is promoting atomisation. $\overline{u}_{\text{gas}} = 20\text{m/s}$, $\overline{u}_{\text{liq}} = 2\text{m/s}$.

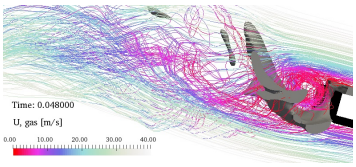

Fig. 6.16: Disintegration by vortex action. A strong vortex core is coming from the top gas channel. $\overline{u}_{\text{gas}} = 20\text{m/s}$, $\overline{u}_{\text{liq}} = 0.5\text{m/s}$.

6.3.1.2.5 Rolls-Royce plc. operating points

It should be noted that in the gas turbine application, the air velocity could be greater than the maximum value investigated so far. For example, in the injection systems of Rolls-Royce mean free stream velocities could be greater than 100m/s, especially at conditions such as take-off and cruise [89]. We thus choose to extend the regime mapping towards higher gas/liquid velocity ratios, which stems from the need to shed some light on the atomisation process at industrially relevant injection conditions. Fig. 6.17 shows the results for $\overline{u}_{\text{gas}} = 40\text{m/s}$ and $\overline{u}_{\text{liq}} = 0.5\text{m/s}$ while Fig. 6.18 displays the results for $\overline{u}_{\text{gas}} = 50\text{m/s}$ and $\overline{u}_{\text{liq}} = 0.5\text{m/s}$. In both instances, we observe a rather peculiar behaviour. A thicker rim connected to the thin liquid film combined with a retraction dynamics qualitatively coincides with the formation of a rim instability driven by surface tension, as described in Chapter 2, Section 2.1.1.2. The Taylor–Culick instability is the result of a low Ohnesorge number ($\text{Oh} < 0.1$), i.e. high viscosity, rim-driven retraction. It should be noted though that there may be an important difference between the rim instability observed here and those seen for example in droplet splashes (Chapter 3 and 4) where the interaction with an energetic gas motion was absent [131].

In Fig. 6.17, the newly formed rim bordering the liquid film at the prefilmer lip gets thicker than the film to which it is attached. As liquid gathers into the rim, it starts to flap gently at the lip through its exposure to the aerodynamic forces in the gas streams (Fig. 6.17a). This perpendicular acceleration sets off a transverse instability. The rim destabilises into a series of transverse waves. The rim corrugations finally lead to its destabilisation into rather thick ligaments (Fig. 6.17f) and disintegration into big droplets (Fig. 6.17h).

In Fig. 6.18, following the disintegration of the liquid rim into tiny liquid structures from $t = 0.58\text{ms}$ to $t = 0.74\text{ms}$, one can observe the dewetting of the prefilmer, imparted by a recession dynamics of the rim of the liquid film (Fig. 6.18b-g). The film retracts under the influence of the capillary force acting at its edge. At $t = 1.84\text{ms}$, the surface tension force then appears to favour the formation of two ligaments, one on either side of the plate (Fig. 6.18h),

before the liquid film starts moving forward again. Again, the accurate application of a dynamic contact angle model would be particularly relevant in the present case in order to account for the complex liquid wetting behaviour observed.

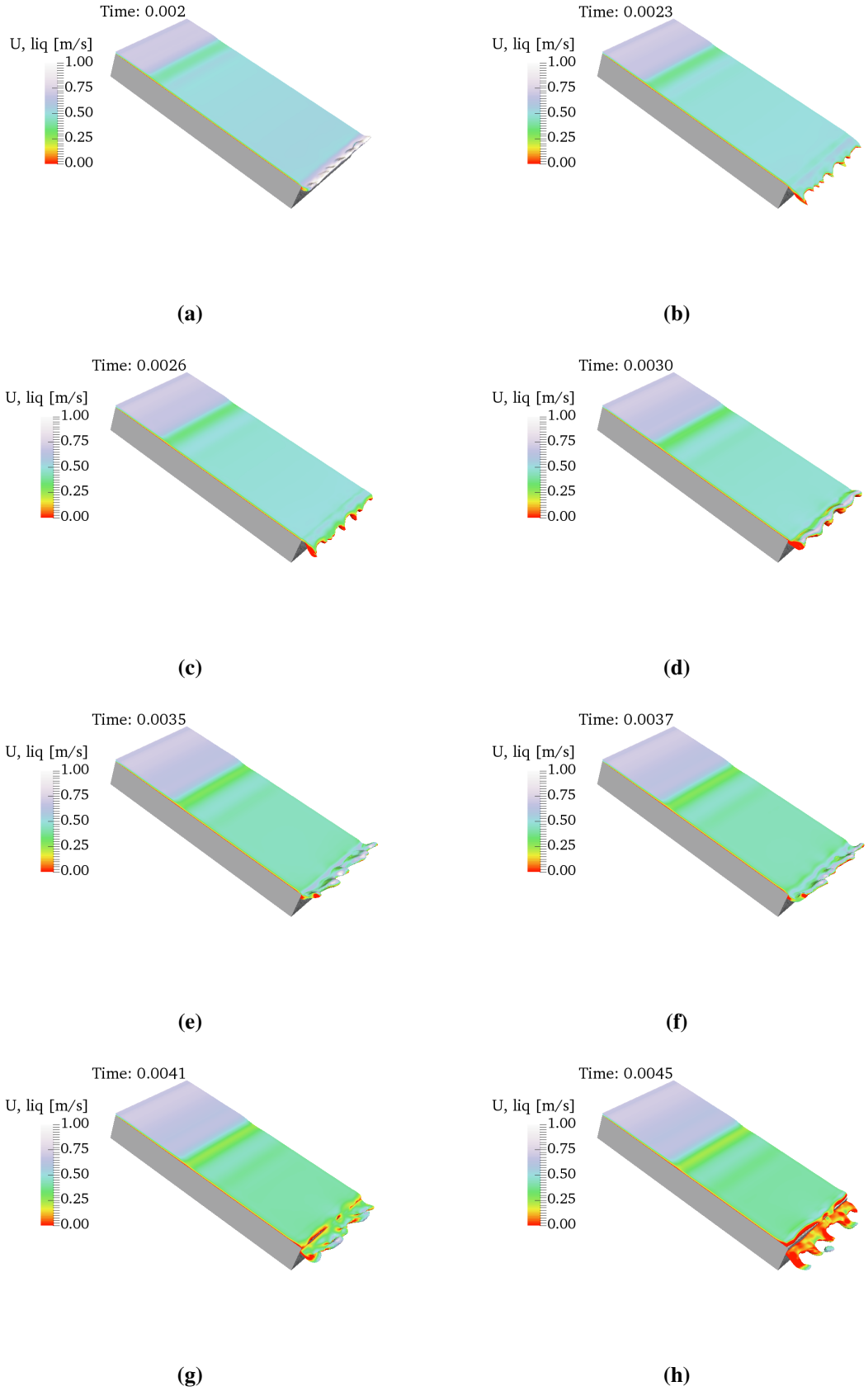

Fig. 6.17: Injection conditions relevant to velocities encountered in the aeronautical industry: $\overline{u}_{\text{gas}} = 40\text{m/s}$, $\overline{u}_{\text{liq}} = 0.5\text{m/s}$. The centreline velocity of the gas parabolic velocity profile is 80m/s. Note that ambient pressure and temperature have been retained for direct comparison with the other operating points investigated as part of our cartography exercise.

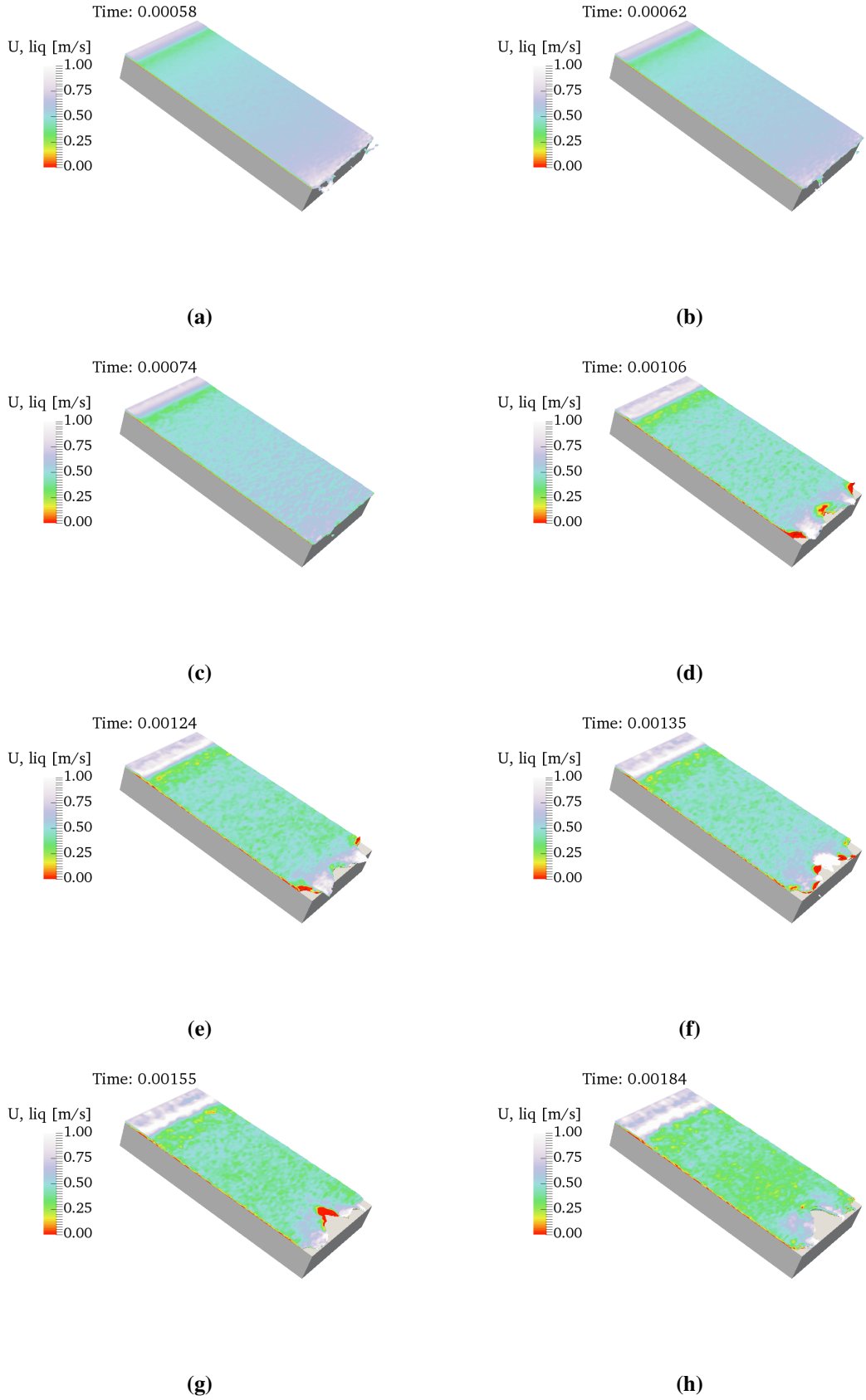

Fig. 6.18: Velocity injection conditions relevant to the aeronautical industry: $\overline{u}_{\text{gas}} = 50\text{m/s}$, $\overline{u}_{\text{liq}} = 0.5\text{m/s}$. The centreline velocity of the gas parabolic velocity profile is 100m/s. Red indicates negative velocities.

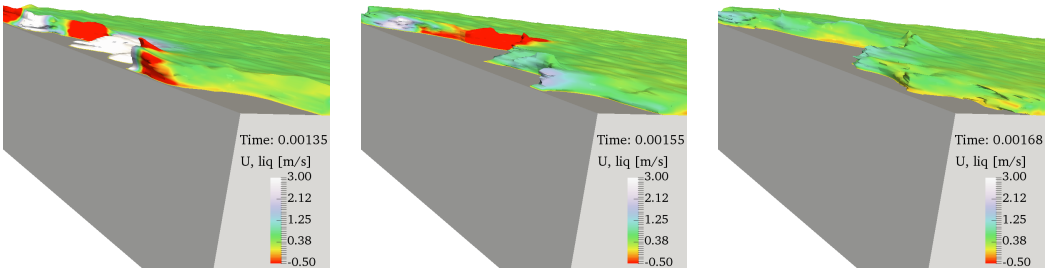

(a) **(b)** **(c)**

Fig. 6.19: Close-up view of the liquid film rim at the prefilmer lip for $\overline{u}_{\text{gas}} = 50\text{m/s}$, $\overline{u}_{\text{liq}} = 0.5\text{m/s}$.

6.3.2 Interfacial behaviour: a shearing matter

6.3.2.1 Formation of surface waves

The velocity profile is unstable before an equilibrium configuration is reached between the gas and liquid streams: a two-phase unidirectional channel Poiseuille flow develops on the upper side of the prefilmer, in accordance with two-phase flow theory over a solid plate [206]. The liquid film is accelerated downstream by the gas, and the shear-driven liquid wall film advances. The development of longitudinal surface instabilities is mainly dependent on the inter-phase velocity difference, a result of the aerodynamic forces from the high-speed coflowing gas, believed to arise from a Kelvin–Helmholtz instability of the mixing layer, as predicted by stability analysis and weakly non-linear theories (see Section 2.1.1.1). This characterises the initial unstable growth of the fundamental undulations of the liquid film. Instantaneous snapshots in Fig. 6.20 illustrate this behaviour, also witnessed and discussed in the several experimental works [e.g. 15, 48]. In addition to longitudinal undulations, transverse instabilities appear. The longitudinal Kelvin–Helmholtz instability foreshadows the appearance of the transverse Rayleigh–Taylor instability. Such a combination of surface waves in both orthogonal directions leads to a periodic variation of the sheet thickness. This causes the formation of ligament-like structures, whereby the sheet thickness is greater than its mean height, and cell-like structures, enclosed in-between two ligaments, whereby the sheet thickness is reduced (Fig. 6.20). The capture of the longitudinal and transverse instabilities that appear further downstream of the injection point confirms the three-dimensionality of the flow as it has transited in the non-linear regime. This suggest that 2-D calculations are unsuitable and therefore tend to validate the need for the 3-D numerical approach taken in this work. However, when both the liquid and gas are injected at very low speeds ($\overline{u}_{\text{gas}} = 5\text{m/s}$ and $\overline{u}_{\text{liq}} = 2\text{m/s}$), it appears that not enough shearing intensity is exerted onto the liquid film

to provoke the formation of strong surface waves, let alone ligaments and droplets (Fig. 6.21). This could be due to either an insufficient absolute value for the gas speed or the absence of enough shearing, or an interplay between both. We postulate that the timescale required for the initiation of shearing instabilities is longer and is happening further downstream, outside the modelled computational domain.

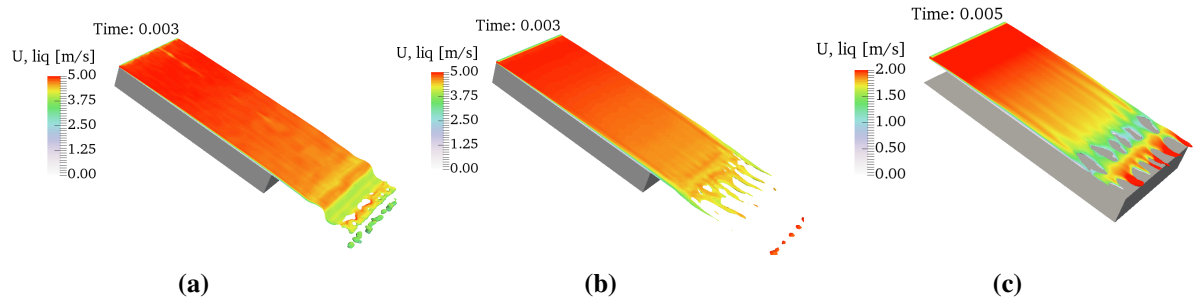

Fig. 6.20: Interface location coloured by liquid velocity. Membrane puncturing as well as longitudinal and transverse ligaments rupturing into drops are visible: **(a)** $\overline{u}_{\text{gas}} = 40\text{m/s}$, $\overline{u}_{\text{liq}} = 5\text{m/s}$; **(b)** $\overline{u}_{\text{gas}} = 20\text{m/s}$, $\overline{u}_{\text{liq}} = 5\text{m/s}$; **(c)** $\overline{u}_{\text{gas}} = 20\text{m/s}$, $\overline{u}_{\text{liq}} = 2\text{m/s}$.

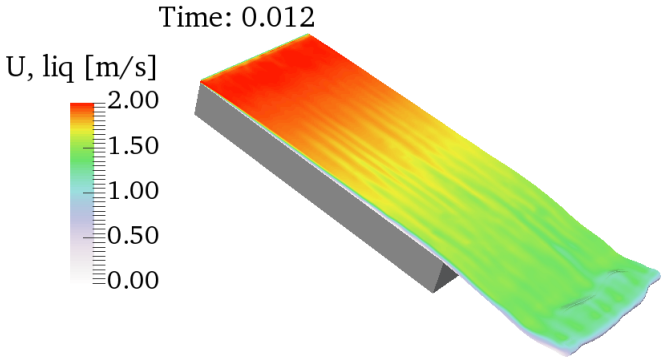

Fig. 6.21: Interface location coloured by liquid velocity for $\overline{u}_g = 5\text{m/s}$, $\overline{u}_l = 2\text{m/s}$. The velocity pattern highlights minor longitudinal and transversal instabilities; the shearing intensity is not enough to destabilise the liquid film.

6.3.2.2 Disintegration into drops

The combination of the two three-dimensional wave modes leads to the formation of cell-like structures, which are responsible for the sheet indentations. These are the precursors of

groups of ligaments. Indeed, it is clear from Fig. 6.20c that the bursting of the membranes associated with the cell-like structures is accompanied by the creation of "liquid cylinders" (Fig. 6.9a-b), both spanwise and streamwise ligaments. When inertial stresses induced by the surrounding high-speed co-flowing gas stream exceed the surface tension stresses opposing the liquid deformation sufficiently, the ligament will subdivide into smaller units. Fragmentation of the ligaments starts along the streamwise direction when ligaments have been generated and elongated in the streamwise direction – under aerodynamic tearing due to the strong streamwise air velocity field (Fig. 6.20b) – whereas ligaments seem to be mostly unstable due to capillary effects (capillary instability of a liquid cylinder that resembles the Plateau–Rayleigh instability) and break apart in the transverse direction when first generated in the transverse direction (Fig. 6.20a).

6.3.3 Competing for inertia: behaviour at the prefilmer lip

6.3.3.1 Vortex shedding

Before the arrival of the liquid film, an unsteady wake appears behind the atomiser edge, similar to the flow behind square cylinders: the vortex rotation patterns are different for each velocity configuration (Fig. 6.22). The pattern of the velocity field resembles vortex shedding (similar to von Kármán vortex streets) inducing alternating vorticity on both sides of the centreline. Vortex shedding is particularly visible in Fig. 6.23a but was noticed in all flow configurations. As the gas is injected on either side of the liquid injection plate and interacts with it, boundary layers will appear on both sides of the injector, generated due to the no-slip condition on all solid surfaces. As the flow gets to the plate lip, and because the prefilmer plate has a certain thickness, the boundary layers detach at the edge of the atomiser. Once the liquid film approaches the trailing edge of the prefilmer plate, the downstream region vortex shedding is suppressed (Fig. 6.23b) and the regularity of the velocity variation is lost. This is due to the vortex streets being unstable to 3-D disturbances. An abrupt change in boundary condition is experienced as the re-arrangement of the entire cross-sectional gas/liquid velocity profile takes place [217]. The vortex streets break down and a wake of irregular rapid velocity fluctuations is produced, confined in the long narrow primary breakup region. This shows the coupled character between the liquid film and the vortex dynamics of the gas flow. Agbaglah et al. [4] also highlighted the presence of annular vortical structures upon liquid injection and reported their strong interactions with liquid structures. As a result, these vortices, resulting from the geometry of the whole system, strongly influence the overall structure of the spray and the final droplet distribution.

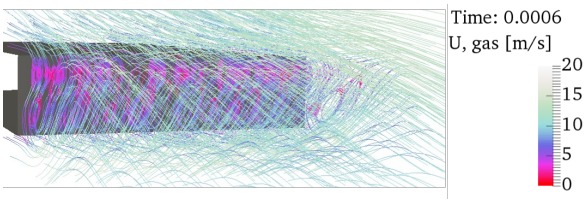

(a) $\overline{u}_g = 10\text{m/s}$, $\overline{u}_l = 1\text{m/s}$

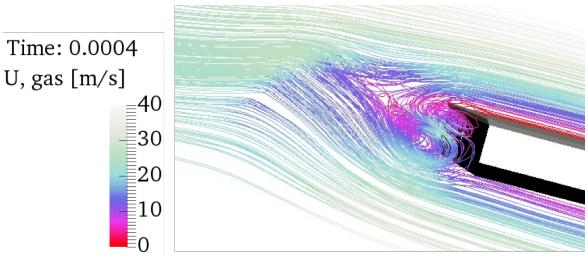

(b) $\overline{u}_g = 20\text{m/s}$, $\overline{u}_l = 0.5\text{m/s}$

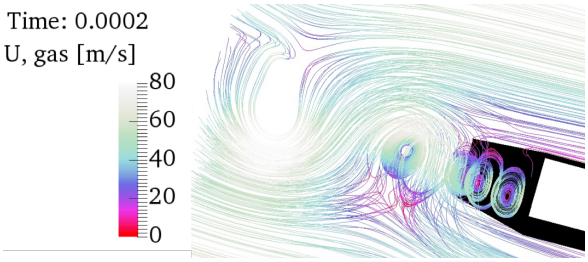

(c) $\overline{u}_g = 40\text{m/s}$, $\overline{u}_l = 5\text{m/s}$

Fig. 6.22: Vortex patterns in the recirculation zone at the prefilmer lip before the arrival of the liquid film.

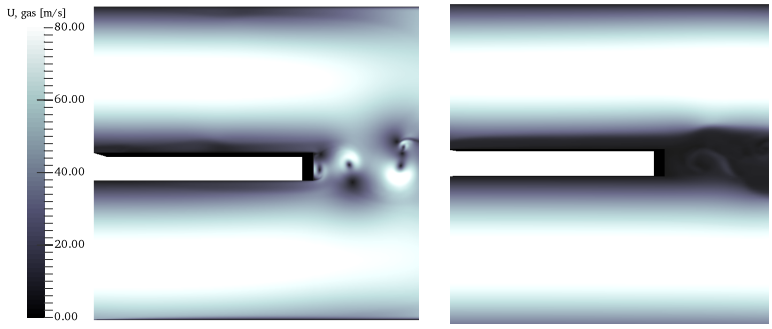

(a) **(b)**

Fig. 6.23: Velocity field magnitude. **(a)** Vortex shedding behind the squared obstacle before the arrival of the liquid film at $t = 0.0002\text{s}$; **(b)** vortex shedding is suppressed by the liquid presence at $t = 0.0185\text{s}$ for $\overline{u}_{\text{gas}} = 40\text{m/s}$, $\overline{u}_{\text{liq}} = 5\text{m/s}$.

6.3.3.2 Liquid film gliding and recirculation zone

Results show that the behaviour and development of the liquid film at the trailing edge is influenced mainly by the relative inertia of the gas and the liquid. Although the liquid occupies a smaller volume in comparison to the gas channels, and has a lower mean velocity, it is approximately a thousand times denser, hence has a major impact on the mass flow rate.

Fig. 6.24 is a view of the two-phase system with $\overline{u}_{\text{gas}} = 40\text{m/s}$ and $\overline{u}_{\text{liq}} = 5\text{m/s}$. The gas adapts itself around the liquid film. Due to its higher velocity, the liquid wall film moves faster along the prefilmer. At 3ms the liquid has already passed the prefilmer lip. The liquid film shoots off the trailing edge of the solid plate into the downstream region. It can be seen that the liquid stream is undulating longitudinally. This is not to be confused with a vortex action mechanism but rather linked to the longitudinal surface waves propagating downstream from the injection point. In fact, as the liquid film gets faster, it concentrates more and more momentum in the x-direction. Thus, any deviation in the movement of the liquid film perpendicular to the x-direction is effectively suppressed.

At the prefilmer lip, a stagnation zone of zero gas velocity co-exists with the liquid film gliding over it. The size of the recirculation zone changes depending on the length of the intact liquid film downstream of the lip. Again, this response to confinement of the recirculation zone is due to the relative inertia of the two fluids, in favour of the liquid. Hence, no severe flapping is observed due to vortex action and the gas stream follows the liquid behaviour. It appears that the liquid film oscillation/flapping downstream of the trailing edge is not responsible for the onset of primary breakup. Here, the instabilities arising from surface waves are responsible for the breakup.

As discussed earlier (Section 6.3.1.2.1), it was reported by Gepperth et al. [72] that only an accumulation-type breakup occurs for any velocity combination considered in their work. However, they observed that when the film thickness exceeds 5 times the atomising edge height, the regime evolves away from the accumulation regime: the liquid accumulation disappears and the film has enough inertia to keep its longitudinal motion and propagates into the chamber [31].

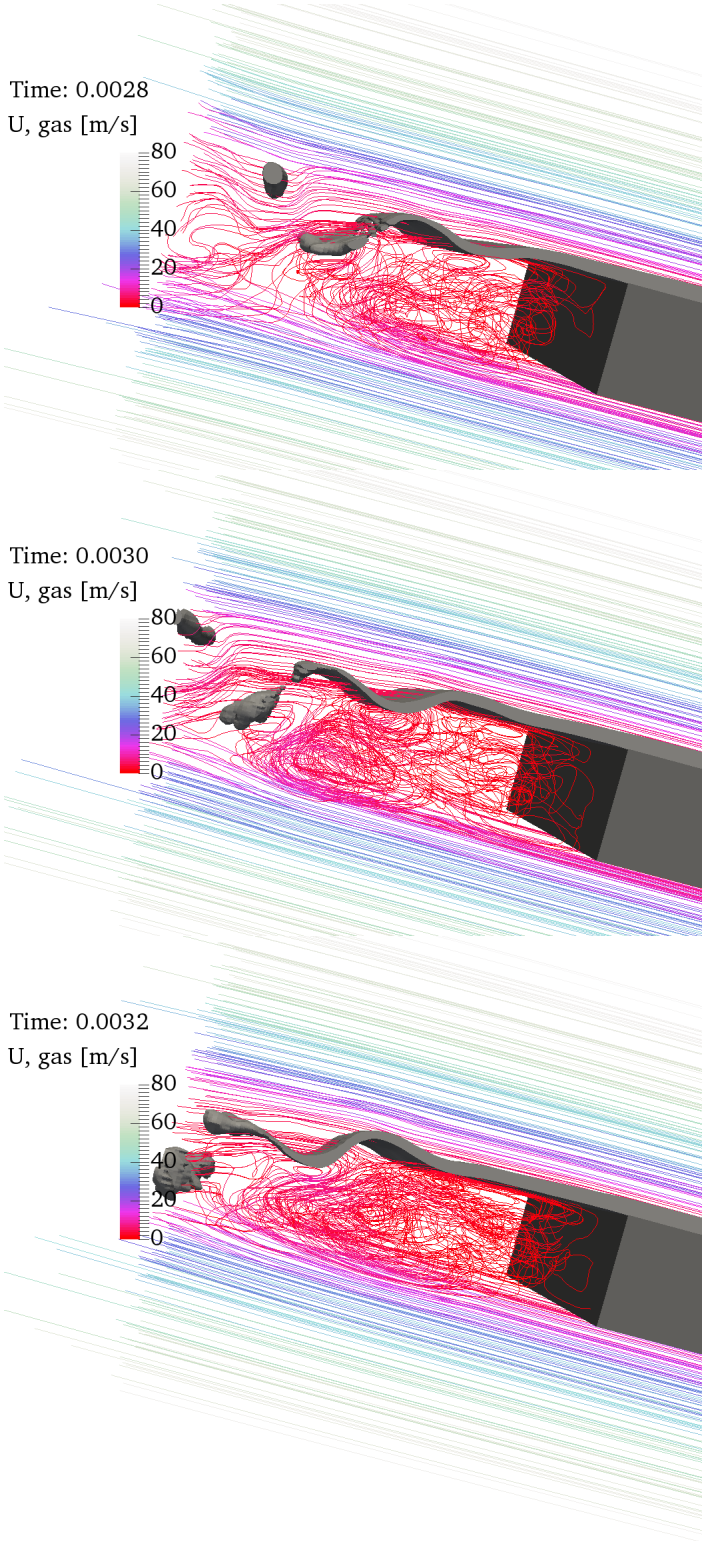

Fig. 6.24: Recirculation zone underneath the liquid film for $\overline{u}_g = 40$m/s and $\overline{u}_l = 5$m/s. The liquid inertia wins over the air displacement.

6.3.3.3 Flapping and accumulation at the trailing edge

In some instances, since the liquid film is thin and flexible, it starts fluttering under the action of aerodynamic forces. The so-called flapping is a consequence of the sinuous Kelvin–Helmholtz instability that has grown with time (see Section 2.1.1.1). We observe the flapping of the liquid film in the longitudinal direction for example in Fig. 6.25. The liquid film is oscillating in a sinusoidal fashion once the liquid has passed the atomiser lip and is supported by the top and bottom gas streams. The latter may be combined with the action of boundary layers detaching at the edge of the atomiser and reattaching themselves on the liquid film. This is the case for the atomisation mechanism discussed in Section 6.3.1.2.4 where vortex action promotes atomisation. These gas vortices acting on the top and bottom surfaces of the liquid film are interacting with the flapping phase interface. The onset of the liquid film sinusoidal oscillation modifies the pressure and velocity fields in the neighbourhood of the gas vortices to be detached. The gas, in turn, must displace the liquid film with its large inertia. Both the flapping interface and vortex sheet evolve together, sustaining one another, following each other's shape. Here, we thus observe a different behaviour in which the inertia of the liquid is no longer dominating over that of the gas, and vive versa. Pringuey [158] has also discussed the formation of Kelvin–Helmholtz rollers on either side of the liquid film when the Kelvin–Helmholtz instability builds up. It was apparent in his results that the vortices in the gaseous phase followed the shape of the interface.

The fact that liquid inertia is influential in the film flapping is confirmed by numerous measurements indicating that the oscillation frequency decreases with increasing film thickness [13, 135]. In addition, an increment in gas boundary layer thickness acts to damp the oscillations of the liquid film. This agreement reinforces our observations that for a liquid velocity held constant at 2m/s, and mean gas speed increasing from 20m/s (Fig. 6.25) to 50m/s, flapping is suppressed. One can therefore deduce that the oscillation of the liquid film, which in some instances controls the disintegration mechanism, is largely conditioned by the inertial forces exerted by the gas on the liquid on each side at the surface of the sheet.

A variation of this flapping phenomenon also takes place as the liquid flow rate is reduced and the liquid bulk accumulates at the prefilmer lip accompanied by intermittent discharges off the atomiser edge (Section 6.3.1.2.1). The deformation of the liquid accumulation at the atomising edge occurs with an intermittent liquid release, it is the result of constant fluid flow entering the prefilmer and longitudinal waves travelling downstream along the wall from the injection point where they are formed (Fig. 6.7). We see how the lip acts as a liquid reservoir and as longitudinal waves advect the high-inertia liquid into that reservoir intermittently, a longitudinal vortex rotation takes place. The vortex rotation in the recirculation zone close to

the prefilmer lip affects the liquid surface and acts to promote the intermittent liquid release and thus accumulation. Here, the liquid film is thus prone to the inertia forces exerted by the gas on each side of its surface. The combination of vortex action (gas inertia-driven) and accumulation (liquid inertia-driven and surface tension driven), appear to both act together to destabilise the liquid film at the trailing edge.

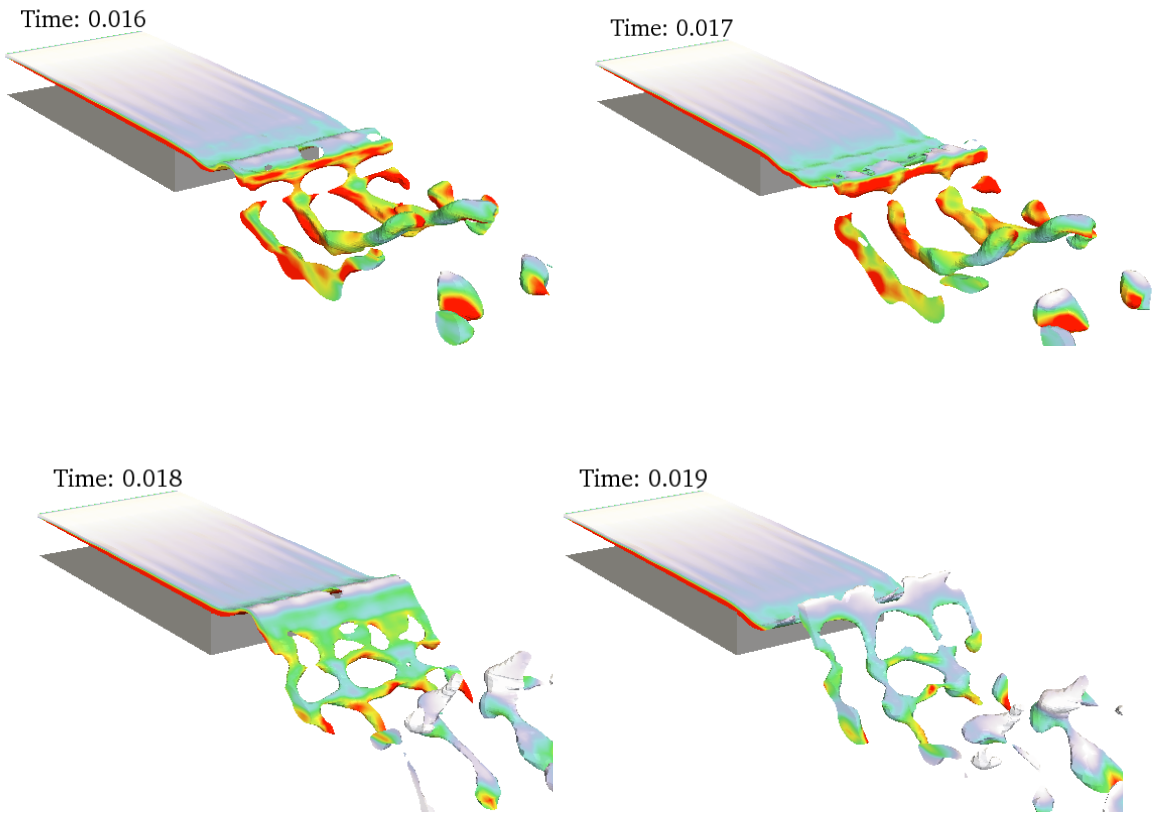

Fig. 6.25: Flapping dynamics of the liquid film for $\overline{u}_{\text{gas}} = 20\text{m/s}$, $\overline{u}_{\text{liq}} = 2\text{m/s}$.

For higher gas velocities, and while holding the liquid flow rate low and constant, the observed rim thickening, rim retraction dynamics and rim instabilities convey the impression that the liquid film destabilisation is counter intuitively not dictated by the gaseous phase inertia, but instead by the surface tension forces and high-inertia forces of the liquid bulk, in a similar manner to the ligament-merging regime where liquid ligaments were unaffected by the gas motion.

6.3.4 Shearing ratio and momentum flux ratio

All of these results show that phenomenological analyses are effective to help interpret and correlate the different behaviours of atomisation by varying the operating conditions to map a wide range of gas and liquid velocities. Our simulations satisfactorily reproduced the series of instabilities. In particular, the longitudinal Kelvin–Helmholtz instability foreshadowing the transverse Rayleigh–Taylor instability, leading to the formation of ligaments. Aerodynamic pinch off and breakup under the Plateau–Rayleigh instability were also witnessed as mechanisms for the disintegration of those ligaments into droplets. The latter conveys the importance of viscous shearing at the phase-interface between the two fluids, which will have a major influence on the occurrence and scales of these instabilities. The shear stress force exerted by the gas on the liquid surface depends on the slope of the velocity profile and the difference in viscosities (Fig. 6.26). As part of a preliminary study that was conducted earlier in this research project [18], and as shall be reported in Chapter 7, we have in some instances evidence of backwards running waves owing to a change in shear stress forces. Chaussonnet [31] noted the importance of shear stress. Indeed, a poor prediction in shear stress as part of his numerical film model, led to a wrong calculation of the liquid film thickness. Furthermore, he postulated that the neglect in modelling surface wave development considerably modified the liquid film velocity and locally impacted the wall shear stress prediction.

The present simulations have also highlighted the sensitivity of the breakup mode to the evolution of the two-phase flow downstream of the trailing edge. The latter is largely conditioned by the imbalance of interfacial forces exerted by both the liquid and the gas. On one hand, the high aerodynamical forces imparted by the gas on the liquid film dictate the liquid evolution, such as its flapping motion. On the other hand, the high inertia of the liquid film dominates over that of the gas and imparts interfacial dynamics obeying its intrinsic surface tension forces. This is supported by the observation that the momentum in the streamwise direction is mainly concentrated within the liquid and that the gas is being "pushed around" to make way for the liquid as shown in Fig. 6.27. The gas has to adapt its evolution around the liquid bulk distortion. Overall, based on the observed atomisation behaviours, the development of the liquid film on the prefilmer plate can locally be dictated by the combination of two physical forces: aerodynamic action (vortex action, membrane puncturing, ligament disintegration) and liquid surface wetting behaviours set by surface tension effects (ligament merging, rim retraction), which seem to play a major role in the atomisation process.

In light of the present numerical results, we propose the following interpretation. The dominant influence of shearing at the interface location was illustrated by an interfacial shear stress ratio in favour of liquid destabilisation for high liquid and high gas velocities, in the "3D wave mode" atomisation regime. Although the predominance of liquid inertial forces and surface tension forces at the prefilmer trailing edge is suggested by the "ligament-merging" regime and "accumulation" regime, as well as the aeronautical industry-relevant operating conditions exhibiting rim-retraction dynamics.

We believe that, despite the widespread postulate that considers the momentum flux ratio (MFR) to be one of the determining factor in classifying atomisation regimes [70, 229], other elements should be considered. In our results, there does not seem to be a linear dependence on the MFR with atomisation quality, which is in contradiction with some experimental works [64, 95]. In fact, Déjean et al. [48] witnessed for an increasing MFR a prevalence in the accumulation regime. Déjean et al. [48] also rightfully incorporated an additional dimensionless ratio based on their observations, to integrate the strong influence of the prefilmer plate length as well as the vorticity layer thickness, effectively mimicking the influence of the shear stress ratio discussed earlier.

According to the present work, the sole use of the MFR to evoke which atomisation mechanism prevails does not seem to give a full picture. A high MFR (i.e. high aerodynamic forces) is not always synonymous with an enhancement in atomisation quality. In fact, the present results lead to the opposite conclusion, whereby for low to medium liquid flow rates, an increase in gas velocity incite the liquid inertia and surface tension forces to govern the liquid film behaviour.

The common understanding that a higher aerodynamic relative Weber number (Eq. 2.3) is responsible for an enhanced atomisation [e.g. 15] is not validated by our numerical work. In fact, for reduced relative velocities (i.e. lower We) moving upwards on the regime cartography of Fig. 6.5, we observed the "3D wave mode regime" with the generation of very small droplets.

Those contradictions are not surprising, as of yet, there is no universal consensus among the scientific community regarding which additional fluid parameters and geometrical parameters characterise the breakup process in liquid film configurations. Hence, a common definition of the relevant non-dimensional groups is still lacking.

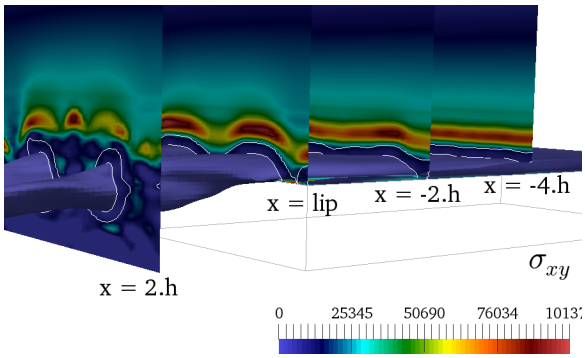

Fig. 6.26: Iso-surface of $\phi_\Gamma = 0.5$ for $\overline{u}_g = 30$m/s and $\overline{u}_l = 2$m/s and 2-D slices at different prefilmer height h locations in the x-direction coloured by shear stress ($\sigma_{xy} = \dfrac{\partial u_x}{\partial y}$).

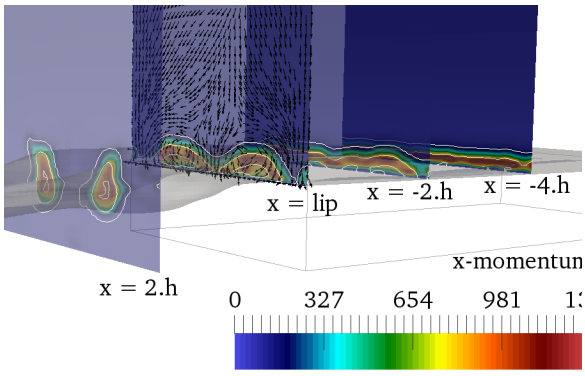

Fig. 6.27: Iso-surface of $\phi_\Gamma = 0.5$ for $\overline{u}_g = 30$m/s and $\overline{u}_l = 2$m/s and 2-D slices at different prefilmer height h locations in the x-direction coloured by momentum (ρu^2).

6.3.5 Discussion

According to the literature, the mechanisms that control primary breakup processes have not yet been fully determined even though several have been proposed. The main instability mechanisms, which control liquid film atomisation, are rather well described. However, the contributions of geometrical and flow characteristics, require further investigations to be fully identified and quantified. This is believed to be the main reason behind numerical and experimental discrepancies and explain a lack of universal primary breakup regime categorisations. The objective of this study was twofold: to extract information on interfacial dynamics and atomisation following a consistent fundamental investigation of the physics in velocity space, and offer a reasoned regime cartography for liquid film atomisation.

An evaluation of the proposed liquid film atomisation theories shows that aerodynamic effects only cannot alone explain the numerical results. However, mechanisms that combine liquid-gas aerodynamic interaction with surface tension effects and inertial differences would be compatible with our results. The specific process by which the nozzle geometry and difference in liquid and gas properties influence atomisation remain to be identified. Although efforts have been made in this regard: for example Déjean et al. [48] studied the influence of prefilmer length and gas channel flow configurations and Gepperth et al. [72] reported on the effects of a change in liquid properties and atomiser edge thickness. It is interesting to note at this stage that Peng et al. [153] established a map of surface wave regimes depending on the gaseous and liquid Reynolds numbers, for different liquid viscosities. Varying the liquid viscosity leads to different regime maps, implying a strong impact of viscosity on surface wave formation. However, we do not expect kerosene viscosity (or water viscosity) to change drastically with temperature and pressure, i.e. with the operating conditions at which the injector nozzle operates. This is because water and kerosene deviate from ideal fluid behaviour to about the same degree for different temperature/pressure regime diagrams (corresponding states in viscosity) [43].

Furthermore, it should be noted that in real applications the two gas streams that interact with the liquid film are usually characterised by different velocities and swirling rotations. This aspect is not considered in the numerical investigations described here. The impact the later may have on the atomisation process and on the distribution of droplets between the two flows remains to be characterised.

Such a fundamental physical investigation provides us with the opportunity to gain knowledge on the overall observed trends. It does not by any means allow a thorough detailed investigation of exact droplet properties, or resolution of the turbulent droplet wake for example. Indeed, considering the estimated sizes and speeds of droplets generated, the droplet wakes indicate a high level of turbulence based on the wake Reynolds number or Stokes number calculation. The turbulent droplet wake would effectively be the smallest turbulent lengthscale to be resolved. The modulation of turbulence by droplet/ligament dynamics – a characteristic of particle-laden flows – in a dense fuel spray is of considerable importance for spray combustion research [196]. If we were to resolve every droplets to the same extent that the liquid film is resolved (~ 5 cells in the liquid film thickness) it would mean increasing the current resolution by approximately $\times 20$, which in the context of this work was computationally exhaustive. To reach this sort of resolution, adaptive mesh refinement (AMR) techniques have been developed and utilised in multiphase flow simulations to resolve the full spectrum of length and time scales of the flow [2, 156]. Nevertheless, for such a wide range of length

scales, the number of grid points that is required to resolve every scale in a true DNS sense, is extremely expensive even with AMR. An alternative approach to resolve the multi-scale challenge of atomisation simulations by introducing sub-grid scale (SGS) models, although the two ideas could be combined. The idea of sub-grid scale modelling could be applied similarly to its implementation in LES formulations: only the physical scales larger than the cell size are resolved, while for the physical scales that are smaller suitable models are introduced to represent the relevant physics. As a result, an ideal SGS model would need to capture a variety of multiphase dynamics, such as the formation of ligaments and droplets, and their breakup, i.e. to reproduce the influence of the residual curvature on the large scales, as well as the effect of both resolved and unresolved turbulence on these phenomena. Such comprehensive SGS models are exceedingly complex and the lack of knowledge of many of the aforementioned multiphase phenomena, as outlined in this thesis and particularly in the present chapter, still requires significant improvement for the development of accurate SGS modelling.

Chapter 7

Atomisation and Breakup of Liquid Kerosene at Elevated Pressure

The detailed numerical simulation of aeronautical combustion chambers at realistic operating conditions has become a major topic of interest in the last decade, answering to the need to enhance engine efficiency and reduce polluting agents. The physics of the atomisation process involves a wide range of phenomena and a strongly multi-scale dynamics, in which a wide variety of liquid structures of different sizes and very different topologies, such as drops and ligaments, are generated following the many hydrodynamic instabilities arising (see Chapter 2). The full numerical simulation of atomising liquid films is thus an extremely complex calculation. Rather than aiming only at industrial-oriented approaches with full-scale calculations of this sort, another option is to advance our fundamental understanding of the process by isolating simplified and small-scale configurations and attempting to extract features that yield physical insight into the mechanisms involved. This fundamental investigation of the physics was the purpose of Chapter 6.

From the industrial point of view, engineers need to study and control spray properties in various ways. For instance, in the aeronautical industry, relatively narrow distributions of droplet sizes are required to ensure uniform evaporation of the droplets prior to combustion. The RCLS method allows high-fidelity numerical simulations of these complex two-phase flows, capturing the primary atomisation physics, as well as capturing the smallest particle dynamics via a droplet tracking algorithm. The overall numerical capability has been tested on simplified numerical tests (Chapter $3-5$) and validated on planar liquid film atomisation cases (Chapter 6). In the present chapter, we intend to capture the dynamics of these phenomena at realistic elevated ambient pressure.

This chapter is organised as follows. Section 7.1 details the computational setup of the numerical simulation of liquid kerosene atomisation at elevated pressure. Section 7.2 describes the results obtained with the RCLS numerical capability to describe this multi-scale problems, in particular the physics of primary breakup observed (instabilities, interface puncturing, flapping, etc). Section 7.3 details the results obtained with the droplet tracking algorithm for the transfer of small drops into a Lagrangian formulation. Finally, Section 7.4 shows some innovative suggestions for alternative surface film injector nozzles based on the physical observations made in this research project.

7.1 Settings of the computation

This section details the computational choices made in modelling liquid film primary breakup following the same three-dimensional planar geometry of the prefilming apparatus introduced in Chapter 6. The computational domain is a cuboid of $16 \times 11 \times 4$ mm^3, where the prefilmer is a flat solid plate of 4mm in width, 8mm in length and of 1mm thickness (see Fig. 6.2b). The entire computational domain is meshed with 2.47×10^6 hexahedral elements. The same boundary conditions are adopted as in the velocity parametric study conducted in Chapter 6 (Fig. 6.2a). The high-fidelity numerical simulation presented here was carried out on the Cambridge HPC cluster, which consists of 9600 2.60GHz Intel Sandy Bridge cores connected by Mellanox FDR Infiniband (600 nodes, 64GB of RAM per 16-cores node). It required 8 nodes and 96 cores and about 430 CPU hours to generate 0.007 seconds of simulated time.

The liquid and the gas are both entering the simulation domain at the inlet plane, with different heights $h_{\text{liq}} = 0.1$mm and $h_{\text{gas,top}} = h_{\text{gas,bottom}} = 5$mm; and at different mean velocities $\overline{u}_{\text{liq}}$ and $\overline{u}_{\text{gas}}$. A continuous laminar gasflow with no swirl is supplied at the inlet plane. The gas emerging is split into two streams that pass the prefilmer on each side. The gas enters the domain with a parabolic velocity profile in order to account as much as possible for upstream flow development in the air supply channels. Its mean speed is taken to be 40m/s, with a centreline velocity of 80m/s. The liquid is continuously fed onto the prefilmer plate through an injector slit of area 4mm$\times$0.1mm with a uniform velocity profile and mean speed of 4m/s. The liquid forms a thin film travelling downstream.

The set of gas and liquid parameters are as follows: air at elevated combustion chamber pressure (aero-engine cruise altitude-like conditions) together with a Jet-A1 type of kerosene fuel at elevated pressure. Operating conditions inside an aero-engine combustion chamber

are not the same as ambient conditions due to the significant compression ratio at which they operate. Typically for a current large civil engine, at take-off:

$$\frac{p_{\text{int}}}{p_{\text{ext}}} = \frac{40 \text{ bars}}{1 \text{ bar}} \tag{7.1}$$

where the subscripts *int* and *ext* mean internal to the combustion chamber and external to the engine, respectively. The compression ratio of $40/1$ is fairly constant during the flight. At cruise altitude ($\sim$35,000 feet), the atmospheric pressure and temperature are ~ 0.20 bar and $\sim$ 220K. Thus at cruise altitude, inside the combustion chamber, the pressure is approximately 10 bar. A change in the operating pressure will cause a change in the density of the air flow, although the density of the liquid fuel will be less affected. In compressors and turbines, one usually idealises the air as an ideal gas undergoing a quasi-static adiabatic process. The equation that relates pressure and temperature to one another is:

$$\frac{T_{\text{int}}}{T_{\text{ext}}} = \left(\frac{p_{\text{int}}}{p_{\text{ext}}}\right)^{\frac{\gamma-1}{\gamma}} \tag{7.2}$$

where γ is the ratio of specific heats for air. Therefore, the temperature at the inlet to the combustion chamber at take-off is about 800K. The liquid fuel is in its supercritical state and requires a special numerical treatment for the simulation of atomisation [43]. At cruise altitude the temperature at the inlet to the combustion chamber is 600K. The air and liquid viscous properties depend on the ambient temperature mostly, rather than pressure. Temperature is thus foreseen to have a non-negligible effect on the atomisation physics. As the temperature of a liquid increases, its viscosity decreases. On the other hand, the viscosity of gases increases as the temperature of the gas increases. The flow conditions chosen for this study that mimic the (p,T) state of the inlet of the combustion chamber at cruise altitude are listed in Table 7.1.

Table 7.1: Physical properties for the spray calculation at cruise altitude with Jet-A1 type fuel.

Phase	ρ [kg/m^3]	μ [kg/m.s]	$\overline{u}$ [m/s]	σ [N/m]
Gas	20	1.7×10^{-5}	40	
Liquid	840	5×10^{-3}	4	0.0261

The order of magnitude of the non-dimensional numbers, as introduced in Section 2.3.1, characterising the flow configuration under consideration are given in Table 7.2. We base our

choice of the lengthscales h_{gas} and h_{liq} on the height of the kerosene and air injection channels.

Table 7.2: Non-dimensional numbers investigated in the high-fidelity numerical simulation of atomisation of liquid kerosene at elevated pressure.

$\bar{u}_{\text{gas}}/\bar{u}_{\text{liq}}$	$\rho_{\text{liq}}/\rho_{\text{gas}}$	$\mu_{\text{liq}}/\mu_{\text{gas}}$	MFR	MR	Oh	$\text{We}_{\text{gas,h}_{\text{liq}}}$	$\text{Re}_{\text{gas,h}_{\text{liq}}}$
10	42	294	2.4	120	0.37	120	4700

The chosen set of numerical parameters for the RCLS method with WENO high-order numerical treatment of discontinuities are given in Chapter 6, Table 6.4. We recall that the liquid indicator function is the CLS field ψ, which goes smoothly from 0 (in the gas phase) to 1 (in the liquid phase). It takes values between 0 and 1 in the transition region. The approximate location of the interface is given by the level-set $\psi_\Gamma = 0.5$.

7.2 Results and Discussion

7.2.1 Instabilities of the liquid film and breakup

We note that the fuel stream, injected at a lower mean velocity than the air, suddenly picks up a higher streamwise speed due to the acceleration imparted by the gas stream. The kerosene film then settles down to lower speeds, closer in magnitude to its original injection velocity at the inlet plane. A velocity equilibrium between the gas and liquid streams develops at the interface. After injection, the liquid homogeneously wets the prefilmer and flows down in a sheared film to the atomising edge. Once the full prefilmer length is wetted, the liquid core starts atomising from the edge of the atomiser lip, as can be seen on Fig. 7.1-7.3. We do not see the development of surface waves on the prefilmer plate. This could be explained by the fact that as the static ambient pressure increases, the amplitude of the surface waves decreases due to the increased inertial resistance of air on the waves, as witnessed also by Bhayaraju & Hassa [15] in their experiments, rendering the bulk liquid less conducive to destabilisation by hydrodynamic instabilities.

There is no liquid phase being accumulated around the atomiser lip. Instead, in Fig. 7.1-7.3, we observe the continuous flapping of the liquid film in the longitudinal direction with intermittent liquid release by breakup events. This is particularly visible in the side-view interface contours in Fig. 7.4. Flapping takes place as the liquid stream is fast enough that the liquid bulk does not accumulate at the prefilmer lip and discharges off the atomiser

edge. The flapping is a consequence of the sinuous Kelvin–Helmholtz instability, which grows downstream with time (as described in Chapter 2). Indeed, the velocity shear at the boundary of the two mediums becomes unstable to the shear-induced Kelvin–Helmholtz instability, which results in large amplitude surface waves at the interface. The resulting Kelvin–Helmholtz instability generates the large-scale, sinuous unstable motion of the liquid that further destabilises the system.

The overall atomisation scenario can be described as follows. First, a liquid reservoir at the atomiser lip is fed by the incoming liquid film. Due to the flapping motion, the liquid is partly immersed in the high-speed airstream. As the sheet significantly obstructs the gas stream, it is exposed to relatively high aerodynamic forces. The latter induces a large shearing on the wave crests which are finally blown away by the air stream (Fig. 7.1, $t = 0.0063$s). The peak of that large-scale undulation announces the birth of bags and streamwise ligaments (Fig. 7.1, $t = 0.0065$s), which later fragment into droplets. In addition, the passage of the crests obstructing the gas stream, associated with the flapping motion, triggers continuous portions of the sheet to detach from the rim. In particular, following the crest of a large-scale longitudinal wave, a transverse liquid cylinder detaches, as visible in Fig. 7.2 at $t = 0.0079$s. A similar behaviour occurs at the troughs of the waves. In Fig. 7.4 at $t = 0.0077$s, as the liquid film is bent towards the top of the domain, being subjected to its flapping mode, it is clear that this enables the disintegration of the liquid film by the action of the aerodynamic forces.

It is worth mentioning that the amplitude of the oscillation of the liquid film is not large. In fact, it is of a similar magnitude to the one witnessed by Pringuey [158] for a non-prefilming geometrical configuration of liquid sheet atomisation, at the same operating conditions as the present work and for a gas/liquid velocity ratio of 20. In addition, the oscillation patterns seem to correspond qualitatively to those observed by Bhayaraju & Hassa [15] for low Weber numbers (i.e. $We_{\text{gas}}, h_{\text{liq}} \sim 100$).

The aerodynamic shearing on the longitudinal surface waves induces a strong axial acceleration. This acceleration then generates an instability that develops on the liquid/gas interface in the transverse direction (Fig. 7.5a *left*). The latter leads to the formation of cell-like structures (discussed in Chapter 2). The bursting of the membranes associated with the cell-like structures is accompanied by the creation of liquid threads due to fingering at the tip of the liquid film that rapidly contract into unstable ligaments under the action of surface tension. It is clear from Fig. 7.5a (*right*) that the cell-like structures forming between the ligaments are the precursors of groups of ligaments elongated in the longitudinal direction (Fig. 7.5b *left*), that remain attached to the rim of the liquid bulk, reaching for the injector

edge. This facilitates the pinch-off events through aerodynamic tearing, into irregularly shaped liquid structures and shedding liquid blobs (Fig. 7.5b *right*).

A change in the development of surface instabilities occurs in which the direction of propagation of the surface wave crests and ligaments is eventually reversed. The air velocity profile underneath the liquid film seems no longer to entrain the liquid film forward, but rather drags it backwards, and liquid blobs are now shed upstream (Fig. 7.6). This change in the flow configuration and shear stress forces acting on the liquid film could be the result of the recirculation zone acting on the underside of the liquid film.

The observed breakup process presented here is similar to the one witnessed in realistic annular burners with prefilming atomisers [70]. The relative importance of the atomisation mechanisms outlined above can greatly influence both the mean drop size and drop size distributions [31], as discussed in Chapter 2, which is the subject of the next section.

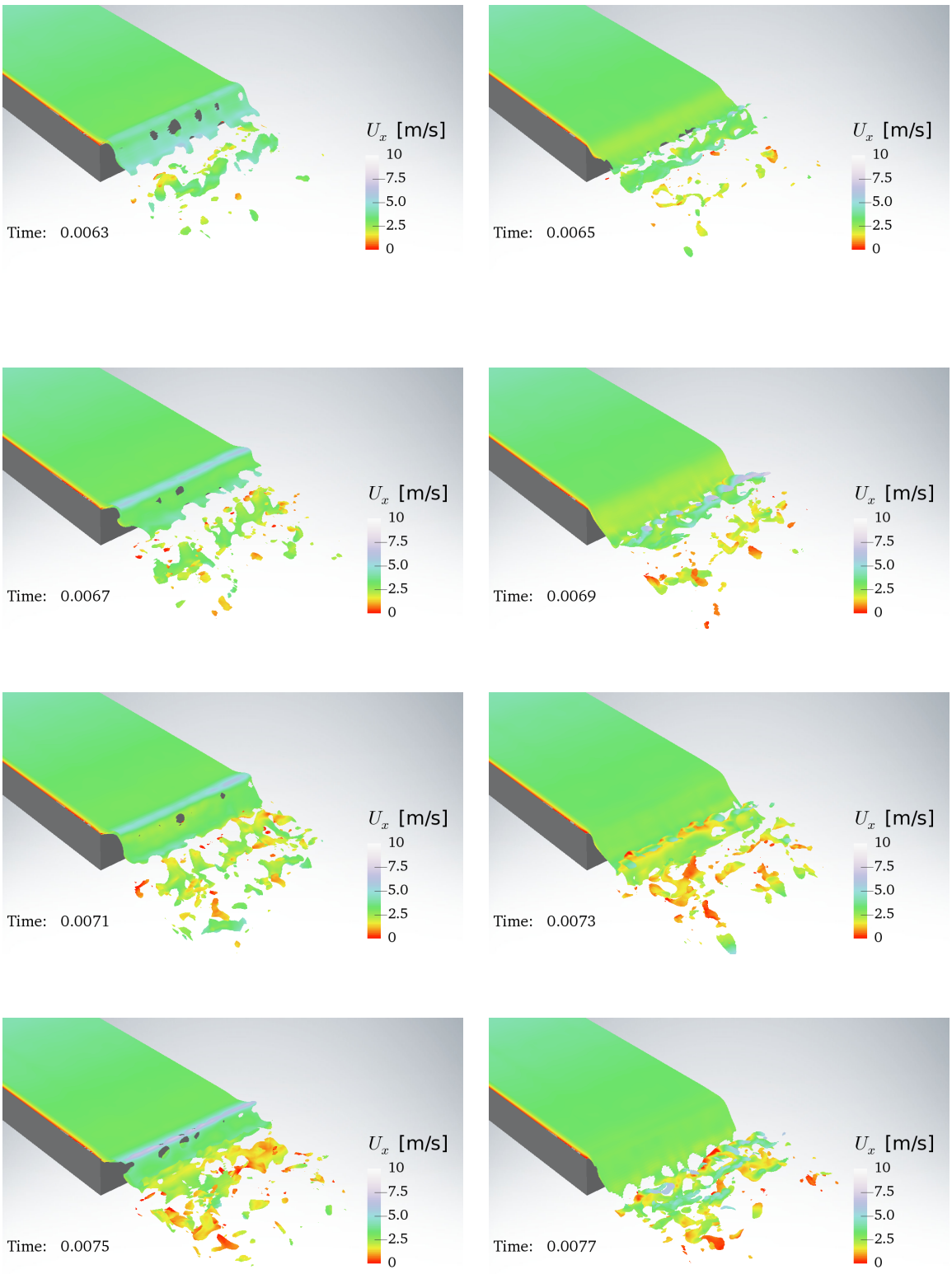

Fig. 7.1: Iso-surface of $\phi_\Gamma = 0.5$ coloured by liquid velocity for $\overline{u}_{\text{gas}} = 40\text{m/s}$, $\overline{u}_{\text{liq}} = 4\text{m/s}$ at cruise-like conditions. Times are in seconds.

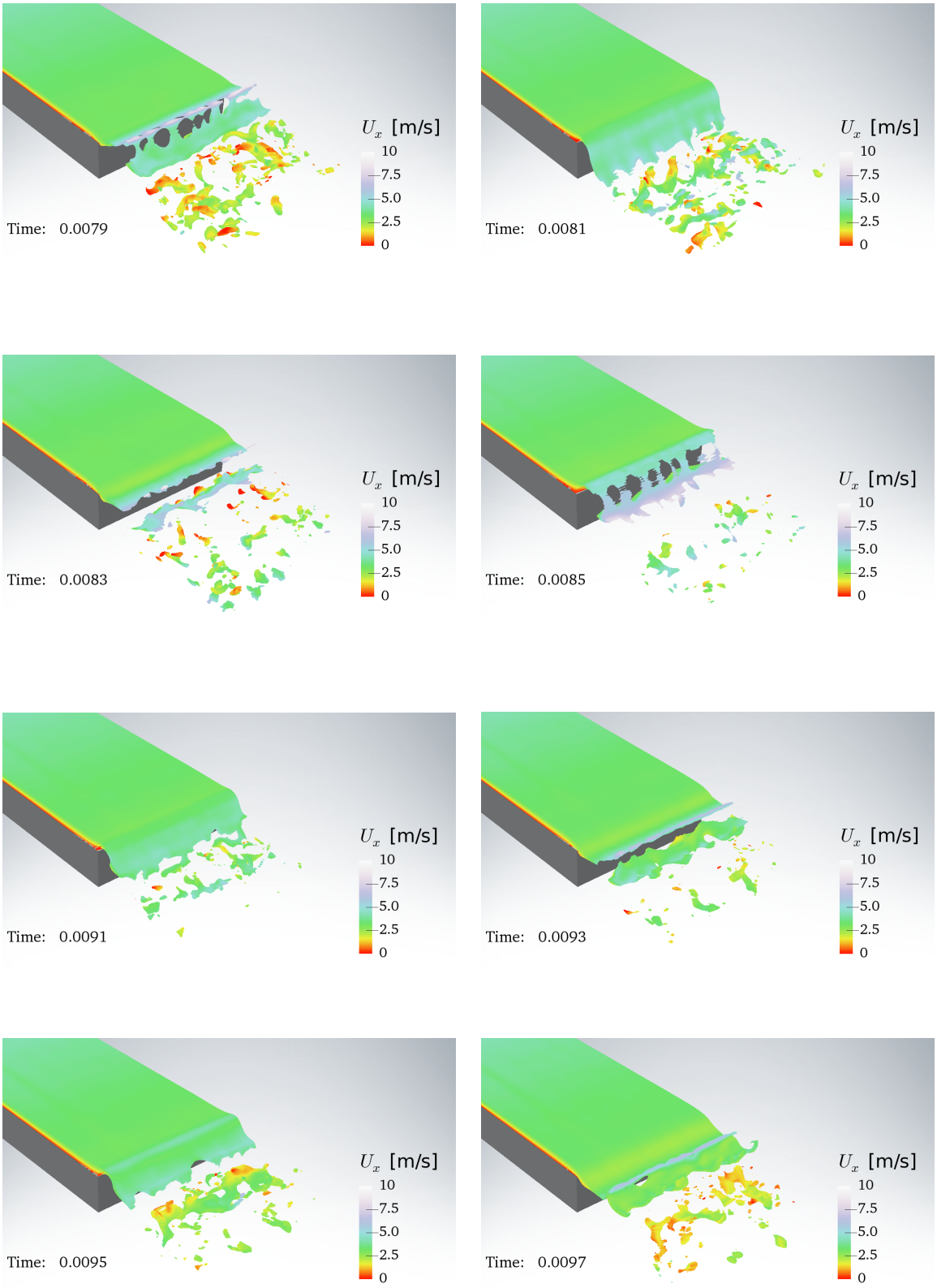
U_x [m/s]
10
7.5
5.0
2.5
0
Time: 0.0079
Time: 0.0081
Time: 0.0083
Time: 0.0085
Time: 0.0091
Time: 0.0093
Time: 0.0095
Time: 0.0097

Fig. 7.2: *(cont.)*

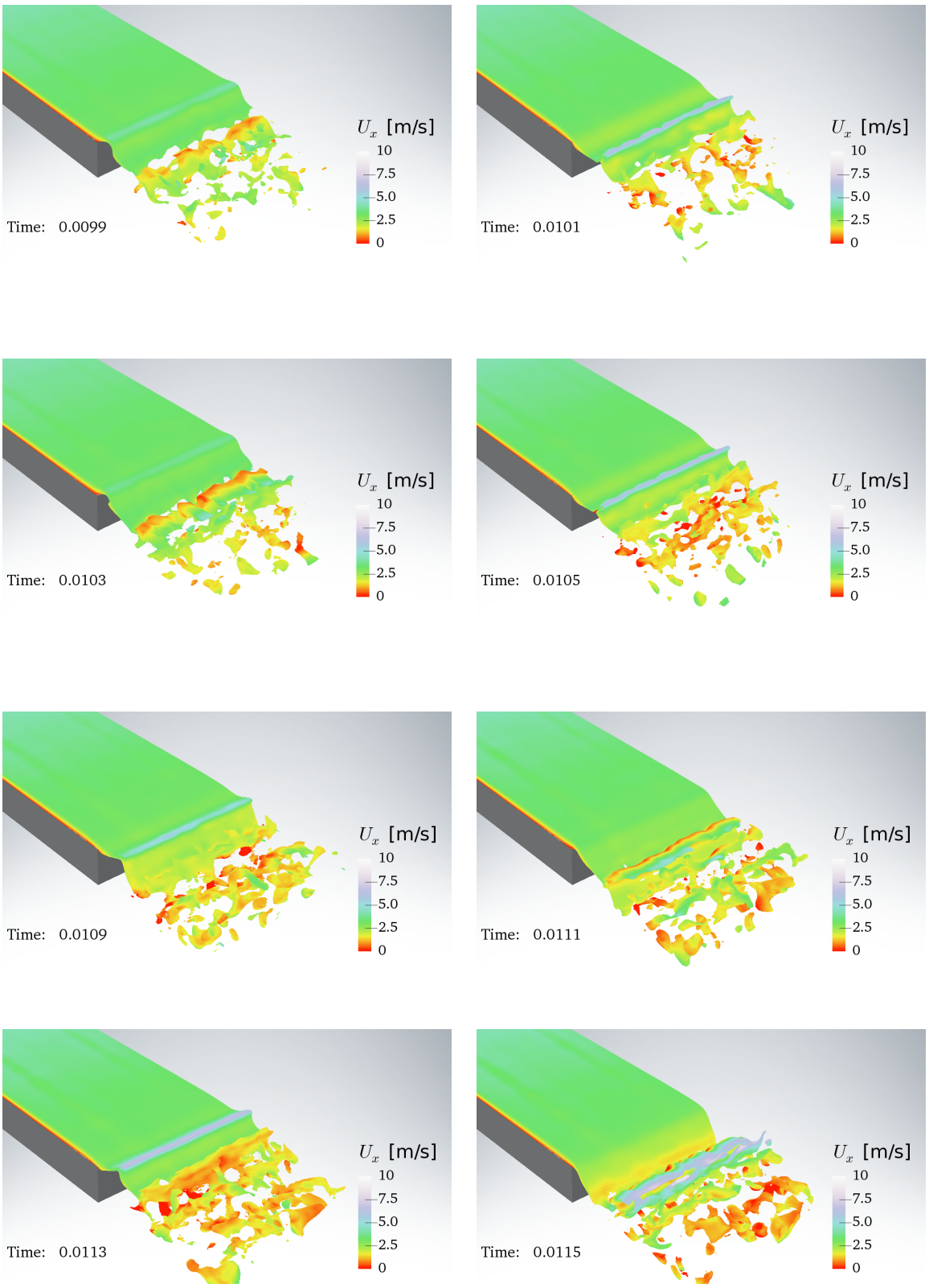
U_x [m/s]
10
7.5
5.0
2.5
0
Time: 0.0099
Time: 0.0101
Time: 0.0103
Time: 0.0105
Time: 0.0109
Time: 0.0111
Time: 0.0113
Time: 0.0115

Fig. 7.3: *(cont.)*

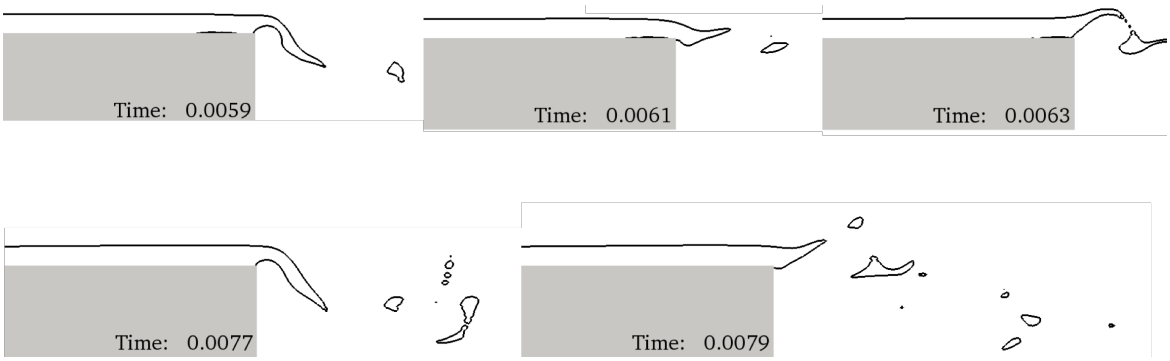

Fig. 7.4: Interface contour in the longitudinal plane. Times are in seconds.

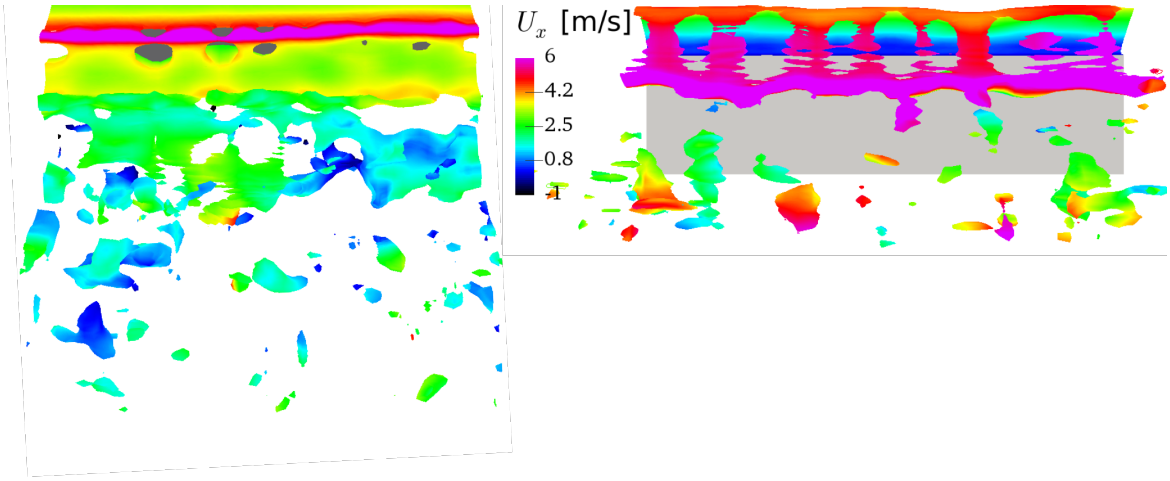

(a)

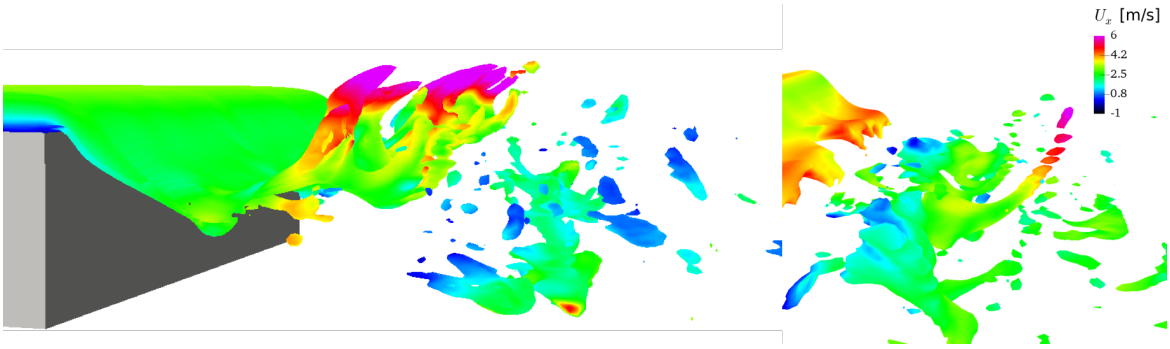

(b)

Fig. 7.5: **(a)** Two different time instant views of membrane puncturing of the liquid film; **(b)** Ligaments stretching away from the liquid film under aerodynamic tearing (*left*) and ligament fragmentation (*right*). The colour on the interface indicates the streamwise velocity.

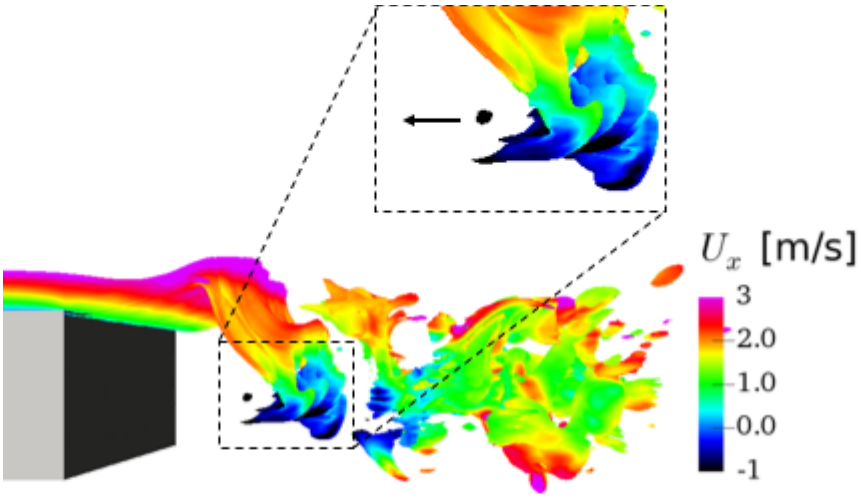

Fig. 7.6: A closeup at the liquid film and the development of a fully 3-D interfacial wave in the counter-streamwise direction, affecting the atomisation process, in which liquid blobs are now shed upstream.

7.2.2 Atomisation and droplet tracking

For the design of a combustion chamber, knowledge of the smallest droplets generated by the airblast nozzle during primary breakup and their properties at realistic operating conditions are valuable pieces of information, as needed by the subsequent stochastic breakup model which handles secondary atomisation to simulate the final fine spray formation, prior to spray combustion modelling. The available empirical correlations to calculate the mean drop size generally produce an underprediction [72]. This is because measurements used to derive these correlations are usually collected in a region where secondary atomisation effects can obscure the initial droplet sizes in the primary breakup region [72]. This is a problem that could be addressed effectively through numerical methods.

The published literature on the numerical simulation of primary breakup with droplet tracking is very scarce. However, a few recent numerical studies have engaged in this numerical challenge. Kim et al. [110] have developed a sub-grid Lagrangian breakup model to couple their conservative level-set method to a Lagrangian tracking method. Their numerical results are compared against the experiments of Marmottant & Villermaux [141]. Ling et al. [131] conducted highly resolved DNS of spray formation in a gas-liquid mixing layer using the Volume-of-Fluid (VoF) method and Fuster et al. [69] on the breakup of a swirling jet with the addition of adaptive mesh refinement. Sauer et al. [183] and Warncke et al. [229] have

developed a post-processing technique in order to extract primary breakup droplet properties from their DNS simulations of a prefilming airblast atomiser (VoF approach), in which a constant sampling plane at the outflow of their computational domain is defined. A detailed comparison of their numerical work with the experimental results of Gepperth et al. [72] found reasonable agreement on the droplet data. However, they recognised the limitations experienced with their VoF approach as the results strongly depend on the value of the liquid volume fraction chosen to express the diffusivity of the interface. According to them, a sharp interface tracking methodology would be a more suitable numerical approach to consider for this exercise [229].

A comprehensive three-dimensional simulation of a liquid film as it exits the orifice of a prefilming airblast atomiser is presented to examine the evolution of the spray in the downstream region of the prefilmer plate. The reader is referred to Section 7.1 for more information on the numerical set up of this simulation as well as a more detailed description and interpretation of the results.

The atomising liquid film at the prefilmer trailing edge and extracted Lagrangian droplet field are analysed on the fly, with the RCLS method equipped with a droplet tracking algorithm, thus facilitating an automated analysis of the disintegration of the liquid film. Quantitative data are obtained through the analysis procedure described in Chapter 4, where in particular, a description is given for the Eulerian to Lagrangian formulation transition criteria for the liquid droplets (size, shape, etc.). As the emphasis of this numerical study is placed on the mechanisms driving the primary breakup, the computational domain is limited to the close vicinity of the injection plane. Consequently, droplet characteristics have been extracted from this calculation close to the atomiser nozzle following primary breakup only. The liquid droplets are tracked down to 8mm downstream of the prefilmer trailing edge, corresponding to the outlet plane of the numerical domain. Each cell containing at least a volume fraction of $\psi = 0.5$ is taken into account for the droplet analysis, i.e. droplets marked by a predefined ψ-threshold of 0.5 are defined as resolved droplets. In addition, a maximum equivalent diameter of 100μm is used, neglecting in the numerical extraction all droplets with a larger computed diameter. Droplet sampling is conducted every timestep. The droplet statistics are then collected during domain reconstruction and post-processed with an external post-processing routine. The Lagrangian droplet field extracted from the simulation is shown in Fig. 7.7 as *black dots* along with the phase interface iso-surface.

It becomes apparent through the analysis of these results that the knowledge of the smallest droplets generated during primary breakup is a fundamental problem caused by the mesh resolution limit of our numerical investigation. As the droplet tracking algorithm relies on

the detection of a sharp transition between the gas-phase ψ-threshold (0.01) and liquid-phase ψ-threshold (0.5), any numerical diffusion in the calculation of the CLS field ψ will affect the numerical routine as it loops through all the neighbouring cells around a particular cell labelled as liquid, until gas is detected. Ling et al. [131] performed a mesh convergence study on their DNS of spray formation in a gas-liquid mixing layer. They found that the coarsest mesh will not only miss the small droplets (as expected) but also the larger ones.

The present simulation is a demonstration of capability in predicting the droplet size distribution. The results of simulations such as the one in Fig. 7.7 may be analysed to produce the probability density functions (PDF) of droplet sizes, as shown in Fig. 7.8. The histogram data is fitted with a distribution of Gaussian type. The mean drop size is found to be $\sim 75\mu$m. Since a maximum equivalent diameter of 100μm is chosen as part of our selection criteria for droplet detection, the histogram data stop at that point. An alternative insight into droplet properties is obtained by the scatter plot of the droplet diameter and velocity in Fig. 7.9. No particular trend is emerging, especially given the small data sample. However, neither did Warncke et al. [229] comment on a trend line in their experimental and numerical results.

With the available computational resources, it was not possible to perform a simulation that continued for a long enough time to yield a statistically steady state of the observed structures. The size distribution of droplet number presented here is not fully converged for the low sample number and low sampling time currently accessible. As the droplet size distribution is sensitive to the sample number, and for shorter simulations the sample number is also smaller, this leads to an overall distribution trend that exhibits more fluctuations, as noted by Ling et al. [131]. However, they also noted that the statistically converged overall distribution trend with fine meshes is recovered for coarser meshes.

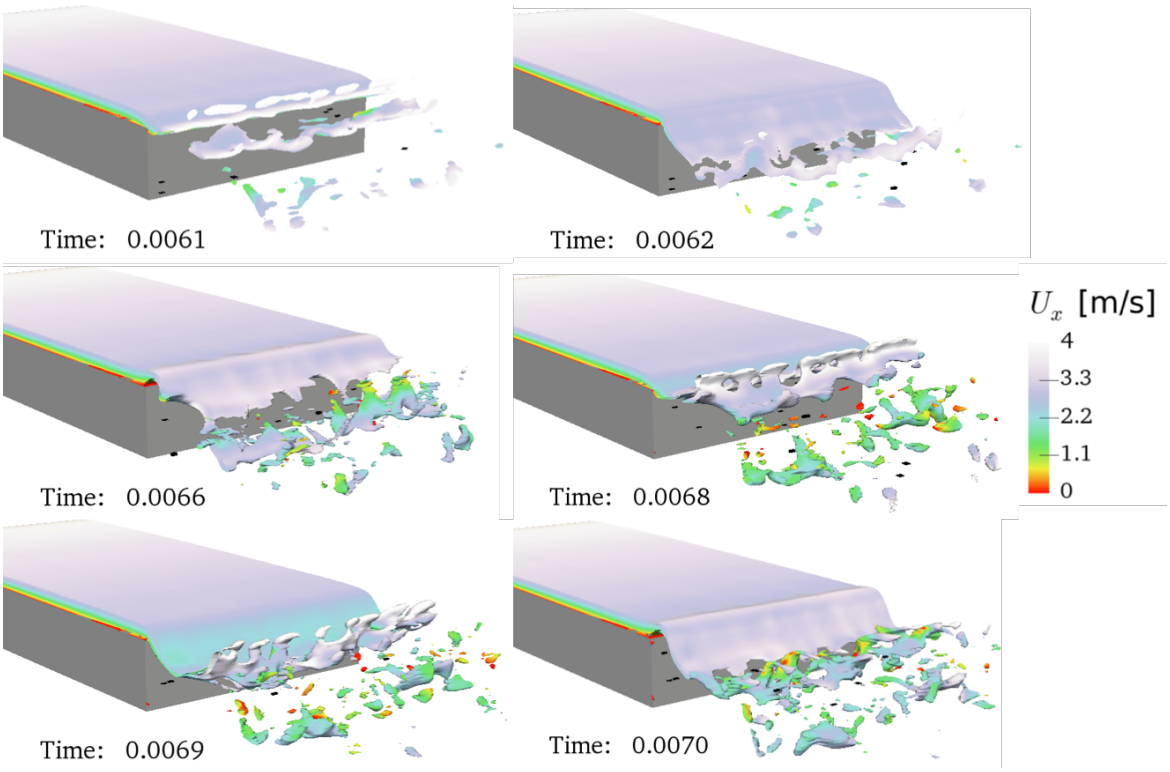

Fig. 7.7: Iso-surface of $\phi_\Gamma = 0.5$ coloured by liquid velocity for $\overline{u}_{\text{gas}} = 40\text{m/s}$, $\overline{u}_{\text{liq}} = 4\text{m/s}$ at cruise-like conditions. The detected primary breakup droplets ($\phi_\Gamma > 0.5$) are highlighted in black.

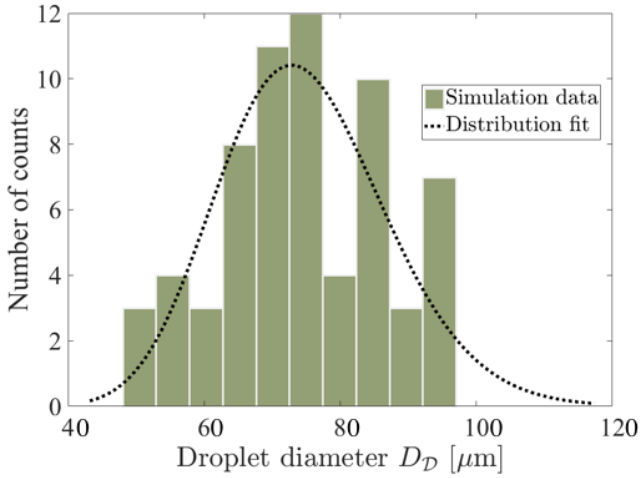

Fig. 7.8: Droplet size distribution of the primary breakup droplets generated during airblast atomisation of a prefilming liquid film. Droplets sampled during the simulation shown in Fig. 7.7.

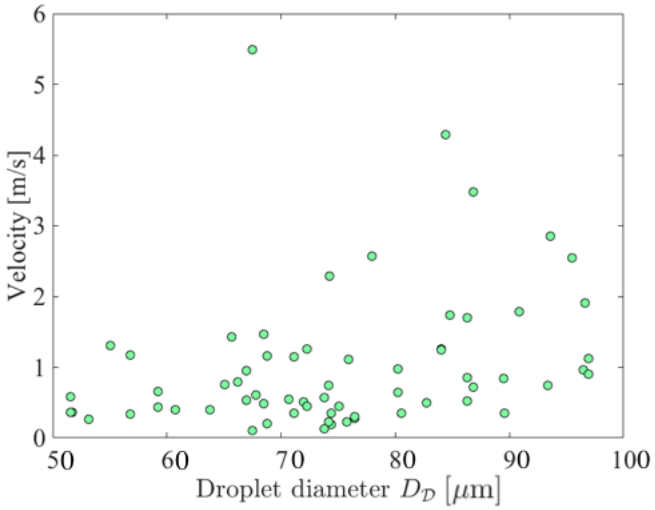

Fig. 7.9: Velocity scatter plot for the droplet size distribution in Fig. 7.7.

7.3 Suggestions for surface film injector nozzles

To supply fuel to a combustion chamber through an injection nozzle with a pre-film zone, wherein the prefilmer comprises a dispersion structure which spreads the fuel and distributes it at the downstream trailing edge, a variety of prefilmer-type designs could be envisioned. Accordingly, as indicated by Fig. 7.10, the present section seeks to provide a selection of innovative alternative geometrical arrangements, following a careful reflection based on the physical observations made in Chapter 6 and the present chapter. In the planar configurations studied in this work, the fuel flows over the surface of a prefilmer prior to being shed from the downstream trailing edge into the swirling airflows. Under certain operating conditions, we noticed a liquid accumulation mechanism at the atomiser lip. Other authors have also witnessed such a breakup scenario [e.g. 15, 70, 72]. Therefore, in certain applications, or for certain operating conditions, it may be desirable to use a fuel transport passage comprising a succession of trailing edges to atomise and disperse the liquid bulk into a cloud of droplets. The dispersion structure may comprise one or more stairs, as described in Fig. 7.10a and Fig. 7.10b, respectively. This novel geometrical arrangement, the “staircase nozzle”, may provide an enhancement in the accumulation mechanism through a cascade effect at the downstream edge of the prefilmer, as the liquid film thickness is comparable to the thickness of the individual stairs. This may allow the atomising device to accumulate on purpose a fixed amount of mass at each stair level, using the adhesive properties of the liquid to attach itself back to the solid surface, before it breaks in the vicinity of the atomising edge.

An alternative planar structure may comprise a series of protruding walls (i.e. bumps), as shown on Fig. 7.11c. We name this geometrical arrangement, the "wavy nozzle". The undulating pattern, or wavy corrugations, may help to encourage the liquid fuel towards a sinusoidal interfacial instability, for subsequent breakup in the "3D wave mode" regime. The wavy corrugations could be manufactured such that a desired wavelength and amplitude of the Kelvin–Helmholtz longitudinal instability is provoked. Indeed, resonance between the free surface and the corrugations could be achieved by forcing the liquid film over each corrugation of wavelength $\lambda_{\text{longitudinal}}$, and amplitude of the order of the liquid film thickness h_{film}. Following the controlled initiation of the longitudinal oscillation of the liquid film, the resulting transverse instabilities would develop on the corrugated solid plate, and with them the cascade of complex atomisation phenomena. It is to be expected that the breakup lengths would be shorter if the initiation of the atomisation process is accelerated and improved. The control over the thin-film wetting behaviour and pattern on the substrate may thus allow the prefilmer to be made shorter (shorter breakup lengths). This may therefore lead to the fuel injector and surrounding components (combustor chamber) being shorter, lighter and cheaper to manufacture.

In an industrial arrangement, the fuel is supplied to the prefilmer using a circumferential geometry comparable to that described in Chapter 1 (Fig. 1.5). Therefore, the cross-section of the prefilmer at the downstream edge needs to be made circular. Such a geometry would supply a circumferential film of fuel onto the prefilmer, and thus creates a uniform circumferential distribution of fuel.

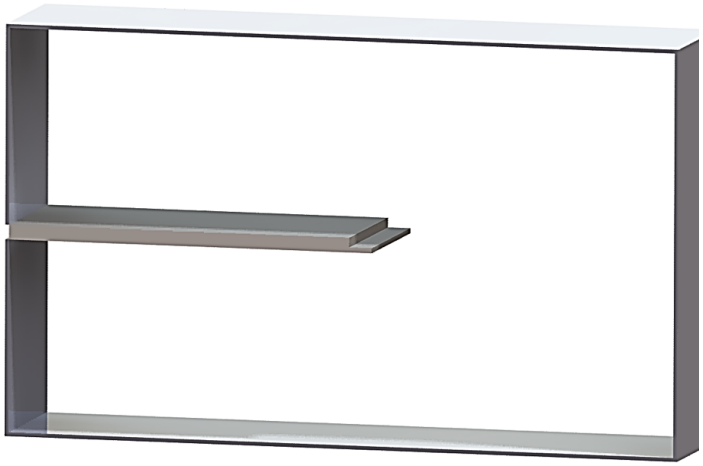

(a)

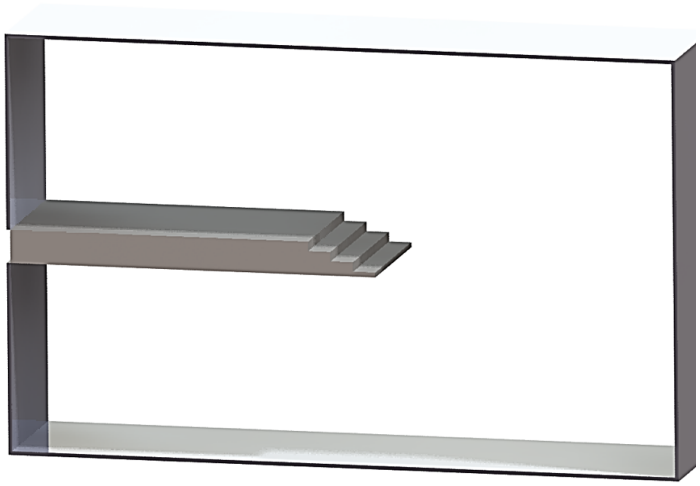

(b)

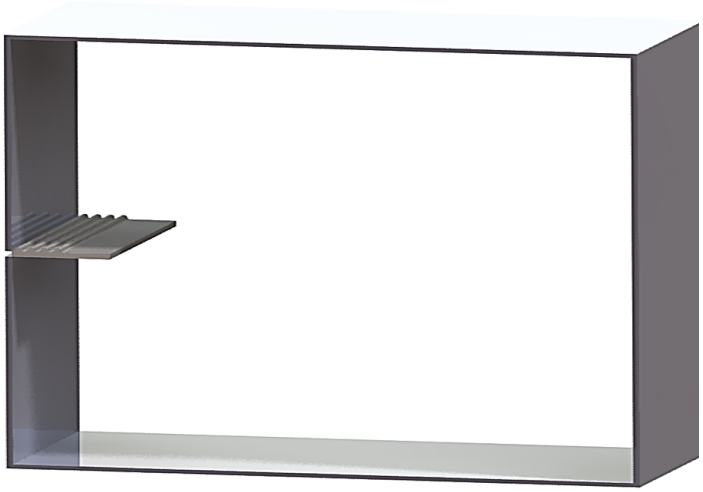

(c)

Fig. 7.10: 3-D CAD designs of the three different potential alternative planar atomiser nozzles with prefilming zone.

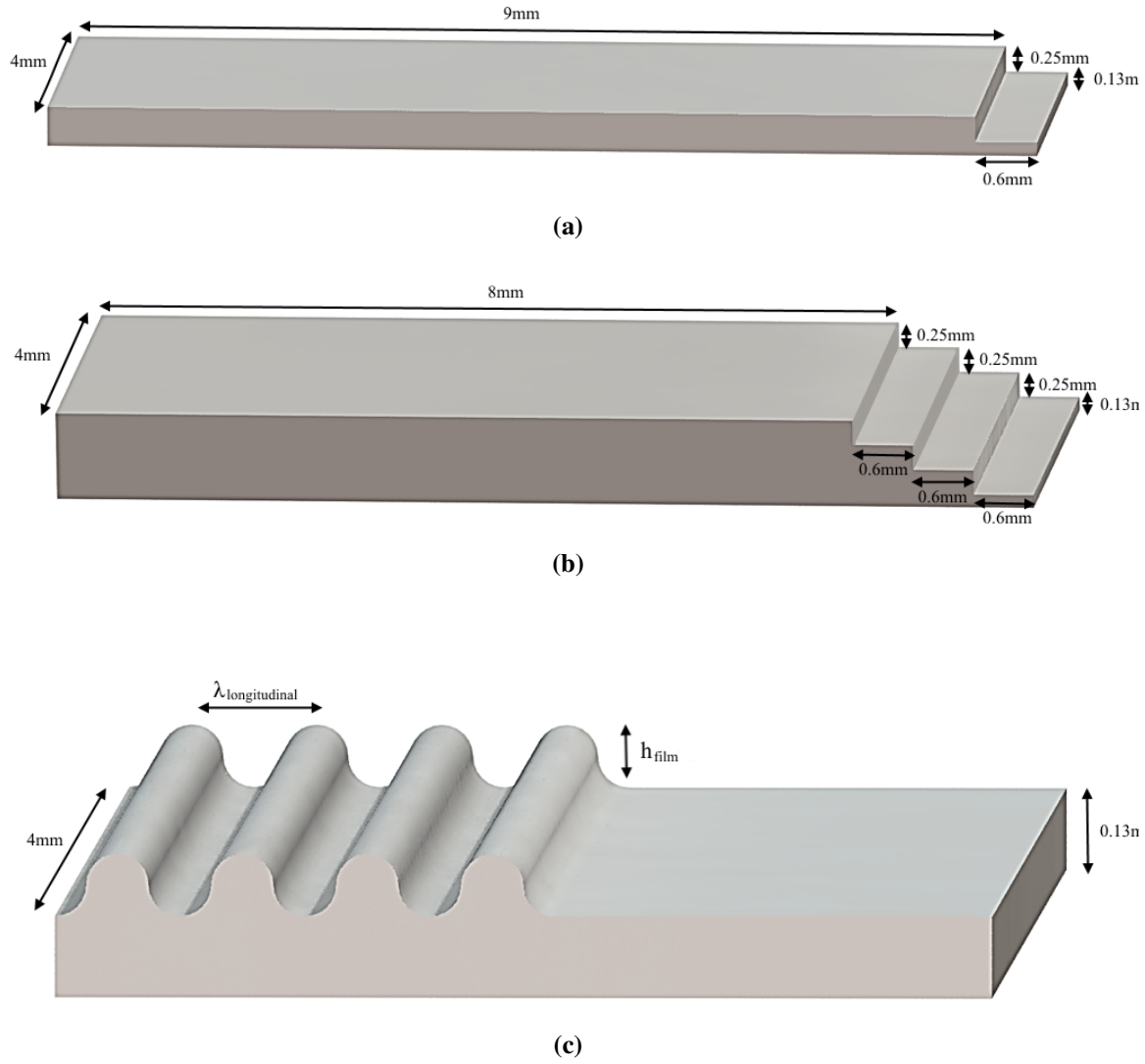

Fig. 7.11: Closeup view of the three different innovative suggestions for surface film injector nozzles: **(a)** and **(b)** the "staircase nozzle"; and **(c)** the "wavy nozzle".

7.4 Final comments

The simulation results clearly show the detailed processes of how the bulk liquid film breaks into ligaments, and finally droplets. The development of interfacial waves is crucial to the sheet disintegration. Full 3-D waves are observed. The development of the ligaments is shown to be generated by fingering at the rim of the liquid film and also by the expansion of membranes puncturing the liquid film. In conclusion, two different modes of disintegration seem to occur simultaneously, which act either individually or together over the course

of the simulation. The appearance of the "3D wave mode" (see Chapter 6) whereby the occurrence of three-dimensional surface instabilities leads to a perforated-sheet disintegration mechanism allows holes to appear delineated by thicker liquid rims. These holes grow until the rims of adjacent holes coalesce, producing ligaments. Hole formation has been witnessed by many experimentalists in this context and is thus well documented [28, 64]. In addition, the flapping of the liquid film induces a "wavy-sheet" atomisation mechanism whereby, as the aerodynamic perturbation amplifies, wave crests are prone to fragment under the action of aerodynamic tearing.

The size distribution of droplets is sampled in the close vicinity of the breaking film. A Gaussian-type distribution is employed to fit the PDF data. A far-reaching consequence of the present work in the future, would be to compare the simulation results to experimental data such as drop size distribution of the resulting spray.

Finally, this chapter aimed to provide a selection of innovative alternative geometrical arrangements for planar injector walls. Those novel designs are intended to promote breakup depending on the operating point and the associated atomisation regime.

Chapter 8

Conclusions and Future Work

Based on the requirements of the aeronautical industry, Pringuey [158] developed a modelling capability for the computation of fuel injection in aero-engine combustion chambers. His modelling strategy led to the creation of a novel high-order WENO scheme for general polyhedral meshes, the development of a robust conservative level-set method to transport the phase interface and the generation of an algorithm to output droplet boundary conditions to combustion codes. The present research project follows on from the work of Pringuey [158] to leverage the capabilities of the multiphase flow solver *RCLSFoam*. In this chapter the main achievements of this research project are summarised in Section 8.1 and some follow-on research topics are suggested in Section 8.2.

8.1 Achievements

8.1.1 Evaluation of the numerical method in low-capillary environments

The performance of the numerical scheme *RCLSFoam* has been demonstrated on typical two-dimensional and three-dimensional benchmark test cases relevant to both multiphase flow modelling and atomisation, and validated against other computational methods in detail. With the intention to overcome a natural tendency to evaluate numerical methods using only test cases close to the specific application for which they were designed in the first place, the RCLS method was applied to the numerical simulation of the deformation of a static droplet in a quiescent atmosphere. The RCLS method was able to minimise the development of spurious currents. In addition, it was able to achieve a good representation of the surface

tension effects, with no off-centre displacement of the droplet, nor distortion of the droplet's interface.

In this low capillary number environment, our results indicate that a well-tuned implementation of the RCLS method is able to work well across a broad range of relevant conditions in multiphase flow modelling. This further demonstrates its robustness and accuracy.

8.1.2 A fundamental investigation of liquid film atomisation with high-fidelity numerical simulations

From the literature review presented in Chapter 2, it became apparent that current understanding of liquid film fragmentation is often contradictory and only partially correlated to the available experimental results, as the data are either too scattered or obtained over insufficient ranges of varied parameters. This state of affairs demonstrates the need for continuing to investigate the physics for several operating conditions. It is desirable to analyse the various instabilities and atomisation mechanisms leading to a given regime formulation for a large series of numerical simulations, consistently. To reach this goal, the modelling tool *RCLSFoam* has been used. We conducted high-fidelity numerical simulations of spray formation from liquid film disintegration to examine whether we are able to reproduce the fluid dynamics of the interface during air-assisted primary breakup, as described in the literature [24, 123, 224] and experiments [15, 48, 71, 72]. We aimed at improving our fundamental understanding of the gas/liquid interaction in the near nozzle region and extrapolating breakup predictions to a multitude of operating conditions.

The computations reproduced faithfully the transient nature of the phase interface behaviour, subject to high shear due to high gas velocities, whereby rapidly growing surface waves are superimposed on the liquid film. The latter symbolises the growth and propagation of Kelvin–Helmholtz longitudinal instabilities along the phase interface. In addition to longitudinal undulations, transverse instabilities appear. Furthermore, it was possible to make a clear distinction between the diverse liquid deformations that originated through hydrodynamic instabilities. We discerned the development of both spanwise and streamwise ligaments and their disintegration into smaller liquid structures under either aerodynamic tearing and/or in a way that resembles the Plateau–Rayleigh instability, as predicted by theoretical predictions and experimental data.

We were able to draw several conclusions about the description of the liquid phase in the dense spray region of prefilming airblast atomisers and to develop an original approach to

classify them. We observed the critical influence of the relative liquid/gas velocity ratio on the atomisation process. Thus the shear stress and difference in inertia between liquid and gas are observed to play a significant role in the atomisation process. It is found that, for some operating conditions, the primary breakup mechanism of the liquid film is rather different from the well established theories on classical liquid sheet breakup on prefilming surfaces. New regime-dependent insights are observed into the physics of liquid film behaviour, for instance, phenomena like "ligament merging" or the liquid rim subjected to the Taylor–Culick instability. In addition, three-dimensional wave modes were observed to co-exist and work together to destabilise the liquid film ("3-D wave mode" regime). Accumulated liquid at the atomising edge undergoes deformation by which droplets are generated ("accumulation" regime). Finally, "vortex action" is another observed mechanism by which the liquid film is fragmented. Those key physical atomisation mechanisms have been mapped out. The proposed cartography helps to predict the evolution of the process according to the operating conditions of the injection system. The effects of the velocities of the liquid and the gas appear to be strongly regime-dependent, highlighting the need to continue investigating the physics in several regime zones.

The second major task of this work was to study the breakup mechanism of a planar liquid film of kerosene Jet A1 fuel in a prefilming airblast atomiser under realistic elevated pressure engine conditions and extract quantitative information on droplet formation.

8.1.3 A study of liquid wetting behaviours

Droplet impacts are of major industrial interest. Indeed, fuel droplets can impact on the walls of injection passages and combustion chambers. We analysed the nature of the destabilisation of a liquid droplet impacting a pre-wetted surface into a non-axisymmetric structure using two-dimensional and three-dimensional configurations. The destabilisation involves similar instability mechanisms to those observed in planar liquid film atomisation: the Rayleigh–Taylor instability and rim instabilities, in conjunction with membrane puncturing and fingering. As part of our investigation on splashing, we also applied the RCLS method to droplet capturing (see Section 8.1.4).

Impacts on pre-wetted substrates and dry surfaces are rather different but share a few common characteristics, in conjunction with being directly relevant to the study of atomisation. During the course of this research project, it became apparent that the study of dynamic wetting behaviours of liquid films on dry solid substrates would be important, as we observed de-wetting of the prefilmer plate under some operating conditions. Thus, the RCLS method was

further developed to include the Kistler dynamic contact angle model, which was validated against experimental data for the simulation of droplet splashing on a dry hydrophobic surface. The droplet rebounding regime was successfully captured by our numerical method. This study has clearly shown the importance of the addition of a reliable model for the accurate estimation of the contact-line forces, especially for the prediction of the receding phase of the drop splash dynamics. During the receding phase, the rim of the lamella thickens under the action of surface tension forces and retracts, in a manner similar to the Taylor–Culick instability observed in the retraction of the thick rim of the planar liquid film studied in Chapter 6.

8.1.4 A study of atomisation and droplet tracking

Under aero-engine conditions, the atomisation process produces a large number of droplets, whose size can reduce to very small values, and even smaller values after secondary breakup. The faithful prediction of the spray requires the simulation of both primary and secondary breakup droplets. Computing the primary drop size distribution is of paramount importance for its transfer to a Lagrangian stochastic spray model in order to describe the secondary breakup process. Therefore another essential building block of the RCLS modelling capability has been the development by Pringuey [158] of an algorithm to output these droplet fields and characteristics following primary breakup. The focus of Chapter 4 has been the thorough validation of this algorithm against several test cases with different challenging physical and numerical requirements, in particular, the Rayleigh–Taylor instability, the breaking of a dam, and droplet splashing. The results indicate that the RCLS method with droplet tracking is able to work well across a broad range of operating conditions.

As part of Chapter 7, we subjected the droplet tracking algorithm to conditions relevant to the atomisation of liquid kerosene in jet engines at elevated ambient pressure and temperature. The physics of the atomisation process involves such a wide range of phenomena and a strongly multi-scale dynamics, in which a wide variety of liquid structures of different sizes and very different topologies are generated following the many hydrodynamic instabilities arising. It is therefore a great numerical challenge to detect and capture liquid droplets in this complex environment and to predict droplet size distributions and velocity diagrams. The RCLS method provides the fidelity needed to capture the dynamics of the phase interface and isolated liquid droplets accurately, and performs cost-effectively on droplet recognition, tracking and transfer.

8.2 Follow-on research topics

Here we offer a set of guidelines for future work based on the investigations conducted in this thesis and the research conclusions made so far.

8.2.1 Influence of fluid properties, geometrical parameters and regime mapping

In the parametric study, only the injection velocities were varied in order to limit the parameters affecting liquid film breakup. The first suggestion for future work is to continue the mapping in velocity space of liquid film atomisation.

To alleviate the complexity of industrial design features only a simplified planar prefilming atomiser was studied to extract fundamental physical information. Changes in length of the prefilming surface can have a significant influence on the atomisation characteristics of the atomiser [48] as well as the height of the prefilmer trailing edge [70].

As yet, there is no consensus among the scientific community regarding which additional fluid parameters and geometrical parameters best characterise the breakup process in liquid film configurations. Hence, a common definition of the relevant non-dimensional groups is still lacking. Better quantification of the influence of liquid and gas properties as well as prefilmer geometrical parameters, liquid film thickness and boundary layer thickness would be helpful. Finally, a validation exercise against linear stability analysis studies such as those of Marmottant & Villermaux [141] and Tammisola [206], and quantitative experimental data such as those of Déjean et al. [48] and Gepperth et al. [72] should be conducted for matching operational conditions.

8.2.2 Dynamic contact angle modelling

For certain observed regimes, the wetting behaviour of the liquid film on the solid substrate appears to have a strong effect on the overall atomisation process. In particular, in the "ligament-merging" regime, in which ligaments amalgamate with one another under the effects of strong surface tension forces, we observe de-wetting of the solid substrate. In addition, in the accumulation regime, the surface roughness of the substrate and corresponding dynamic contact angles of the liquid appear to be crucial in accurately predicting the capillary action at the prefilmer lip, where a meniscus forms.

Future work thus needs to be devoted in part to a better understanding, through numerical simulation with dynamic contact angle modelling, of the liquid wetting behaviour on the solid substrate and liquid capillary attachment at the prefilmer lip. The contact angle hysteresis changes depending on the liquid properties, substrate properties and environmental conditions (temperature of the liquid, wall temperature of the substrate, etc.). The body of work on experimental investigations of both advancing and receding contact angles is rather scarce. Roisman et al. [177] reports values for advancing and receding contact angles for water over a stainless steel surface. Lam et al. [118] measured these angles for n-dodecane on a silicon wafer. Both of these studies are good candidates to form the basis of modelling for contact angles to represent the liquid film in the present context of aero-engine kerosene injection.

8.2.3 Numerical detection of spray formation

Future work towards improving the droplet tracking algorithm should include a two-way coupling between the detected Lagrangian droplets and the resolved Eulerian fluid flow. Not only does the fluid exert a fluid-dynamic force on the droplets, but this force is also exerted back to the fluid with an opposite sign [132]. Indeed the fluid-dynamic force acting on each individual droplet is crucial to Lagrangian point particle models, since it determines both the droplet motion and the backward effect to the fluid.

Hence, the development strategy should account for the implementation of an aerodynamic drag force term – considered to be the only non-negligible force – and would allow droplets to be transferred smoothly as input to an existing secondary break-up model to simulate the whole atomisation process with a single CFD solver. Moreover, it would be helpful to account for droplet evaporation (phase change), which would open up a pathway to include combustion in the model should this be required in the future by industry.

For both simplified and realistic atomiser geometries, the quantitative validation against droplet size distributions and droplet velocity distributions obtained through experiments would provide the most useful assessment of the performance of the numerical tool.

It should be mentioned that to avoid the disappearance of small-scale liquid structures whose radius is of sub-grid scale order, due to numerical diffusion, local adaptive mesh refinement (AMR) is required. AMR has proved effective in capturing the formation and evolution of the smallest droplet clouds [69, 244].

8.2.4 Application to innovative alternative fuel injector geometries

Future work is to take advantage of (i) the “staircase nozzle” and (ii) the “wavy nozzle”, two innovative alternative geometrical arrangements for prefilmer plates. Following a careful reflection based on the physical observations made in Chapter 6 and 7, control over the thin-film wetting behaviour and pattern on the substrate could be envisioned as a way to channel the fuel and improve the atomisation process and subsequent dispersion of liquid droplets. In this context, improved models for advancing and receding contact angles are necessary, as discussed in Section 8.2.3.

References

[1] Aboukhedr, M., Gavaises, M., Georgoulas, A., Marengo, M., & Vogiatzaki, K. (2016). Numerical investigation of droplet spreading on porous and non-porous surfaces. In *Proceedings of the* 27th *Annual Conference of the Institute for Liquid Atomization and Spray Systems – ILASS Europe*. Brighton, United Kingdom.

[2] Agbaglah, G. (2011). Parallel simulation of multiphase flows using octree adaptivity and the volume-of-fluid method. *Comptes Rendus Mécanique*, **339**, 194–207.

[3] Agbaglah, G., Thoraval, M.-J., Thoroddsen, S. T., Zhang, L. V., Fezzaa, K., & Deegan, R. D. (2015). Drop impact into a deep pool: vortex shedding and jet formation. *Journal of Fluid Mechanics*, **764**, R1.

[4] Agbaglah, G. G., McCaslin, J., & Desjardins, O. (2015). Numerical simulations of air-blast atomization of a liquid layer. In *Proceedings of the* 27th *Annual Conference of the Institute for Liquid Atomization and Spray Systems – ILASS Americas*. Raleigh, North-Carolina.

[5] Amat, S., & Ruiz, J. (2017). New WENO Smoothness Indicators Computationally Efficient in the Presence of Corner Discontinuities. *Journal of Scientific Computing*, **71**, 1265–1302.

[6] Arai, T., & Hashimoto, H. (1985). Disintegration of a thin liquid sheet in a cocurrent gas stream. *International Journal of Turbo and Jet-Engines*, **3**, 301–306.

[7] Arienti, M., & Sussman, M. (2014). An embedded level set method for sharp-interface multiphase simulations of diesel injectors. *International Journal of Multiphase Flow*, **59**, 1–14.

[8] Arienti, M., & Sussman, M. (2017). A Numerical Study of the Thermal Transient in High-Pressure Diesel Injection. *International Journal of Multiphase Flow*, **88**, 205–221.

[9] Bachelor, G. K. (1967). *An introduction to fluid dynamics*. Cambridge University Press.

[10] Bärow, E., Koch, R., & Bauer, H. J. (2013). Comparison of oscillation modes of spray and gaseous flames. In *Eighth Mediterranean Combustion Symposium*, EGTSC-26.

[11] Behrendt, T. (2003). *Strömung und Verbrennung in einem neuen Düsenkonzept für die magere Vormischverbrennung in Fluggasturbinen*. Ph.D. thesis, DLR Forschungsbericht.

[12] Berberovic, E. (2010). *Investigation of Free-surface Flow Associated with Drop Impact: Numerical Simulations and Theoretical Modeling*. Ph.D. thesis, Technischen Universität Darmstadt.

[13] Berthoumieu, P., & Lavergne, G. (2001). Video techniques applied to the characterization of liquid sheet breakup. *Journal of Visualization*, **4**, 267–275.

[14] Bhayaraju, U. (2007). *Analysis of Liquid Sheet Breakup and Characterisation of Plane Prefilming and Nonprefilming Airblast Atomisers*. Ph.D. thesis, Technischen Universität Darmstadt.

[15] Bhayaraju, U., & Hassa, C. (2009). Planar liquid sheet breakup of prefilming and nonprefilming atomizers at elevated pressures. *Atomization and Sprays*, **19**, 1147–1169.

[16] Bianchi, G. M., Pelloni, P., Toninel, S., Scardovelli, R., Leboissetier, A., & Zaleski, S. (2005). Improving the Knowledge of High-Speed Liquid Jets Atomization by Using Quasi-Direct 3D Simulation. In *SAE Technical Paper*, 2005-24-089.

[17] Bilger, C., Aboukhedr, M., Vogiatzaki, K., & Cant, R. S. (2017). Evaluation of two-phase flow solvers using Level Set and Volume of Fluid methods. *Journal of Computational Physics*, **345**, 665–686.

[18] Bilger, C., & Cant, R. S. (2014). Numerical investigation of shear-driven liquid film primary breakup assisted by coaxial gas streams. In *Proceedings of the 26th Annual Conference on Liquid Atomization and Spray Systems – ILASS Europe*. Bremen, Germany.

[19] Bilger, C., & Cant, R. S. (2016). Mechanisms of Atomization of a Liquid Sheet: A Regime Classification. In *Proceedings of the 27th Annual Conference on Liquid Atomization and Spray Systems – ILASS Europe*. Brighton, UK.

[20] Bilger, C., & Cant, R. S. (2016). Sampling of the Velocity Space: An Agenda for Liquid Sheet Atomization Analysis. In *Proceedings of the 28th Annual Conference on Liquid Atomization and Spray Systems – ILASS Americas*. Dearborn, MI.

[21] Brackbill, J., Kothe, D., & Zemach, C. (1992). A continuum method for modeling surface tension. *Journal of Computational Physics*, **100**, 335–354.

[22] Braun, S., Höfler, C., Koch, R., & Bauer, H.-J. (2013). Modeling fuel injection in gas turbines using the meshless smoothed particle hydrodynamics method. In *ASME Turbo Expo 2013: Turbine Technical Conference and Exposition*, GT2013-94027.

[23] Braun, S., Wieth, L., Koch, R., & Bauer, H. J. (2015). Influence of Trailing Edge Height on Primary Atomization: Numerical Studies Applying the Smoothed Particle Hydrodynamics (SPH) Method. In *Proceedings of the* 13th *Triennial International Conference on Liquid Atomization and Spray Systems – ICLASS*. Tainan, Taiwan.

[24] Bremond, N., Clanet, C., & Villermaux, E. (2007). Atomization of undulating liquid sheets. *Journal of Fluid Mechanics*, **585**, 421–456.

[25] Brenner, M. P., & Gueyffier, D. (1999). On the bursting of viscous sheets. *Physics of Fluids*, **11**, 737–739.

[26] Buelow, P., Williams, B., Bretz, D., Spooner, M., Mohamed, C., & Gill, H. (2012). Lean direct injection atomizer for gas turbine engines. US Patent 8,156,746.

[27] Carentz, H. (2000). *Etude de la Pulvérisation d'une Nappe Liquide Mince*. Ph.D. thesis, Université Pierre et Marie Curie.

[28] Carvalho, I. S., Heitoyr, M. V., & Santos, D. (2002). Liquid film disintegration regimes and proposed correlations. *International Journal of Multiphase Flows*, **28**, 773–789.

[29] Chandrasekhar, S. (1961). *Hydrodynamic and Hydromagnetic Stability*. Oxford University Press.

[30] Charru, F. (2007). *Instabilités hydrodynamiques*. Les Ulis, France: EDP Sciences.

[31] Chaussonnet, G. (2014). *Modeling of liquid film and breakup phenomena in Large-Eddy Simulations of aeroengines fueled by airblast atomizers*. Ph.D. thesis, Institut National Polytechnique de Toulouse.

[32] Chaussonnet, G., Koch, R., Bauer, H. J., Sänger, A., Jakobs, T., & Kolb, T. (2017). Sph simulation of an air-assisted atomizer operating at high pressure: Influence of non-newtonian effects. In *ASME Turbo Expo 2017: Turbomachinery Technical Conference and Exposition*, GT2017-63033.

[33] Chaussonnet, G., Müller, A., Holz, S., Koch, R., & Bauer, H. J. (2017). Time-response of recent prefilming airblast atomization models in an oscillating air flowfield. In *ASME Turbo Expo 2017: Turbomachinery Technical Conference and Exposition*, GT2017-63041.

[34] Chaussonnet, G., Riber, E., Vermorel, O., Cuenot, B., Gepperth, S., & Koch, R. (2013). Large Eddy Simulation of a prefilming airblast atomizer. In *Proceedings of the* 25$^{\text{th}}$ *Annual Conference of the Institute for Liquid Atomization and Spray Systems – ILASS Europe*. Chania, Greece.

[35] Chrigui, M., Sadiki, A., Feras, Z. B., Roisman, I., & Tropea, C. (2008). Numerical and Experimental Study of Spray Produced by an Airblast Atomizer Under Elevated Pressure Conditions. In *ASME Turbo Expo 2008: Power for Land, Sea, and Air*, GT2008-51305.

[36] Clark, C. J., & Dombrowski, N. (1974). An experimental study of the flow of thin liquid sheets in hot atmospheres. *Journal of Fluid Mechanics*, **64**, 167–175.

[37] Comer, A. L. (2012). *Optimisation of Liquid Fuel Injection in Gas Turbine Engines*. Ph.D. thesis, University of Cambridge.

[38] Couderc (2007). *Développement d'un code de calcul pour la simulation d'écoulements de fluides non miscibles. Application à la désintegration assistée d'un jet liquide par un courant gazeux*. Ph.D. thesis, ENSAE Toulouse.

[39] Cousin, J., & Dumouchel, C. (1996). Effect of viscosity on linear instability of a flat liquid sheet. *Atomization and Sprays*, **6**, 563–576.

[40] Cox, R. G. (1986). The dynamics of the spreading of liquids on a solid surface. part 1. viscous flow. *Journal of Fluid Mechanics*, **168**, 169–194.

[41] Cuenot, B., Vicquelin, R., Riber, E., Moureau, V., Lartigue, G., Figuer, A., Mery, Y., Lamouroux, J., Richard, S., Gicquel, L., Schmitt, T., & Candel, S. (2016). Advanced Simulation of Aeronautical Combustors. *Journal Aerospace Lab*, **11**, 1–9.

[42] Cumpsty, N. (2003). *Jet Propulsion: A Simple Guide to the Aerodynamic and Thermodynamic Design and Performance of Jet Engines*. Cambridge University Press.

[43] Dahms, R. N., & Oefelein, J. C. (2013). On the transition between two-phase and single-phase interface dynamics in multicomponent fluids at supercritical pressures. *Physics of Fluids*, **25**, 092103.

[44] Davidson, M. R. (2000). Boundary integral prediction of the spreading of an inviscid drop impacting on a solid surface. *Critical Review Solid State Material Science*, **55**, 1159–1170.

[45] de Villiers, E., Gosman, A., & Weller, H. (2004). Large eddy simulation of primary diesel spray atomization. In *SAE Technical Paper*, 2004-01-0100.

[46] Déjean, B. (2015). *Etude expérimentale de l'atomisation d'une nappe liquide avec et sans zone de pré-film en vue de sa modélisation – Influence des conditions limites*. Ph.D. thesis, Institut Supérieur de l'Aéronautique et de l'Espace (ISAE).

[47] Déjean, B., Berthoumieu, P., & Gajan, P. (2016). Experimental study on the influence of liquid and air boundary conditions on a planar air-blasted liquid sheet, part i: Liquid and air thicknesses. *International Journal of Multiphase Flow*, **79**, 202–213.

[48] Déjean, B., Berthoumieu, P., & Gajan, P. (2016). Experimental study on the influence of liquid and air boundary conditions on a planar air-blasted liquid sheet, part ii: prefilming zone length. *International Journal of Multiphase Flow*, **79**, 214–224.

[49] Deshpande, S. S., Anumolu, L., & Trujillo, M. F. (2012). Evaluating the performance of the two-phase flow solver interFoam. *Computational Science & Discovery*, **5**, 014016.

[50] Desjardins, O. (2008). *Numerical methods for liquid atomization and application in detailed simulations of a diesel jet*. Ph.D. thesis, Stanford University.

[51] Desjardins, O., Moureau, V., Knudsen, E., Herrmann, M., & Pitsch, H. (2007). Conservative level set/ghost fluid method for simulating primary atomization. In *Proceedings of the* 20^{th} *Annual Conference of the Institute for Liquid Atomization and Spray Systems – ILASS Americas*. Chicago, IL.

[52] Dianat, M., Skarysz, M., & Garmory, A. (2017). A Coupled Level Set and Volume of Fluid method for automotive exterior water management applications. *International Journal of Multiphase Flow*, **91**, 19–38.

[53] Dimonte, G., Youngs, D. L., Dimits, A., Weber, S., Marinak, M., Wunsch, S., Garasi, C., Robinson, A., Andrews, M. J., Ramaprabhu, P., Calder, A. C., Fryxell, B., Biello, J., Dursi, L., MacNeice, P., Olson, K., Ricker, P., Rosner, R., Timmes, F., Tufo, H., Young, Y. N., & Zingale, M. (2004). Density ratio dependence of Rayleigh–Taylor mixing for sustained and impulsive acceleration histories. *Physics of Fluids*, **16**, 1668–1693.

[54] Dombrowski, N., & Foumeny, E. A. (1998). On the stability of liquid sheets in hot atmospheres. *Atomization and Sprays*, **8**, 235–240.

[55] Dowling, A. P., & Stow, A. P. (2003). Acoustic analysis of gas turbine combustors. *Journal of Propulsion and Power*, **19**, 751–764.

[56] Duke, D., Honnery, D., & Soria, J. (2010). A cross-correlation velocimetry technique for breakup of an annular liquid sheet. *Experiments in Fluids*, **49**, 435–445.

[57] Dumouchel, C. (2008). On the experimental investigation on primary atomization of liquid streams. *Experiments in Fluids*, **45**, 371–422.

[58] Dunn-Rankin, D. (2008). *Lean Combustion*. Burlington: Academic Press.

[59] Eggers, J. (2011). The subtle dynamics of liquid sheets. *Journal of Fluid Mechanics*, **672**, 1–4.

[60] Einsenklam, P. (1961). Atomisation of liquid fuel for combustion. *Journal of the Institute of Fuel*, **34**, 130–143.

[61] Faeth, G. M., Hsiang, L. P., & Wu, P. K. (1995). Structure and breakup properties of sprays. *International Journal of Multiphase Flow*, **21**, 99–127.

[62] Farago, Z., & Chigier, N. (1992). Morfological classification of disintegration of round liquid jets in a coaxial air stream. *Atomization and Sprays*, **2**, 137–153.

[63] Fermi, E., & von Neumann, J. (1953). Taylor instability of incompressible liquids. Part 1. Taylor instability of an incompressible liquid. Part 2. Taylor instability at the boundary of two incompressible liquids. Tech. rep., Los Alamos Scientific Laboratory. AECU-2979.

[64] Fernandez, V., Berthoumie, P., & Lavergne, G. (2009). Liquid sheet disintegration at high pressure: An experimental approach. *Comptes Rendus Mécanique*, **337**, 481–491.

[65] Ferrari, A., Magnini, M., & Thome, J. R. (2017). A Flexible Coupled Level Set and Volume of Fluid (flexCLV) method to simulate microscale two-phase flow in non-uniform and unstructured meshes. *International Journal of Multiphase Flow*, **91**, 276–295.

[66] Francois, M. M., Cummins, S. J., Dendy, E. D., Kothe, D. B., Sicilian, J. M., & Williams, M. W. (2006). A balanced-force algorithm for continuous and sharp interfacial surface tension models within a volume tracking framework. *Journal of Computational Physics*, **213**, 141–173.

[67] Fraser, R., Dombrowski, N., & Routley, J. (1963). The atomization of a liquid sheet by an impinging air stream. *Chemical Engineering Science*, **18**, 339–353.

[68] Fraser, R. P., Eisenklam, P., Dombrowski, N., & Hasson, D. (1962). Drop formation from rapidly moving liquid sheets. *AIChE Journal*, **8**, 672–680.

[69] Fuster, D., Bagué, A., Boeck, T., Le Moyne, L., Leboissetier, A., Popinet, S., Ray, P., Scardovelli, R., & Zaleski, S. (2009). Simulation of primary atomization with an octree adaptive mesh refinement and VOF method. *International Journal of Multiphase Flow*, **35**, 550–565.

[70] Gepperth, S., Bärow, E., Koch, R., & Bauer, H. (2014). Primary atomization of prefilming airblast nozzles: Experimental studies using advanced image processing techniques. In *Proceedings of the 26th Annual Conference on Liquid Atomization and Spray Systems – ILASS Europe*. Bremen, Germany.

[71] Gepperth, S., Guildenbecher, D., Koch, R., & Bauer, H.-J. (2010). Pre-filming primary atomization: experiments and modeling. In *23rd Annual Conference on Liquid Atomization and Spray Systems*. Brno, Czech Republic: Institute for Liquid Atomization and Spray Systems.

[72] Gepperth, S., Guildenbecher, D., Koch, R., & Bauer, H. J. (2012). Ligament and Droplet Characteristics in Prefilming Airblast Atomization. In *12th Triennial International Conference on Liquid Atomization and Spray Systems*. Heidelberg, Germany: Institute for Liquid Atomization and Spray Systems.

[73] Gepperth, S., Koch, R., & Bauer, H. J. (2013). Analysis and comparison of primary droplet characteristics in the near field of a prefilming airblast atomizer. In *ASME Turbo Expo 2013: Turbine Technical Conference and Exposition*, GT2013-94033.

[74] Gingold, R. A., & Monaghan, J. J. (1977). Smoothed particle hydrodynamics: theory and application to non-spherical stars. *Monthly Notices of the Royal Astronomical Society*, **181**, 375–389.

[75] Giusti, A. (2013). *Development of numerical tools for the analysis of advanced airblast injection systems for lean burn aero-engine combustors*. Ph.D. thesis, Università degli studi Firenze.

[76] Gopala, V. R., & van Wachem, B. G. M. (2008). Volume of fluid methods for immiscible-fluid and free-surface flows. *Chemical Engineering Journal*, **141**, 204–221.

[77] Gorokhovski, M., & Herrmann, M. (2008). Modeling primary atomization. *Annual Review of Fluid Mechanics*, **40**, 343–366.

[78] Gueyffier, D., Li, J., Nadin, A., Scardovelli, R., & Zaleski., S. (1999). A volume of fluid interface tracking with smoothed surface stress methods for three-dimensional flows. *Journal of Computational Physics*, **152**, 423–456.

[79] Guildenbecher, D. R. (2016). Recent Developments in Experimental Methods for Quantification of High-speed, Aerodynamically Driven Liquid Breakup. In *Proceedings of the* 28th *Annual Conference of the Institute for Liquid Atomization and Spray Systems – ILASS Americas*. Detroit, MI.

[80] Guildenbecher, D. R., López-Rivera, C., & Sojka, P. E. (2009). Secondary atomization. *Experiments in Fluids*, **46**, 371–402.

[81] Guo, Y., Lian, Y., & Sussman, M. (2016). Investigation of drop impact on dry and wet surfaces with consideration of surrounding air. *Physics of Fluids*, **28**, 073303.

[82] Hagerty, W. W., & Shea, J. F. (1959). A study of the stability of plane fluid sheets. *Journal of Applied Mechanics*, **22**, 509–514.

[83] Hardalupas, Y., Pergamalis, H., Taylor, A. M. K. P., Cossali, G. E., & Marengo, M. (2002). Comparison of front-tracking and front-capturing computations with experimental images of drop impact onto shallow liquid pools. In 18th *Annual Conference on Liquid Atomization and Spray Systems*. Zaragoza, Spain: Institute for Liquid Atomization and Spray Systems.

[84] Harvie, D. J. E., Davidson, M. R., & Rudman, M. (2006). An analysis of parasitic current generation in volume of fluid simulations. *Applied Mathematical Modelling*, **30**, 1056–1066.

[85] He, X., Zhang, R., Chen, S., & Doolen, G. D. (1999). On the three-dimensional Rayleigh–Taylor instability. *Physics of Fluids*, **11**, 1143.

[86] Herrmann, M. (2004). On mass conservation and desingularization of the Level Set/Vortex Sheet method. *Center for Turbulence Research Annual Research Briefs*, (pp. 15–30).

[87] Herrmann, M. (2010). A parallel Eulerian interface tracking/Lagrangian point particle multi-scale coupling procedure. *Journal of Computational Physics*, **229**, 745–759.

[88] Herrmann, M., & Gorokhovski, M. (2008). An outline of an LES subgrid model for liquid/gas phase interface dynamics. In *Proceedings of the Center for Turbulence Research Summer Program*. Stanford, CA.

[89] Hicks, R. (2016). private communication. Rolls-Royce plc.

[90] Hirt, C., & Nichols, B. (1981). Volume of Fluid (VoF) method for the dynamics of free boundaries. *Journal of Computational Physics*, **39**, 201–225.

[91] Hoffman, R. (1975). A study of the advancing interface. i. interface shape in liquid-gas systems. *Journal of Colloid and Interface Science*, **50**, 228–241.

[92] Hong, M. (2003). *Atomisation et mélange dans les jets coaxiaux liquide-gaz*. Ph.D. thesis, LEGI, Grenoble.

[93] Hsiao, M., Lichter, S., & Quintero, L. G. (1988). The critical Weber number for vortex and jet formation for drops impinging on a liquid pool. *Physics of Fluids*, **31**, 3560–3562.

[94] Hughes, J. P., Rakowski, C. E., & Decourchelle, A. (2000). Electron Heating and Cosmic Rays at a Supernova Shock from Chandra X-Ray Observations of 1E 0102.2–7219. *The Astrophysical Journal Letters*, **543**, L61.

[95] Inamura, T., Shirota, M., Tsushima, M., Kato, M., Hama-jima, S., & Sato, A. (2012). Spray Characteristics of Prefilming Type of Airblast Atomizer. In *Proceedings of the* 12th *Triennial International Conference on Liquid Atomization and Spray Systems – ICLASS*. Heidelberg, Germany.

[96] Ireland, P. J., & Desjardins, O. (2016). Toward liquid jet atomization in supersonic crossflows. In *Proceedings of the* 28th *Annual Conference of the Institute for Liquid Atomization and Spray Systems – ILASS Americas*. Detroit, MI.

[97] Ireland, P. J., & Desjardins, O. (2017). Improving particle drag predictions in Euler-Lagrange simulations with two-way coupling. *Journal of Computational Physics*, **338**, 405–430.

[98] Jaegle, F., Senoner, J.-M., Garca, M., Bismes, F., Lecourt, R., Cuenot, B., & Poinsot, T. (2011). Eulerian and lagrangian spray simulations of an aeronautical multipoint injector. *Proceedings of the Combustion Institute*, **33**, 2099–2107.

[99] Jain, M., Prakash, R. S., Tomar, G., & Ravikrishna, R. V. (2015). Secondary breakup of a drop at moderate Weber numbers. *Proceedings of the Royal Society A: Mathematical, Physical and Engineering Sciences*, **471**, 20140930.

[100] Janicka, J., Sadiki, A., Schäfer, M., & Heeger, C. (2012). *Flow and combustion in advanced gas turbine combustors*, vol. 102. Springer Science & Business Media.

[101] Jasak, H., & Weller, H. G. (1995). Interface-tracking capabilities of the InterGamma differencing scheme. Tech. rep., Imperial College London.

[102] Jenkins, K., & Cant, R. (1999). Direct Numerical Simulation of turbulent flame kernels. In D. Knight, & L. Sakell (Eds.) *Recent Advances in DNS and LES*, (pp. 191–202). New York: Kluwer Academic.

[103] Johnson, R., Jacobs, H., & Boehm, F. (1975). *Direct contact heat transfer between two immiscible liquids in laminar flow between parallel plates*. Ph.D. thesis, Mechanical Engineering, University of Utah.

[104] Josserand, C., Ray, P., & Zaleski, S. (2016). Droplet impact on a thin liquid film: anatomy of the splash. *Journal of Fluid Mechanics*, **802**, 775–805.

[105] Josserand, C., & Zaleski, S. (2003). Droplet splashing on a thin liquid film. *Physics of Fluids*, **15**, 1650.

[106] Kadau, K., Germann, T. C., Hadjiconstantinou, N. G., Lomdahl, P. S., Dimonte, G., Holian, B. L., & Alder, B. J. (2004). Nanohydrodynamics simulations: an atomistic view of the Rayleigh-Taylor instability. *Proceedings of the National Academy of Sciences of the United States of America*, **101**, 5851–5855.

[107] Kane, J. H. (1994). *Boundary element analysis*. NJ: Prentice Hall: Englewood Cliffs.

[108] Kelvin, L. W. T. (1871). Hydrokinetic solutions and observations. *Philosophical Magazine*, **42**, 362–377.

[109] Kelvin, L. W. T. (1890). Oscillations of a liquid sphere. In *Mathematical and Physical Papers Vol. 3*, (pp. 384–386). London: Clay and Sons.

[110] Kim, D., Desjardins, O., Herrmann, M., & Moin., P. (2007). The primary breakup of a round liquid jet by a coaxial flow of gas. In *Proceedings of the 20*th *Annual Conference on Liquid Atomization and Spray Systems – ILASS Americas*. Chicago, IL.

[111] Kistler, S. F. (1993). Hydrodynamics of wetting. In J. C. Berg (Ed.) *Wettability*, (pp. 717–718). New York: Marcel Dekker.

[112] Klein, R., Sadiki, S., & Janika, T. (2003). A digital filter based generation of in- flow data for spatially developing direct numerical simulation or large eddy simulations. *Journal of Computational Physics*, **186**, 652–665.

[113] Kobel, P., Obreschkow, D., Dorsaz, N., de Bosset, A., Tinguely, M., & Farhat, M. (2011). Bubbles in drops: from cavitation to exploding stars. In *64*th *Annual Meeting of the APS Division of Fluid Dynamics*. Baltimore, MD: American Physical Society.

[114] Krüss GmbH (2017). *Krüss Advancing your Surface Science*. https://www.kruss.de/services/education-theory/glossary/contact-angle/ [Accessed: January 2017].

[115] Kull, H. J. (1991). Theory of the Rayleigh–Taylor instability. *Physics Reports, North–Holland*, **206**, 197–325.

[116] Labourasse, E., Lacanette, D., Toutant, A., Lubin, P., Vincent, S., Lebaigue, O., Caltagirone, J.-P., & Sagaut, P. (2007). Towards large eddy simulation of isothermal two-phase flows: Governing equations and a priori tests. *International Journal of Multiphase Flow*, **33**, 1–39.

[117] Lafaurie, B., Nardone, C., Scardovelli, R., Zaleski, S., & Zanetti, G. (1994). Modelling merging and fragmentation in multiphase flows with surfer. *Journal of Computational Physics*, **113**, 134–147.

[118] Lam, C. N. C., Wu, R., Li, D., Hair, M. L., & Neumann, A. (2002). Study of the advancing and receding contact angles: liquid sorption as a cause of contact angle hysteresis. *Advances in Colloid and Interface Science*, **96**, 169–191.

[119] Lamb, H. (1916). *Hydrodynamics*. Cambridge University Press. Fourth Edition.

[120] Lasheras, J. C., & Hopfinger, E. J. (2000). Liquid jet instability and atomization in a coaxial gas stream. *Annual review of fluid mechanics*, **32**, 275–308.

[121] Lee, H. G., & Kim, J. (2013). Numerical simulation of the three-dimensional Rayleigh–Taylor instability. *Computers & Mathematics with Applications*, **66**, 1466–1474.

[122] Lefebvre, A. H. (1980). Airblast atomization. *Progress in Energy Combustion Science*, **6**, 233–261.

[123] Lefebvre, A. H. (1989). *Atomization and Sprays*. New-York: Hemisphere Publishing Corporation.

[124] Lefebvre, A. H. (2000). Fifty years of gas turbine fuel injection. *Atomization and Sprays*, **10**, 251–276.

[125] Levich, V. (1962). *Physicochemical Hydrodynamics*. Englewood Cliffs, NJ: Prentice-Hall. Pp. 636–546.

[126] Lewis, D. J. (1950). The instability of liquid surfaces when accelerated in a direction perpendicular to their planes (II). *Proceedings of the Royal Society*, **202**, 81–96.

[127] Lhuissier, H., & Villermaux, E. (2011). The destabilization of an initially thick liquid sheet edge. *Physics of Fluids*, **23**, 1–4.

[128] Lin, S. P., & Reitz, R. D. (1998). Drop and spray formation from a liquid jet. *Annual Review of Fluid Mechanics*, **30**, 85–105.

[129] Lind, S. J., Stansby, P. K., & Rogers, B. D. (2016). Incompressible-compressible flows with a transient discontinuous interface using smoothed particle hydrodynamics (SPH). *Journal of Computational Physics*, **309**, 129–147.

[130] Lind, S. J., Stansby, P. K., Rogers, B. D., & Lloyd, P. M. (2015). Numerical predictions of water-air wave slam using incompressible-compressible smoothed particle hydrodynamics. *Applied Ocean Research*, **49**, 57–71.

[131] Ling, Y., Fuster, D., Zaleski, S., & Tryggvason, G. (2017). Spray formation in a quasiplanar gas-liquid mixing layer at moderate density ratios: A numerical closeup. *Physical Review Fluids*, **2**, 014005.

[132] Ling, Y., Zaleski, S., & Scardovelli, R. (2015). Multiscale simulation of atomization with small droplets represented by a Lagrangian point-particle model. *International Journal of Multiphase Flow*, **76**, 122–143.

[133] Liu, F., Kang, N., & Li, Y. (2017). Numerical investigation on the mechanism of ligament formation aroused by Rayleigh–Taylor instability. *Computers & Fluids*, **154**, 236–244.

[134] Liu, X.-D., Osher, S., & Chan, T. (1994). Weighted Essentially Non-oscillatory Schemes. *Journal of Computational Physics*, **115**, 200–212.

[135] Lozano, A., & Barreras, F. (2001). Experimental study of the gas flow in an air-blasted liquid sheet. *Experiments in Fluids*, **31**, 367–376.

[136] Lozano, A., Barreras, F., Siegler, C., & Löw, D. (2005). The effects of sheet thickness on the oscillation of an air-blasted liquid sheet. *Experiments in Fluids*, **39**, 127–139.

[137] Lozano, A., Calvo, E., García, J. A., & Barreras, F. (2011). Mode transitions in an oscillating liquid sheet. *Physics of Fluids*, **23**, 044–103.

[138] Mansour, A., & Chigier, N. (1990). Disintegration of liquid sheets. *Physics of Fluids*, **2**, 706–719.

[139] Mansour, A., & Chigier, N. (1991). Dynamic behavior of liquid sheets. *Physics of Fluids*, **3**, 2971–2980.

[140] Marmottant, P. (2001). *Atomisation d'un liquide par un courant gazeux*. Ph.D. thesis, INPG, Grenoble.

[141] Marmottant, P., & Villermaux, E. (2004). On spray formation. *Journal of Fluid Mechanics*, **498**, 73–111.

[142] Marty, S., Matas, J.-P., & Cartellier, A. (2013). Study of a liquid-gas mixing layer: Shear instability and size of produced drops. *Comptes Rendus Mécanique*, **341**, 26–34.

[143] Matas, J.-P., Marty, S., Dem, M., & Cartellier, A. (2015). Influence of turbulence on the instability of an air-water mixing layer. *Physical Review Letters*, **115**, 074501.

[144] Ménard, T., Tanguy, S., & Berlemont, A. (2007). Coupling Level Set/VOF/ghost fluid methods: Validation and application to 3D simulation of the primary break-up of a liquid jet. *International Journal of Multiphase Flow*, **33**, 510–524.

[145] Menikoff, R., & Zemach, C. (1983). Rayleigh–Taylor instability and the use of conformal maps for ideal fluid flow. *Journal of Computational Physics*, **51**, 28–64.

[146] Michael, G., & Margrit, K. (2013). Simulation of droplet impact with dynamic contact angle boundary conditions. In G. Michael (Ed.) *Singular Phenomena and Scaling in Mathematical Models*, (pp. 297–325). Springer International Publishing.

[147] Miehe, A. (2010). *Aufgabenstellung zur Diplomarbeit Entwicklung Entwicklung eines numerischen Modells für Wärmeübergangsprozesse an Grenzflächen strömenden Fluiden*. Ph.D. thesis, Technishe Universität Bergakademie Freiberg.

[148] Navier, C.-L. (1823). *Mémoire sur les lois du mouvement des fluides*. Ph.D. thesis, L'Académie royale des Sciences.

[149] Oğuz, H. N., & Prosperetti, A. (1990). Bubble entrainment by the impact of drops on liquid surfaces. *Journal of Fluid Mechanics*, **219**, 143–179.

[150] Olsson, E., & Kreiss, G. (2005). A conservative level set method for two phase flow. *Journal of Computational Physics*, **210**, 225–246.

[151] Olsson, E., Kreiss, G., & Zahedi, S. (2007). A conservative level set method for two phase flow II. *Journal of Computational Physics*, **225**, 785–807.

[152] Osher, S., & Sethian, J. (1988). Fronts propagating with curvature-dependent speed: Algorithms based on hamilton-jacobi formulations. *Journal of Computational Physics*, **79**, 12–49.

[153] Peng, C. A., Jurman, L., & McCready, M. (1991). Formation of solitary waves on gas-sheared liquid layers. *International Journal of Multiphase Flow*, **17**, 767–782.

[154] Plateau, J. (1873). *Statique Expérimentale et Théorique des Liquides Soumis aux Seules Forces Moléculaires*. Paris: Gauthier–Villars.

[155] Plesset, M. S., & Whipple, C. G. (1974). Viscous effects in Rayleigh-Taylor instability. *Physics of Fluids*, **17**, 1–7.

[156] Popinet, S. (2009). An accurate adaptive solver for surface-tension-driven interfacial flows. *Journal of Computational Physics*, **228**, 5838–5866.

[157] Popinet, S., & Zaleski, S. (1999). A front-tracking algorithm for accurate representation of surface tension. *International Journal for Numerical Methods in Fluids*, **30**, 775–793.

[158] Pringuey, T. (2012). *Large Eddy Simulation of Primary Liquid-Sheet Breakup*. Ph.D. thesis, University of Cambridge, Department of Engineering.

[159] Pringuey, T., & Cant, R. S. (2012). High order schemes on three-dimensional general polyhedral meshes – application to the level set method. *Communications in Computational Physics*, **12**, 1–41.

[160] Pringuey, T., & Cant, R. S. (2014). Robust Conservative Level Set method for 3D mixed-element meshes – Application to LES of primary liquid-sheet breakup. *Communications in Computational Physics*, **16**, 403–439.

[161] Puckett, E. G., Almgren, A. S., Bell, J. B., Marcus, D. L., & Rider, W. J. (1997). A High-Order Projection Method for Tracking Fluid Interfaces in Variable Density Incompressible Flows. *Journal of Computational Physics*, **130**, 269–282.

[162] Raeini, A. Q., Blunt, M. J., & Bijeljic, B. (2012). Modelling two-phase flow in porous media at the pore scale using the volume-of-fluid method. *Journal of Computational Physics*, **231**, 5653–5668.

[163] Raessi, M., & Pitsch, H. (2009). Modeling interfacial flows characterized by large density ratios with the level set method. (pp. 159–169).

[164] Rayleigh, J. (1883). Investigation of the character of the equilibrium of an incompressible heavy fluid of variable density. *Proceedings of the Royal Society of London*, **14**, 170–177.

[165] Rayleigh, J. W. S. (1878). On the stability of jets. *Proceedings of the Royal Society of London*, **10**, 4–13.

[166] Rayleigh, J. W. S. (1879). On the capillary phenomena of jets. *Proceedings of the Royal Society of London*, **29**, 71–97.

[167] Raynal, L. (1997). *Instabilité et entrainement à l'interface d'une couche de mélange liquide-gaz*. Ph.D. thesis, Université Joseph Fourier, Grenoble.

[168] Reitz, R. D. (1978). *Atomization and other breakup regimes of a liquid jet*. Ph.D. thesis, Princeton University, New Jersey.

[169] Reitz, R. D., & Bracco, F. V. (1982). Mechanism of atomization of a liquid jet. *Physics of Fluids*, **25**, 1730–1742.

[170] Renardy, M., Renardy, Y., & Li, J. (2001). Numerical simulation of moving contact line problems using a volume-of-fluid method. *Journal of Computational Physics*, **171**, 243–262.

[171] Renardy, Y., & Renardy, M. (2002). Prost: A parabolic reconstruction of surface tension for the volume-of-fluid method. *Journal of Computational Physics*, **183**, 400–421.

[172] Rioboo, R., Tropea, C., & Marengo, M. (2001). Outcomes from a drop impact on solid surfaces. *Atomization and Sprays*, **11**, 155–165.

[173] Ristorcelli, J. R., & Clark, T. T. (2004). Rayleigh–Taylor turbulence: self-similar analysis and direct numerical simulations. *Journal of Fluid Mechanics*, **507**, 213–253.

[174] Rizk, N., & Lefebvre, A. (1980). The influence of liquid film thickness on airblast atomization. *Journal for Engineering for Power*, **102**, 706–710.

[175] Rizkalla, A., & Lefebvre, A. (1975). The influence of air and liquid properties on airblast atomization. *Journal of Engineering for Power*, **97**, 316–320.

[176] Rizkalla, A. A., & Lefebvre, A. H. (1975). Influence of liquid properties on airblast atomizer spray characteristics. *Journal of Engineering for Power*, **97**, 173–177.

[177] Roisman, I. V., Opfer, L., Tropea, C., Raessi, M., Mostaghimi, J., & Chandra, S. (2008). Drop impact onto a dry surface: Role of the dynamic contact angle. *Colloids and Surfaces A: Physicochemical and Engineering Aspects*, **322**, 183–191.

[178] Rolls-Royce (2015). *The Jet Engine*. Chichester, United Kingdom: John Wiley & Sons, 5th ed.

[179] Rutland, D. F., & Jameson, G. J. (1971). A nonlinear effect in the capillary instability of liquid jet. *Journal of Fluid Mechanics*, **46**, 267–271.

[180] Sanders, N. (2006). Fuel injection apparatus. US Patent App. 11/116,259.

[181] Sattelmayer, T., & Witting, S. (1986). Internal flow effects in prefilming airblast atomisers: mechanisms of atomization and droplet spectra. *Journal of Engineering for Gas Turbines and Power*, **108**, 465–472.

[182] Sauer, B. (2014). *Direct numerical simulation of the primary breakup of aircraft engine related two-phase flows*. Ph.D. thesis, Technischen Universität Darmstadt.

[183] Sauer, B., Sadiki, A., & Janicka, J. (2016). Embedded dns concept for simulating the primary breakup of an airblast atomizer. *Atomization and Sprays*, **26**, 187–215.

[184] Savart, F. (1833). Mémoire sur la constitution des veines liquides lancées par des orifices circulaires en mince paroi. *Annales de Chimie et de Physique*, **53**, 337–339.

[185] Savart, F. (1833). Mémoire sur le choc de deux veines liquides animées de mouvements directement opposés. *Annales de Chimie et de Physique*, **55**, 257–310.

[186] Savart, F. (1833). Mémoire sur le choc d'une veine liquide lancée sur un plan circulaire. *Annales de Chimie et de Physique*, **54**, 56–87.

[187] Savart, F. (1833). Suite du mémoire sur le choc d'une veine liquide lancée sur un plan circulaire. *Annales de Chimie et de Physique*, **54**, 113–145.

[188] Savva, N., & Bush, J. W. M. (2009). Viscous sheet retraction. *Journal of Fluid Mechanics*, **626**, 211–240.

[189] Scardovelli, R., & Zaleski, S. (1999). Direct numerical simulation of free-surface and interfacial flow. *Annual Review of Fluid Mechanics*, **31**, 567–603.

[190] Scharfman, B. E., & Techet, A. H. (2014). Three-Dimensional Spray Analysis using Light Field Imaging. In *Proceedings of the 26th Annual Conference on Liquid Atomization and Spray Systems – ILASS Europe*. Bremen, Germany.

[191] Senoner, J.-M. (2010). *Simulations aux grandes échelles de l'écoulement diphasique dans un brûleur aéronautique par une approche Euler-Lagrange*. Ph.D. thesis, Institut National Polytechnique de Toulouse.

[192] Sharp, D. H. (1984). An overview of Rayleigh–Taylor instability. *Physica D: Nonlinear Phenomena*, **12**, 3–18.

[193] Shikhmurzaev, Y. (2007). *Capillary flows with forming interfaces*. Boca Raton, London: Chapman & Hall/CRC.

[194] Shinjo, J., & Umemura, A. (2010). Simulation of liquid jet primary breakup: Dynamics of ligament and droplet formation. *International Journal of Multiphase Flow*, **36**, 513–532.

[195] Shinjo, J., & Umemura, A. (2011). Detailed simulation of primary atomization mechanisms in diesel jet sprays (isolated identification of liquid jet tip effects). *Proceedings of the Combustion Institute*, **33**, 2089–2097.

[196] Shinjo, J., Xia, J., & Umemura, A. (2015). Droplet/ligament modulation of local small-scale turbulence and scalar mixing in a dense fuel spray. *Proceedings of the Combustion Institute*, **35**, 1595–1602.

[197] Shu, C.-W., & Osher, S. (1988). Efficient implementation of essentially non-oscillatory shock-capturing schemes. *Journal of Computational Physics*, **77**, 439–471.

[198] Šikalo, Š., Wilhelm, H. D., Roisman, I. V., Jakirlić, S., & Tropea, C. (2005). Dynamic contact angle of spreading droplets: Experiments and simulations. *Physics of Fluids*, **17**, 1–13.

[199] Sirignano, W. A., & Mehring, C. (2000). Review of theory of distortion and disintegration of liquid streams. *Progress in Energy and Combustion Science*, **26**, 609–655.

[200] Som, S., & Aggarwal, S. (2010). Effects of primary breakup modeling on spray and combustion characteristics of compression ignition engines. *Combustion and Flame*, **157**, 1179–1193.

[201] Squire, H. B. (1953). Investigation of the instability of a moving liquid film. *British Journal of Applied Physics*, **4**, 167–169.

[202] Stapper, B. E., & Samuelsen, G. S. (1990). An experimental study of the breakup of a two-dimensional liquid sheet in the presence of co-flow air shear. In *Proceedings of the* 28th *Aerospace Sciences Meeting of the American Institute of Aeronautics and Astronautics*, 90-0461. Reno, Nevada.

[203] Sui, Y., Ding, H., & Spelt, P. D. M. (2014). Numerical simulations of flows with moving contact lines. *Annual Review of Fluid Mechanics*, **46**, 97–119.

[204] Sussman, M., & Puckett, E. G. (2000). A coupled level set and volume-of-fluid method for computing 3d and axisymmetric incompressible two-phase flows. *Journal of Computational Physics*, **162**, 301–337.

[205] Sussman, M., Smereka, P., & Osher, S. (1994). A level set approach for computing solutions to incompressible two-phase flow. *Journal of Computational Physics*, **114**, 146–159.

[206] Tammisola, O. (2011). *Numerical stability studies of one-phase and immiscible two-phase jets and wakes*. Ph.D. thesis, Royal Institute of Technology KTH Mechanics, Stockholm, Sweden.

[207] Tanner, L. H. (1979). The spreading of silicone oil drops on solid surfaces. *Journal of Physics D: Applied Physics*, **12**, 1473–1482.

[208] Tauber, W., Unverdi, S. O., & Tryggvason, G. (2002). The nonlinear behavior of a sheared immiscible fluid interface. *Physics of Fluids*, **14**, 2871–2885.

[209] Taylor, G. (1963). Generation of ripples by wind blowing over a viscous liquid. In G. Batchelor (Ed.) *The Scientific Papers of Sir Geoffrey Ingram Taylor Vol. 3*, chap. 25, (pp. 244–254). Cambridge University Press.

[210] Taylor, G. I. (1950). The instability of liquid surfaces when accelerated in a direction perpendicular to their planes. *Proceedings of the Royal Society*, **201**, 192–196.

[211] Taylor, G. I. (1959). The dynamics of thin sheets of fluid. ii. waves on fluid sheets. *Proceedings of the Royal Society of London. Series A. Mathematical and Physical Sciences*, **253**, 296–312.

[212] Taylor, G. I., & Howarth, L. (1959). The dynamics of thin sheets of fluid. i. Water bells. *Proceedings of the Royal Society of London. Series A. Mathematical and Physical Sciences*, **253**, 289–295.

[213] Thoraval, M.-J., Takehara, K., Etoh, T., Popinet, S., Ray, P., Josserand, C., Zaleski, S., & Thoroddsen, S. (2012). von Kármán vortex street within an impacting drop. *Physical Review Letters*, **108**, 264506.

[214] Thoroddsen, S. T. (2002). The ejecta sheet generated by the impact of a drop. *Journal of Fluid Mechanics*, **451**, 373–381.

[215] Thoroddsen, S. T., Etoh, T. G., & Takehara, K. (2003). Air entrapment under an impacting drop. *Journal of Fluid Mechanics*, **478**, 125–134.

[216] Tomar, G., Fuster, D., Zaleski, S., & Popinet, S. (2010). Multiscale simulations of primary atomization. *Computers and Fluids*, **39**, 1864–1874.

[217] Tritton, D. J. (1977). *Physical Fluid Dynamics*. Wokingham, England: Van Nostrand Reinhold.

[218] Tryggvason, G. (1988). Numerical simulations of the Rayleigh–Taylor instability. *Journal of Computational Physics*, **75**, 253–282.

[219] Tryggvason, G. (1990). Computations of three-dimensional Rayleigh–Taylor instability. *Physics of Fluids*, **2**, 656–659.

[220] Tryggvason, G., Scardovelli, R., & Zaleski, S. (2011). *Direct numerical simulations of gas–liquid multiphase flows*. Cambridge University Press.

[221] Ubbink, O., & Issa, R. (1999). A method for capturing sharp fluid interfaces on arbitrary meshes. *Journal of Computational Physics*, **153**, 26–50.

[222] Van Dyke, M. (1982). *An album of fluid motion*. Parabolic Press.

[223] Villermaux, E. (2007). Fragmentation. *Annual Review of Fluid Mechanics*, **39**, 419–446.

[224] Villermaux, E., & Clanet, C. (2002). Life of a flapping liquid sheet. *Journal of Fluid Mechanics*, **462**, 341–363.

[225] Visser, C. W., Frommhold, P. E., Wildeman, S., Mettin, R., Lohse, D., & Sun, C. (2015). Dynamics of high-speed micro-drop impact: numerical simulations and experiments at frame-to-frame times below 100ns. *Soft Matter*, **11**, 1708–1722.

[226] Voinov, O. V. (1976). Hydrodynamics of wetting. *Fluid Dynamics*, **11**, 714–721.

[227] von Helmholtz, H. L. F. (1868). On the discontinuous movements of fluids. *Monthly Reports of the Royal Prussian Academy of Philosophy in Berlin*, **23**, 215–228.

[228] Vuorinen, V., Hillamo, H., Kaario, O., Nuutinen, M., Larmi, M., & Fuchs, L. (2011). Effect of droplet size and atomization on spray formation: A priori study using large-eddy simulation. *Flow Turbulence Combustion*, **86**, 533–561.

[229] Warncke, K., Gepperth, S., Sauer, B., Sadiki, A., Janicka, J., Koch, R., & Bauer, H. J. (2017). Experimental and numerical investigation of the primary breakup of an airblasted liquid sheet. *International Journal of Multiphase Flow*, **91**, 208–224.

[230] Weiss, D. A., & Yarin, A. L. (1999). Single drop impact onto liquid films: Neck distortion, jetting, tiny bubble entrainment, and crown formation. *Journal of Fluid Mechanics*, **385**, 229–254.

[231] Weller, H. G., Tabor, G., Jasak, H., & Fureby, C. (1998). A tensorial approach to computational continuum mechanics using object-oriented techniques. *Journal of Computational Physics*, **12**, 620–631.

[232] Williams, A. (1990). *Combustion of Liquid Fuel Sprays*. St Louis, Missouri: Butterworth-Heinemann.

[233] Williams, M. W., Kothe, D. B., & Puckett, E. G. (1998). Accuracy and convergence of continuum surface tension models. In W. Shyy (Ed.) *Fluid Dynamics at Interfaces*, (pp. 347–356). Cambridge University Press.

[234] Yarin, A. (2006). Drop impact dynamics: Splashing, Spreading, Receding, Bouncing. *Annual Review of Fluid Mechanics*, **38**, 159–192.

[235] Yecko, P., & Zaleski, S. (2000). Two-phase Shear Instability: Waves, Fingers, and Drops. *Annals of the New York Academy of Sciences*, **898**, 127–143.

[236] Yokoi, K. (2008). A numerical method for free-surface flows and its application to droplet impact on a thin liquid layer. *Journal of Scientific Computing*, **35**, 372–396.

[237] Yokoi, K. (2013). A practical numerical framework for free surface flows based on CLSVOF method, multi-moment methods and density-scaled CSF model: Numerical simulations of droplet splashing. *Journal of Computational Physics*, **232**, 252–271.

[238] Yokoi, K., Vadillo, D., Hinch, J., & Hutchings, I. (2009). Numerical studies of the influence of the dynamic contact angle on a droplet impacting on a dry surface. *Physics of Fluids*, **21**, 072102.

[239] York, J. L., Stubbs, H. E., & Tek, M. R. (1953). The mechanisms of disintegration of liquid sheets. *Transactions of ASME*, **75**, 1279–1286.

[240] Young, T. (1805). An essay on the cohesion of fluids. *Philosophical Transactions of the Royal Society of London*, **95**, 65–87.

[241] Yuan, Y., & Lee, T. R. (2013). Contact angle and wetting properties. In G. Bracco, & B. Holst (Eds.) *Surface Science Techniques*, vol. 51, (pp. 3–34). Berlin, Heidelberg: Springer Series in Surface Sciences.

[242] Zalesak, S. T. (1979). Fully Multidimensional Flux-Corrected Transport Algorithms for Fluids. *Journal of Computational Physics*, **31**, 335–362.

[243] Zaleski, S., Yecko, P., Boeck, T., Li, J., & Lopez-Pages, E. (2007). Ligament formation in sheared liquid-gas layers. *Theoretical and Computational Fluid Dynamics*, **2**, 59–76.

[244] Zuzio, D., Estivalèzes, J.-L., & DiPierro, B. (2017). An improved multiscale Eulerian–Lagrangian method for simulation of atomization process. *Computational Science & Discovery*. DOI 10.1016/j.compfluid.2016.12.018.

Appendix A

Analysis of planar Poiseuille flows between parallel plates

A.1 Standard single-phase Poiseuille flow

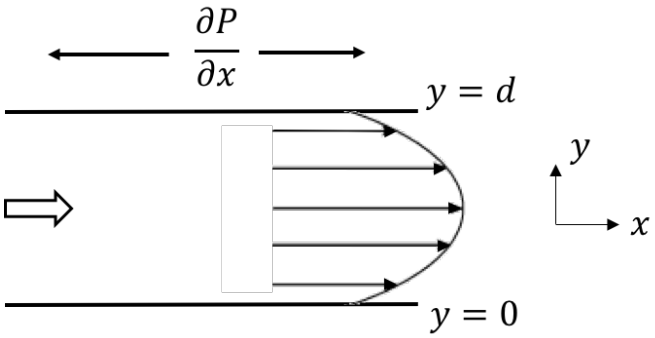

Fig. A.1: Channel pressure drop in single-phase Poiseuille flow.

A Poiseuille flow is a channel pressure-induced shear flow in a long duct, as depicted in Fig. A.1. The resulting Poiseuille equation gives the pressure drop in a fully-developed incompressible laminar Newtonian fluid of viscosity μ in steady flow between parallel plates. Starting from the continuity equation, for a fully-developed flow, the velocity component normal to the walls is zero, which implies that velocity does not change in the x-direction – $u = u(y)$ only. The y-momentum equation, subject to no body forces and assuming the flow to be steady, becomes

$$\frac{\partial p}{\partial y} = 0$$

which implies that pressure does not depend on y. Therefore the x-momentum equation yields

$$\mu \frac{\partial^2 u}{\partial y^2} = \frac{\partial P}{\partial x}. \tag{A.1}$$

Eq. A.1 represents a simple equation between the shear stress at the walls and the total drag force in the system. The latter being the pressure difference Δp between the outlet and the inlet boundary pressure. No-slip boundary conditions are imposed on the horizontal walls: $u = 0$ at $y = 0$ and $y = d$. Two consecutive integrations of Eq. A.1 yield

$$\frac{\partial u}{\partial y} = \frac{1}{\mu}\frac{\partial P}{\partial x} y + A$$
$$u(y) = \frac{1}{\mu}\frac{\partial P}{\partial x}\frac{y^2}{2} + Ay + B.$$

The application of the no-slip boundary condition to the above expression for $u(y)$ results in

$$u(y) = \frac{1}{\mu}\frac{\partial P}{\partial x}\frac{y^2}{2} - \frac{1}{\mu}\frac{\partial P}{\partial x}\frac{dy}{2} \boxed{= \frac{1}{2\mu}\frac{\partial P}{\partial x}(y^2 - yd)} \tag{A.2}$$

Eq. A.2 is the planar Poiseuille flow velocity profile. We observe that since the definition of Δp implies $\Delta p < 0$ always holds, it follows that $u(y) > 0$ as indicated in Fig. A.1. Thus the axial velocity profile is parabolic. The maximum axial velocity $u_{\max}$ occurs at the centreline and is given by $2 \times \overline{u}$.

A.2 Two-phase Poiseuille flow

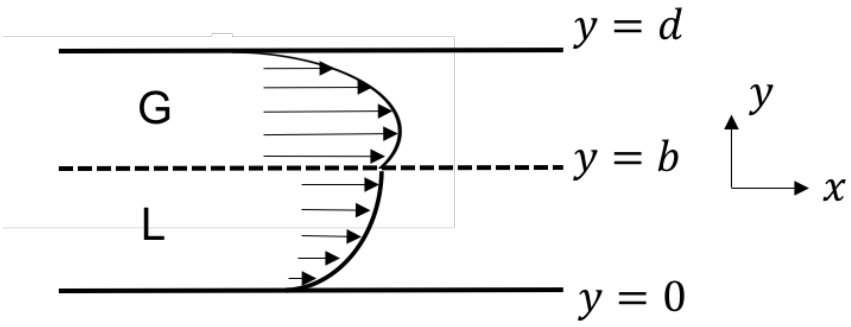

Fig. A.2: Channel pressure drop in two-phase Poiseuille flow.

Another analytical solution to the Navier–Stokes equations can also be derived leading to a two-phase Poiseuille flow. A horizontally-stratified flow of two fluids between two parallel

walls is considered as shown in Fig. A.2. The two-phase Poiseuille flow is a simple interfacial flow. If b is the distance between the bottom horizontal boundary and the interface, and d the distance between the two horizontal boundaries; with $\frac{\partial P}{\partial x}$ linearly increasing along x, the velocity u and pressure p can be calculated by assuming the velocity to be parallel to the x-axis and by assuming the continuity of the velocity and viscous stress tensor at the interface.

For a fully-developed channel flow, and neglecting the gravity and surface tension forces, the steady Navier–Stokes equations become, in terms of force balance, a competition between the pressure forces and the shear stress forces due to the wall velocity gradients:

$$\mu_L \frac{\partial^2 u_L}{\partial y^2} = \frac{\partial P}{\partial x} \tag{A.3}$$

$$\mu_G \frac{\partial^2 u_G}{\partial y^2} = \frac{\partial P}{\partial x} \tag{A.4}$$

subject to the following boundary conditions:

$$\begin{cases} u_L = 0 & \text{at } y = 0 \ \ (1) \\ u_G = 0 & \text{at } y = d \ \ (2) \\ u_L = u_G & \text{at } y = b \ \ (3) \\ \mu_G \dfrac{\partial u_G}{\partial y} = \mu_L \dfrac{\partial u_L}{\partial y} & \text{at } y = b \ \ (4) \end{cases} \tag{A.5}$$

Upon integration we get a velocity profile for u_L and u_G

$$u_L(y) = \frac{1}{\mu_L} \frac{\partial P}{\partial x} \frac{y^2}{2} + A_L y + B_L \tag{A.6}$$

$$u_G(y) = \frac{1}{\mu_G} \frac{\partial P}{\partial x} \frac{y^2}{2} + A_G y + B_G. \tag{A.7}$$

Given the boundary conditions in Eq. A.5 and since the pressure gradient must be equal along the interface, the velocity profile of the two fluids in a two-phase Poiseuille flow are expressed in terms of the pressure gradient. Eq. A.6 and Eq. A.7 become

$$\begin{aligned} u_L(y) &= \frac{1}{\mu_L} \frac{\partial P}{\partial x} \frac{y^2}{2} + \frac{K}{2\mu_L} \frac{\partial P}{\partial x} y \\ &\boxed{= \left[\frac{1}{2\mu_L} y^2 + \frac{K}{2\mu_L} y \right] \frac{\partial P}{\partial x}} \end{aligned} \tag{A.8}$$

$$\begin{aligned} u_G(y) &= \frac{1}{\mu_G}\frac{\partial P}{\partial x}\frac{y^2}{2} + \frac{K}{2\mu_G}\frac{\partial P}{\partial x}y - \frac{1}{\mu_G}\frac{\partial P}{\partial x}\frac{d^2}{2} - \frac{K}{2\mu_G}\frac{\partial P}{\partial x}d \\ &= \boxed{\left[\frac{1}{2\mu_G}(y^2-d^2) + \frac{K}{2\mu_G}(y-d)\right]\frac{\partial P}{\partial x}} \end{aligned} \tag{A.9}$$

where we define

$$K = \frac{\mu_L b^2 - \mu_G b^2 - \mu_L d^2}{\mu_G b - \mu_L b + \mu_L d}. \tag{A.10}$$

As in the case of the standard Poiseuille flow profile (see Section A.1), one can now derive an expression for the mean fluid velocity in each channel of the domain in terms of the pressure gradient. In the bottom liquid channel:

$$\begin{aligned} \overline{u_L} &= \frac{1}{b}\int_0^b u_L(y)dy \\ &= \frac{1}{b}\left[\frac{b^3}{2\mu_L} + \frac{Kb^2}{4\mu_L}\right]\frac{\partial P}{\partial x}\Big|_L. \end{aligned}$$

Hence the pressure gradient in the liquid channel can be determined based on the average speed:

$$\therefore \boxed{\frac{\partial P}{\partial x}\Big|_L = \frac{\overline{u_L}}{\frac{b}{4\mu_L}\left(\frac{2b}{3} + K\right)}} \tag{A.11}$$

The pressure gradient as a function of the average speed in fluid G results in:

$$\begin{aligned} \overline{u_G} &= \frac{1}{d-b}\int_b^d u_G(y)dy \\ &= \frac{1}{d-b}\left[\frac{1}{6\mu_G}(-2d^3 - b^3 + 3d^2 b) + \frac{K}{4\mu_G}(d^2 - b^2 + 2db)\right]\frac{\partial P}{\partial x} \end{aligned}$$

$$\therefore \boxed{\frac{\partial P}{\partial x}\Big|_G = \frac{\overline{u_G}}{\frac{3d^2 b - 2d^3 - b^3}{6\mu_G(d-b)} - \frac{K}{4\mu_G}(d-b)}} \tag{A.12}$$

In order to avoid a gradient in the cross-sectional direction, the pressure gradient of both fluids in the x-direction must be the same. This results in a dependency between the two average speeds. The physical problem is mathematically over-constrained. Therefore, if the properties of the two fluids and the channel heights are fixed, only one mean fluid speed can be selected freely [103, 147]. Either $\frac{\partial P}{\partial x}$ must be the same in the liquid and the gas channel, which means that we do not control the resulting $\overline{u_G}$ and $\overline{u_L}$, since they are automatically set when $u_G(y)$ and $u_L(y)$ are calculated based on Eq. A.8 and Eq. A.8 (see Fig. A.3a). On the

other hand, if one indeed chooses $\overline{u_G}$ and $\overline{u_L}$ in order to solve for Eq. A.12 and Eq. A.12, the resulting two-phase velocity profile

$$u_G\left(y, \frac{\partial P}{\partial x}\Big|_G\right);\ u_L\left(y, \frac{\partial P}{\partial x}\Big|_L\right)$$

is unphysical. Note in Fig. A.3b the gas profile centreline velocity and the unequal pressure gradients.

Rather than to fix the mean injection speed of each fluid – $\overline{u}_G$ and $\overline{u}_L$ – one might choose to fix their corresponding mass flow rate $\dot{m}_{G,L} = \rho_{G,L}\, \mathbf{u}_{G,L}\, h$, where h is the height of the fluid channel, either b for the liquid or $(d-b)$ for the gas. We then solve for Eq. A.11 and Eq. A.12 as a function of b. The point at which the two pressure gradients are equal gives the liquid height that should be used for the liquid injection channel (see Fig. A.4a). For a lower liquid mass flow rate, the liquid film thickness goes down, as expected (Fig. A.4b). We are therefore not in control of the liquid film injection height, but there exists a physical solution to the problem.

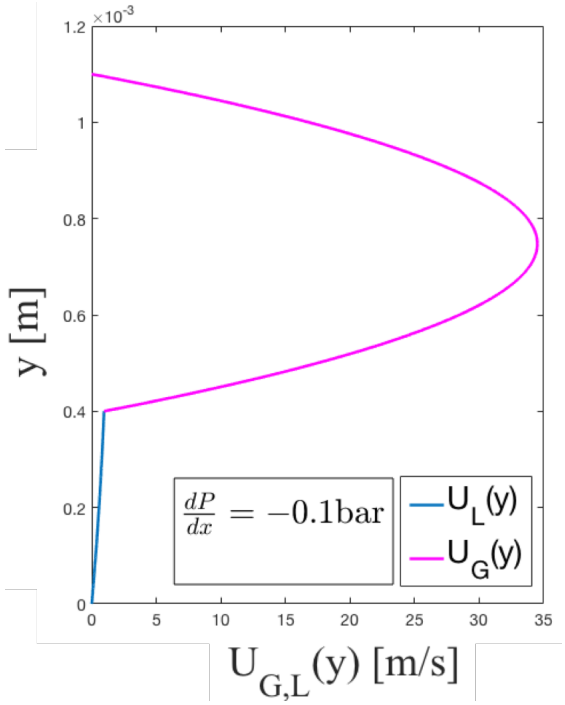

(a) Fixed pressure drop in both fluid channels set to -0.01bar. The velocities adapt themselves.

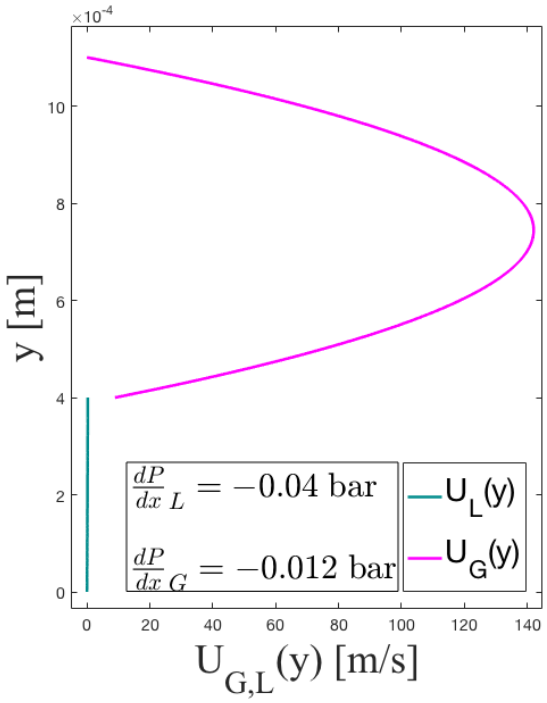

(b) We chose freely the mean injection velocities in each channel: $\overline{u_G} = 20$m/s and $\overline{u_L} = 5$m/s. The pressure gradients turn out not to be equal.

Fig. A.3: Two-phase Poiseuille flow profiles from Eq. A.8 and Eq. A.9. Both fluid channel heights are fixed. We then either fix the pressure drop in both channels (**a**) or the mean injection speeds (**b**).

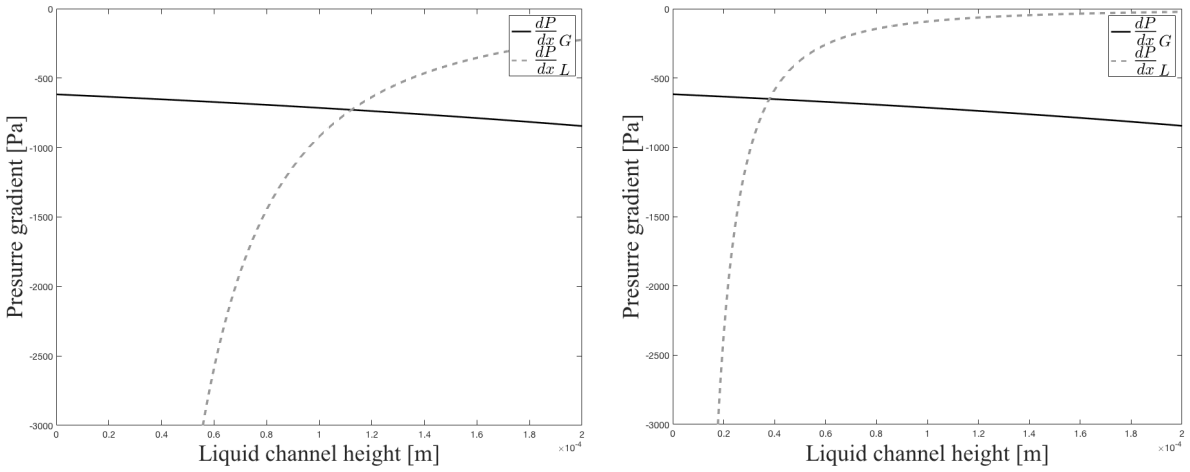

(a) $\dot{m}_G = 0.015$kg/s and $\dot{m}_L = 2.6 \times 10^{-6}$kg/s. **(b)** $\dot{m}_L$ reduced down to $= 2.6 \times 10^{-7}$kg/s

Fig. A.4: Pressure gradient in each fluid channel as a function of the liquid channel height from Eq. A.11 and Eq. A.12. Experimental data for mass flow rates in prefilming airblast atomisation are from Gepperth et al. [70]. The liquid channel height b has been relaxed. We solve for b when the two pressure gradients are equal.

A.3 Analytical solution for two-phase Poiseuille flow with wall slip

Our purpose here is to report that an exact solution of the Navier–Stokes equations with a slip boundary can be determined, which is different from the previous conventional Poiseuille flow. In this framework, the no-slip condition for the velocity is relaxed at the top wall boundary and the fluid is allowed to slip at the contact line, which eliminates the stress singularity. If we now relax the upper boundary condition to be consisting of a wall slip by setting $\overline{u_G} = u_d$ at $y = d$, Eq. A.6 and Eq. A.7 are now subject to

$$\begin{cases} u_L = 0 & \text{at } y = 0 \ \ (1) \\ \mu_G \dfrac{\partial u_G}{\partial y} = \mu_L \dfrac{\partial u_L}{\partial y} & \text{at } y = b \ \ (2) \\ u_L = u_G & \text{at } y = b \ \ (3) \\ u_G = u_d & \text{at } y = d \ \ (4) \end{cases} \tag{A.13}$$

Eq. A.6 becomes

$$\begin{aligned} u_L(y) &= \frac{1}{\mu_L}\frac{\partial P}{\partial x}\frac{y^2}{2} + \frac{K}{2\mu_L}\frac{\partial P}{\partial x}y + \frac{J}{2\mu_L}u_d y \\ &\boxed{= \Big[\frac{1}{2\mu_L}y^2 + \frac{K}{2\mu_L}y\Big]\frac{\partial P}{\partial x}\Big|_L + \frac{J}{2\mu_L}u_d y} \end{aligned} \tag{A.14}$$

and Eq. A.7 becomes

$$\begin{aligned} u_G(y) &= \frac{1}{2\mu_G}\frac{\partial P}{\partial x}(y^2-d^2) + \frac{K}{2\mu_G}\frac{\partial P}{\partial x}(y-d) + \frac{J}{2\mu_G}u_d(y-d) + u_d \\ &\boxed{= \Big[\frac{1}{2\mu_G}(y^2-d^2) + \frac{K}{2\mu_G}(y-d)\Big]\frac{\partial P}{\partial x}\Big|_G + \frac{J}{2\mu_G}u_d(y-d) + u_d} \end{aligned} \tag{A.15}$$

where K is defined by Eq. A.10 and

$$J = \frac{2\mu_L\mu_G}{[\mu_G b - \mu_L b + \mu_L d]} \tag{A.16}$$

Both $u_L(y)$ and $u_G(y)$ depend on u_d and their respective pressure gradient $\frac{\partial P}{\partial x}\Big|_L$ and $\frac{\partial P}{\partial x}\Big|_G$.

Integrating Eq. A.14 and Eq. A.15, the average velocities in the liquid and gas channels become

$$\begin{aligned} \overline{u_L} &= \frac{1}{b}\int_0^b u_L(y)dy \\ &\boxed{= \frac{1}{6\mu_L}\frac{\partial P}{\partial x}b^2 + \frac{K}{4\mu_L}\frac{\partial P}{\partial x}b + \frac{Ju_d}{4\mu_L}b} \end{aligned} \tag{A.17}$$

$$\begin{aligned} \overline{u_G} &= \frac{1}{d-b}\int_b^d u_G(y)dy \\ &\boxed{= \frac{1}{d-b}\frac{1}{6\mu_G}\frac{\partial P}{\partial x}\Big[-2d^3 - b^3 + 3d^2 b\Big] - \Big[\frac{K}{4\mu_G}\frac{\partial P}{\partial x} + \frac{J}{4\mu_G}u_d\Big](d-b) + u_d} \end{aligned} \tag{A.18}$$

If we now wish to fix $\overline{u_G}$ and $\overline{u_L}$, as well as b and d, we can solve Eq. A.17 and Eq. A.18 as simultaneous equations to obtain a unique combination of $\frac{\partial P}{\partial x}$ and u_d – subject to the compatibility conditions in Eq. A.13 – that allows a physical solution to exist. We first solve Eq. A.17 for u_d which gives,

$$\overline{u_L} - \frac{1}{6\mu_L}\frac{\partial P}{\partial x}b^2 - \frac{K}{4\mu_L}\frac{\partial P}{\partial x}b = \frac{Jbu_d}{4\mu_L}$$

$$u_d = \frac{4\mu_L \overline{u_L}}{Jb} - \frac{2b}{3J}\frac{\partial P}{\partial x} - \frac{K}{J}\frac{\partial P}{\partial x}$$
$$\boxed{= \left[-\frac{2b}{3J} - \frac{K}{J}\right]\frac{\partial P}{\partial x} + \frac{4\mu_L \overline{u_L}}{Jb}} \tag{A.19}$$

Now substituting u_d in Eq. A.18 to solve for $\frac{\partial P}{\partial x}$, assuming the pressure gradient is the same in both fluids

$$\overline{u_G} = \frac{1}{d-b}\frac{1}{6\mu_G}\frac{\partial P}{\partial x}[-2d^3 - b^3 + 3d^2 b]$$
$$- \frac{K}{4\mu_G}\frac{\partial P}{\partial x}(d-b) - \frac{J}{4\mu_G}(d-b)\left[\frac{4\mu_L \overline{u_L}}{Jb} - \frac{2b}{3J}\frac{\partial P}{\partial x} - \frac{K}{J}\frac{\partial P}{\partial x}\right]$$
$$+ \left[\frac{4\mu_L \overline{u_L}}{Jb} - \frac{2b}{3J}\frac{\partial P}{\partial x}\bigg|_G - \frac{K}{J}\frac{\partial P}{\partial x}\right]$$

And therefore,

$$\frac{\partial P}{\partial x} = \left[\frac{-\mu_L \overline{u_L}}{\mu_G b}(d-b) - \frac{4\mu_L \overline{u_L}}{Jb} + \overline{u_G}\right] \times \left[\frac{-2d^3 + 4d^2 b - 2db^2}{(d-b)6\mu_G} - \frac{2b + 3K}{3J}\right]^{-1} \tag{A.20}$$

Fig. A.5 shows the result obtained for chosen mean injection speeds, as well as geometrical dimensions and slip line velocity. It is therefore possible to relax the upper boundary condition into a slip condition and get a physical two-phase Poiseuille flow profile with no cross-sectional pressure gradient.

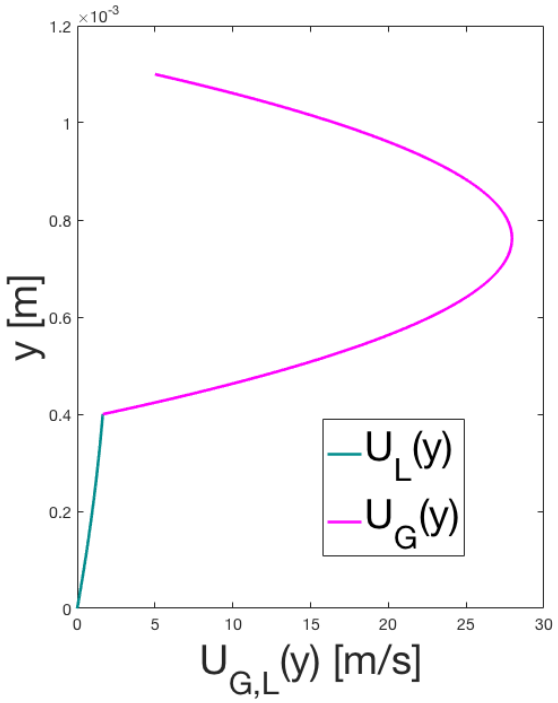

Fig. A.5: Two-phase Poiseuille flow profile with chosen mean injection speeds ($\overline{u}_G = 5$m/s and $\overline{u}_L = 0.26$m/s), as well as geometrical dimensions and slip line velocity ($u(y = d) = 5$m/s).